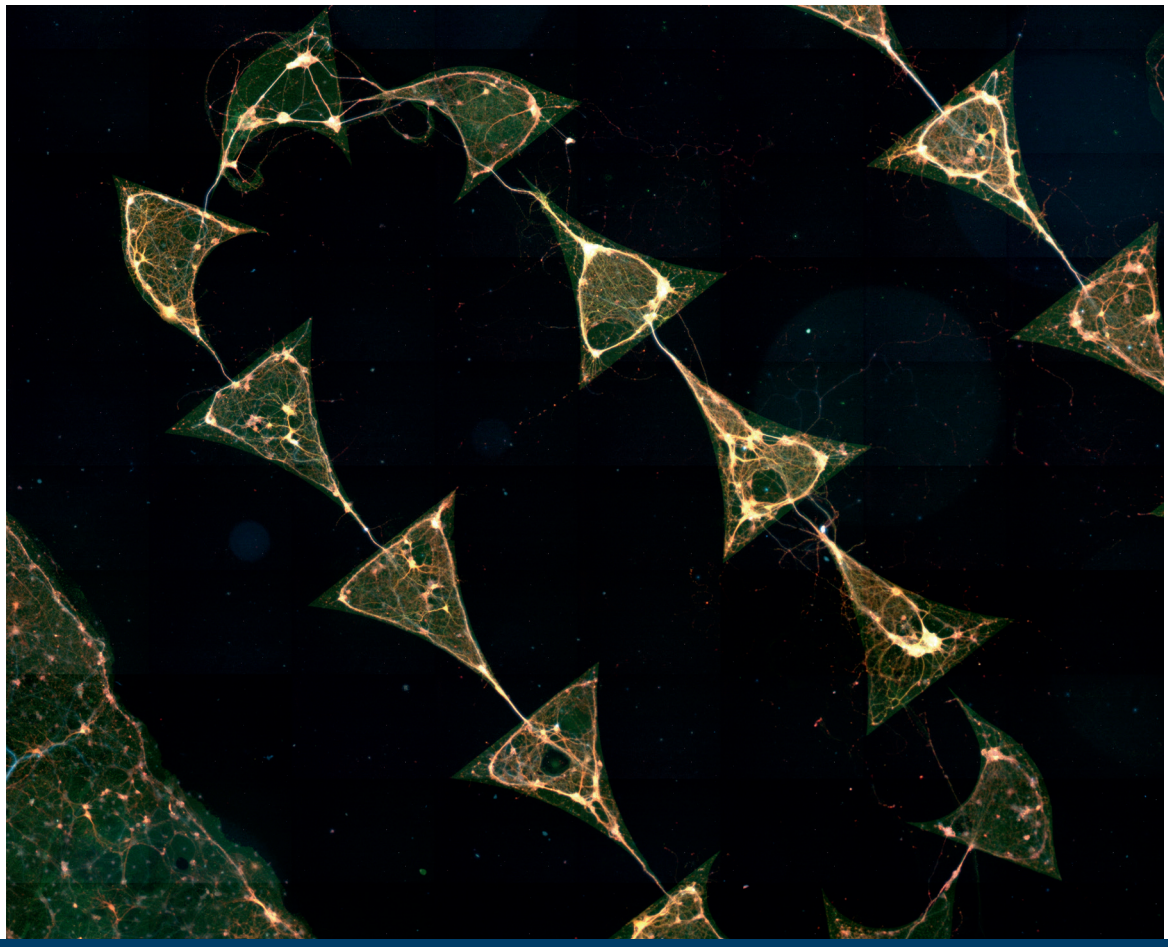

Optogenetic and electrical investigation of network dynamics in patterned neuronal cultures

Timm Jakob Julian Hondrich

Information
Band / Volume 68
ISBN 978-3-95806-555-0

Mitglied der Helmholtz-Gemeinschaft

JÜLICH
Forschungszentrum

Schriften des Forschungszentrums Jülich
Reihe Information / Information Band / Volume 68

Forschungszentrum Jülich GmbH
Institute of Biological Information Processing
Bioelectronics (IBI-3)

Optogenetic and electrical investigation of network dynamics in patterned neuronal cultures

Timm Jakob Julian Hondrich

Schriften des Forschungszentrums Jülich
Reihe Information / Information Band / Volume 68

ISSN 1866-1777 ISBN 978-3-95806-555-0

Bibliografische Information der Deutschen Nationalbibliothek.
Die Deutsche Nationalbibliothek verzeichnet diese Publikation in der
Deutschen Nationalbibliografie; detaillierte Bibliografische Daten
sind im Internet über http://dnb.d-nb.de abrufbar.

Herausgeber und Vertrieb:	Forschungszentrum Jülich GmbH Zentralbibliothek, Verlag 52425 Jülich Tel.: +49 2461 61-5368 Fax: +49 2461 61-6103 zb-publikation@fz-juelich.de www.fz-juelich.de/zb
Umschlaggestaltung:	Grafische Medien, Forschungszentrum Jülich GmbH
Druck:	Grafische Medien, Forschungszentrum Jülich GmbH
Copyright:	Forschungszentrum Jülich 2021

Schriften des Forschungszentrums Jülich
Reihe Information / Information, Band / Volume 68

D 82 (Diss. RWTH Aachen University, 2021)

ISSN 1866-1777
ISBN 978-3-95806-555-0

Vollständig frei verfügbar über das Publikationsportal des Forschungszentrums Jülich (JuSER)
unter www.fz-juelich.de/zb/openaccess.

"Someone once tried to build a machine as efficient as the brain. The only problem was, it would have had to be bigger than London — do you remember London? — and powered by the entire European grid. And that was just a human brain. Mine's much more complex."

THE 4TH DOCTOR, DOCTOR WHO

Abbreviations

µCP	microcontact printing
R_m	membrane resistance
AAV	adeno-associated virus
ACC	average clustering coefficient
AIS	axon initial segment/action potential initiation site
AP	action potential
ATP	adenosine triphosphate
cal-AM	calcein-acetoxymethylester
CaM	calmodulin
ChR2	channelrhodopsin 2
CSV	comma seperated value
CT1	curved triangle 1 pattern
CVD	chemical vapor deposition
DI	deionized
DIV	day *in vitro*
dsCT	downscaled CT1 patterns
ePSP	excitatory postsynaptic potential
EtHD	ethidium homodimer
fComInput	functional community input pattern
FITC	fluorescein isothiocyanate
FOTCS	(tridecafluoro-1,1,2,2-tetrahydrooctyl)trichlorosilane
GC	genome copies

GECI	gentically encoded calcium indicator
GEf	global efficiency
GFP	green fluorescent protein
GLYMO	(3-glycidyloxypropyl)trimethoxysilane
GTE	generalized transfer entropy
GUI	general user interface
HBSS	Hank's balanced salt solution
IPI	inter-peak interval
iPSP	inhibitory postsynaptic potential
ITO	indium tin oxide
MEA	microelectrode array
MIP	maximum intensity projection
MOI	multiplicity of infection
NB	Neurobasal
neuroCAP	neuronal pattern for circulating action potentials
neuroCapTiH	modified version of neuroCAP
PBS	phosphate-buffered saline
PDMS	polydimethylsiloxane
PLL	poly-L-lysine
POP	polyolefine plastomer
PS	polystyrene
RIE	reactive ion etching
ROI	region-of-interest
ROI	region-of-interest
slm	standard litre per minute
SNE	synchronous network event
SPP	surface plasmon polariton
TE	transfer entropy
UV	ultraviolet
Xcor	cross-correlation

Abstract

Our nervous system is one of the most complex systems on earth. To investigate some of the nervous system's basic principles, neuronal cell cultures provide a highly controllable, experimental platform of reduced complexity. These basic principles include periods of synchronous neuronal activity that can be an important mediator of higher functions such as memory. Another basic principle governing the nervous system's functionality is its modularity. Anatomical modularity can be modeled *in vitro* using neuronal patterning techniques, one of which is microcontact printing. The functional connectivity of such patterned networks was interrogated using optogenetic techniques, such as calcium indicators and light-gated ion channels, or electrophysiological methods, such as patch-clamping or microelectrode arrays. In the first part of this thesis, I modified different methods offering control over neuronal cell cultures. The control over cellular localization could be improved by chemically uncoupling substrate from coating via the silane GLYMO. This prevents cells almost completely from growing on the cell-repellent background instead of the cell-attractive pattern. Moreover, microelectrode arrays with holey gold as a conductive material were used for electrical recordings. With its plasmonically induced, threefold increase in transparency compared to solid gold, holey gold can be combined with tools for controlling neurons optically, such as optogenetics. In the second and third part of this thesis, I investigated the functional properties - such as signal propagation, synchronicity, and network connectivity - of modular patterned neuronal networks in an all-optical approach. The triangular, anatomical modules direct neuronal action potentials preferentially towards their tip and subsequent modules. This is true for both main designs, an elliptic one and one with a small upstream module connected to a larger population. This directionality, and an increased calcium response to same-module stimulations, indicates that triangular anatomical modules also represent functional modules. Although the mean connectivity strength within the triangular module seems to contradict this assump-

tion, the coherence of synchronous network events differs slightly when elicited in different modules. However, the synchronicity of the stimulus affects network event coherence much more strongly than stimulus location. In conclusion, I could show using an optimized experimental system that the dynamics of neuronal synchronous network events depend on the position and coherence of their initiating activity in a multi-modular network.

Zusammenfassung

Unser Nervensystem ist eines der komplexesten Systeme unseres Planeten. Um einige der grundlegenden Prinzipien des Nervensystems experimentell zu untersuchen, können leicht zu kontrollierende neuronale Zellkulturen verwendet werden. Diese grundlegenden Prinzipien umfassen Zeitabschnitte synchroner neuronaler Aktivität, die ein wichtiger Bestandteil von höheren Hirnfunktionen, wie Erinnerung, sind. Ein weiteres die Funktionalität des Nervensystems beeinflussendes, Prinzip ist die Modularität. Anatomische Modularität kann *in vitro* durch in festgelegten Mustern wachsende neuronale Netzwerke modelliert werden, zum Beispiel mit Hilfe des Mikrokontaktdrucks. Die Funktionalität solcher Netzwerke wurde durch optogenetische Techniken, z.B. Kalzium-Indikatoren oder lichtsensitive Ionenkanäle, oder elektrophysiologische Methoden, z.B. Patch-Clamp oder Mikroelektrodenarrays, untersucht. Im ersten Teil dieser Arbeit veränderte ich verschiedene Methoden zur Ausübung von Kontrolle über neuronale Zellkulturen. Die Kontrolle über die Position der Zellen wurde durch die chemische Entkopplung (durch GLYMO) des Substrats von der Beschichtung erhöht. Dies verhindert fast gänzlich das Wachstum von Zellen auf dem zellabweisenden Hintergrund, anstatt auf dem zellfreundlichen Muster. Des Weiteren wurden Mikroelektrodenarrays mit löchrigem Gold als leitfähigem Material für die Aufnahme elektrischer Signale genutzt. Mit seinem plasmonisch angeregten, dreifachen Anstieg der Transparenz im Vergleich zu solidem Gold, kann löchriges Gold mit Hilfsmitteln zur optischen Kontrolle über Neuronen, wie der Optogenetik, kombiniert werden. Im zweiten und dritten Teil dieser Arbeit untersuchte ich die funktionellen Eigenschaften - wie Signalweiterleitung, Synchronizität und Netzwerkkonnektivität - von modularen, neuronalen Netzwerken mit einem rein optischen Ansatz. Die anatomischen Dreiecksmodule lenken neuronale Aktionspotentiale bevorzugt in Richtung ihrer Spitze und anschließender Module. Dies gilt für beide Hauptdesigns, eine Ellipse aus Dreiecken und eines mit einem vor eine große Population vorgelagerten Dreiecksmodul. Diese Direktionalität, zusammen

mit einer erhöhten Kalziumantwort auf Stimulationen des gleichen Moduls, deutet an, dass anatomische Dreiecksmodule auch funktionellen Modulen entsprechen. Obwohl die durchschnittliche Konnektivitätsstärke innerhalb der Dreicksmodule dieser Annahme zu widersprechen scheint, unterscheidet sich die Kohärenz von in verschiedenen Modulen ausgelösten synchronen Netzwerkereignissen leicht. Jedoch wirkt sich die Synchronizität des Stimulus stärker auf die Kohärenz der Netzwerkereignisse aus als der Stimulationsort. Ich konnte also mit Hilfe eines optimierten experimentellen Systems zeigen, dass die Dynamik neuronaler synchroner Netzwerkereignisse von der Position und Kohärenz ihrer intialen Aktivität in einem multi-modularen Netzwerk abhängt.

Table of Contents

Introduction

"How do we think?" For ages, people have been wondering about our ability to think from a religious, philosophical, psychological, and biological point of view. Although the field of neuroscience rapidly increased our understanding of the incredibly complex brain (see section 1.1), many of the underlying principles governing neuronal computation and its modulation by manifold biological processes remain elusive. Neuroscience tackles the challenge of uncovering such basic principles on different levels or scales. The invention of new technological tools such as multi-photon microscopy, ever improving computers, or CRISPR/Cas has started a huge wave of studies conducted *in vivo*. However, some of the basic, generic principles of neuronal networks independent of their location in the nervous system can also be investigated in highly controllable and manipulatable neuronal cell culture systems *in vitro* (see section 1.1.2). These basic principles include: the encoding of information through sparse neuronal activity; the modulation of neuronal activity; the presence of coordinating cells; synchronicity within neuronal networks; the hierarchical modularity of such networks; and more. In this thesis, I refined or optimized techniques for controlling the behavior of neuronal networks, such as optogenetics, MEA devices and neuronal patterning. Then, I used such methods - in particular optogenetics and neuronal patterning - to investigate synchronicity and directionality in modular neuronal networks (see section 1.1.3).

By now, neurons in culture can be controlled and manipulated in various ways, one of which is neuronal patterning (for general reviews, see Aebersold et al. (2016); Martinez-Rivas et al. (2017)) via microcontact printing (μCP; see section 1.4). Although μCP is a well-established technique using different coating solutions (Albers and Offenhäusser, 2016; Nam et al., 2006; Offenhäusser et al., 2007), its reliability strongly depends on the substrate and application. One of these applications is the investigation of patterned neuronal networks with optogenetics (see section 1.3). As many microscopy setups depend on transparent substrates, a cheap option for such a substrate is glass. However, glass is a quite undefined and variable material so that it has to be modified (Hondrich et al., 2019b)

or chemically uncoupled from the coating (Hofmann, 2009; Nam et al., 2006) to allow for precise and reliable patterning. On microelectrode arrays (MEA; see section 1.2.2) (Spira and Hai, 2013; Stett et al., 2003), the passivation materials are usually (with exceptions, such as the polyimide HD-8820) less variable than glass. However, for each passivation material and pattern, the μCP process needs to be optimized to ensure reliable recordings. Ideally, such MEAs can be combined with optogenetic techniques (Chen et al., 2017; Mosbacher et al., 2020; Yoo et al., 2020), for which a completely transparent MEA device is beneficial. Although many standard materials used as MEA substrates (e.g. quartz glass) and passivations (e.g. polyimides (Im and Seo, 2016) or ONO (Hofmann et al., 2011)) are inherently transparent, the conducting material is usually not. The most commonly used transparent materials are indium tin oxide (ITO) (Gross et al., 1985) and the non-standard material graphene (Kireev et al., 2017a), although ITO is usually not used for the electrode opening itself (Multi Channel Systems MCS GmbH). In Chapter 3 of this thesis, I tackled the above mentioned challenges and set out to improve μCP on glass via chemical uncoupling, to establish MEA recordings from population patterns (Albers et al., 2015), and to test holey gold as a transparent and tunable electrode material potentially suitable for its combination with optogenetics.

Dual optogenetic systems for combined calcium imaging and neuronal laser stimulation are increasingly used in *in vivo* studies (Emiliani et al., 2015; Kim et al., 2017; Ronzitti et al., 2018). Electrophysiological methods have a higher temporal resolution and directly measure APs, rather than the pooled calcium influx during multiple APs (see also section 1.1.1.2 and section 1.1.1.3). However, spatial resolution of optical techniques is often superior, making a direct correlation of a recorded signal and the anatomical position of the recorded cell possible (see also section 1.3). With adeno-associated viruses as a delivery vector, a large fraction of the imaged cells (up to 90%) can be monitored (Jin et al., 2016). Curiously, such dual optogenetic, all-optical systems have rarely been used in neuronal cell cultures (Hu et al., 2019; Mosbacher et al., 2020). Despite its advantages, this methodology has, to my knowledge, never been attempted to be used in combination with patterned neuronal networks. After having successfully used calcium imaging to monitor

the spontaneous activity of patterned neurons in section 4.3 of Chapter 4, I established an all-optical system for patterned neuronal networks in section 4.4, and used it in section 4.5 and Chapter 5.

Following the investigation and refinement of different methods for controlling neuronal networks *in vitro*, I turned towards their application. Cellular patterning was first applied with the aim to establish a system for fundamental research of cell growth and cell activity modulation (Mrksich et al., 1997). Patterning was then adapted for neuronal cultures, mainly to align soma positioning with MEA electrodes (James et al., 2004) and control neurite outgrowth and thereby microcircuit connectivity (Offenhäusser et al., 2007). However, Feinerman et al. (2005) started to use neuronal patterning to investigate signal propagation in axonal tracts *in vitro*. Later, the same group utilized neuronal patterning to influence the output direction of a neuronal population signal in what they referred to as "neuronal diodes" (Feinerman et al., 2008). With a set of differently patterned neuronal populations (including diodes), they could build "neuronal logic devices" and even the prototype of a neuronal oscillating device. Inspired by this study, Albers and Offenhäusser (2016) optimized the diode design and such population patterning for μCP. Furthermore, they implemented these optimized, curved triangle (CT) patterns into a larger loop pattern to observe neuronal circulating action potentials (neuroCAP) (Albers, 2016). Forró et al. (2018) implemented a similar loop pattern using microchambers as patterning technique and could achieve signal propagation in a preferential direction. However, in this pattern, the analysis of individual neurons is very challenging due to strong cluster formation. Moreover, the study lacks an evaluation of the pattern's ability to allow for full action potential (AP) circulation. In Chapter 4, I investigated whether downscaling CT patterns preserves their directionality (following Irina Tihaa's unpublished work). Moreover, I aimed to improve the design of the neuroCAP pattern and optically investigated signal propagation across multiple CT structures in such a modular loop.

Synchronous network events (SNE) are a ubiquitous phenomenon in the nervous sys-

tem (see section 1.1.3) and can be observed across scales and experimental systems. These systems range from *in vivo* experiments (Egorov and Draguhn, 2013) over brain slices (Buzsáki, 2015) down to neuronal cell cultures (Lonardoni et al., 2017; Pasquale et al., 2008; Wagenaar et al., 2006b). Neuronal cell cultures are a rather simple system, which allows computational simulations to more accurately model such a neuronal network than an extremely complex environment such as a living brain. Therefore, such models offer increasingly precise insights into the generation and characteristics of SNEs (Fardet et al., 2018; Gritsun et al., 2010; Masquelier and Deco, 2013). However, these models usually try to explain the influence of a few, selected properties (like adaptive synapses in Fardet et al. (2018)) on SNE behavior, thereby neglecting the influence of other certain aspects of a biological neuronal network. One of these aspects is the impact of anatomical and functional modularity on network activity and SNE generation (see also section 1.1.3.2). A series of studies could demonstrate that anatomical modules are separate computational entities with unique intra-modular attributes such as a high functional connectivity (Tsai et al., 2008) and fast spike sequences (Pan and Sinha, 2009). These modular entities control each other in a variable fashion (Tsai et al., 2008). They communicate via slower spike sequences (Pan and Sinha, 2009) that get more segregated and diverse with reduced anatomical connection strengths (Yamamoto et al., 2018). Other factors increasing the diversity of slow, inter-modular spike sequences are an increased coordinating activity by inhibitory neurons (Shein-Idelson et al., 2016) and stronger modularity (Okujeni et al., 2017). On the other hand, functional modules can be "hidden" within homogeneously growing networks, thus not always correlating with anatomical modules (Lonardoni et al., 2017). These communities with high functional connectivity based on their spontaneous activity most likely initiate SNEs (Lonardoni et al., 2017), probably via the activity of certain leader cells (Pasquale et al., 2017). Using the optimized set of methods described above, I investigated in Chapter 5 the impact of evoked modular activity on SNE generation. For this, I developed a neuronal pattern containing a small module of individual (unclustered) neurons connected to a larger neuronal network. Moreover, I examined the functional influence of different modes of evoked activity on the neuronal networks growing in such patterns using SNE characterization and graph theoretical connectivity models.

Chapter 1

Fundamentals

1.1 The nervous system and its neurons

Already in ancient Egypt, some researchers may have suspected the importance of the inconspicuous whitish gray mass within a human skull for body control. They termed this mass "brain". However, the general public probably regarded the organ as negligible, indicated by the removal of the mass during mummification (as compared to other organs) (González, 2018). In the millenia following the first neuroscientific insights in ancient Egypt, only few occasional researchers slowly added to humanity's understanding of the brain. They mainly contributed with insights into brain structure. Then, in the 19th century, the density of important neurophysiological discoveries rapidly increased. Jean-Pierre Flourens partly disabled body control of animals by systematically introducing lesions to different parts of their brains. Emil du Bois-Reymond and Hermann von Helmholtz measured the speed of electrical pulses through nerves, and Richard Caton recorded electrical activity in the cerebrum of animals. Camillo Golgi discovered a staining method for neurons that was used by Charles Scott Sherrington and, most extensively, by Santiago Ramón y Cajal to demonstrate that the nervous system comprised a multitude of individual units (neurons, see Figure 1.1 A) separated by and communicating via small gaps (synapses) (Bear et al., 2007e). At the same time, Rudolf Virchow discovered that the mass between the neurons, so far termed glia (Greek for "glue"), also consisted of individual cells, for example astrocytes and microglia, supporting the neurons around them (Benjamin Kacerovsky and Murai, 2016). Today, we know that the nervous system integrates sensory information, enables higher cognitive functions, and plays a role in the

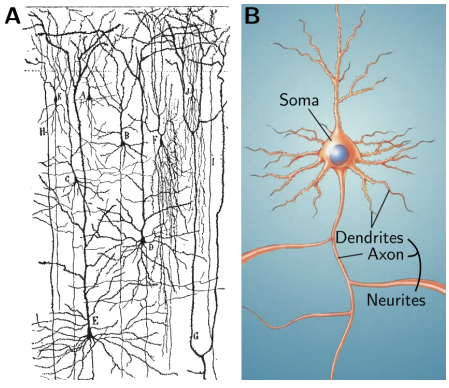

Figure 1.1 – Neurons. (A) Santiago Ramón y Cajal drew thousands of neurons that he stained with the Golgi staining. **(B)** A stereotypical neuron comprises a soma with the nucleus, and branched neurons that are further subdivided into dendrites and the axon. Both adapted from Bear et al. (2007e).

control or at least regulation of every bodily function. A wide variety of tools exist to investigate the brain and its neurons on different scales and in different modalities.
In this fundamentals section, I will first review the development, structure and function of neuronal networks as the building blocks of the nervous system. Then, I will elucidate the techniques and methods used in this thesis.

1.1.1 The Neuron - Structure and Function

The cells forming the nervous system can be subdivided into glia and neurons. Glia cells play many important roles in nutrient distribution (astroglia), neuronal immune responses (microglia), isolation of neurons (oligodendrocytes), amongst others (Benjamin Kacerovsky and Murai, 2016). However, the main focus of this thesis lies on neurons and their networks. A neuron can be described as the smallest functional unit of the nervous system's eletrical network activity. A mature neuron usually is divided into three major compartments. The cell body (or soma) contains the nucleus and some of the other essential cellular components such as parts of the endoplasmic reticulum and Golgi complex. Dendrites receive inputs from upstream neurons. And axons send outputs to (sometimes very far away) downstream neurons (see Figure 1.1 B).

1.1.1.1 Resting Potential

The entire cell membrane of a neuron contains ion channels and transporters that enable the neuron to modify the electrical potential across the membrane. The main types of ions playing a role in this membrane potential include potassium (K^+), sodium (Na^+), chloride (Cl^-), and calcium (Ca^{2+}). At rest, these ions are kept at approximately constant concentrations (Table 1.1) by active ion transporters (most importantly the Na^+/K^+ exchanger and the Ca^{2+} pump) that convert chemical energy in the form of adenosine triphosphate (ATP) into kinetic energy of the pumping process (Bear et al., 2007c). For a membrane selectively permeable for one of these ions, the equilibrium potential E_{ion} due to the ionic conductances across the membrane can be calculated via the Nernst equation (Bear et al., 2007c):

Ion	Concentration outside [mM]	Concentration inside [mM]	Equilibrium potential [mV]
K^+	5	100	-80
Na^+	150	15	62
Ca^{2+}	2	$\leq$0.0002	123
Cl^-	150	13	-65

Table 1.1 – Ion concentrations and equilibrium potentials of the ions mainly contributing to neuronal membrane potentials.

$$E_{ion} = 2.303 \, \frac{RT}{zF} \, log_{10} \frac{[ion]_{out}}{[ion]_{in}} \tag{1.1}$$

where R is the gas constant, T is the temperature, z is the charge of the ion, F is Faraday's constant, and $[ion]_{out}$ and $[ion]_{in}$ are the concentrations outside of and inside the cell, respectively. At room temperature, the term $2.303\frac{RT}{zF}$ can be calculated as 61.54 mV for K^+ and Na^+, -61.54 mV for Cl^-, and 30.77 mV for Ca^{2+}. In a resting neuron, K^+ has the greatest influence on the membrane potential via K^+ channels whilst Na^+ has the second-largest influence via leak currents through the membrane and not completely closed channels. Ca^{2+} and Cl^- can be neglected due to their minor influence. Considering this, the resting membrane potential V_m of a stereotypical neuron can be calculated with the a modified Nernst equation (Equation 1.1), the Goldman equation (Bear et al., 2007c):

$$V_m = 61.54 \; mV \; log_{10} \frac{P_K[K^+]_{out} + P_{Na}[Na^+]_{out}}{P_K[K^+]_{in} + P_{Na}[Na^+]_{in}} \tag{1.2}$$

where P_{Na} and P_K denote the relative permeabilities of the respective ions. Choosing $P_{Na} = 1$ and $P_K = 40$ (meaning that the membrane is 40 times more permeable to K^+ than to Na^+), we get a resting membrane potential of -65 mV (Bear et al., 2007c). This corresponds well with experimental values via the patch clamp technique (see section 1.2.1).

1.1.1.2 Action Potential

When the dendrites of a neuron receive an input, the neuronal membrane gets slightly depolarized (see also next section). If the depolarization by multiple inputs is strong

enough, very fast voltage-gated Na^+ channels open at a certain threshold voltage, usually around -50 mV (see Figure 1.2). This textbook view has recently been called into question as Sardi et al. (2017) suggested that neurons might in fact have multiple threshold voltages. Because the equilibrium potential of Na^+ is much more positive than that of K^+ (see Table 1.1), Na^+ starts to stream into the cell and quickly depolarizes the cell to about +30 mV. At this time point (1-2 ms after the opening of the channels), the voltage-gated Na^+ channels close and depolarization-triggered, voltage-gated K^+ channels open. Consequently, K^+ starts streaming out of the cell, repolarizing the cell. However, the efflux of K^+ ions continues until a potential close to potassium's equilibrium potential (-70 to -80 mV). This hyperpolarization occurs due to the high concentration intracellular Na^+ ions and the slow closing time of the voltage-gated K^+ channels. Finally, the membrane potential and ion concentrations are restored to their resting state by the closing of voltage-gated K^+ channels and the Na^+/K^+ exchanger. The whole process from the onset of depolarization to the restoration of the resting potential is called the action potential (AP) and lasts about 3-5 ms (Bear et al., 2007d). The membrane current I_m generated by the above described ion channels during an AP was elegantly described by Hodgkin and Huxley (1952):

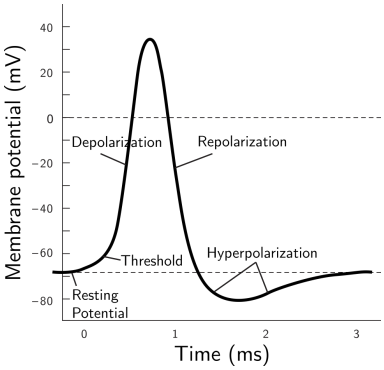

Figure 1.2 – The action potential. An action potential has a typical duration of 1-5 ms and includes distinct phases. Adapted from Bear et al. (2007d).

$$I_m = g_{leak}(V_m - E_{leak}) + g_K n^4 (V_m - E_K) + g_{Na} m^3 h (V_m - E_{Na}), \tag{1.3}$$

where $1/g_{leak}$ is the passive membrane resistance R_{leak}, and g_K and g_{Na} are the conductances of the respective ion channels. E_{leak} is the resting potential of the membrane, and E_K and E_{Na} are the reversal potentials of the ion channels. This formula was adapted and extended multiple times from then on to describe different types of neurons and include

more types of ionic currents (Dayan and Abbott, 2001b).

While Na^+ and K^+ fluxes are the driving forces behind the AP, the somatic, intracellular Ca^{2+} concentration also changes (Ali and Kwan, 2019; Grienberger and Konnerth, 2012; Smetters et al., 1999). During depolarization, somatic voltage-gated L-type Ca^{2+} channels (see also Figure 1.9 A) open alongside presynaptic, also voltage-gated, P/Q- and N-type channels (see also Figure 1.3) (Ali and Kwan, 2019; Wang et al., 2019b). The resulting increase of the Ca^{2+} concentration by about 40 nM is enhanced by the release of calcium from intracellular stores such as the endoplasmic reticulum via calcium-activated ryanodine receptors (see also Figure 1.9 A) (Grienberger and Konnerth, 2012). This leads to an overall increase in Ca^{2+} of about 10 to 100 times of its concentration at rest. This increase happens within less than 2 ms, after which the Ca^{2+} concentration is slowly reset with a decay time constant of about 100 ms. Ca^{2+} reset is mediated by the Na^+/Ca^{2+} exchanger of the cell membrane and mitochondria, the SERCA pump of the endoplasmic reticulum, and other players.

The voltage-gated Na^+ channels cannot be reopened after closing at depolarization during the so-called the refractory period. Therefore, APs progress along the axon in one direction. Usually, the AP is generated at the axon hillock, a piece of membrane - close to the soma - that exhibits a high density of voltage-gated Na^+ channels (also called the action potential initiation site or axon initial segment (AIS)). The AP then propagates towards the tip of the axon (see also the following section), where a synapse with a downstream neuron is formed. In some cases, retrograde APs have been reported that back-propagate into the dendritic tree instead of the axon (Bakkum et al., 2013; Markram et al., 1995).

1.1.1.3 Synapses, the Postsynaptic Potential, and Intraneuronal Computation

Neurons are interconnected via synapses. A synapse chemically uncouples the electrical activity of two neurons from each other with a short delay of roughly 1 ms. It is formed by specialized parts of the cell membranes of a pre- and a postsynaptic neuron, and the gap (20-50 nm) between them (Bear et al., 2007a). Newer models include a third cellular player in a synapse - an astrocytic glia cell that supports the efficient signal transduction

from one neuron to the next (Bazargani and Attwell, 2016). The specialized membrane region of the presynaptic neuron is called the axon terminal or synaptic bouton whereas the membrane region of the postsynaptic neuron is a small protrusion called a dendritic spine. Another type of synapse is electrical synapses, or gap junctions, that allow for an immediate propagation of the membrane potential to the next cell.

The synaptic bouton of a chemical synapse is filled with a number of vesicles containing neurotransmitters that are used to transmit a signal to the postsynaptic neuron (see also Figure 1.3). When an AP (see previous section) arrives at the axon terminal, it opens voltage-gated Ca^{2+} channels so that the Ca^{2+} concentration is rapidly increased (see Table 1.1). Within microseconds, neurotransmitter is released from the synaptic vesicles into the synaptic cleft in the following process. The increased Ca^{2+} is sensed by Synaptotagmin in the vesicle membrane, and Munc13-like and Sec1/Munc18-like proteins in the cell membrane (Kiessling et al., 2018; Rizo and Xu, 2015). These proteins initiate the assembly of a SNARE protein complex. This in turn mediates the fusion of the vesicle membrane with the cell membrane, finally releasing the neurotransmitter. The neurotransmitter diffuses through the cleft and binds to receptors in the postsynaptic membrane. Excess neurotransmitter molecules are recycled by astrocytes and specific transporters in the presynaptic membrane.

Neurotransmitter receptors are subdivided into two large groups, transmitter-gated ion channels and G-protein-coupled, or metabotropic, receptors. These groups can further be classified by the neurotransmitter they respond to and their effect in the postsynaptic neurons. Some transmitters (such as glutamate) open cation channels, eliciting an excitatory postsynaptic potential (ePSP) via influx of Na^{+}. Other transmitters (e.g. glycine and gamma-aminobutyric acid (GABA)) open anion channels so that Cl^{-} will stream into the cell. In adult cells, this influx will lead to an inhibitory postsynaptic potential (iPSP) by hyperpolarizing the membrane. During development, the intracellular Cl^{-} concentration is much higher than in adult cells, leading to an excitatory function of GABAergic Cl^{-} channels (Egorov and Draguhn, 2013). The aforementioned neurotransmitters and a wide range of others including amino acids (glutamate, glycine, etc.), amines (acetylcholine, dopamine, epinephrin, etc.), and small peptides (neuropeptide Y, substance P, somato-

statin, etc.) can also interact with metabotropic receptors. They activate an intracellular G-protein in the postsynaptic membrane that either opens an ion channel with a certain delay or activates a signaling cascade by triggering the release of a second messenger such as cyclic adenosine monophosphate (cAMP) or Ca^{2+}. This signaling cascade can have diverse effects on gene regulation and protein expression, metabolism, and other functions via the activation of so-called immediate early genes. One well-studied effect of these cascades is synaptic plasticity, which decreases or increases synaptic strength over seconds up to minutes (short-/long-term depression/potentiation).

A cortical neuron usually receives inputs through thousands of synapses at its dendritic tree from hundreds to thousands of neurons (Bear et al., 2007a). Many of these synapses elicit ePSPs or iPSPs in the dendritic tree that are integrated by the neuron in a complex process of spatio-temporal summation (reviewed by London and Häusser (2005)). In spatial summation, different compartments of the dendritic tree receive synaptic inputs almost simultaneously. In temporal summation, the same dendritic compartment receives synaptic inputs at slightly different time-points below the decay constant of the preceding PSP (1-15 ms). The complexity of dendritic computation is increased because of the possibility of combinations of spatial and temporal summation, the mixture of ePSPs and iPSPs, and different passive and active properties of dendritic trees. Passive properties are inherent characteristics of a dendritic tree. Firstly, dendrites behave similar to electrical cables, thereby serving as linear filters of a PSP, a property that has different effects depending on the distance of the synapse to the AIS. Secondly,

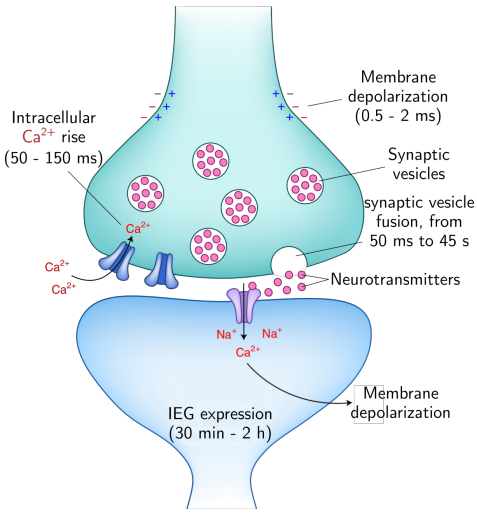

Figure 1.3 – A chemical synapse. The time scales of synaptic transmission range from milliseconds up to hours and depend largely on Ca^{2+}, neurotransmitters, and Na^{+}. Adapted from (Wang et al., 2019b).

the aforementioned spatio-temporal summation itself is a passive property. Thirdly, a synaptic input locally changes membrane conductances to certain ions, thereby introducing a dependency of the spatio-temporal summation on the exact distance and timing of the other synaptic inputs. This change of conductance can even occur without a change in membrane potential, for example in shunting inhibition. Active properties are less well understood than passive properties. They influence to what extent a dendritic tree or compartment can respond to a synaptic or intracellular input. This process is highly dependent on the local distribution of voltage-gated sodium channels in the dendritic membrane. Firstly, backpropagation of APs in the same cell can serve as an intracellular feedback mechanism. Secondly, conductances at synapses seem to be scaled with distance from the AIS, thus amplifying the PSPs generated by more distant synapses. Thirdly, local dendritic spikes act as a tool to heavily influence the PSPs in a surrounding region. And fourthly, global dendritic spikes are elicited by separate spike initiation zones within the dendritic tree. All these computational properties of dendrites enable the neuron to fire an AP at the precise time at which it is needed within a network (Bear et al., 2007a; London and Häusser, 2005). Usually, computational models explaining the functional principles of neuronal networks (see also section 1.1.3) only take into account a fraction of these mechanisms of synaptic summation. On the other hand, an experimental system as used in this thesis naturally integrates the neurons' synaptic and conductive properties. In combination with patterning techniques, networks of such physiological neurons with defined connectivity can be engineered, enabling the investigation of synaptic (in single cell networks) (Fricke et al., 2011) and network mechanisms (Yamamoto et al., 2018).

1.1.2 Development of Cortical Neurons

At the time point when the cortex is dissected from a rat embryo (embryonic day 18/E18) in this thesis, the cerebral cortex has already formed in the brain. The prerequisites for this complex structure are already fixed in the gastrula stage (E6-8) when ectoderm, mesoderm, and endoderm separate from each other. When the cortex is dissected and dissociated for a cell culture, the neurons sink onto the substrate and adhere within a few minutes. Once adhered, the neuron starts to form lamellipodia that turn into neurites within half a day.

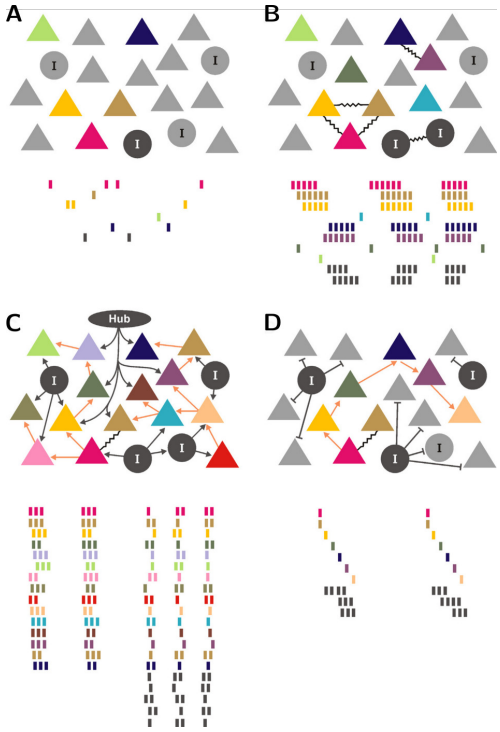

Figure 1.4 – Stages of neuronal network development. First, individual glutamatergic and other excitatory neurons (triangles) and still excitatory GABAergic interneurons (I) exhibit sporadic firing (**A**) that gets more synchronized as first weak synapses and sub-networks form (**B**). The neurons further interconnect, and connection strength and directionality increases, resulting in global network events (**C**). As GABAergic neurons turn into inhibitory regulator hubs, and certain sub-networks are strengthened due to synaptic potentiating and depressing mechanisms, defined and reproducible firing patterns emerge (**D**), useful for the execution of specific tasks. Adapted from Egorov and Draguhn (2013).

During the next day, one of the neurites elongates and starts to become the axon while the other neurites will become branched dendrites in the following two to three days. Over the next few days, the neurites will further branch out and form synapses with other neurons (Fukata et al., 2002), starting to exhibit individual sporadic activity (Figure 1.4 A). From then on, the neurons undergo a developmental process that is in some aspects similar to the one found *in vivo* (Egorov and Draguhn, 2013). At around day-in-vitro (DIV) 7, the first synapses are mature and can propagate APs leading to first small synchronized (sub)network firing events (Figure 1.4 B). While the neurons mature, they express more and more synaptic and ion channel proteins, leading to improved encoding of higher firing frequencies and thus synchronization and improved communication with other neurons (Egorov and Draguhn, 2013; Nikitin et al., 2017). Therefore, the network starts exhibiting stereotypical synchronous network bursts recordable by electrical (section 1.2) or optogenetic (section 1.3) techniques. In these networks, GABAergic neurons are not yet inhibitory (see section 1.1.1.3), leading to a mainly excitatory network with large global synchronicity(Figure 1.4 C). At this point, the neuronal networks exhibit a high connectivity as a

basis for their upcoming refinement. In week 4 or more, stable subnetworks of inhibitory and excitatory neurons slowly form, reducing synchronous activity to specific subpopulations with complex spatio-temporal firing patterns (Egorov and Draguhn, 2013; Kapucu et al., 2017) (Figure 1.4 D). These activity patterns of certain subnetworks can represent the neural basis of specific tasks. *In vivo*, these tasks include basic computations for higher functions such as cognition, sensing, or motion. *In vitro*, the nature of these tasks is more abstract but may be used, for example, for memory mechanisms (Dranias et al., 2013).
During that process, neurite outgrowth is steered by a mixture of chemical and physical environmental cues. The neurite, and in particular the axon, uses a hand-like structure called the growth cone to find its way to a specific target structure (Dent et al., 2011; Gallo and Letourneau, 2004; Lowery and Vactor, 2009; Sanes et al., 2011a; Vitriol and Zheng, 2012). Physical cues include the stiffness and topography of the substrate, while chemical cues include gradients of molecules released from cells, or extracellular matrix components of other cells. In the brain, these cues guide the axon towards their destination, usually another neuron. In the cortex, this neuron can be located in the same or a different cortical layer, or in a different brain region, in case of projection neurons (Sanes et al., 2011b). *In vitro*, the guidance cues can be used to encourage or prevent neuronal growth in chosen regions, and to guide axons and dendrites along defined patterns (see section 1.4).

1.1.3 Network Activity

Individual neurons interconnect via synapses to form functional neuronal networks. These networks are the basis for most higher functions of the brain. In addition to the individual neuronal action potentials (as described above), the combined activity of these neurons exhibits emergent properties only visible within the complete network as opposed to individual neurons (much like individual pixels on a screen do not contain much information, whereas together they form an image) (Yuste, 2015). One very prominent of these properties is network bursts, in which a large fraction of neurons in a network fire almost at the same time (Figure 1.5 A). Since periods of rapid firing in individual neurons (often occurring when a neuron participates in a network burst) are also called bursts in literature,

I will refer to network bursts as synchronous network events (SNE) in this thesis. Other such emergent properties are more indirect and can be quantified via graph theoretical models of the network. In these models, changes in the network's abilities for integration and segregation of its neurons, its resilience towards perturbations, and the character of neurons with special functionality (such as hub neurons) can be measured.

1.1.3.1 Synchronous Network Events

Neuronal activity patterns can be assigned an "energy" value (borrowed from ferromagnetism), resulting in an energy landscape with favorable energy states. A SNE is such a favorable state, or attractor (Yuste, 2015). Attractors also include other stable spatio-temporal firing patterns, e.g. for memory fixation. Generally, the high synchronization or coherence between neurons in a network during a SNE was proposed to serve as a phase of higher input gain of the neurons participating in the SNE. This leads to rhythmic phases of higher excitability during SNEs (more efficient communication) as opposed to phases of mixed and lower excitability outside of these coherent events, and therefore to the concept of "communication through coherence" (Fries, 2015). More specifically, SNEs exhibit diverse functions in very different brain regions and cell types. These functions range from respiratory rhythmogenesis(Rybak et al., 2014) to memory consolidation (Buzsáki, 2015). As described in the previous section, SNEs represent a developmental maturation hallmark of neuronal networks in cell culture (Luhmann et al., 2016; Wagenaar et al., 2006a) and *in vivo* (Chiu and Weliky, 2001). It may also serve as a model for slow-wave sleep (Saberi-Moghadam et al., 2018). Due to the similarity of SNEs in culture and in some systems *in vivo*, primary neuronal cell cultures have been used frequently as a model system to investigate SNEs (Gritsun et al., 2010; Lonardoni et al., 2017; Pasquale et al., 2017; Penn et al., 2016; Takahashi et al., 2010; Teppola et al., 2019; Wagenaar et al., 2006a,b).

A SNE usually comprises a pre-phase and a main phase (Gritsun et al., 2010) (Figure 1.5 B). Starting in the pre-phase, sporadic activity in a small subset of neurons (leader cells (Bauermeister et al., 2020; Pasquale et al., 2017)) recruits (almost) the complete network to the event. Additional and optional flanking and tail-phases probably rep-

resent the activation of distinct (functional) subnetworks. Different models have been proposed and refined over time to explain SNE behavior in culture (Fardet et al., 2018; Gritsun et al., 2010; Masquelier and Deco, 2013; Pasquale et al., 2008; Wilson and Cowan, 1972). Although even very simple models (Wilson and Cowan, 1972) with as few as two independent variables (Tyukin et al., 2019) can explain the tendency of a network to exhibit SNEs, the exact initiation, dynamics and regulation of SNEs are much more complex. A more complex physical model based on biological experimental studies (Masquelier and Deco, 2013; Penn et al., 2016) provided evidence that many neurons in a cell culture could be self-sustaining oscillators that can generate spontaneous, regular SNEs. In this new model by Fardet et al. (2018), neurons are assumed to be adaptive by exhibiting Na^+ and H^+ leak currents $I_{Na,P}$ (Penn et al., 2016) and I_h (Lüthi and McCormick, 1998). By lowering their excitability upon repeated excitation (adaptability) and firing/oscillating spontaneously (leak currents), these neurons are sufficient to generate SNEs without any additional mechanisms such as intrinsic bursting, short-term plasticity (Gritsun et al., 2010), or inhibitory neurons. This lack of importance of inhibition contradicts a large body of evidence stating the importance of GABAergic regulation in neuronal networks (Egorov and Draguhn, 2013). Therefore, such physical models may explain very well how a neuronal network can exhibit a specific feature (such as SNEs) in a specific state, but have to be considered with care when generalizing to other states of a network. This

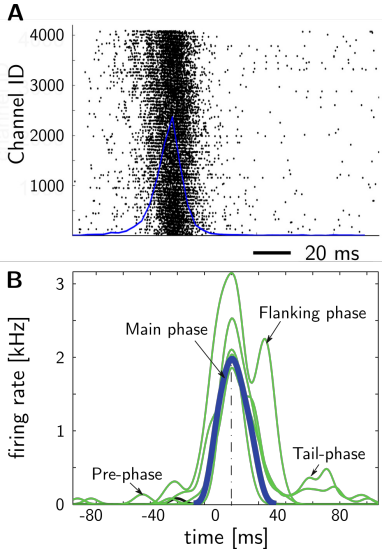

Figure 1.5 – Synchronous network events. (A) Neuronal networks exhibit synchronous network events, often associated with bursts of APs withing individual cells. Adapted from Lonardoni et al. (2017). **(B)** A SNE can be subdivided in different phases. Sporadic activity in some neurons (potentially leader neurons) in the pre-phase recruits a larger portion of the network in the main phase. Sometimes, the main phase is accompanied by a flanking phase, that may indicate activation of a separate subnetwork. Finally, a tail-phase may follow the main phase in a similar manner but not as pronounced as the flanking phase. Adapted from Gritsun et al. (2010).

specific state can be the homogeneous distribution of neurons, or a certain developmental stage where GABAergic neurons may not play a role due to their excitatory nature (see section 1.1.2).

Biologically, experimental studies have found that SNEs seem to rely on three main factors (Egorov and Draguhn, 2013) and their related phenomena: a) glutamatergic, excitatory synapses that facilitate fast initiation (AMPA receptors) of SNEs and define and regulate spatio-temporal firing patterns during SNEs (NMDA/AMPA receptors) (Teppola et al., 2019). Recruitment of neurons to an emerging SNE due to AMPA receptors is initiated and/or conducted by leader (Pasquale et al., 2017) or pioneer (Bauermeister et al., 2020) cells. The definition of spatio-temporal firing patterns does not only rely on the type of glutamate receptor (Teppola et al., 2019) but also on the type of stimulus (Bauermeister et al., 2020; Pasquale et al., 2017) or firing pattern (Lonardoni et al., 2017) a neuronal (sub-)population receives and the location of SNE initiation (Lonardoni et al., 2017; Orlandi et al., 2013). b) GABAergic, regulatory neurons that coordinate (in a mature network by inhibition) firing activity in their local environment (Egorov and Draguhn, 2013) as so-called hub neurons. However, although GABAergic neurons serve as hub neurons (Cossart, 2014) not all hub neurons are necessarily GABAergic. These hub neurons can steer the initiation and progression of SNEs (Okujeni et al., 2017) and as much as directly determine the frequency of network oscillations in hippocampal slices (Capogna and Pearce, 2011). c) Gap-junctions as a direct coupling mechanism between spatially close neurons (maybe in initiation regions or between hub cells to form anatomical "rich clubs", see section 1.1.3.2) (Egorov and Draguhn, 2013). Additionally, mechanisms such as glial transmitter recycling contribute to the complexity and frequency of SNE generation (Huang et al., 2017).

1.1.3.2 Network Connectivity and Modularity

In neurobiological systems, three categories of connectivity have been defined (Feldt et al., 2011): 1) anatomical or structural connectivity, defined via the axons and dendrites between the neurons; 2) functional connectivity, usually defined by a measure of statistical correlation between the individual neurons in the network; 3) effective connectivity, usu-

ally defined by testing the causal relationships between two neurons, e.g. by stimulating a neuron and monitoring the direct response of this stimulation in other neurons. These definitions can be applied to differently scaled neuronal networks, ranging from cell cultures to brain regions. Connectivity measures can be used to construct graph theoretical models to investigate indirect emergent network properties. Graphs comprise nodes (or vertices) and connections (or edges) between the nodes. The connections can be directed or undirected and weighted or binary. Functional connectivity matrices are most widely used to construct graphs of cell culture networks. These matrices have commonly been based on the statistical measures of cross-correlation (Lonardoni et al., 2017; Pasquale et al., 2017), mutual information (Wrosch et al., 2017), transfer entropy (Stetter et al., 2012), and combinations of those (Wrosch et al., 2017). The graph model can then be used to extract connectivity measures, such as the clustering coefficient, the efficiency of the network, the in- and out degree of the connections, the so-called assortativity, and more (for a comprehensive review, see Rubinov and Sporns (2010), and for details of measures used in this thesis, see section 2.5.6).

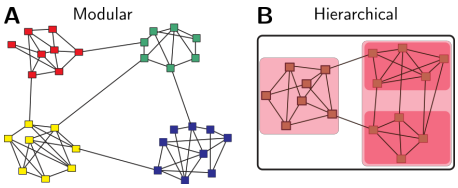

Figure 1.6 – Modularity and small-world networks. Small-world networks have a high clustering coefficient and are very efficient, i.e. have short path lengths. Special cases of small-world networks are modular (**A**) and hierarchical modular (**B**) networks. Adapted from Meunier et al. (2010).

Investigating the connectivity of neurobiological systems, a recurring feature of these networks is the so-called hierarchical modularity as a sub-category of small-worldedness of the network (Meunier et al., 2010) (Figure 1.6). Small-world networks form sub-networks or modules (clustering) that are interconnected with other modules via few, specific long-range connections (short paths/high efficiency). Hierarchical modularity refers to a network containing modules, which in turn can contain sub-modules, which again can contain sub-sub-modules, and so on (Meunier et al., 2010) ("turtles all the way down"). With a small-world network architecture, sub-tasks can be performed in adaptable and exchangeable modules with low wiring cost while at the same time keeping inter-modular

communication efficient. Additionally, the time scales of intra- and inter-modular communication can be separated (Pan and Sinha, 2009). Due to this temporal and functional separation of neuronal activity, small-world networks exhibit a complex firing dynamics, i.e. a mixture of segregated inter-modular and integrated intra-modular firing (Shanahan, 2008; Sporns et al., 2000). However, the anatomical connections between the modules can influence the functional architecture of the network. For example, small-worldedness and the resulting dynamical richness of the activity is weakened when the modules are strongly connected to each other (Moriya et al., 2017; Yamamoto et al., 2018). In turn, this can lead to an enhanced transmission fidelity of spike codes between modules (DeMarse et al., 2016). Additionally, the connectivity between modules does not rely only on the physical connections but also regulatory mechanisms such as inhibition. Disinhibition of modular networks alters the module-to-module communications towards a more activity-dependent state (Shein-Idelson et al., 2016). Another feature that sometimes appears in neuronal networks is the so called "rich-club" behavior or positive assortativity, which means that central nodes such as hub nodes are interconnected with each other (Gal et al., 2017; Teller et al., 2014). Functionally, this behavior seems to occur in cell culture systems when the anatomical network has a small-world architecture (i.e. the cells have grown in interconnected clusters) (Teller et al., 2014).

1.2 MEAs and Electrophysiology

The first methods to investigate the function of the nervous system were electrophysiological. Whilst in the beginning blank wires and crude devices such as simple galvanometers were used to identify electrical currents within nerves, the technology to measure electrical neuronal activity has become more and more sophisticated. In this section, I will focus on two techniques that were used in this thesis to investigate the activity of primary cortical cell cultures - the patch-clamp technique and microelectrode arrays (MEA) .

1.2.1 Whole-Cell Patch Clamp

The patch clamp technique was developed by Sakmann and Neher (1984) to investigate the variable currents and potentials across the cell membrane of a neuron, and their dependence certain types of molecules such as ion channels. A platinum wire in a glass pipette with a tip diameter of 1 - 3 µm serves as the recording electrode of the intracellular voltage against the extracellular voltage measured by a Ag/AgCl reference or ground electrode in the extracellular measuring solution. The glass pipette is then closely attached to the cell membrane, indicated by a very high sealing resistance R_{seal} (> 1 GΩ) between recording and reference electrode (this is the so-called "gigaseal") due to the complete cell insulating the two electrodes (Figure 1.7 A). The membrane "patch" attached to the pipette is ruptured and a defined electrolyte in the pipette replaces the cytosol of the cell. The intra- and extracellular ion concentrations determine the passive membrane potential according to the Goldman equation (see Equation 1.2).

The membrane potential can now be "clamped" at a certain value through the recording electrode while measuring the current ("voltage clamp"). Voltage clamp experiments can be used to accurately estimate the conductances of individual ion channel types, as ion channels are voltage- and time-dependent but not current-dependent. Alternatively, the injected current can be clamped while measuring the resulting membrane potential ("current clamp"). With current clamp experiments, membrane potential changes due to synaptic inputs or action potentials can be measured. Since the cell membrane behaves like a leaky capacitor, current clamp induces a capacitive charging effect in the membrane

until reaching a steady state voltage.

The circuit formed by the patch electrode and membrane can be described by electrical equivalent circuits (Figure 1.7 B), usually comprising resistors, capacitors and voltage sources (Ypey and DeFelice, 1997). The patch amplifier can be described as a voltage source (E_{pc}) and a (low) output resistance (R_{pc}) in series. In parallel to that are the capacitance (C_{pip}) and the resistance (R_{pip}) of the patch pipette. In series with R_{pip} is the cell membrane, which is a membrane capacitance (C_m) in parallel with membrane resistance R_m (or inverse conductance) and voltage source E_m (see Figure 1.7). This three component equivalent circuit of the cell membrane is only comparable with the passive properties of a membrane, failing to accurately model membrane behavior during an AP or other activity. The membrane voltage can be described as (Ypey and DeFelice, 1997):

$$V_m(t) = A\, e^{\frac{-t}{T_1}} + B\, e^{\frac{-t}{T_2}} + D, \qquad (1.4)$$

where A, B, and C are constants and T_1 and T_2 are complex functions of $\tau_{s,pip} = R_{pc}C_{pip}$ and $\tau_{pip,m} = R_{pip}C_m$, respectively. For a current clamp experiment, $R_{pc} >> R_m, R_{pip}$ can be assumed, leading to a very long exponential capacitive charging effect as compared to voltage clamp (where $R_{pc} << R_{pip} << R_m$).

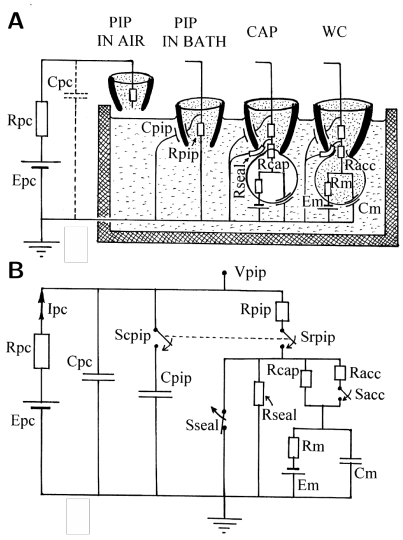

Figure 1.7 – The patch-clamp technique. **(A)** Schematic representation of the different steps in a whole-cell (WC) patch-clamp experiment. Besides R_{pc}, E_{pc}, C_{pip}, R_{pip}, R_m, C_m, and E_m, which are explained in section 1.2.1, R_{cap} is the resistance of the patched membrane that is replaced by the access resistance R_{acc} when the membrane is opened, and is in parallel to the sealing resistance R_{seal} that is usually above 1 GΩ. **(B)** An equivalent circuit representing the patch-clamp experiment in **A**, with switches representing the transition of one step to another. Adapted from Ypey and DeFelice (1997).

1.2.2 Microelectrode Arrays

Developed in the 1960s and 1970s (Pickard, 1979), MEAs are one of the most abundantly used systems for measuring neuronal electrical activity *in vitro* (Hofmann et al., 2011; Novak and Wheeler, 1988; Pasquale et al., 2008; Stett et al., 2003) and *in vivo* (Blau et al., 1997; Obien et al., 2015; Wei et al., 2015). They are classically fabricated via photolithography methods. As a substrate, wafers made from silicon or glass are used. On this substrate, an adhesion layer, usually Ti or Cr, is applied, followed by a conductive layer (Figure 1.8 A). Starting with only noble metals (Hofmann et al., 2011; Pickard, 1979; Seo et al., 2017), many conductive materials are now available, some with additional properties such as higher flexibility and softness (Blau et al., 1997; Jeong et al., 2020; Kireev et al., 2017a; Park et al., 2019; Vosgueritchian et al., 2012), biocompatibility (Ahn et al., 2014; Blau et al., 1997; Jeong et al., 2020), transparency (Cao et al., 2014; Gross et al., 1985; Kireev et al., 2017a; Ryynänen et al., 2018; Vosgueritchian et al., 2012; Wang et al., 2019a), or improved resistance (Cao et al., 2014; Vosgueritchian et al., 2012). The conductive layer is covered with an insulating layer, the passivation, which is opened at the electrode sites and the contact pads for connection to an amplifier system. Also for the passivation, a multitude of different materials are available, the most common of which include polyimides (Im and Seo, 2016), silicon dioxide and/or silicon nitride layers (Hofmann et al., 2011; Multi Channel Systems MCS GmbH), or atomic layer deposited metal oxides (Yuan et al., 2020). For MEAs used *in vitro*, a square electrode layout is very common (Hofmann

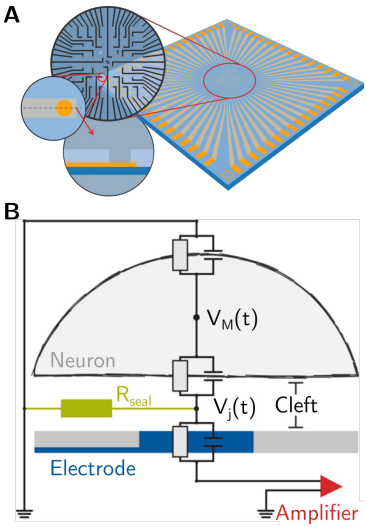

Figure 1.8 – Microelectrode arrays. (A) Schematic representation of a MEA. The actual array is in the middle of a chip and comprises a grid of electrode openings (in this thesis 64) that consist of a substrate, a conducting layer, and a passivation in the simplest case. **(B)** An equivalent circuit representing the point contact model used to describe the mechanism of a cellular recording with a MEA. Note the similarities (especially the sealing resistance R_{seal}) to the patch-clamp technique (see Figure 1.7). Adapted from Weidlich (2017).

et al., 2011; Kireev et al., 2017a; Multi Channel Systems MCS GmbH), unless the application demands a different design, as it for example makes sense in microfluidic systems. Usually, the MEA is read out by connecting a pre-amplifier or headstage to the contact pads at the outer edge of the chip. The headstage is then connected to a main amplifier which can be connected to a computer for data storage (for details, see section 2.3.3.1). When MEAs are used in cell culture systems, the interface between an electrode and a cell can be expressed by using electrical equivalent circuits. A commonly used circuit is the so-called point contact model in which the area of the cell and electrode at the interface (or junction) are neglected for simplicity (see Figure 1.8 B). However, it is important to note that a smaller electrode will increase the electrode impedance Z while at the same time increasing thermal noise during voltage-based recordings and therefore decreasing signal to noise ratio (Obien et al., 2015). This effect can be circumvented by using non-standard MEA designs such as nanocavity MEAs, in which the electrode size is increased in a nanometer-high cavity below the passivation to decrease electrode impedance while preserving a single cell resolution through a small electrode opening (Hofmann et al., 2011). Disregarding these area effects, the point contact model defines the electrode, the membrane at the electrode (junctional membrane), and the membrane on the opposite site of the cell (free membrane) as capacitor-resistor combinations (Spira and Hai, 2013)(see section 1.2.1 and Figure 1.8 B). The most important element is the so-called sealing resistance R_{seal}, which is increased the tighter the cell is coupled to the electrode and in turn increases the measured voltage. This R_{seal} is usually three to four orders of magnitude lower than in a patch clamp experiment, and therefore is under constant effort to be improved (Hofmann et al., 2011; Spira and Hai, 2013; Weidlich, 2017).

1.3 Optogenetics

1.3.1 Calcium Sensing and Image Processing

Changes in calcium concentration play a major role in many different intracellular signaling pathways, ranging in scale from quickly subsiding microdomains directly around individual calcium channels up to long-lasting global cellular events. To visualize the calcium signals in the cells of the nervous system (especially APs in neurons, section 1.1.1.2 and Figure 1.9 A, and diverse events in astrocytes and other glia (Bazargani and Attwell, 2016)), calcium imaging has become a widely used technique in neuroscience. Improvement of chemical dyes like Fura-2 in the 1980s resulted in the reliable indicator Fluo-4. Following these dyes, the technique was further improved by the introduction of genetically encoded calcium indicators (GECI; for extensive reviews, see Grienberger and Konnerth (2012); Lin and Schnitzer (2016); Wang et al. (2019b)). These GECIs can be targeted to specific cell types and even specific intracellular sites via their gene promoters, and are stable for much longer than chemical indicators (Grienberger and Konnerth, 2012). The GCaMP family (excitable by blue light and emitting green light) has become the most popular group of GECIs. These proteins are based on a circular green fluorescent protein (GFP) variant in a weakly fluorescent conformation that is attached to a calmodulin

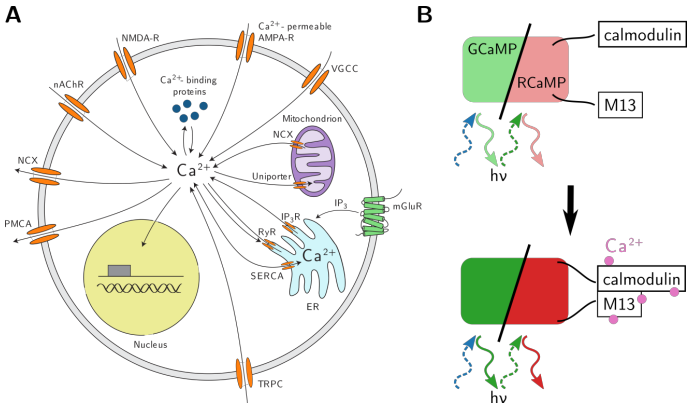

Figure 1.9 – Calcium Imaging. (A) Apart from the synapse (see Figure 1.3), calcium can stream into the cell via diverse pathways, including amplification steps from the ER. This leads to an 10 to 100-fold increased Ca^{2+} concentration during an AP. **(B)** The working principle of the calcium indicators of the GCaMP and RCaMP families. Adapted from Grienberger and Konnerth (2012).

(CaM) protein (Figure 1.9 B). When calcium ions bind to the M13 domain of the CaM, calmodulin changes the conformation of itself and the circular GFP, leading to a much stronger fluorescence of GFP (Grienberger and Konnerth, 2012). While GCaMP1 (Nakai et al., 2001) still had severe disadvantages compared to Fluo-4 in terms of signal-to-noise ratio, GCaMP3 was already on par with the chemical dye (Tian et al., 2009). With the GCaMP6 variants GCaMP6s (slow), m (medium), and f (fast), Chen et al. (2013) could make a breakthrough in the field. Even the fast variant (resolving individual APs), with weakest fluorescence intensity, was performing better than the classical chemical dyes. These improved sensors can be combined with highly efficient transduction of the cells via adeno-associated viruses (AAV) leading to very high transfection efficiencies. GCaMP6 has since been further improved (jGCaMP7) to fit specific applications such as widefield or two-photon microscopy (Dana et al., 2019). With these sensors, fluorescence changes down to below 10% (Grienberger and Konnerth, 2012) can be visualized which corresponds to single APs. Other calcium signals are usually much slower and/or weaker than AP-induced ones so that they are easily distinguishable or not even detectable in network-scale calcium imaging (Augustine et al., 2003). To enable multicolor imaging or the combination with optogenetic actuators, the most established of which respond to light in the blue wavelength range, red GECIs based on red fluorescent proteins were developed. One early variant was the GECI R-GECO1 (Zhao et al., 2011) based on the red fluorescent protein mApple, which shows photo-switching behavior in blue light (Shaner et al., 2008). Since this photo-switching is not well-suited for combination with optogenetic actuators, the non-switchable variant RCaMP1 based on mRuby was developed (Akerboom et al., 2013). These early variants were equally inferior in signal-to-noise ratio as GCaMP1. Therefore, Dana et al. (2016) developed the improved GECIs jRCaMP1a (brighter, but less dynamic range when resolving APs), jRCaMP1b (less bright, but increased dynamic range), and jRGECO1a (brightest, but photo-switching in blue light).

To record calcium imaging movies, fluorescence microscopy setups with high-speed cameras and adequately strong light sources are used (Grienberger and Konnerth, 2012; Lin and Schnitzer, 2016) (see also section 2.4.1). Confocal microscopes enable longer recordings due to the minimized exposure of the individual GECIs to light and thereby reduced

photo-toxicity. The tools for post-processing and analysis of calcium imaging movies are under constant improvement (Burchert and Schneider, 2016; Cantu et al., 2020; Giovannucci et al., 2019; Kaifosh et al., 2014; Mukamel et al., 2009; Pnevmatikakis, 2019; Reichinnek et al., 2012; Rueckl et al., 2017; Shibue and Komaki, 2020; Stringer and Pachitariu, 2019) (for an overview, see e.g. Bonifazi and Massobrio (2019)). For a detailed example of one implementation, also refer to section 2.4.2.1. Usually, in the first step, regions-of-interest (ROIs) around the neurons are extracted from the calcium imaging movies. For this, the movie can be normalized to a $\Delta F/F_0$ movie with F_0 as a baseline (sometimes time-dependent, sometimes space-dependent) (Rueckl et al., 2017). This removes constantly active or inactive neurons. In *in vivo* recordings, this normalization is followed by a step of correcting movement artifacts (Pnevmatikakis, 2019; Pnevmatikakis et al., 2016). Next, ROIs are detected, usually using a series of filtering and thresholding operations (Burchert and Schneider, 2016; Diego et al., 2013; Giovannucci et al., 2019; Reichinnek et al., 2012; Rueckl et al., 2017) but now also extended to novel techniques such as deep learning (Soltanian-Zadeh et al., 2019). With the current state technology and algorithms, this ROI detection is rarely error-free, which is why most tools include the option of manually checking and modifying the results of the automatic ROI detection (Burchert and Schneider, 2016; Giovannucci et al., 2019; Kaifosh et al., 2014; Rueckl et al., 2017). From the ROIs, a mean intensity trace can be extracted, in which the calcium events are clearly visible. These events can be detected by simple peak-finding algorithms such as the `find_peaks` routines of MATLAB® or `SciPy` in `python`. Alternatively, a deconvolution can be used to infer spike rates from the calcium intensity traces (Cantu et al., 2020; Friedrich et al., 2017; Jewell et al., 2019; Pnevmatikakis et al., 2016; Shibue and Komaki, 2020; Stringer and Pachitariu, 2019; Theis et al., 2016) suitable for some statistical analysis of firing probabilities. However, exact spike times cannot be assumed with this methodology (Theis et al., 2016), preventing an analysis of spatio-temporal calcium peak patterns. As a third alternative, methods can be used that use the $\Delta F/F_0$ traces directly, without the need to infer or detect spikes or peaks. This includes cross-correlations between neurons (Eichler et al., 2003) and information theory-based concepts like mutual information and transfer entropy (Bonifazi and Massobrio, 2019; Schreiber, 2000; Stetter

et al., 2012). Neuronal ensembles can also be directly estimated from calcium traces with less common methods (Mölter et al., 2018).

1.3.2 Optogenetic actuators

The ability to perceive light is a common principle in many cells, ranging from single cellular organisms like algae (Litvin et al., 1978) over plants (photosynthesis) to the eyes of mammals. This ability relies on proteins that transduce photons into an intracellular signal in the form of a second messenger like cyclic guanosine monophosphate (cGMP) in case of the mammalian photoreceptors of the eye (Bear et al., 2007b), or ionic current in case of some photoreceptive algae like *Chlamydomonas reinhardtii* (Litvin et al., 1978). Optogenetic approaches utilize this photo-transduction to stimulate electrogenic cells optically. However, almost three decades passed until the first major studies using genetically targeted, optically activated ion channels (now called optogenetic tools) in mammalian cells (Boyden et al., 2005; Nagel et al., 2003) (described in detail in Deisseroth and Hegemann (2017), Guru et al. (2015), and Deisseroth (2015)).

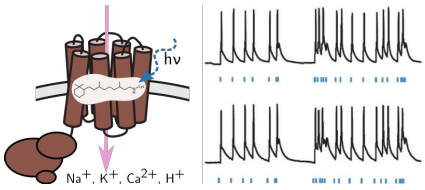

Figure 1.10 – Optogenetic actuators. Channelrhodopsin is a 7-transmembrane receptor with a bound retinal (left). Upon stimulation with blue light, APs are reliably elicited in neuronal cells expressing channelrhodopsin 2 (right). Adapted from Deisseroth (2015) and Deisseroth and Hegemann (2017).

The most common optogenetic actuator is the cation channel channelrhodopsin 2 (Boyden et al., 2005), abbreviated ChR2 in its functional form after its host organism *Chlamydomonas reinhardtii* (Figure 1.10 left). The (non-functional) channel itself is a so-called opsin, which needs a molecule of all-*trans*-retinal to actually transduce light signals. Retinal is produced in sufficient amounts by the neurons in a tissue, tissue slice or even primary neuronal cell cultures to produce functional ChR2 (Guru et al., 2015). When a photon hits the all-*trans*-retinal inside the opsin, the retinal photoisomerizes into 13-*cis*-retinal, which in turn leads to a conformational change in the surrounding protein, opening the cation channel pore (Deisseroth, 2015). The cation influx depolarizes the cell, leading to an AP (see also section 1.1.1.2).

By using this technique, a spatially and temporally highly precise stimulation of a neuronal network is possible (Figure 1.10 right): the spatial resolution is limited by the precision of the motor steering a laser, the resolution of the camera used to direct the laser spot, the expression level of ChR2 (Maybeck et al., 2016), and the size and power of the laser spot activating the channels; the temporal resolution is limited by the re-activation kinetics of the ChR2, leading to a certain delay after an activation until the next full activation can be conducted (Deisseroth and Hegemann, 2017) (a disadvantage more pronounced in earlier variants of ChR2).

Just as for calcium indicators, variants of ChR2 have been produced over time (Guru et al., 2015). Another disadvantage of optogenetic actuators may be the dependence on the exact construct used as different ChR variants seem to be able to elicit different network activity (Jun and Cardin, 2020). The excitation wavelength ranges have been shifted from blue (ChR2) to longer wavelengths (blue and green: Chronos (Klapoetke et al., 2014); green: C1V1 (Yizhar et al., 2011); red: Chrimson (Klapoetke et al., 2014), ReaChR (Lin et al., 2013)). The activation and inactivation kinetics have been improved (e.g. Chronos (Klapoetke et al., 2014)). Step function opsins can even modify neuronal firing rates instead of generating individual APs (Guru et al., 2015). Moreover, variants that are not channels but active proton pumps are available. Additionally, two other classes of optogenetic actuators lead to inhibition of the stimulated cell (e.g. via Cl^- influx or K^+ efflux), or to the activation of a second messenger such as cAMP (activating intracellular signaling cascades; for an overview, see Guru et al. (2015)).

1.4 Patterning Neuronal Networks

As mentioned in section 1.1.2, developmental guidance cues can be used to direct neuronal growth *in vitro*. A variety of cell culture patterning techniques have been designed to position neurons on top of MEAs (James et al., 2004; Jungblut et al., 2009; Nam et al., 2006), construct logical "bio"-gates (Albers and Offenhäusser, 2016; Feinerman et al., 2008), investigate the microcircuitry and signal integration of neurons and their networks (Chen et al., 2017; Feinerman et al., 2005; Forró et al., 2018), or to multiplex drug testing procedures (Langhans, 2018). Patterning techniques rely on different aspects of neuronal guidance and can be subdivided into physical and chemical techniques.

Firstly, microfluidics (Millet and Gillette, 2012; Peyrin et al., 2011; Renault et al., 2015, 2016; Taylor et al., 2005) and microchambers (Faid et al., 2005; Forró et al., 2018; Joo et al., 2018) physically restrict neurons in a confined space in excellently defined patterns. However, they rely on complicated assembly and seeding techniques. The cells growing in such devices are hard to access for some monitoring techniques such as patch-clamp or immunocytochemistry, and tend to cluster due to the confinement. Secondly, surface topographies can be used to achieve an overall directionality of growth but the positioning of somata or complex patterns are hard to achieve (Aebersold et al., 2016; Faid et al., 2005; Haq et al., 2007; Milos et al.; Rajnicek et al., 1997; Simitzi et al., 2017).

Thirdly, the surface chemistry of a substrate can be tuned to achieve cell-attractive (mostly with mild hydrophilicity (Bacakova et al., 2011)) patterns and cell-repellent backgrounds (mostly hydrophobic or toxic (Bacakova et al., 2011)). The hydrophilicity of a surface depends on the interplay between a liquid and a substrate, and can be quantified by the work of adhesion W_a. The contact angle θ of a drop of water on the substrate depends on W_a and the surface free energy of the liquid γ_L (Youssef et al., 2001):

$$\theta = cos^{-1}(\frac{W_a}{\gamma_L} - 1) \tag{1.5}$$

Therefore, it can be used as a measure for hydrophilicity. Another measure is the so-called ζ potential which was not used in this thesis but is explained for example in Bacakova et al. (2011). As cell-attractive coatings, poly-L-lysine (PLL) (Albers and Offenhäusser,

2016; James et al., 2004; Nam et al., 2006; Wu et al., 2018), fibronectin (Feinerman et al., 2008; Mrksich et al., 1997), laminin (Albers and Offenhäusser, 2016; Feinerman et al., 2008), amongst other molecules (Aebersold et al., 2016; Bacakova et al., 2011; Faid et al., 2005; Offenhäusser et al., 2007; Xu et al., 2016) have been used. Cell-repellent coatings include polyvinyl alcohol (PVA) (Wu et al., 2018), polyethylene glycol (PEG) (Mrksich et al., 1997; Offenhäusser et al., 2007), (3-glycidyloxypropyl) trimethoxysilane (GLYMO) (Markov et al., 2018; Nam et al., 2006), and a variety of other molecules (Aebersold et al., 2016; Faid et al., 2005; Feinerman et al., 2008; Martinez-Rivas et al., 2017; Offenhäusser et al., 2007; Yamamoto et al., 2016). The most common substrates to which these substances have been applied are glass (Aebersold et al., 2016; Feinerman et al., 2008; Nam et al., 2006), gold (Feinerman et al., 2008; Mrksich et al., 1997), and different MEA passivations (Aebersold et al., 2016; Chang et al., 2001; James et al., 2004; Martinez-Rivas et al., 2017; Nam et al., 2006). The actual patterning procedures are almost as manifold as the used materials and depend on the compostion of the coatings, the exact deposition procedure (which may include other layers, e.g. for adhesion), and the scale and number of substrates (Aebersold et al., 2016; Nam et al., 2006; Wu et al., 2018). Photolithography-based methods are quite common but limited to the standard wafer-scale (sometimes even only specific wafer sizes such as 4-inch wafers) (Aebersold et al., 2016; Wu et al., 2018). A method with fewer photolithographic steps and extending the scale beyond wafers, but equally common is the technique of microcontact printing (μCP).

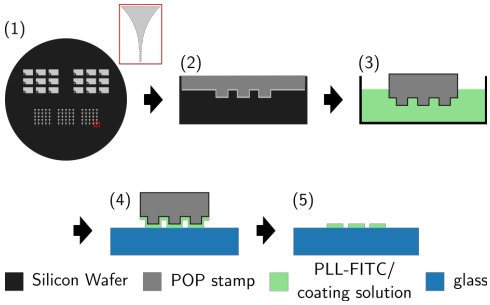

Figure 1.11 – The microcontact printing technique. A silicon wafer serves as a mold (1) for a polymer stamp (2). After cutting, the stamps are bathed in a coating solution (3), and the coating is transferred to a substrate (4) generating a partly cell adhesive, partly cell repellent substrate (5).

1.4.1 Microcontact Printing

The technique of μCP is relatively simple (Figure 1.11): At first, stamps are fabricated by casting or pressing a polymer to a re-usable, usually photolithographically prepared mold (Aebersold et al., 2016; Albers and Offenhäusser, 2016; Martinez-Rivas et al., 2017; Mrksich et al., 1997). The stamps are then cut from the wafer form and placed in a coating solution for adhesion of the solution to the stamp. Finally, the coating molecules are transferred to the substrate of choice, which may already be modified by a different process (Nam et al., 2006). Although polydimethylsiloxane (PDMS) is the most common stamp polymer, other polymers such as polyolefine plastomer (POP) may be used to decrease sagging errors when printing small patterns (Albers and Offenhäusser, 2016; Schwaab et al., 2013). The actual printing step can be performed manually or with a stamping device (Samhaber et al., 2016).

In the beginning, μCP was used to pattern endothelial cells into simple stripes (Mrksich et al., 1997). As the technique got more established, it was adapted for other cell types such as neurons and more complex patterns. For neuronal cultures, the spatial resolution now ranges from individual dendrites (Charrier et al., 2010; Fricke et al., 2011; Mourzina et al., 2006; Offenhäusser et al., 2007; Roth et al., 2012; Wheeler and Brewer, 2010; Yamamoto et al., 2016) or even dendritic spines (Schwaab et al., 2013) to whole populations (Albers and Offenhäusser, 2016; Feinerman et al., 2008).

Chapter 2

Materials and Methods

2.1 Microcontact Printing

In μCP , a polymer stamp is used to transfer a coating molecule to a substrate in specific pattern (Figure 2.1 A). The stamp is produced by casting a polymer into a photolithographically fabricated wafer-scale mold. For applications in cell biology, it is then incubated in a cell-adhesive molecule or protein, such as poly-L-lysine (PLL) or laminin.

2.1.1 Stamp Fabrication

Stamps were fabricated as described in Hondrich et al. (2019b) and Albers and Offenhäusser (2016). In detail, the different patterns used in this thesis were written into a chrome layer on top of a borosilicate wafer via electron beam writing to produce a dark field chrome mask. A 5 to 12 μm thick layer of AZ4562 positive photoresist (Clarion GmbH, Mörfelden-Walldorf, Germany) was spin coated onto a dehydrated 0.6-mm-thick standard silicon wafer (500 diameter, MEMC Electronic Materials, O'Fallon, MO, USA), and dried for 60 s at 130 °C. The layout was transferred to the wafer by using UV-photolithography with the dark field chrome mask. After a baking step for 90 s at 140 °C, the resist was developed in MF-24-A (Süss MicroTec, Garching near Munich, Germany) for 50 s and stopped by washing in Milli-Q water. Afterwards, reactive ion etching with SF_6 at 500 W was applied for 1 min 20 s to transfer the patterns into the silicon wafer to a depth of 4.5 μm. In an additional step, RIE was used to clean the resists from the wafer. As a last step, (tridecafluoro-1,1,2,2-tetrahydrooctyl)trichlorosilane (FOTCS) was deposited on the surface of the wafer via chemical vapor deposition (45 mbar for 1.5 h) as a release layer for the stamp polymer.

Polyolefine plastomer (POP) stamps were fabricated by hot embossing (Albers and Offenhäusser, 2016; Schwaab et al., 2013). Briefly, the patterns were transferred to POP by heating and pressing a film of POP between a wafer containing patterns and a plain wafer. The wafer-sized POP plate was subsequently cut into individual stamps of ~1-2 cm^2. Polydimethylsiloxane (PDMS; Sylgard 184, Dow Corning Corporation) stamps were fabricated by mixing base and curing agent 10:1, degassing the mixture overnight at -20 °C, and casting the PDMS into the prepared wafer. The PDMS on the wafer was heated

to 60 °C overnight and carefully peeled off. Individual stamps of ~1-2 cm^2 were cut out using a scalpel. The cleanroom fabrication was conducted by Michael Prömpers.

2.1.2 Chemical Vapor Deposition of GLYMO

To enhance the contrast between pattern and background, different strategies were tested during the course of this thesis, as described in Hondrich et al. (2019b). In brief, capillary deposition of MnO_2 and a hydrophobizing heat treatment of borosilicate glass coverslips (VWR, Radnor, PA, USA; Ø18 mm, see section 2.1.3) did not achieve as reliable patterning as the pre-treatment of the glass with (3-glycidyloxypropyl)trimethoxysilane (GLYMO), and an optional background hydrophobization with dodecylamine.

Chemical Vapor Deposition (CVD) was used to coat the coverslips with GLYMO (Sigma Aldrich, Germany) according to GhoshMoulick et al. (2009): The glass coverslips were cleaned in 2% Hellmanex III detergent (Hellma GmbH & Co. KG, Müllheim, Germany) in an ultrasound bath and rinsed three times with Milli-Q water. They were washed once in Milli-Q water, transferred to ethanol, dried in a nitrogen stream, and activated in O_2 plasma for 30 min at 0.7 mbar and 80 W power. After transferring the activated coverslips to a desiccator containing a ceramic, pre-heated ground disc and glass beaker in a water- and oxygen-free argon atmosphere (200 °C; Figure 2.1 C). The deposition was conducted by adding 150

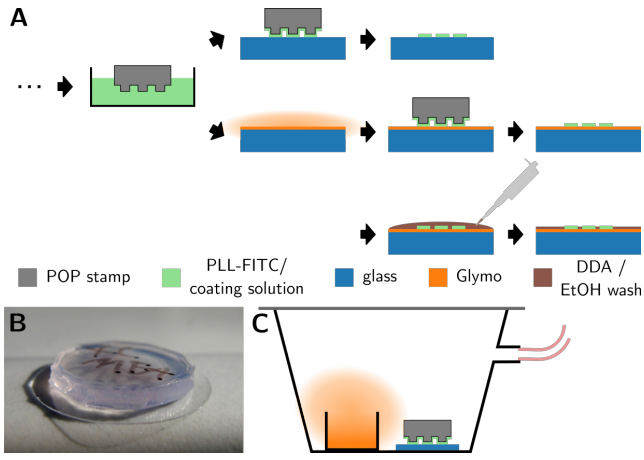

Figure 2.1 – Microcontact printing. (A) Improved microcontact printing (for the basic process, see Figure 1.11) with GLYMO and DDA application (see text). **(B)** A cut-out POP stamp on top of a glass coverslip. **(C)** GLYMO silanization of glass coverslips or MEAs takes place in a desiccator inside an atmospheric chamber.

µl of GLYMO to the glass beaker, and keeping the pressure at 5 mbar for 1.5 h.

2.1.3 Microcontact Printing Process

POP stamps were used for GLYMO-treated and unmodified glass substrates, and for MEAs with a HD8820 passivation (see section 2.3.2). Substrates without GLYMO modification were sterilized beforehand in 70% ethanol or 1 h of irradiation with ultraviolet (UV) light, and the following stamping process was conducted under sterile conditions. Substrates with GLYMO modification were sterilized with UV light or 70% ethanol after the printing process. The POP stamps were cleaned in 70% ethanol for 10-15 min in an ultrasound bath. The patterned side of the stamps was washed once with Milli-Q water. Excess water was removed in a nitrogen stream, and the stamps were incubated on ice for >20 min in Hank's balanced salt solution (HBSS) with 10 µg/ml PLL labeled with the green fluorescent marker fluorescein isothiocyanate (FITC; Sigma Aldrich, Munich, Germany) . The coating solution on the stamps was dried in a nitrogen stream, and the stamps were placed onto the substrate of choice (Figure 2.1 B). For alignment with MEA electrodes, a FINEPLACER® Lambda (Finetech GmbH & Co. KG, Germany; sterilized by wiping with 70% ethanol) was used to position the stamp. To ensure the microcontact between stamp and substrate, a 40 g weight was placed on top of the stamps for ~2 min. The stamps remained on the substrates for >20 min, and were carefully removed afterwards (whole process: Figure 2.1 C).

PDMS stamps were used for MEAs with a ONONO passivation (see section 2.3.2.1) to avoid ripping off the passivation due to strong adherence to the substrate. The PDMS stamps were cleaned for 5 min in 2% Hellmanex detergent. The stamps were washed with MilliQ water, incubated in 10% sodium dodecyl sulfate (Sigma Aldrich, Germany) for 15 min, quickly dipped once into MilliQ water to remove excess detergent, and incubated in the same way as POP stamps. Before printing, the backside of a stamp was stabilized with a glass microcoscopy coverslip. No weight was used, and the stamps were incubated on the substrate for >5 min.

2.2 Cell Culture

Cell culture systems are useful tools to dissect basic mechanisms in a system with reduced complexity as compared to tissues or living organisms. In this thesis, the HL-1 cardiomyocyte cell line was used to test a new MEA design (holey MEAs). Primary cortical cell cultures were used to investigate basic network functionality in a neuronal populations.

2.2.1 HL-1 Cells

The HL-1 cell line was used to test the ability of holey MEAs (section 2.3.2.2) to record electrophysiological signals and the transparency of holey gold. Frozen HL-1 cells (Claycomb et al., 1998) (cell line) were thawed and cultured in a T25 flask until they formed a confluent layer (100% surface coverage) and displayed electrical activity with frequencies between ~0.8-5 Hz (Lai et al., 2018; Sartiani et al., 2002). Substrates were coated with fibronectin (10 µg/ml; Sigma Aldrich, Germany) to improve cell adhesion. The confluent layer of cells was disattached and dissociated with 0.05% Trypsin-EDTA (Sigma Aldrich, Germany). The cells were split at a ratio dependent on the surface area of the substrate (MEAs: 2.54 cm^2, gold chips in 6-well cell culture plates: 9.60 cm^2) and seeded in Claycomb medium, supplemented with 10% fetal bovine serum, 100 U/ml penicillin, 100 µg/ml streptomycin, 0.1 mM norepinephrine, and 2 mM L-glutamine (all from Sigma Aldrich, Germany). The cells were incubated at 37 °C and 5% CO_2 for 3 days until they formed a confluent layer once again. The medium was changed 5 times per week and 1-3 h before recording sessions.

2.2.2 Preparation of Primary Cortical Cells

Primary cortical neurons were isolated from E18 Wistar rats as published before by Brewer et al. (1993). The brains were removed from the rats, and the cortex was dissected. The cells of three cortices were digested in 0.05% Trypsin for 10 min at 37 °C and 5% CO_2. At 5 min of incubation, the suspension was swiveled once. The digestion was stopped by transferring the cortices into a reaction tube containing fresh Neurobasal (NB) medium (Life Technologies, Carlsbad, CA, USA) supplemented with 1% (v/v) B27 (Thermo Fisher

Experiment	# Seeded Cells	Density (cells/mm^2)	DIV
fComInput for opt. stim. and calcium imaging	200k	208	20-28
neuroCapsTiH plastic dishes for calcium imaging	150k-200k	170-227	20-29
neuroCapsTiH coverslips for calcium imaging	200k	208	21-24
neuroCapsTiH coverslips/GLYMO for opt. stim. and calcium imaging	200k	208	20-28
scaledTriangles	200k	208	15-18
jRCaMP1b and ChR2-GFP testing	100k	104	20
aminothiols on gold	200k	208	6
aminothiols on MEAs	150k	132	18

Table 2.1 – Neuronal cell densities and measurement/recording DIVs for different experiments. Data for experiments that are not listed here will be given in the respective results chapters. Experiment labels correspond to chapters Chapter 3 to Chapter 5.

Scientific (Gibco), USA), 0.5 mM L-glutamine (Thermo Fisher Scientific (Gibco), USA), and 0.05 mg/ml Gentamicin (Sigma Aldrich, Germany). The cortices were washed thrice with NB medium, mechanically dissociated using an Eppendorf pipette with a 100-1000 µl tip, and left to settle for 1 min to allow glia cells to adhere to the reaction tube. The supernatant was diluted and used to seed the cells at an appropriate density (Table 2.1). The cultures were incubated at 37 °C and 5% CO_2 for up to day *in vitro* (DIV) 28, depending on the experiment (see Table 2.1). The supplemented NB medium was completely exchanged ~1-4 h after seeding, thereafter half of the NB medium was exchanged twice per week.

All animal experiments were approved by Landesumweltamt für Natur, Umwelt und Verbraucherschutz Nordrhein-Westfalen, Recklinghausen, Germany, under the numbers 81-02.04.2018.A190 and 84-02.04.2015.A173. Both HL-1 cells and neurons were monitored with one of two simple Axiovert light microscopes (Zeiss, Germany) during cultivation.

2.2.3 Homogeneous Coating of Substrates

Sterilization was conducted differently for various substrates: Glass coverslips were quickly sterilized in a flame; glass coverslips with GLYMO and MEAs were either disinfected

with 70% EtOH or for 30 min in UV light; gold substrates were disinfected with 70% EtOH. Homogeneous coating was conducted by applying 10 µg/ml PLL (depending on the experiment, labeled with FITC) in Hank's balanced salt solution (HBSS; Sigma Aldrich, Germany) for 20–30 min at RT. The sample was washed three times with HBSS, and the liquid was completely aspirated.

2.2.4 Transduction

Primary neuronal cultures were transduced with adeno-associated virus (AAV) encoding for an optogenetic actuator or sensor. AAVs were added to the supplemented NB medium in an adequate dilution leading to a multiplicity of infection (MOI) of 2.4E5 genome copies/cell (GC/cell) for AAV6 pAAV.Syn.GcaMP6f.WPRE.SV40 (Chen et al., 2013) (a gift from Douglas Kim & GENIE Project; UPenn Vector Core, USA), 4.395E5 GC/cell for AAV9 pAAV.Syn.NES-jRCaMP1b.WPRE.SV40 (Dana et al., 2016) (a gift from Douglas Kim & GENIE Project; Addgene viral prep # 100851-AAV9; http://n2t.net/addgene:58880; RRID:Addgene_100851), 0.25E5 GC/cell for AAV8 pAAV-Syn-ChR2(H134R)-GFP (Boyden et al., 2005) (a gift from Edward Boyden; Addgene viral prep # 58880-AAV8; http://n2t.net/addgene:58880; RRID:Addgene_58880), and 1.8E4 GC/cell for AAV6 hSyn-Ch2opt-mKate (packaged by UPenn Vector Core, USA). The medium of the cell culture was then completely exchanged with the virus-containing medium at DIV 7 for patch clamp experiments, or 9 or 10 for all optical experiments. At the next bi-weekly medium change (3-5 days later), the virus-containing medium was completely exchanged with supplemented NB medium not containing AAVs to remove excess virus particles that did not infect the cells.

2.2.5 Live/Dead Stainings

Calcein-acetoxymethylester (cal-AM; Thermo Fisher Scientific (Gibco), USA) and ethidium homodimer (EtHD; Thermo Fisher Scientific (Gibco), USA) were supplied to the cell culture medium in a 1:1000 dilution. Cells were incubated at 37° C and 5% CO_2 for 20-40 min, washed once with fresh pre-warmed medium, and analyzed using fluorescence microscopy.

2.2.6 Immunocytochemistry

Immunostainings are a standard technique for fluorescently labeling proteins and large molecules in cells by applying a primary antibody that binds to a specific antigen/target and a secondary antibody coupled to a fluorophore that amplifies and visualizes the bound primary antibodies. Substrates were fixed in pre-warmed (37 °C) 4% paraformaldehyde at RT for 10-15 min, and washed thrice with phosphate-buffered saline (PBS; made from salts acquired from Sigma Aldrich, Germany). The fixed samples were permeabilized with 0.3% Triton X-100 (Sigma Aldrich, Germany) in blocking buffer (1% bovine serum albumin and 2% goat serum in PBS; both Sigma Aldrich, Germany) for 15 min at RT, rinsed thrice with PBS, and blocked with blocking buffer for 1 h at RT. The primary antibody was applied for >3 h at RT (dilutions in blocking buffer: chicken anti-Neurofilament Heavy Chain, abcam, UK, ab4680, 1:400; rabbit anti-Synaptophysin, abcam, UK, ab14692, 1:260; rabbit anti-MAP2, abcam, UK, ab32454, 1:500), and the substrates were washed 3x with PBS. Next, the secondary antibody was applied for 1.5 h at RT (dilutions in blocking buffer: goat anti-chicken DyLight350, life technologies, USA, SA5-10069, 1:130; goat anti-rabbit AlexaFluor 633, life technologies, USA, A21071, 1:500), and the substrates were washed 2x with PBS and once with deionized water. The substrates were then mounted to glass microscopy slides in a mounting solution (Agilent Dako, USA), dried over night at RT, and sealed with nail polish. They were then stored at 4 °C for imaging. Imaging was conducted at an AxioImager Z1 (Zeiss, Germany) in combination with an HXP metal halide light source with appropriate optical filters (DAPI, Green, and DsRed as in Table 2.2, plus an additional FarRed (Zeiss 26) filter: excitation, 575-625; dichroic, 645; emission, 669-710).

2.3 Microelectrode Arrays and Gold Macro Electrodes

2.3.1 Gold Macro Electrodes

Homogeneous Au macro electrodes were used for determining the transparency of holey gold and for initially testing thiol application. E-beam assisted metal evaporation was used to deposit a Ti adhesion layer (~5 nm) and a conductive Au layer (~40 nm) onto 4" quartz wafers (Plan Optik AG, Germany). The wafer was diced into electrodes (1.6 x 3 cm^2) for further usage. The cleanroom fabrication was conducted by Michael Prömpers or Marko Banzet.

2.3.1.1 Modifications for Holey Gold

In case of holey gold macro electrodes, Polystyrene (PS) particles with low functionalization (Bang Laboratories, USA) served as a lift-off mask before metalization. The particles were deposited by Funnel Assisted Interfacial Assembly, as described in detail in Schöps et al. (2018). In brief, a the 4" quartz wafer was cleaned and hydrohpilized in oxygen plasma at 0.7 mbar with 200 W for 5 min to ensure successful colloidal lithography. Subsequently, the wafer was placed horizontally on a sample holder and transferred to a beaker filled with MilliQ water. A PS particle (Ø380 nm) dispersion (5%) in water was added to an equal amount of 0.02% Triton-X 100 in ethanol, leading to a aqueous solution with 50% ethanol, 2.5% particles, and 0.01% Triton-X 100. The particles were added to the surface of the water in the beaker containing the cleaned wafer. At the water surface, the particles formed a monolayer, which was transferred to the entire wafer surface by reducing the water level in the beaker.

Next, the particle size was reduced while increasing the inter-particle distance but keeping the lattice constant (distance between the centers of any two particles) the same. This was achieved by performing reactive ion etching (RIE, Oxford Instruments, Great Britain) with a gas combination of O_2 and CHF_3 in a ratio of 40:10 sccm. The etching conditions were set to 0.026 mbar, 0 °C and a RF power of 30 W for 4 min. The metalization was performed as for homogeneous gold. Finally, the wafer was stripped of the particles with adhesive cello-tape and afterwards cleaned by sonication in acetone. The cleanroom

fabrication was conducted by Michael Prömpers, Marko Banzet, or Bohdan Lenyk.

2.3.1.2 Thiol Application

Substrates were activated in oxygen-plasma for 30s at 0.7 mbar and 200 W, abundantly rinsed with EtOH, bathed in EtOH for 10 min, and rinsed again. All beakers and equipment was also rinsed with EtOH. Thiols were mixed with EtOH in the appropriate ratios to achieve fractions of 2 mM (see section 3.2.1), and the mixture applied to the samples. The containers were backfilled with nitrogen, sealed, and incubate for 24 h. After this time, the samples were again rinsed, bathed for 10 min, and rinsed again with EtOH, dryed in a nitrogen stream, and used as soon as possible because prolonged storage oxidizes thiols (Schoenfisch and Pemberton, 1998).

2.3.2 Fabrication

MEAs were fabricated with the classical photolithography approach on quartz or silicon wafers. The negative photoresists LOR3B and nLOF2020 (both Microchem Corp., USA) were spin coated onto a 4" wafer in a double layer. After exposure to 350 nm UV light (55 mJ/cm^2), the wafer was baked at 110 °C for 1 min, and developed in MIF326 (Microchem Corp., USA) for 35 s to decrease the resist in the area of electrodes, feed lines, and contact pads.

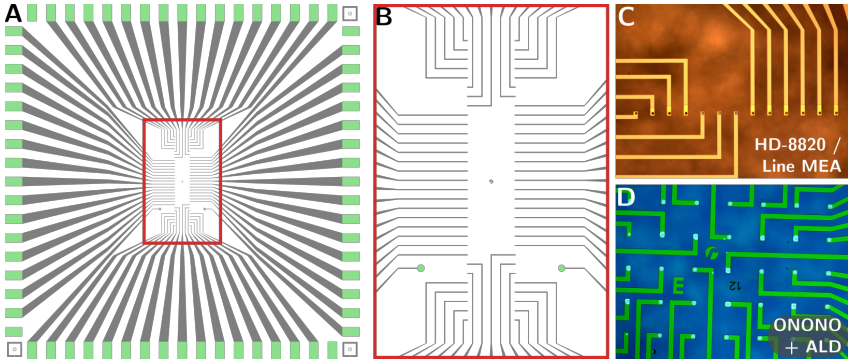

Figure 2.2 – Microelectrode array design variation and etching. (A) Line MEAs are an alternative design option to regular square MEAs (Figure 1.8). **(B)** Zoom-in of the electrode area. **(C-D)** Back etched nano-cavity electrodes under HD-8820 (**C**) and ONONO (**D**) passivations.

The development was stopped by rinsing the wafer in water. Subsequently, e-beam assisted metal evaporation was performed to deposit an adhesion layer of Ti (10-30 nm), a conductive layer of Pt (200 nm) or Au (200 nm), and (in case of nanocavity MEAs) a sacrificial layer of Cr (100 nm). The double layer of resist was removed with acetone and isopropanol to lift off the excess metal. A passivation layer of the polyimide HD-8820 (Hitachi DuPont MicroSystems, LLC) was spin coated onto the wafer, and a soft bake was conducted at 140 °C for 4 min. The area of the electrode openings and contact pads was exposed to UV light with a power density of 250 mJ/cm^2, and the wafer was developed in MIF326 for 90 s. The polyimide was fully polymerized during a hard bake step in a convection oven with N_2 atmosphere at 350 °C for 30 min with a very slow temperature increase and decrease. Finally, the wafer was covered with AZ5214 (Microchem Corp., USA) and diced into 9 MEAs of ~24 mm side length for further usage.

After fabrication, the MEAs were cleaned for 2 min in acetone, isopropanol, and water to remove residues of resist. Glass rings (usually 18 mm inner diameter; for HL-1 cell experiments, 16 mm inner diameter) were dipped into PDMS (10:1 relation of base to curing agent), excess PDMS was removed on a tissue paper, and the rings were placed on the MEAs. The PDMS was cured for 30 min at 110 °C or overnight at room temperature. The glass rings served as cell culture medium containers.

In case of nanocavity MEAs, the sacrificial layer of Cr was etched by placing a drop of Chromium etchant (Sigma Aldrich, Germany) on the electrode area for ~8-12 min (determined by a test etching for each new MEA batch). The result evaluated by DIC microscopy (Figure 1.8 C-D) with a simple Axioplan 2 microscope with a EC Epiplan-Neofluar 10x/0.25 HD DIC ∞/0 objective and corresponding Wollaston prisms and polarizers (all from Zeiss, Germany). The cleanroom fabrication was conducted by Marko Banzet.

2.3.2.1 Different passivation: ONONO

As an alternative to the polyimide HD-8820, MEAs were passivated with 5 alternating layers of SiO_2 (O; 200 nm thick) and Si_3N_4 (N; 100 nm thick), termed ONONO (800 nm thick). After the metalization step in the above described process, the ONONO passiva-

tion was applied using plasma-enhanced chemical vapor deposition (PECVD; SENTECH Instruments GmbH, Germany). SiO_2 was generated with a gas mixture of 7.3 standard litre per minute (slm) SiH_4 and 10.5 slm O_2 at 1 Pa, while Si_3N_4 was generated using 7.8 slm SiH_4 and 10 slm N_2 at 8 Pa. The layers were deposited at 280 °C and an inductively coupled plasma radio frequency of 500 W. After ONONO deposition, the wafer was dehydrated at 150 °C for 15 min, covered with the positive photoresist AZ5214 via spin coating, and baked at 110 °C for 1 min. The resist was exposed to UV light and developed in MIF326 to remove the resist in the areas of the electrode openings and contact pads. The electrodes and pads are opened using RIE with CF_4 (20 sccm), CHF_4 (20 sccm), and O_2 (2 sccm) at 0.002 mbar, a RF power of 150 W and bias voltage of 350 V. The resist was removed by subsequently washing the wafer with acetone, isopropanol and water. The cleanroom fabrication was conducted by Marko Banzet.

2.3.2.2 Non-standard conducting layer: holey MEAs

Holey MEAs were fabricated in the same way as described above. However, before the metalization step the wafer with the patterned photoresist was cleaned in oxygen plasma at 0.7 mbar with 200 W for 5 min, followed by the colloidal lithography described in section 2.3.1.1 (see Figure A.1). The particles were stripped only after removing the patterned photoresist with acetone for metalization lift off. The HD-8820 passivation was applied as described for standard MEAs. The fabrication was conducted by Bohdan Lenyk.

2.3.3 Cell Recordings

2.3.3.1 Equipment and Software

To record electrophysiological signals via MEAs, a custom-built amplification system was used. In this system, a MEA was inserted into a headstage with a 10.1x pre-amplification, and the headstage was connected to a main BioMAS amplifier (Ecken et al., 2003; Eick et al., 2009; Maybeck et al., 2016). This amplifier operated in a maximum output range of ± 10 V and had a built-in gain of 1x, 10x, or 100x, an analogue 3 kHz low pass filter, and a high pass filter with cutoff frequencies of 0.1 Hz, 1 Hz, 10 Hz, or 72 Hz. Its

coupling could be switched between AC and DC mode. With the BioMAS system, up to 64 channels with an additional 16 channels for external sources could be recorded. When using voltage-controlled stimulation, a current measurement board could be connected to record the injected current. The analogue amplified voltage traces were then transmitted to a computer via an AD converter (Texas Instruments, USA).
The amplifier was controlled via a LabView 2016 software (version BioMAS-dev_2018-10-16). The software offered the option for channel selection, stimulation pulses and controlling the functions mentioned above, such as gain. The raw data was written onto the hard drive of the computer as a .dat file, with a .xml file containing meta data about the recording.

2.3.3.2 Recording

For HL-1 cells, the cell culture medium was changed ~1-2 h before the recording session. MEAs with cultured cells (neurons or HL-1 cells) were transferred to the headstage in a BioMAS setup. A Ag/AgCl pellet reference electrode cleaned with ethanol and water was carefully submerged in the cell culture medium without damaging the cells. Faulty channels outside of the output voltage range of the amplifier (due to bad contacts or a damaged conductive layer) were identified in DC coupling mode with a main amplifier gain of 1x and excluded from the recording. Then, recordings were performed in AC coupling mode with a gain of 10x, and a 1 Hz or 72 Hz filter for HL-1 cells or neurons, respectively. If voltage changes in a shape resembling an AP were recorded, the cells were killed by adding a saturated 400 mM KCl solution to the cell culture medium (ratio 1:50 to 1:100) to verify the cellular origin of the voltage changes. If the cells were to be imaged after the recording session, the cells were not killed so as to not alter the morphology due to changed osmotic pressure.

2.3.3.3 Analysis

A custom-written `python` program (BioMAS Viewer, version 1.9) was used to extract the voltage traces from the .dat and .xml files. The software could also be used to plot the traces, and to perform simple procedures such as filtering, Fourier transforming, a simple

peak detection, and exporting to other formats such as comma separated value (CSV). Using the CSV file and `python`, the data could be further analyzed. A semi-automatic peak detection based on the `find_peaks` algorithm of the `SciPy` library and a self-written graphical user interface (GUI) was implemented. The detected voltage peaks were analyzed for their shape, amplitude, and frequency using `SciPy` and `numpy`.

2.3.3.4 Cleaning MEAs after recordings

MEAs without GLYMO were cleaned by incubating the cells in 0.05% Trypsin-EDTA for 15 min, rinsing them with deionized (DI) water, and checking the removal with a light microscope. If necessary, the digestion with Trypsin was repeated. Finally, the MEAs were rinsed with DI water for >1 h. MEAs with GLYMO silanization that were intended to be reused were cleaned with 2% Hellmanex detergent, and also rinsed with DI water for >1 h. MEAs with GLYMO silanization intended for a completely new silanization or other procedure were first cleaned in 2% Hellmanex detergent, rinsed with DI water for >1 h, and then cleaned in O_2 plasma at 100 W and 0.5 mbar for 5 min to remove the silanes and PLL.

2.4 Optical Recordings and Stimulations

Optogenetic tools can be used to record from and stimulate neuronal networks with a very high spatial and increasingly high temporal precision. For this, fluorescence microscopes, laser systems, and amplifiers have to be combined in rather complex setups. Since these setups can then be used for a huge variety of different experiments, the experimental procedures have to be defined clearly.

2.4.1 Microscopy and Amplifier Setups

2.4.1.1 All Optical Stimulation and Recordings

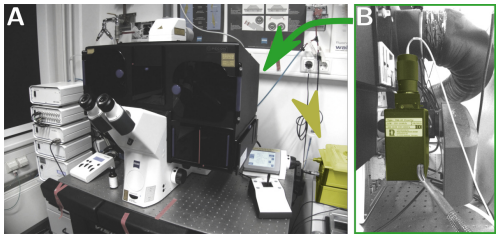

Figure 2.3 – Setup for all optical stimulations and recordings. Components belonging to the ROE laser system are highlighted in yellow. **(A)** Front view of the setup. Note the black incubation chamber on the microscope, the hardware controllers on the left and the laser and UGA-42 control boxes on the right (yellow arrow head). **(B)** Back view of the setup as indicated by green arrow. The gray box on the right contains the Colibri.2 LEDs. The large tubing at the top provides heating of the incubation chamber. Laser components include the optical fibers coupled into a UGA-42 mirror system.

For an all optical approach, a fluorescence microscopy setup was optimized for conducting calcium imaging via either the green indicator GCaMP6f or the red indicator jRCaMP1b and simultaneous stimulation via the optogenetic actuator ChR2-GFP excitable by blue laser light. An inverted Axio Observer.Z1 microscope (Zeiss, Germany) with integrated xy-stage (Merzhäuser, Germany) was used (Figure 2.3 A). To keep the sample at incubation conditions (37 °C, 5% CO_2, 100% humidity) during imaging, the sample holder is enclosed in a humidifiable heating chamber and can be covered with a lid for CO_2 supply. The fluorescence microscopy light source is a Colibri.2 LED system (Zeiss, Germany) with exchangeable LEDs for broad spectrum white light, 365 nm or 385 nm UV light, 445 nm or 470 nm blue light, 505 nm green light, and 590 nm or 625 nm red light (Figure 2.3 B). For fluorescence of different wavelengths, one of the filter sets in Table 2.2 was used. For optical stimulation of ChR2, a blue 473 nm

Designation	Excitation [nm]	Dichroic mirror cutoff [nm]	Emission [nm]
DAPI (Zeiss 49)	355-383	395	420-470
Green (Zeiss 38)	450-490	495	500-550
DsRed (Zeiss 43)	538-562	570	570-640
All Optical	—	580	590 long pass
DIC	—	—	—

Table 2.2 – Filter sets for the all optical setup.

laser (100 mW maximum power output) controlled by a UGA Firefly device (both Rapp Optoelectronics, Germany). The combination of UGA-42 Firefly and laser was calibrated after each startup process. The laser was coupled into the light path after the Colibri.2 illumination system but before the fluorescence filter sets (Figure 2.3 B). The laser system was connected to a trigger box (Zeiss, Germany) to allow for precise alignment of stimulation and recording. To combine fluorescence microscopy of jRCaMP1b with optical stimulation of ChR2, a 561 nm ± 27 nm bandpass filter was moved from the filter cube to the Colibri.2 system directly after the white light LED, thus gaining green excitation light without blocking the laser. Images were recorded with a high speed pco.edge 5.5 sCMOS camera (PCO, Germany) in streaming mode to enable acquisition rates of 100 Hz. The setup was controlled via the imaging software ZEN 2012 blue edition (Zeiss, Germany) with the experiment designer extension and a live image streaming capability via custom-made macros (provided by Rapp Optoelectronics, Germany) to the ROE SysCon software for UGA-42 and laser control (Rapp Optoelectronics, Germany).

2.4.1.2 Electrophysiology and Optical Stimulation

For stimulation via ChR2 and simultaneous electrophysiological recordings with MEAs or whole-cell patch clamp, an Axio Scope.A1 upright fluorescence microscope (Zeiss, Germany) was equipped with a blue 473 nm laser (200 mW maximum power output) controlled by a UGA40 device (both Rapp Optoelectronics, Germany). The setup was described in detail by Maybeck (2011) and is depicted in Figure 2.4. The combination of UGA40 and laser was calibrated after each startup process. A 532 nm (Rapp Optoelectronics, Germany) and a 980 nm (Photontec, Germany) laser were also attached to the setup but

were not used in this thesis. A broad band HXP light source (Zeiss, Germany) and an adequate filter set (Table 2.3) could be used to visualize green (e.g. Ch2-GFP) or red (e.g. Ch2opt-mKate) fluorescence. The excitation filter of the Laser Red filter set (Table 2.3) was located in the part of the light path before the laser was coupled in to avoid filtering of the laser.

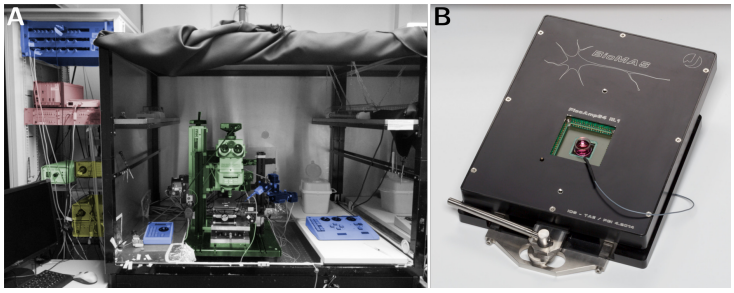

Figure 2.4 – Setup for optical stimulations and electrophysiological recordings. (A) Components of the patching system are highlighted in blue and include the main amplifier (top left), the motor control pads (right and left of microscope), motor main controllers (not visible, in the rack on the left), and the holding arms for headstages and patch pipettes (at the microscope). MEA components are highlighted in red and include the main amplifier (left) and its power source (standing on the left on top) and AD converter (standing on the right on top). Laser components in the rack are highlighted in yellow. From top to bottom: 532 nm laser, 473 nm laser, UGA-40 control box. Other optical components of the microscope are highlighted in green. **(B)** Headstage (preamplifier) of a the BioMAS system. An exemplary MEA device with reference electrode was placed in the middle (containing red medium). The silver lever in front is used to push the headstage up to avoid damage to the connecting pins.

For image acquisition, an AxioCam MRm (Zeiss, Germany) camera was mounted to the microscope. For MEA recordings, the equipment and software described in section 2.3.3.1 were used. Patch clamp recordings and stimulations were conducted with an EPC9 double amplifier with a corresponding pre-amplifier (Heka Elektronik Dr. Schulze GmbH, a) (both HEKA, Germany). The pre-amplifier was mounted on a holder movable by electrical motors (Luigs & Neumann, Germany) in three axes and manually rotatable. The motors were controlled by a micro manipulator SM1 (Luigs & Neumann, Germany). An additional motor, controlled by a micro manipulator SM6 (Luigs & Neumann, Germany), was installed on the microscope body to allow for a motorized fine focus control. The three controller devices (EPC9, BioMAS amplifier, UGA40) could be interconnected with standard BNC connector cables to enable precise synchronization within experiments.

Designation	Excitation [nm]	Dichroic mirror cutoff [nm]	Emission [nm]
DIC	—	—	—
Laser Green	462-497	501	519-549
Laser Red	—	580	590 long pass

Table 2.3 – Filter sets for the setup for optical stimulation and electrical recordings.

The EPC9 amplifier was controlled in voltage or current clamp mode by the Tida software (Heka Elektronik Dr. Schulze GmbH, b) (version 5.05; HEKA, Germany). The UGA device and laser were controlled by the UGA-40 software (Rapp Optoelectronics, Germany). The camera was read out either via the AxioVision software (release 4.8; Zeiss, Germany) or the UGA control software.

2.4.2 Calcium imaging

Calcium imaging on its own allows for monitoring the spontaneous network activity of neuronal populations. Neuronal cultures were transduced with the green calcium indicator GCaMP6f under a Synapsin promoter at DIV 7 or 10 (see also section 2.2.4) and recorded at DIV 21 to 30 in the setup described in section 2.4.1.1. Although an exposure time of 5 or 10 ms was used, the streaming speed of the PCO.edge camera limited the frame rate to between 100 and 200 Hz with the exact frame time points being saved as meta data for later analysis. A 4x4 binning was applied to improve signal-to-noise ratio of the weakly fluorescent signals. The 488 nm LED of the Colibri.2 system was used in combination with the green fluorescence filter set Green (Zeiss 38) (see Table 2.2) and a 5x EC Plan-Neofluar (NA = 0.16) objective.

2.4.2.1 Post-Processing of Calcium Imaging Movies

From the calcium imaging movies, regions-of-interest (ROI) and their mean intensity traces were semi-automatically extracted. Subsequently, peaks were detected in the extracted traces. All data were post-processed in `python`.

The automatic ROI detection within the movies was based on the methods described by Reichinnek et al. (2012) and Rueckl et al. (2017), while the detected ROIs were manually checked using the samuROI GUI (Rueckl et al., 2017). First, the raw intensity $F(x, y, t)$

of a movie with spatial coordinates x and y, and the time t was normalized (Rueckl et al., 2017):

$$\hat{F}(x,y,t) = \frac{F(x,y,t) - F_0(t)}{F_0(t)}, \tag{2.1}$$

where $F_0(t) = \tilde{F}(x,y,t)$ with $\tilde{F}$ as the (time-dependent) median of each image in the raw movie (Figure 2.5 A (top traces), B (black traces)). The maximum intensity projection (MIP) of the normalized movie $\hat{F}$ was calculated as $M(x,y) = \hat{F}_{max}(x,y,t)$ with F_{max} as the maximum values of all pixels (x,y) over t.

Next, the wavelet-based decomposition described by Reichinnek et al. (2012) was used to preprocess the MIP for ROI detection. In brief, a series of $k = (0,1,2)$ smoothing convolutions were performed on the MIP, starting with the (wavelet) kernel

$$A_0 = \begin{pmatrix} 0.0625 & 0.25 & 0.375 & 0.25 & 0.0625 \\ 0.25 & 1 & 1.5 & 1 & 0.25 \\ 0.375 & 1.5 & 2.25 & 1.5 & 0.375 \\ 0.25 & 1 & 1.5 & 1 & 0.25 \\ 0.0625 & 0.25 & 0.375 & 0.25 & 0.0625 \end{pmatrix}. \tag{2.2}$$

Each step k, $2^{(k-1)} - 1$ zeros were inserted between each row and column of A_0, resulting in an extended wavelet function A_k. The resulting smoothed images M_k (with $M_0 = M(x,y)$) were subtracted from each other in each step according to $W_k = M_{k-1} - M_k$, where W_k is a wavelet scale image in which round objects are highlighted. The last wavelet scale image W_2 was binarized with all intensities above the 99.1 percentile set to 1, and all other set to 0. In the binarized image, ROI contour pixels were detected in a sliding square window of 10 pixels diameter (~26 µm) as pixels that a) did not have only neighboring pixels with the value 1, b) did not have only neighboring pixels with the value 0, c) themselves were equal to 1, and d) belonged to a square window with a sum of more than 12.5. Finally, the contour pixels were classified into individual ROI contours by detecting continuously adjacent pixels.

The automatically detected ROIs were loaded into the samuROI GUI and verified manually.

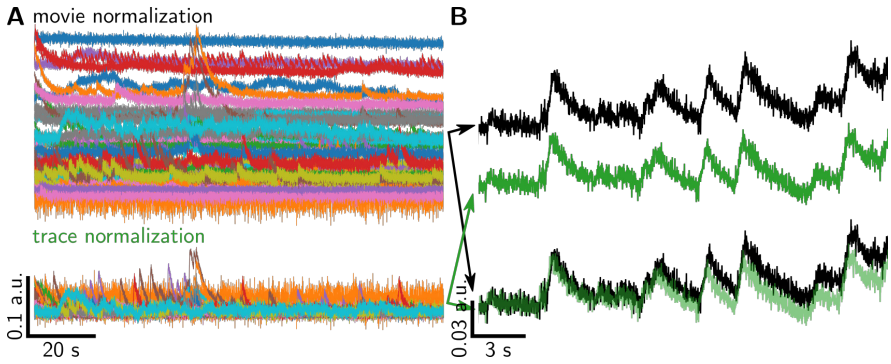

Figure 2.5 – Normalization of calcium imaging movies. (A) Top: $\Delta F/F_0$ traces according to normalization of the movie Equation 2.1. Note that the baseline of the traces differs largely. Bottom: $\Delta F/F_0$ traces according to normalization of the raw mean intensity traces $F(t)$ according to Equation 2.3. **(B)** Traces normalized as in **A**, top panel, (black) or in **A**, bottom panel, (green) as individual (top) or overlayed (bottom) traces, as indicated by arrows of the same color.

ROIs without any intensity changes potentially derived from calcium changes were not taken into account for further analysis. The polygons describing the borders of ROIs from the samuROI class were used to extract the raw mean intensity of all pixels within a ROI over time.

The individual raw mean intensity traces $F(t)$ were then normalized to $\hat{F}(t)$ according to:

$$\hat{F}(t) = \frac{F(t) - F_5(t)}{F_5(t)}, \tag{2.3}$$

where $F_5(t)$ is the sliding 5^{th} percentile in a $\pm$ 2000 frame window. Commonly, $\hat{F}(t)$ is referred to as $\Delta F/F_0$ which will also be done in this thesis.

2.4.3 Combined calcium imaging and optical stimulation

For combined calcium imaging and optical stimulation using optogenetics, neuronal cultures were transduced with the red calcium indicator jRCaMP1b and the actuator ChR2 at DIV 9 or 10 (see also section 2.2.4). A complete workflow for these experiments (and also mostly for section 2.4.2) is depicted in Figure 2.9.

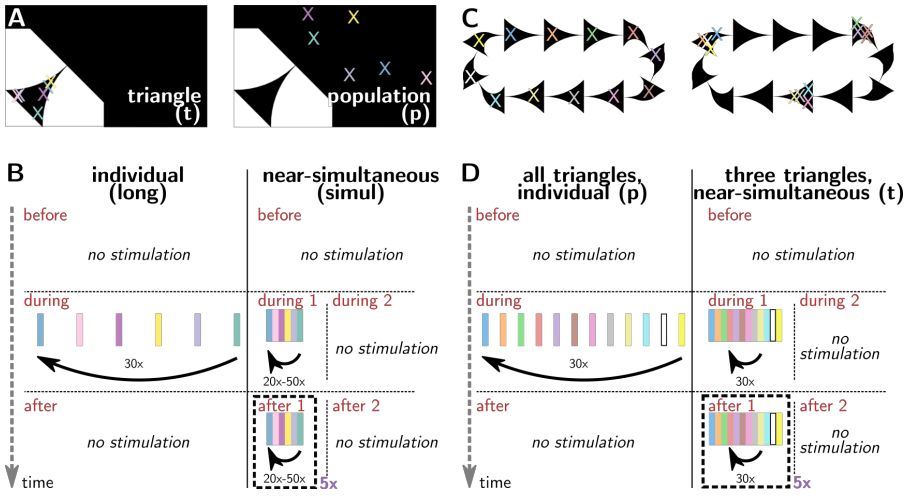

Figure 2.6 – Stimulation routines for all optical experiments. (A,C) Exemplary stimulus locations (depending on the exact location of the neurons) for the fComInput (**A**; 6 neurons; see Chapter 5) and the neuroCapTiH (**C**; 12 neurons; see Chapter 4) µCP pattern designs. Color code corresponds to **B** and **D**. **(B)** Four different stimulation routines (*t_simul*, *t_long*, *p_simul*, *p_long*) were used for the fComInput patterns, each split into three phases: a control phase *before* stimulation; a stimulation phase (*during*); and a control phase *after* stimulation. In *long* stimulations, a 50 ms pulse with a 500 ms delay was chosen. In case of *simul* stimulation (5 ms pulse, 0 ms delay), stimulating the the same 6 neurons as often as in the *long* stimulation results in a very short pulse (in the range of seconds). Therefore, this short pulse (comprising 20-50 cycles of stimulation of all 6 neurons) was triggered manually 5x (marked violet and bold-faced) again in the first half of the *after* phase to witness the effects of a longer total time span of stimulation. To include appropriate control *after* the experiment, as in *long*, the second half of the *during* and *after* phases served as control phases analogous to *after* in *long*. **(D)** In neuroCapTiH patterns, three stimulus routines were used: *p* has 50 ms pulses with 95 ms delay with a stimulus in every triangle (example shown in **C**, left panel); *t* has 5 ms pulses with 0 ms delay with three groups of stimuli in 1-2 triangles distributed through the pattern (example shown in **C**, right panel), and the same splitting of *during* and *after* phases described in **B**; and *test* which uses the same settings as *long* in fComInput patterns in **B** at three of the twelve locations in *t* and **C**, left panel.

The cultures were recorded for 6 min each in the setup described in section 2.4.1.1 at DIV 21 to 30 (Table 2.1). The cultures were imaged with 5 ms or 10 ms exposure times with a 5x EC Plan-Neofluar (NA = 0.16) or 10x Plan-Apochromat (NA = 0.45) objective. A 4x4 binning was applied to improve signal-to-noise ratio of the weakly fluorescent signals. Before recording and stimulating, the laser spot positions were selected based on a fluorescence image taken in the green channel (of ChR2-GFP). The positions were transferred as polygon shapes to this image for later analysis. The laser output power was set to 0.38 mW, with an effective power density on the sample of 1210 mW/mm^2 at a spot size of 314

μm^2. The laser stimulation pulses were 50 ms or 100 ms long. Depending on the pattern of the culture, different stimulation locations and sequences were chosen (see Figure 2.6, Chapter 4, and Chapter 5).

2.4.3.1 Additions to Post-Processing

Some additional post-processing steps had to be implemented into the workflow described in section 2.4.2.1. Due to the experimental process and the resulting file size, the experiment was split into three blocks, which were analyzed individually. The ROIs of all experimental blocks (e.g. "before", "during", "after", see also Figure 2.6) were combined and duplicate ROIs were merged after semi-automatic ROI detection. A mean intensity trace for each ROI spanning all blocks was extracted. Moreover, before ROI detection, frames showing the extremely bright laser stimulus artifacts were removed. For this, the mean intensity of each frame was calculated to get one mean intensity trace of the movie $F_{movie}(t)$ (Figure 2.7 A-C, blue trace). This trace was normalized to $\hat{F}_{movie}(t) = F_{movie}(t)/\tilde{F}_{movie}$. Laser artifacts were only cut in movies, for which $max(\hat{F}_{movie}(t)) - median(\hat{F}_{movie}(t)) > 0.0055$ (Figure 2.7 D). To remove the laser artifacts, a threshold was defined as $F_{movie,thresh}(t) = F_{movie,10}(t) + (F_{movie,max} - F_{movie,min})/x$ (green line in Figure 2.7 A-C), where$F_{movie,max}$ and $F_{movie,min}$

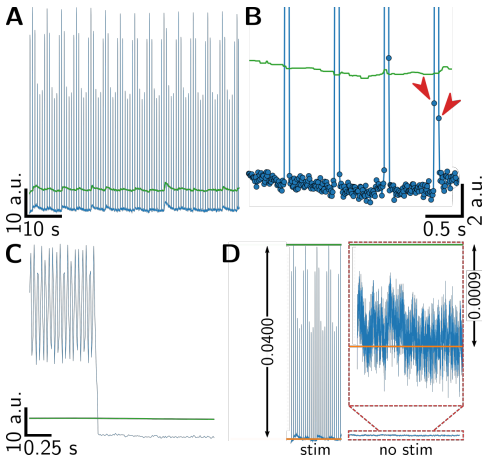

Figure 2.7 – Removing laser artifacts. (A-C) Mean intensity traces $F_{movie}(t)$ (blue) including large laser artifacts (peak-like shape) and their corresponding thresholds $F_{movie,thresh}(t)$ (green) for individual stimulation (**A**, magnified in **B**), and near-simultaneous stimulation (**C**). Note the points in **B** belonging to an artifact but under the detection threshold (red arrow heads). **(D)** Normalized mean intensity trace $\hat{F}_{movie}(t)$ (blue), its median (orange) and maximum (green) for a stimulated trace (left panel; note the clearly visible laser artifacts) and a not stimulated trace (right panel). The bottom dashed red box is in the same scale as the stimulated trace in the left panel. The top dashed red box is a magnification of the bottom one.

Salt	Molar mass of substance [g/mol]	Final concentration [mM]	Mass for 200 ml solution [g]
NaCl	58.44	2	0.023
KCl	74.55	120	1.789
$MgCl_2$-hexahydrate	203.3	4	0.163
HEPES	238.3	5	0.238
EGTA	380.4	0.2	0.015
Mg-ATP	507.2	0.2	0.020

Table 2.4 – Salt concentrations for intracellular patch solution. The pH value was adjusted to 7.3 with 1 M KOH. Osmolarity was adjusted roughly to 260 mOsmol/kg with glucose and measured for the exact value. Everything was prepared on ice.

are the maximum and minimum of $F_{movie}(t)$, x is a freely choosable value, and $F_{movie,10}(t)$ is the sliding 10^{th} percentile in a window arbitrarily defined as ± half the length in ms taken as frames of the longest laser stimulus in the recording. All frames at time points t for which $F_{movie}(t) > F_{movie,thresh}(t)$ were removed and the time points were saved for further usage. In movies with individual stimulations (see previous section, Chapter 4, and Chapter 5), x was 10 (Figure 2.7 A), and in movies with near-simultaneous stimulations, x was 4 (Figure 2.7 C). Because some frames at the beginning and/or ending of a laser pulse were unnaturally high but below $F_{movie,thresh}(t)$ (Figure 2.7 B, red arrow heads), 2 frames more than the actual stimulus length were removed from the movie. The intensity value in the cut time points was replaced by the pixel-wise mean of the frame before and the frame after the laser artifact: $F_{cut}(x,y) = \frac{F_{before}(x,y)+F_{after}(x,y)}{2}$.

2.4.4 Patch clamp and optical stimulation

With a combination of the whole cell patch clamp technique and optical stimulation using optogenetic tools, the influence of a small network of neurons on an individual neuron can be investigated. For these experiments, neuronal cell cultures were transduced with ChR2 at DIV 7 (see also section 2.2.4) and measured at DIV 15-18 (Table 2.1) with the setup and materials described in section 2.4.1.2. Bringing a glass capillary including Ag/AgCl electrode into whole cell patch clamp configuration is a well established procedure and its theory is described in section 1.2.1. Briefly, a glass capillary with an opening corresponding to a resistance of 7-10 MΩ in solution and containing a Ag/AgCl electrode was filled

Salt	Molar mass of substance [g/mol]	Final concentration [mM]	Mass for 1 l solution [g]
NaCl	58.44	120	7.013
KCl	74.55	3	0.224
$MgCl_2$-hexahydrate	203.3	1	0.203
HEPES	238.3	10	2.383
$CaCl_2$	110.98	2	0.222

Table 2.5 – Salt concentrations for extracellular patch solution. The pH value was adjusted to 7.3 with 1 M NaOH.

with intracellular patch solution (Table 2.4) and inserted into the pre-amplifier. The cell culture medium was replaced with extracellular patch solution (Table 2.5), pre-heated and adjusted to the osmolarity of the cell culture medium by adding glucose or water. The glass capillary was brought close to the cell under constant, slightly positive pressure to avoid clogging in voltage clamp mode until an increase in the membrane resistance (R_m) of ~1 MΩ was measured. The positive pressure was released and a slight negative pressure (suction pulse) was applied to attach the capillary to the membrane, as indicated by an increase of R_m to more than 1 GΩ. After adjusting the holding potential to -50 mV to -70 mV (which was also used in the experiments), the membrane was opened by applying short negative pressure pulses (indicated by a decrease of R_m to ~200-400 MΩ). Depending on the experiment, current or voltage traces were recorded (in voltage or current clamp mode, respectively), always accompanied by the TTL voltage pulse indicating a laser pulse. In current clamp mode, the current measured at the holding potential in voltage clamp mode was used as a holding current. Before each experiment involving optical stimulation, the cell's ability to generate APs was tested using a series of current steps in current clamp configuration (from $I_{hold} - 100$ pA to $I_{hold} + 1000$ pA in 20 steps). A laser output power of 0.8 mW was used, with an effective power density of 577 mW/mm^2 at a spot size of 1385 µm^2 on the sample. The locations and sequences used in the experiments involving optical stimulation are described in more detail in Chapter 4.

2.4.4.1 Analysis of Patch-Clamp Recordings

Patch-clamp recordings were analyzed with custom-written `python` scripts. Times in the voltage trace, $V(t)$, during which the cell was stimulated and times after stimulation were defined according to the square TTL signal in the AD recording channel (connected to the UGA-40 control box) of the EPC9 amplifier. Within the designated periods during stimulation and after stimulation, peaks were detected in the differentiated voltage traces, $\frac{dV}{dt}(t)$, using `SciPy`'s `find_peaks`. The height parameter was 5x the standard deviation of $\frac{dV}{dt}(t)$, and the distance parameter was set to 100 samples (10 ms). If no peaks were detected but the maximum of the designated $V(t)$ period was larger than the standard deviation of the whole trace $V(t)$, and the maximum within the stimulated region was located more than 20 ms after the start of stimulation, an ePSP instead of an AP was assumed. In this case, the maximum was taken as the peak value in the designated period. From all of these peaks, the activity ratio (number of peaks/number of blocks), the mean response delay, mean amplitude, and mean number of spontaneous peaks after each stimulus location were extracted from the defined periods.

2.5 Data Analysis of Neuronal Network Recordings

2.5.1 Peak Detection in Calcium Traces

Intensity peaks in $\Delta F/F_0$ traces extracted from calcium imaging movies (see section 2.4.2.1) were detected semi-automatically using the `find_peaks` algorithm of the `SciPy python` library, and a self-written GUI for verifying the detected peaks (for exemplary trace sections, see Figure 2.8 A). Before peak finding, the $\Delta F/F_0$ traces were average filtered by convolving the traces with a 0.2 s long kernel of ones (Figure 2.8 A, C). As a baseline for parameter estimation, a 100 frame long time window $F_{base}(t)$ was determined at the time points for which the standard deviation $\sigma(F)$ is minimal. The parameters for `find_peaks`

Parameter	Value
height	$\overline{F}_{base}(t) + b\,\sigma(F(t))$
prominence	$3b\,\sigma(F_{base}(t))$
distance	0.2 s
wlen	2 s
width	0.2 s

Table 2.6 – Parameters for initial peak finding. The thresholding value b was set to 5.

are summarized in Table 2.6. The amplitudes of the detected peaks were saved for further analysis, whereas the time points of the peaks were further refined: After peak detection, the $\Delta F/F_0$ traces were average filtered by convolving the traces with a 0.1 s long kernel of ones, and differentiated over 50 ms (Figure 2.8 B, D). The maximum value of the differentiated traces in a 0.4 s long window before each detected peak was taken as the new peak value, as it is closer to the onset of the peak, and therefore a better estimation of the time point of the much faster AP (Figure 2.8 D; see also section 1.1.1.2). This peak estimation is not accurately estimating the exact onset of each peak, and very small peaks are poorly reflected in the differentiated trace. However, it shifts the peak time points in a controlled fashion towards earlier values that depend on the upwards slope of the original peaks. This results in a much more precise assignment of peaks to certain stimuli (Figure 2.8 D), and a more precise timing of peaks within SNEs.

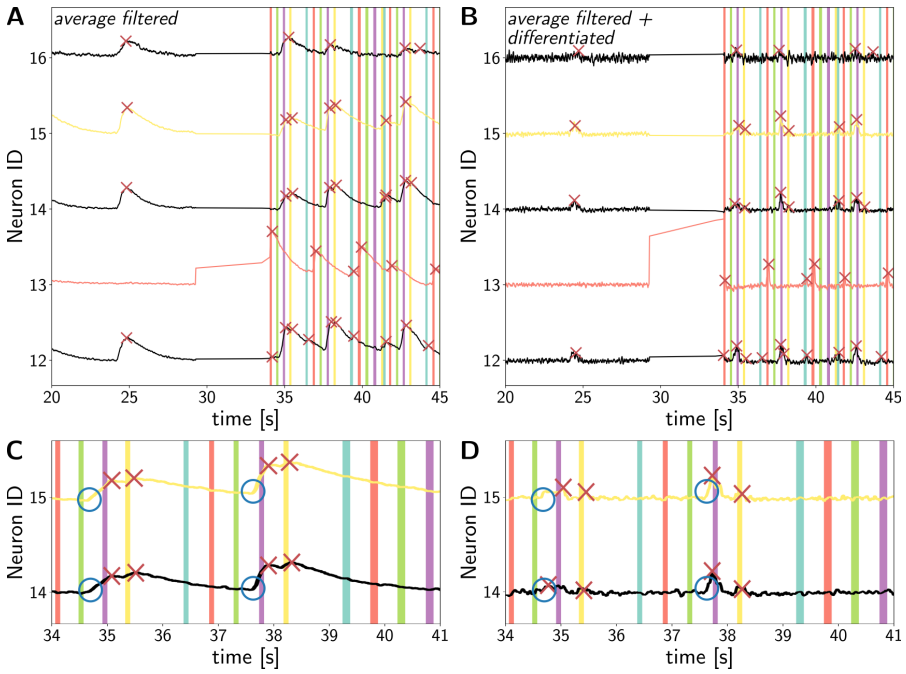

Figure 2.8 – Filtered and differentiated traces with detected peaks. Exemplary average filtered (0.1 s kernel length) with originally detected peaks (**A**, magnified in **C**) and additionally differentiated (over 50 ms) $\Delta F/F_0$ traces with shifted peaks towards the maximum value in a 0.4 s window before the original peak location (**B**, magnified in **D**). Vertical colored bars indicate stimuli, with the same colors corresponding to the same stimulated neuron. Blue circles in (**C**-**D**) indicate the position of the onset of the peaks, for reference. Note that the peaks in **D** mostly lie between the same two stimuli as the blue circled onset, whereas the peaks in **C** (i.e. the maxima) sometimes are located after a subsequent peak.

2.5.2 Synchronous Network Event Detection

SNEs were detected using a simple thresholding algorithm. The peak trains $s(t)$ (for $s(t_{peak}) = 1$ and $s(t_{nopeak}) = 0$) of all neurons u in a network U were summed to get a combined peak train with all calcium event time points $S(t) = \sum_{u \in U} s_u(t)$. A smoothed, combined, approximate firing rate for the n peaks in $S(t)$ was calculated based on Dayan and Abbott (2001a) using a window function of duration $\Delta t = 500$ ms:

$$r(t) = \sum_{i=1}^{n} w(t - t_i), \tag{2.4}$$

where the window function is

$$w(\tau) = \begin{cases} 1 & \text{if } -\Delta t/2 \leq \tau < \Delta t/2 \\ 0 & \text{otherwise.} \end{cases}$$

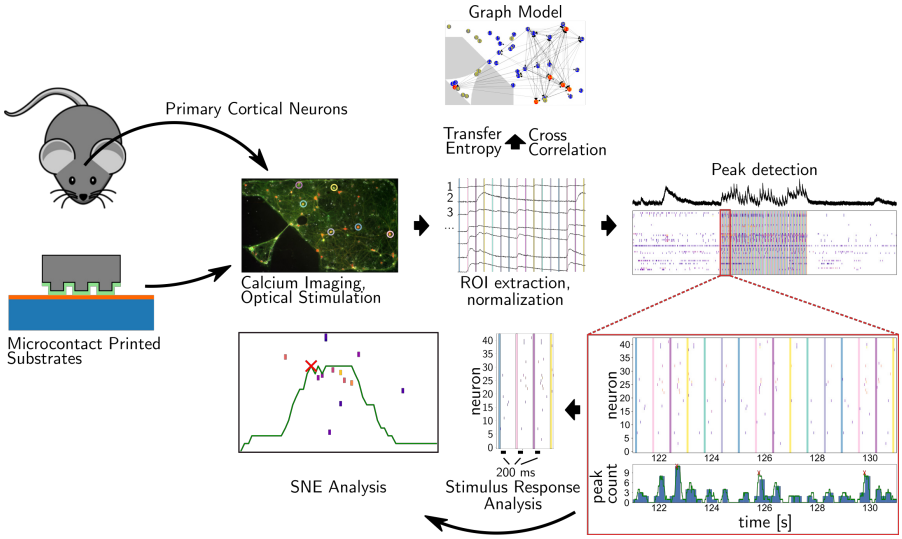

Figure 2.9 – Complete workflow for all optical recordings and stimulations and analysis. Primary neurons are seeded onto µCP substrates, and imaged and stimulated or only imaged. ROIs and mean intensity traces are extracted, normalized to $\Delta F/F_0$ traces, and directly used for cross-correlation- and transfer entropy-based graph model construction. Additionally, calcium peaks were semi-automatically detected, shifted towards the peaks of the traces' first derivative, and used to find SNEs in the recordings. The peak trains were used to analyze the effective response to individual stimuli, and the SNEs were analyzed for their duration and similarity between different stimulation routines.

Two thresholds were chosen as the height parameter for the `find_peaks` algorithm of the SciPy `python` library to detect minor synchronous activity between more than 20% of the population and major SNEs of more than 50% of the population. Since $r(t)$ contains the same peaks at adjacent time points due to the overlap of $w(\tau)$, the actual peaks in a window of duration Δt around each network event peak time point were designated as peaks within a network event.

2.5.3 Edit Distance

The edit distance or Levenshtein distance was established as a measure for the similarity between words. It counts the minimum amount of operations (insertions, deletions, substitutions) needed to transform one word into the other. In this thesis, the implementation by Pasquale et al. (2017) (see especially Supplementary Figure 5) was used to determine the edit distance between the temporal neuronal patterns in different SNEs. In brief, an ASCII character was assigned to each neuron measured in a network (neuron 1 = 'a', neuron 2 = 'b', ...). The ASCII characters were written in the order in which the neurons elicited a calcium event during an SNE. For example, if neuron 2 fired first, neuron 1 fired second, and neuron 3 fired third, this would correspond to the string 'bac'. The edit distances of these strings were calculated, and the two strings were shuffled 200 times. The normalized edit distance was then defined as the fraction of edit distances between the shuffled strings that were smaller than the actual edit distance between the original strings. If this fraction was below 0.05, the SNEs were considered significantly similar.

2.5.4 Cross-Correlations

Cross-correlation (Xcor) is widely used to determine functional connections between neurons in a network (Bonifazi and Massobrio, 2019). XCor between two discrete neuronal signals (spike trains or other processes like calcium intensity traces) $f_x(t)$ and $f_y(t)$ is defined simply as:

$$R_{xy}(\tau) = \sum_{t_0}^{t_0+T_{tot}} \overline{f_x(t)} f_y(t+\tau), \tag{2.5}$$

where t is discrete time step of the total time T_{tot} of $f_x(t)$ and $f_y(t)$ and τ is a discrete time step of a time span around $\tau = 0$ (i.e. the correlation between the two processes). R_{xy} was then normalized against the autocorrelation functions of x and y to obtain the scaled partial covariance density (Eichler et al., 2003):

$$\hat{R}_{xy}(\tau) = \frac{R_{xy}}{\sqrt{r_x r_y}}, \tag{2.6}$$

where r_x and r_y are the maxima of $R_{xx}(\tau)$ and $R_{yy}(\tau)$ at $\tau = 0$, respectively. By determining τ_{max} at the maximum of $\hat{R}_{xy}(\tau)$, the average delay between an event in $f_x(t)$ and an event in $f_y(t)$ can be found. Thus, the maximum of $\hat{R}_{xy}(\tau)$ was used as the weight of a connection with the direction $X \longrightarrow Y$ if $\tau_{max} < 0$ and with the direction $Y \longrightarrow X$ if $\tau_{max} > 0$.

2.5.5 Generalized Transfer Entropy

The concept of transfer entropy (TE) and generalized transfer entropy (GTE) was researched and an algorithm was designed and implemented by Müllender (2020) under my close supervision, and afterwards further extended and modified by myself. The TE between two processes describes the information (or entropy) transferred between the two processes by measuring how strongly a process X depends on the past states of process X and the second process Y. It is stronger if more surprising, improbable events occur. TE's basis is the information content of the discrete process X_i, the Shannon entropy $H(X_i) = \sum_{x_i \in A} p(x_i) log_2 \frac{1}{p(x_i)}$, where p is the probability that X_i is in state $x_i \in A$ at time point i. The base of the logarithm determines the unit of the entropy, with the common unit bits for a base of 2. The derivation from the Shannon entropy over the Kullback entropy to TE, utilizing the concept of Markov chains, is described and reviewed in detail by Kaiser and Schreiber (2002) and summarized in less detail, but for properties specific to my experimental system, by Müllender (2020). Finally, the TE between processes X_i and Y_i for the past k states of X_i and the past l states of Y_i is defined as (Schreiber, 2000):

$$T(X_{i+1}|X_i^{(k)}, Y_i^{(l)}) = \sum_{x_{i+1}, x_i^{(k)}, y_i^{(l)}} p(x_{i+1}, x_i^{(k)}, y_i^{(l)}) log_2 \frac{p(x_{i+1}|x_i^{(k)}, y_i^{(l)})}{p(x_{i+1}|x_i^{(k)})}, \tag{2.7}$$

where $p(a|b)$ is the conditional probability that a occurs if b also occurs. The TE is non-symmetric, as opposed to mutual information, another measure for the information transfer between two processes.

Taking into account that in calcium imaging, the exposure time of the camera (10-20 ms) is roughly 2-10 times larger than the duration of an AP (2-5 ms), Stetter et al. (2012)

proposed a generalized form of TE. In generalized TE, same bin interactions are taken into account, and a threshold value is introduced that eliminates consideration of SNEs (see section 1.1.3) in TE. In this thesis, one of the main points is to elicit SNEs via stimulation and compare the stimulated networks to spontaneously active networks. Therefore, a modified version of generalized TE (from here on GTE) was used that is defined as:

$$T(X_{i+1}|X_i^{(k)}, Y_i^{(l)}) = \sum_{x_{i+1}, x_i^{(k)}, y_{i+1}^{(l)}} p(x_{i+1}, x_i^{(k)}, y_{i+1}^{(l)}) log_2 \frac{p(x_{i+1}|x_i^{(k)}, y_i^{(l)})}{p(x_{i+1}|x_i^{(k)})}. \tag{2.8}$$

In spite of a less accurate estimation of the functional connections between neurons, stationarity was assumed for processes X_i and Y_i to reduce computing time, and because I was mainly interested in the relative change in GTE between different stimulation conditions, and not the absolute transferred information. The larger of the GTEs for $X \longrightarrow Y$ and $Y \longrightarrow X$ was used as a weight for the connection between neurons X and Y.

2.5.6 Graph Theoretical Model

Graph theoretical models serve as a useful tool for the analysis of complex networks (for a review, see Rubinov and Sporns (2010)). A graph model consists of nodes, in my case the neurons in a network, and edges, in my case the functional connections between neurons in a network. Two different ways of assigning weights and directions to the edges were used: a) Xcor (see Equation 2.6, section 2.5.4), b) a modified GTE (see Equation 2.8, section 2.5.5). In this thesis, the `python` package `NetworkX` 2.4 was used. The graph analysis was first implemented for Xcor and GTE by Müllender (2020) under my close supervision, and afterwards slightly adjusted (compare Müllender (2020) and this thesis), and extended by other network measures. The determined topology measures were the density, the global efficiency, and the average clustering coefficient (see section 5.4.1). Moreover, the number of equal hub nodes, sink nodes, source nodes, and nodes with the 0.5% strongest edges between experimental conditions were counted (see section 5.4.3 and next section). For comparison of connectivity measures, random graphs were calculated using the `gnm_random_graph` method of `NetworkX`. This method creates a random, directed graph with the same number of edges and nodes. The original edge

weights were then shuffled randomly and applied to the random graphs.

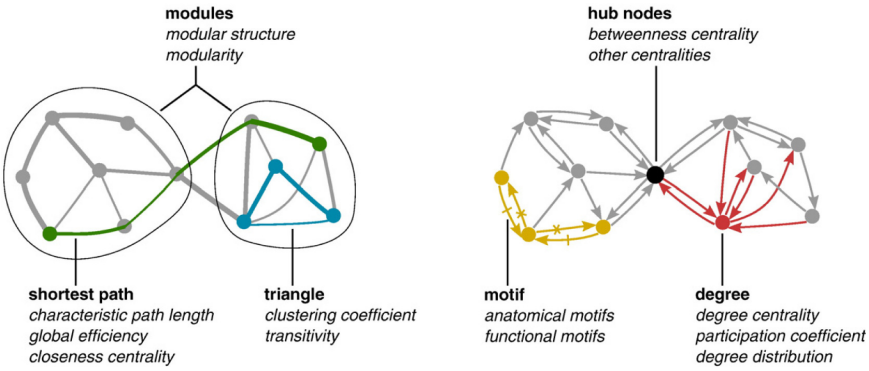

Figure 2.10 – Connectivity measures derived from graph models. A few basic measures are the basis for global connectivity parameters. The shortest path length can be used to describe the efficiency of a network. Triangles of nodes are usually a good indicator for clustering within a network. Hub nodes indicate connecting nodes between different subnetworks or modules. Motifs are recurring patterns in edge weight and direction between multiple nodes. Finally, the degree of a node defines how much that node participates in the network. Taken from Rubinov and Sporns (2010).

2.5.6.1 Sink, Source, and Hub Nodes

In directed graphs, sink and source nodes are the nodes of the most in- or outgoing edges, respectively. The number of incoming edges to a node i is called the in degree $k_i^{in} = \sum_{j \in N} a_{ji}$, where N are the nodes in the network and a_{ji} is the edge between nodes j and i. The out degree is defined analogously as $k_i^{out} = \sum_{j \in N} a_{ij}$. In this thesis, all nodes with k_i^{out} higher than 0.5 standard deviations above the mean are considered source nodes. Sink nodes are defined analogously for k_i^{in}.

Hub nodes can be determined via a measure called the betweenness centrality which describes how many shortest paths between other nodes pass through this node (Figure 2.10 right). Betweenness centrality is therefore defined as (Rubinov and Sporns, 2010):

$$b_i = \frac{1}{(n-1)(n-2)} \sum_{h,j \in N, h \neq j, h \neq i, j \neq i} \frac{\rho_{hj}(i)}{\rho_{hj}}, \tag{2.9}$$

where $\rho_{hj}(i)$ is the number of shortest paths between nodes h and j through node i and ρ_{hj} is the number of shortest paths between nodes h and j. In this thesis, all nodes with b_i higher than one standard deviation above the mean are considered hub nodes. A higher threshold was chosen to yield comparable numbers of hub, sink and source nodes. As these node numbers are based on very different measures ($k_i^{in/out}$ or b_i), keeping them roughly in the same order of magnitude provide some guidance that these numbers are not underestimated or overestimated.

2.5.6.2 Density

The density is a measure combining the number of nodes and edges in a graph. It is 0 for a graph without edges and 1 for a complete graph (in which all nodes are connected to all other nodes). It is described as:

$$d = \frac{m}{n(n-1)}, \tag{2.10}$$

where n is the number of nodes and m is the number of edges in the network.

2.5.6.3 Global Efficiency

The global efficiency (GEf) describes how well information can spread to all nodes of a network. It is maximal in a fully connected network and becomes smaller if more nodes lie between any two nodes (Figure 2.10 left). For n nodes N, the global efficiency is defined as (Rubinov and Sporns, 2010)

$$E = \frac{1}{n} \sum_{i \in N} \frac{\sum_{j \in N, j \neq i} d_{ij}^{-1}}{n-1} \tag{2.11}$$

at nodes i and j, where d_{ij} is the shortest path length between nodes i and j. In this thesis, the shortest path length is taken as $d_{ij}^{w,\longrightarrow} = \sum_{a_{uv} \in g_{i \longrightarrow j}^{w}} w_{uv}^{-1}$, where $g_{i \longleftrightarrow j}$ is the shortest geodesic path between nodes i and j and w_{uv} is the weight of the edge a_{uv}. Thus, the global efficiency is inversely correlated to the shortest path length.

2.5.6.4 Average Clustering Coefficient

Clustering around a single node can be described as the fraction of neighboring nodes that are also neighbors of each other, or the number of triangles around a node. The average clustering coefficient (ACC) describes the degree to which clusters, or subnetworks, of nodes exist in the whole network (Figure 2.10 left). Networks with a high clustering coefficient and high global efficiency are called small-world networks. The number of triangles around node i are defined as $t_i = (\hat{W} + \hat{W}^T)^3_{ii}$ (Fagiolo, 2007), with $\hat{W} = \{w_{ij}^{\frac{1}{3}}\}$ as the matrix obtained by taking the 3rd root of each entry of the weight matrix. On the other hand, the number of all possible triangles around a node i is $T_i = (k_i^{out} + k_i^{in})(k_i^{out} + k_i^{in} - 1) - 2\sum_{j \in N} a_{ij}a_{ji}$ (Fagiolo, 2007). The average over all nodes N of these measures is the ACC (Fagiolo, 2007):

$$C = \frac{1}{n} \sum_{i \in N} \frac{t_i}{2T_i}. \tag{2.12}$$

2.6 Statistical Comparisons

Different statistical tests were used as indicated in the respective text and figures. For small sample sizes of uneven size (< 20 data points), the non-parametric pooled bootstrap test with $B = 100000$ (from hereon referred to as bootstrap test) was used. The `R` implementation by Dwivedi et al. (2017) (Appendix A.1) was reproduced in `python`. For normally distributed samples, the independent, two-sample t-test (referred to as t-test) of the `SciPy.stats` library was used (sample sizes > 10, as the t-test already provides reliable results for small samples (de Winter, 2013)). For large (> 20), non-normally distributed samples, the Mann-Whitney-U test of the `SciPy.stats` library or the non-parametric pooled bootstrap test was used. Multiple comparisons were conducted using Bonferroni-corrected Dunn's multiple comparison test or t-test for normally distributed samples. For non-normally distributed and small samples, Mann-Whitney-U or bootstrap tests were used for all comparisons and afterwards Bonferroni-corrected. To test for overall significance within multiple samples (not between individual pairs), sometimes the Kruskal-Wallis-H test of the `SciPy.stats` library was used.

Boxplots are displayed in the standard implementation of the `python` module `PyPlot` in the `matplotlib` library: Boxes extend to the upper and lower quartile, the median is indicated as a line, whiskers extend to the last data point within the upper and lower quartile $\pm$ 1.5 x interquartile range, and outliers beyond that range are displayed as individual data points, or all data points are displayed as gray crosses. Text in the corresponding section referring to boxplots will give the median. If relevant to the displayed data sets, the first quartile (Q1) and third quartile (Q3) are also stated. Sometimes, only the median will be given for clarity if the distributions show a similar spread. Errorbars in bar plots indicate the standard deviation. Text referring to bar plots will give the mean $\pm$ standard deviation. Statistical significance is indicated by asterisks corresponding to the p-values ($***$ (yellow): $p < 0.001$; $**$ (orange): $0.001 < p < 0.01$; $*$ (red): $0.01 < p < 0.05$).

Correlations were investigated with the `linregress` function of the `SciPy.stats` library in `python`. The function outputs the slope and intercept of a linear function fitted to a dataset. Moreover, Pearson's correlation coefficient R and a p-value stating the statistical significance of the difference to a regression slope of 0 is given. The color of the p-value in plots corresponds to the color code of asterisks.

Chapter 3

Observing Patterned Neurons

Different *in vitro* techniques enable researchers to exert control over various aspects of neuronal cell cultures. Micro-electrode arrays have been used as a major electrophysiological technique for the investigation of such neuronal cultures (see section 1.2.2). Moreover, optogenetic tools have become more and more important recently as the tools themselves and the microscopy setups around them are constantly improved and fine-tuned (section 1.3). Additionally, patterning techniques for neuronal networks continuously help to understand the basics of neuronal networks *in vitro* (see section 1.4). Ideally, these tools can be combined to correlate direct electrical activity of cells growing on electrodes with calcium imaging of these cells and extend this correlation to the complete neuronal network. However, there are some challenges when combining these methods. MEA electrode materials are usually not transparent, limiting their combination with many optogenetic approaches. Also, MEA passivations behave differently from substrates such as glass used to develop patterning techniques and for pure optical investigations. Moreover, patterning itself highly depends on the substrate and needs to be optimized to achieve clearly defined patterns while avoiding cell clumping. In this Chapter, I describe different approaches of how to tackle improving certain aspects of these methods for controlling neuronal networks.

This chapter was in part reproduced from Hondrich et al. (2019b) and Hondrich et al. (2019a).

3.1 Improvements in Microcontact Printing

3.1.1 Polystyrene and GLYMO Improve Patterning

Glass is a widely used material for culturing cells, as it is cheaply produced, is biocompatible and transparent. Due to its low autofluorescence and transparency, it is also well suited for the combination of cells with optogenetics. Early microcontact printing experiments intending to influence cellular guidance and/or patterning were established on bare glass surfaces (see also section 1.4.1). Although this can lead to well-defined cell

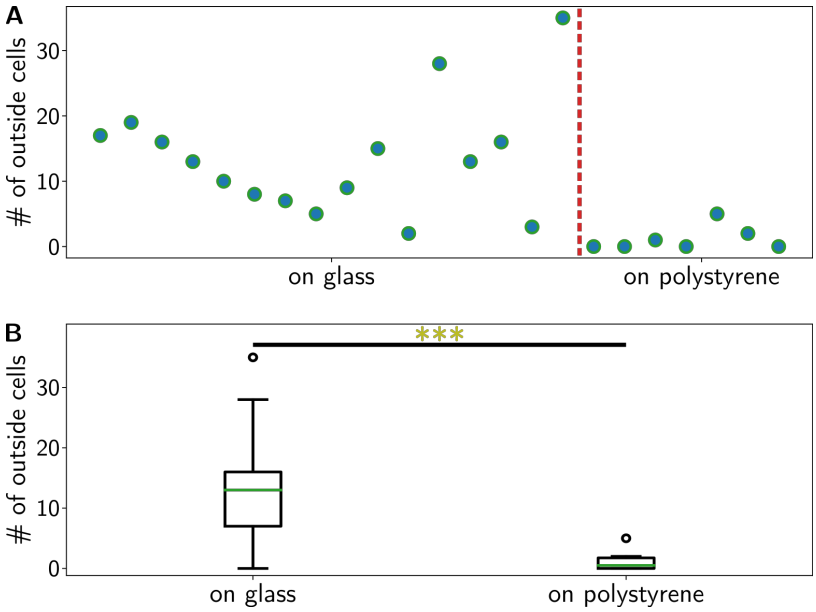

Figure 3.1 – Polystyrene improves the patterning quality of microcontact printing. **(A)** Development of printing quality measured by the number of cells growing outside of the pattern. Each point represents one experiment. Apart from cells growing outside of the pattern in all experiments, the variability between experiments is very high. On Polystyrene, variability and outside cell number is reduced. **(B)** Pooled comparison of the experiments in **A**. Bootstrap test: $p < 0.001$

patterns, the undefined nature of commonly used borosilicate glass and a fabrication not optimized for its use as a highly reproducible surface results in a high variation between and even within individual lots of glass (see Figure 3.1 A and Figure 3.2 A).

As a first variation to achieve higher reproducibility, I exchanged the glass substrate for polystyrene (PS) cell culture dishes. On this substrate, the amount of cells growing outside the pattern could be reduced (median: 0.5 cells, Q1: 0.0, Q3: 1.75; Figure 3.1 B) as compared to glass (median: 13.0 cells, Q1: 7.0, Q3: 16.0). The field-of-view was ~5.261 mm^2 with a printed area of ~2.021 mm^2, leaving an unpatterned area of ~3.240 mm^2. However, PS shows some optical artifacts or impurities rendering it less ideal than glass for imaging purposes (stripe pattern in background of Figure 3.2 B, magnified in C). Also, cells were still growing outside of the pattern, albeit less than on glass (Figure 3.1). Moreover, the coating molecule PLL is only physisorbed to the substrate (Offenhäusser et al., 2007) and does not covalently bind, which could lead to weak cell adhesion to the substrate. Although on glass coverslips cell adhesion is certainly important, it is essential for µCP on MEAs to provide a close coupling of cells to the electrodes (see section 1.2.2).

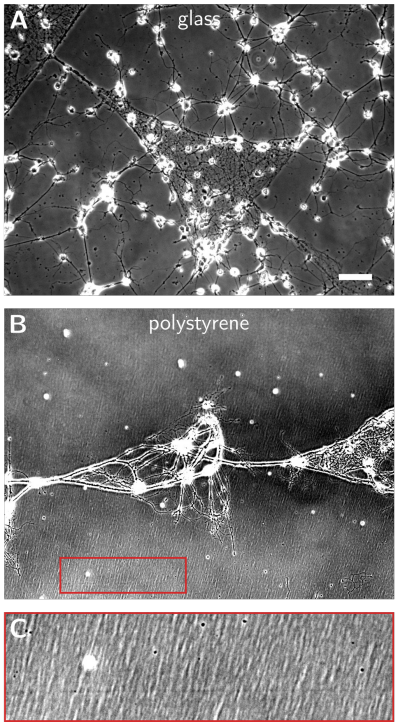

Figure 3.2 – Patterned neuronal cultures on glass and polystyrene. Phase contrast micrographs of patterned neuronal cultures on glass (**A**) and PS (**B**). A magnification of the area in the red box in **B** is shown in **C**. Scale bar in **A** corresponds also to **B** (100 µm) and **C** (306 µm). **A** was modified from Hondrich et al. (2019b).

3.1.1.1 GLYMO and DDA Improve Patterning Quality

To take into account the above-mentioned points, I extended the standard microcontact printing procedure by an additional chemical uncoupling step of the glass substrate and the µCP coating. To implement this uncoupling step, I modified and extended the application

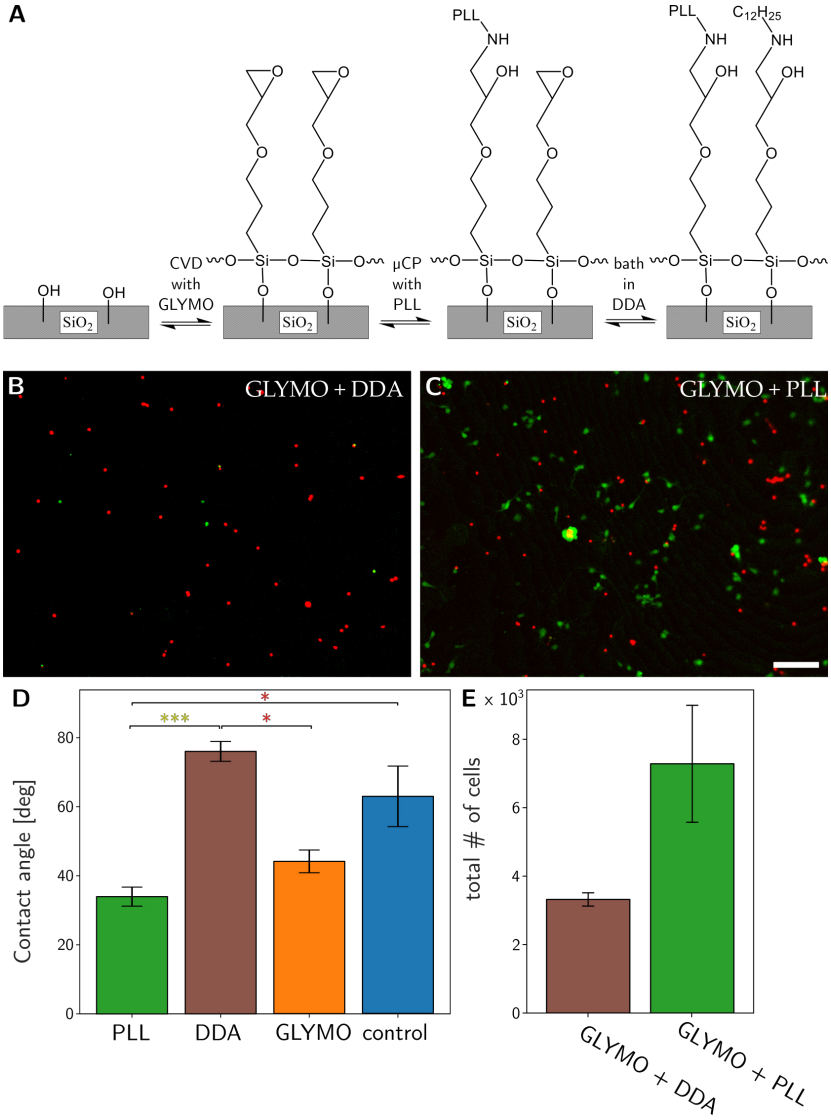
A
PLL
NH
OH
$C_{12}H_{25}$
CVD with GLYMO
μCP with PLL
bath in DDA
OH
OH
SiO_2
B
GLYMO + DDA
C
GLYMO + PLL
D
Contact angle [deg]
0
20
40
60
80
***
*
*
PLL
DDA
GLYMO
control
E
x 10^3
total # of cells
0
2
4
6
8
GLYMO + DDA
GLYMO + PLL

← **Figure 3.3 – Mechanisms and properties of glymo-silanized substrates. (A)** The proposed reactions during GLYMO-based modifications of μCP on idealized glass. Compare with the steps in Figure 2.1. **(B-C)** Live/dead staining via cal-AM (green, alive) and EtHD (red, dead) of neurons growing on glass coated with GLYMO and bathed in DDA (**B**) and coated with GLYMO and bathed in PLL (**C**). Scale bar: 100 μm. **(D)** Comparison of contact angles θ between glass treated homogeneously with GLYMO and PLL, DDA, or EtOH, and untreated glass (control) (n = 6). The color code of the bars corresponds to Figure 2.1. Dunn's multiple comparison test with Bonferroni correction yielded $p_{PLL/DDA} = 9.05 \times 10^{-5}$; $p_{PLL/EtOH} = 0.9183$; $p_{PLL/control} = 0.0225$; $p_{DDA/EtOH} = 0.0225$; $p_{DDA/control} = 0.9183$; $p_{EtOH/control} = 0.8499$. **(E)** Total number of living and dead cells (n = 3 cell cultures per condition). The complete figure was modified from Hondrich et al. (2019b).

of GLYMO (see section 2.1.2) (Hondrich et al., 2019b), which was first published by Nam et al. (2006) and Hofmann (2009). During reproduction, modification, and first tests, I was supported by practical student Oliver Deußen (Deußen, 2019), and during investigation of cell patterning with this technique, I was supported by the Master's student Caroline Grannemann (Grannemann, 2019).

Methodically, GLYMO was applied to an oxygen plasma-activated glass substrate using chemical vapor deposition. During this, a condensation reaction should lead to a bonding between the silane backbone of GLYMO and the hydroxyl groups of the activated glass (Branch et al., 1998). Simultaneously, the silane backbone additionally interconnects, forming a monolayer of GLYMO (Markov et al., 2017) (Figure 3.3 A). During transfer of PLL onto GLYMO via a POP stamp (see section 2.1.3), the amino group of PLL binds to GLYMO's epoxy ring (Nam et al., 2006). As a last step, the samples were washed in hydrophobic dodecylamine (DDA) and EtOH or only EtOH. Washing with DDA should lead to a condensation reaction of DDA with GLYMO's epoxy ring and a protection from hydrolysis in water or EtOH during storage, alongside an even further reduced cell growth outside of patterns. Washing with EtOH should have no effect on the epoxy ring.

Four different types of substrates are in contact with cells after patterning in differently treated samples (untreated glass/control, GLYMO+PLL, GLYMO+DDA, GLYMO+EtOH). Therefore, the contact angle θ (see section 1.4) was measured by photographing a drop of water on top of these substrates in profile. Hydrophobicity of the substrate types increased in the order PLL < EtOH < control < DDA ($34.0° \pm 2.8° < 44.1° \pm 3.3° < 62.9° \pm 8.8° < 76.0° \pm 2.9°$; Figure 3.3 D). The standard deviation of θ on the control substrate is twice as large (8.8°) as on other substrates, which is in accordance with the highly vari-

able cell growth on glass substrates shown in Figure 3.1. Although θ on the control and θ on GLYMO+DDA or GLYMO+EtOH are not significantly different, the variability is reduced by the chemical uncoupling. As expected, PLL strongly decreases hydrophobicity, resulting in a cell-attractive coating. Most importantly, the strongest difference of θ is exhibited between GLYMO+PLL and GLYMO+DDA, but not between GLYMO+PLL and GLYMO+EtOH. This suggests that the separation between background and foreground of the pattern should be most pronounced on DDA-treated glass substrates.

To test whether the modifications have an effect on cell growth in general, I conducted a live/dead staining using calcein-acetoxymethylester (cal-AM, green, alive) and ethidium

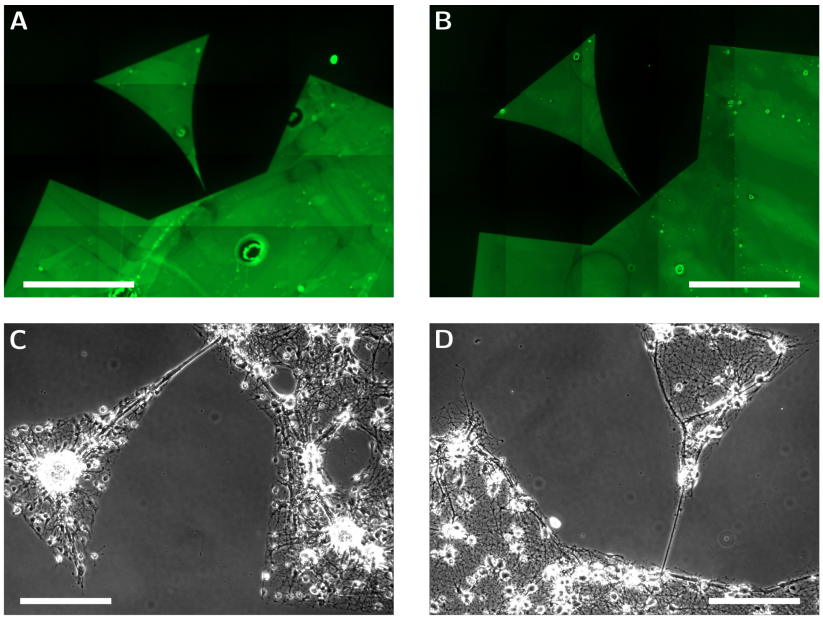

Figure 3.4 – Microcontact printing on different GLYMO-silanized substrates. (A-B) Exemplary fluorescence micrographs of the fComInput pattern (see Chapter 5) printed with PLL-FITC (green) on GLYMO with subsequent DDA application (**A**) or on GLYMO subsequently washed with EtOH (**B**). Scale bars: 500 µm. **(C-D)** Phase contrast micrographs of neurons on the glass treated as in **A** (C; DIV14) or as in **B** (D; DIV14). Scale bars: 100 µm. Figure modified from Hondrich et al. (2019b).

homodimer (EtHD, red, dead) of primary cortical neurons (see section 2.2.2) on GLYMO+DDA (Figure 3.3 B) and GLYMO + PLL (Figure 3.3 C). Both the live/dead ratio and the total

number of cells was higher on PLL-coated substrates (ratio: 28.93% ± 10.08%; total number: 7259 ± 1703) than on DDA-coated ones (ratio: 14.32% ± 7.83%; total number: 3308 ± 194; Figure 3.3 E).

Next, µCP was conducted and primary cortical neurons were seeded onto substrates treated with GLYMO and washed with EtOH or bathed in DDA. The printing procedure lead to a clearly defined PLL pattern on both substrate types (Figure 3.4 A, B). Moreover, neurons were growing in equally well-defined patterns on both substrates (Figure 3.4 C, D).

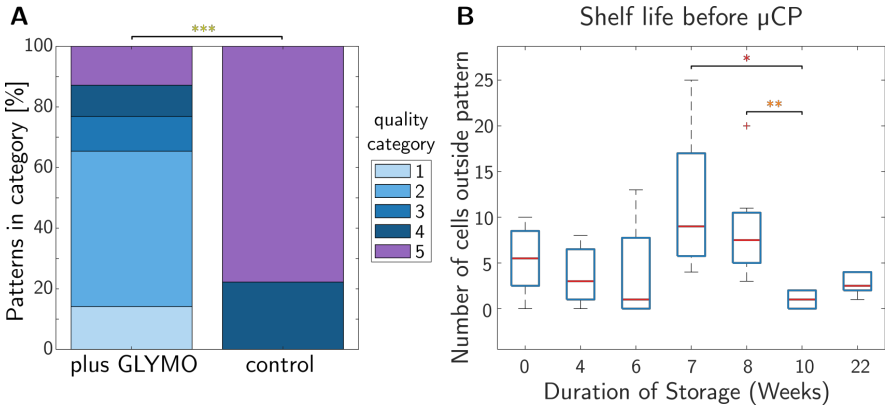

Figure 3.5 – The quality and shelf-life of neuronal patterns on GLYMO-treated substrates. (A) Fraction of patterns in each quality category at DIV5 (see Figure A.2) on GLYMO-treated substrates subsequently bathed in DDA (plus GLYMO; n = 78) compared to untreated glass (control; n = 9). Mann-Whitney-U test yielded $p = 9.6 \times 10^{-6}$. **(B)** Long term shelf life of GLYMO-silanized glass before µCP treatment and DDA wash, measured by the same quality categories as in **A**. Dunn's multiple comparison test with Bonferroni correction yielded (only p values < 0.05) $p_{week7/week10} = 0.0044$; $p_{week8/week10} = 0.0237$. Figure modified from Hondrich et al. (2019b).

However, due to the results from the contact angle measurements, I decided to continue with DDA-treated substrates in future experiments since these should restrict outside-growing cells even more. For quantification of the neuronal patterns on DDA-treated GLYMO-silanized glass, Grannemann (2019) defined the quality categories 1 to 5, from 1 (only dead cells outside of the pattern) as the best defined patterns to 5 (no pattern visible, cells grow homogeneously or are dead) as the least well defined ones (for example images, see Figure A.2). This analysis showed that neurons on substrates with GLYMO+DDA

were growing significantly more in higher categories (median: category 2) than neurons grown on patterned, but otherwise untreated coverslips (median: category 5; Figure 3.5 A), which is in accordance with the qualitative analysis in Nam et al. (2006) and Figure 3.4. Finally, the shelf life of GLYMO-silanized substrates was quantified by applying the same quality categories to patterns that were printed after up to 22 weeks of storage. The quality of patterns was stable throughout the whole time with only non-significant variations (Figure 3.5 B). Thus, GLYMO-silanization before and a DDA bath after μCP on glass coverslips, reliably and stably improves the quality of neuronal patterns.

3.1.2 Population Patterns Are Difficult to Record via MEAs

Neuronal cell cultures are often recorded via MEAs (see section 1.2.2). To compare optical recordings via optogenetic tools with electrophysiological ones, I aimed to transfer the μCP technique to MEAs. This has been done before with single cell patterns (Chang et al., 2001; James et al., 2004; Nam et al., 2006) but has not been attempted with μCP of population patterns. An optimal pattern quality is the prime objective on substrates used in recordings with optical methods. However, in MEA recordings the first goal is to establish reliable recordings from many electrodes so that a network investigation is possible at all. Therefore, I did not quantify the patterning quality, although patterning itself seemed to be reliable in many cases (for examples, see Figure 3.6 A-B). On homogeneous coatings, such MEA recordings are a very well-established technique (Gritsun et al., 2010; Lonardoni et al., 2017; Sardi et al., 2017; Stett et al., 2003; Wagenaar et al., 2006a,b). Although I varied multiple patterning and recording conditions, I was able to only record APs in roughly 0.1% of all electrodes on 4 out of 102 MEAs (3.9%) that I used for patterning (for an example of these recordings, see Figure 3.6 C-E). The varied conditions included the type of coating, the type of MEA passivation (see section 2.3.2), the cell density, the stamp material and other conditions. The different tested conditions are listed in Table 3.1. The latter of these conditions include ONONO as a passivation material because it has a weaker autofluorescence than the polyimide HD-8820 (see Figure A.4). On these substrates, PDMS stamps had to be used to avoid rupturing the passivation layer. With these PDMS stamps, patterning was then comparable to patterns achieved

with POP stamps on HD-8820. As only neurons in fComInput patterns (see section 5.1) were successfully recorded (but not neurons in neuroCapTiH patterns, see section 4.1), the pattern itself seemed to have the biggest influence on neuronal recordings. Indeed, the population part of the fComInput pattern resembles a part of a homogeneous neuronal culture which might explain its higher recording probability. On homogeneous coatings, the coating itself is thicker as it is usually applied in a bathing approach.

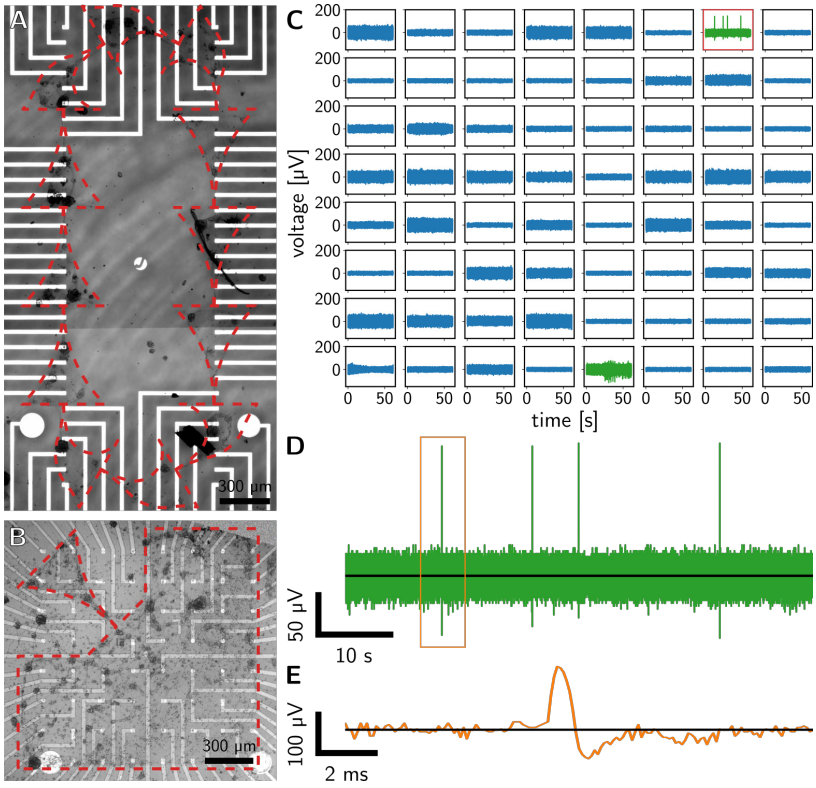

Figure 3.6 – Neuronal patterning and recordings on MEAs. (A-B) Phase contrast micrograms of neurons growing in a neuroCapTiH pattern on line MEAs (**A**) and in a fComInput pattern on standard MEAs (**B**). **(C-E)** Examples of MEA recordings in different scales. **(C)** All channels of a MEA recording from a fComInput pattern. **(D)** Magnification of the channel in **C** in a red box. **(E)** Magnification of the first AP (orange box) in **D**.

Additionally, neurons are often seeded with a higher density which, on a patterned substrate, can easily lead to the formation of cell clusters that detach from the substrate.

Thirdly, cells growing in a dense network benefit from cofactors and extracellular molecules that increases network maturation and health. However, this does not explain the reduced recording efficiency as compared to single cell patterns. A possible explanation for this low efficiency of recordings from population patterns is their larger scale. As opposed to a single cell pattern that restricts growth to an area immediately surrounding the electrode opening of a MEA, population patterns allow for a random distribution of the cells within the boundaries of the pattern. For example, the area of 12 µm-diameter electrode openings covers ~86.3% of the area of simple grid patterns used by Hofmann (2009); Nam et al. (2006). On the contrary, electrode openings only cover ~0.3% of the area of the neuroCapTiH pattern and ~1.8% of the area of the fComInput pattern. Therefore, the chance of a cell growing exactly on top of an electrode is lower. In combination with a low cell density to avoid clusters (in which individual cells cannot be recognized) and a less continuous coating (as compared to homogeneous bath coatings), the probability of a successful recording will be dramatically reduced.

Pattern	Number of MEAs	Number of Electrodes	Number of Active Electrodes	Coating	Cell Count	Stamp Material	Passivation
neuroCapTiH	7	434	0	laminin	100k	POP	HD8820
neuroCapTiH	10	620	0	ECM	100k	POP	HD8820
neuroCapTiH	6	372	0	ECM	25k	POP	HD8820
neuroCapTiH	6	372	0	ECM	50k	POP	HD8820
neuroCapTiH	12	744	0	gelatine ECM	25k	POP	HD8820
neuroCapTiH	3	186	0	ECM plasma	25k	POP	HD8820
neuroCapTiH	3	186	0	ECM	25k	POP	HD8820
neuroCapTiH	3	186	0	ECM plasma	50k	POP	HD882
neuroCapTiH	3	186	0	ECM	50k	POP	HD8820
fComInput	3	186	0	ECM plasma	50k	POP	HD8820
fComInput	3	186	1	ECM	50k	POP	HD8820
fComInput	7	434	0	GLYMO	80k/120k	POP	HD8820
fComInput	5	310	0	GLYMO	100k/150k	POP	HD8820
fComInput	5	310	0	GLYMO	100k	POP	ONONO
fComInput	5	310	0	GLYMO	150k	POP	ONONO
fComInput	2	124	0	GLYMO	150k	POP	ONONO
fComInput	2	124	0	plasma PLL	150k	POP	ONONO
fComInput	3	186	0	GLYMO	100k	PDMS	ONONO (possibly faulty)
fComInput	3	186	0	GLYMO	125k	PDMS	ONONO (possibly faulty)
fComInput	3	186	0	GLYMO	100k	PDMS	ONONO (possibly faulty)
fComInput	4	248	2	GLYMO no DDA	100k	PDMS	ONONO
fComInput	4	248	3	plasma PLL	100k	PDMS	ONONO

Table 3.1 – Various experimental conditions for testing MEA recordings of patterned neuronal cultures. PLL - poly-L-lysine, GLYMO - (3-glycidyloxypropyl)trimethoxysilane (see previous section and section 2.1); ECM - ECM Gel from Engelbreth-Holm-Swarm murine sarcoma (E1270, Sigma Aldrich, Germany); POP - polyolefine plastomer, PDMS - polydimethoxysilane (see section 2.1.1); HD8820 - a polyimide, ONONO - layers of SiO_2 (O) and Si_3N_4 (N; see both in section 2.3.2).

3.2 Thiols on Gold Electrodes

Thiols have previously been applied to gold substrates to improve cellular growth on this material (Chang et al., 2001; Mrksich et al., 1997). In theory, applying thiols to electrodes of MEAs using gold as a conducting layer could improve the adhesion of a cell to the electrode when using μCP on these MEAs (see previous section). As μCP stamps usually have a flat printing area, the coating substance will most likely only be printed on the passivation around the actual electrode. This will lead to cells avoiding the electrode, having a detrimental effect on the sealing and R_{seal}, and thus signal-to-noise ratio (see section 1.2.2).

3.2.1 Thiols Improve Adhesion to Large Gold Surfaces

Previous studies suggested that a mixture of polar (e.g. aminothiols) and unpolar (e.g. alkanethiols) thiols could be used to achieve cell-attractive coatings on a gold surface (Gilles et al., 2012; Mrksich et al., 1997). In an attempt to combine these suggestions, I rather arbitrarily chose to test a mixture of the unpolar alkanethiol HS-$(CH_2)_9CH_3$ and the slightly longer polar aminothiol HS-$(CH_2)_{11}$-NH_2.

I mixed the aminothiols with the alkanethiols in molar ratios of 0%:100%, 2.5%:97.5%, 25%:75%, 50%:50%, 75%:25%, and 100%:0% with 2 mM as 100%, and applied these mixtures to large gold substrates fabricated on quartz wafers (section 2.3.1). After this, neurons were seeded onto these substrates, and stained with cal-AM and EtHD to determine the live/dead ratio and amount of adhering cells at the different ratios of thiols. The total amount of cells and the live/dead ratio increased with growing fractions of aminothiols in the mixture (Figure 3.7 A), which is in accordance with previously published results (Chang et al., 2001). At 50% to 100%, the number of cells is clearly above the bare gold. However, these results have a sample size of 1 and therefore have to be regarded with caution. For example, PLL was intended as a positive control but exhibits as few live cells as bare gold, which may be due to an anomalous substrate rather than a failure of the technique itself. Nevertheless, for the following experiments on MEAs, the 75% aminothiol fraction was chosen as the mean of the range with most cell growth.

3.2.2 Thiols do not Clearly Improve Recording Quality

The 75%:25% molar ratio of aminothiols:alkanethiols was applied to nanocavity MEAs with gold electrodes under HD-8820 passivation in combination with μCP of a flat, homogeneous layer of PLL (without pattern). PLL was applied in this way to avoid coating the electrode area with the usual bath application, thereby negating any thiol-based effect on cell adhesion. In total, four different conditions were chosen: a) printed PLL on MEAs with thiols (ThPrint); b) homogeneous PLL applied in a bath as a control (noThHomPLL); c) printed PLL with no thiols (noThPrint); d) only thiols (onlyThiols). After live/dead staining, the number of cells growing on the large reference electrodes of the MEAs (see Figure 1.8 or Figure 2.2) was used as a way to quantify cell adhesion on the gold surfaces of the MEA (Figure 3.7 B). Surprisingly, the numbers of cells were highly comparable on the electrodes. Moreover, cells were also growing on the passivation of all samples, including onlyThiols, meaning that the plasma activation of the MEAs must have enabled the HD-8820 passivation to bind thiols. Similarly, the number of active channels (Figure 3.7 C) and the signal-to-noise ratio (not shown) was comparable when recording neuronal activity with the MEAs. To ascertain if thiol application could be prevented on passivation, I repeated the experiment (this time, on HD-8820 and ONONO passivation, see section 2.3.2) without plasma activating the surface before thiol/control EtOH application. On reference electrodes, the cell numbers do not differ significantly in the different conditions although on homogeneous PLL most cells seem to grow on ONONO-passivated MEAs (Figure 3.7 D). Although the same seeding density was used, cell density was much higher on plasma-treated samples (Figure 3.7 B) than on samples without plasma treatment (Figure 3.7 D). The cell density on ONONO-passivated MEAs is also higher on the passivation in the electrode array area of the MEAs (Figure 3.7 E). This seems to indicate that the ONONO passivation is inherently more favorable for neuronal growth than HD-8820 passivation when combined with a PLL coating. On the other hand, few cells were growing on MEAs (both passivation and reference electrodes) treated with thiols or EtOH as a control on both passivations. This proves that thiol application on the passivation material can be prevented by excluding prior plasma treatment. A beneficial effect of thiols on the growth of electrodes cannot be seen directly. Probably,

the lack of a neuronal population surrounding the electrodes perturbs healthy neuronal growth of individual cells (as opposed to PLL-treated substrates where more neurons are growing in general).

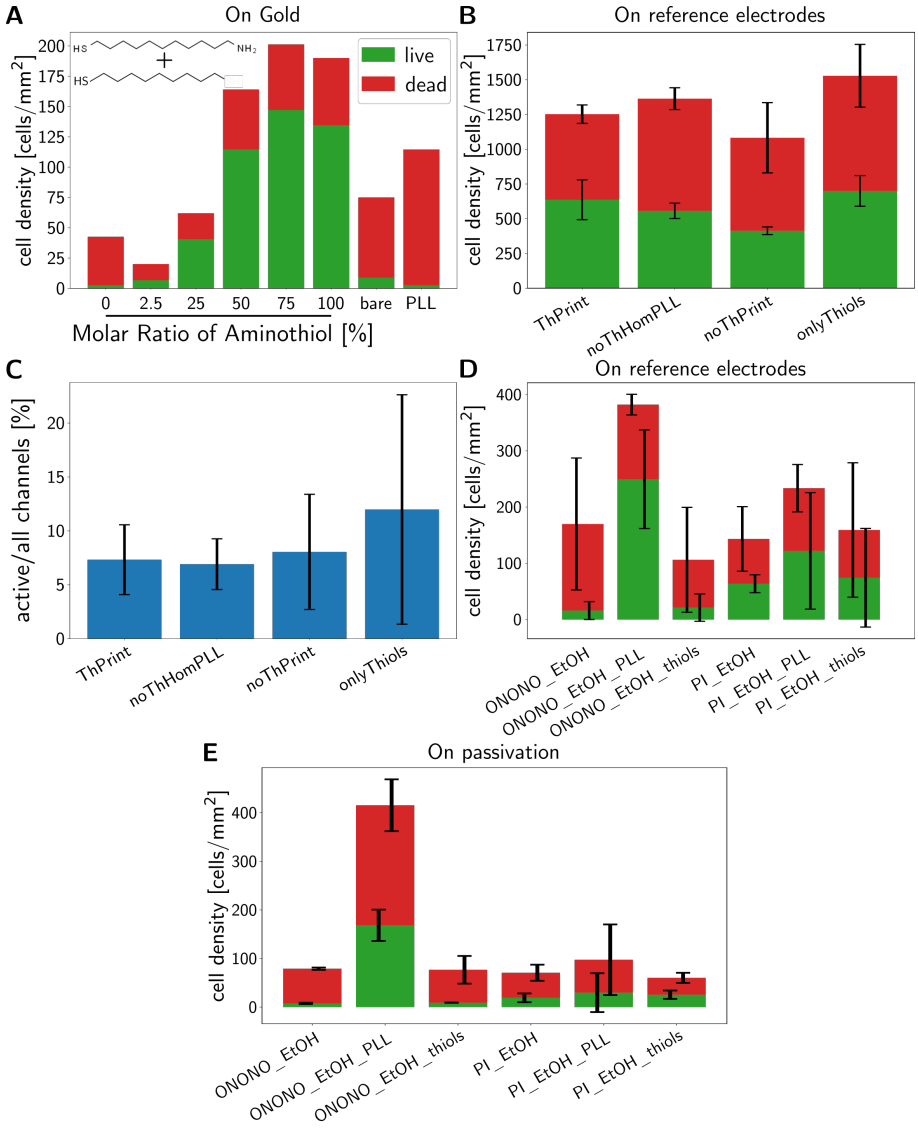

← **Figure 3.7 – Thiols on gold electrodes. (A)** Comparison of the cell number on large gold surfaces at different molar ratios of the aminothiol HS-$(CH_2)_{11}$-NH_2 (top left corner, top molecule) and the alkanethiol HS-$(CH_2)_9CH_3$ (top left corner, bottom molecule) acquired by live/dead staining (n=1 per condition). **(B-C)** Comparison of the cell numbers on the large reference electrodes (**B**) and the number of channels showing neuronal activity (**C**) at different combinations of thiols and PLL on MEAs with gold electrodes (described in section 3.2.2). **(D-E)** Comparison of the cell numbers on the reference electrode (**D** or cell densities on the complete imaged passivation (**E**) of MEAs without oxygen plasma treatment.

Taken together, these results indicate strongly that thiols do not have a strong enough effect *on their own* on the sealing resistance and the cell-electrode interface to influence MEA recordings. However, the effect seen on large gold surfaces (Figure 3.7 A) (Chang et al., 2001) suggests that thiols might have a cumulative positive effect on recording quality together with other techniques. A potential drawback in the combination with other techniques (such as GLYMO application to the surface, see section 3.1.1.1) is the requirement of excluding plasma treatment to prevent thiols from binding to the passivation. However, by applying agents (such as GLYMO) first the effect of oxygen plasma on the passivation could be shielded for subsequent thiol application. As an additional outcome, I could add further evidence to the beneficial influence of an oxygen plasma treatment on cell adhesion (Ohsugi et al., 2005). Interestingly, at least without this plasma treatment, ONONO passivation seems to have a more positive effect on cell adhesion and survival when coated with PLL. Cell adhesion on ONONO as compared to HD-8820 is not increased without PLL. Possibly, the amino end group of PLL could interact with oxygen or hydroxyl groups on the ONONO surface (compare also silicon-based glass surface in Figure 3.3 A) as opposed to the undefined and variable surface of HD-8820. Thus, ONONO seems to be better suited to study neuronal cell cultures in the future. Thiols may add a mild positive effect on recording quality but may be difficult to combine with other methods depending on plasma treatment of the substrate.

3.3 Transparent, Holey MEAs for Electrophysiology

Coupling optical techniques such as neuronal stimulation via optogenetic tools, calcium imaging, or simple phase contrast or fluorescence microscopy for the exact localization and control of cells with electrophysiological devices becomes more and more important *in vivo* (Park et al., 2019; Thunemann et al., 2018) and *in vitro* (Chen et al., 2017; Kim et al., 2017; Thompson et al., 2014). A standard material like gold (even without its plasmonic properties) offers some advantages over other transparent materials such as indium tin oxide (ITO) or graphene. Gold's impedance is lower, and it is more flexible than ITO (Cao et al., 2014; Gross et al., 1985; Tran et al., 2018). Graphene is harder to handle and less stable than gold (Reina et al., 2017). To circumvent gold's disadvantage - its low transparency - gold nanohole arrays can be used (holey gold). Holey gold was developed as a meta material for surface plasmon polariton (SPP)-based biosensing (Qi et al., 2018; Sharpe et al., 2008) or other nano-optical techniques (Luo et al., 2019). However, such gold was recently introduced as a conductive material for MEA devices with transparent electrodes (Seo et al., 2017). Bohdan Lenyk and Dmitry Kireev then implemented a novel way of fabricating such holey gold substrates (Schöps et al., 2018) into the standard process of MEA fabrication, which is described in detail in Hondrich et al. (2019a), section 2.3.1.1, and section 2.3.2.2. I used the HL-1 cardiomyocyte-like cell line (Claycomb et al., 1998) to test the applicability of these novel MEAs for microscopy and electrophysiology.

3.3.1 Plasmonically-Enhanced Transparency of Holey Gold and MEA Electrodes

As expected, holey gold offers a higher transparency than solid gold of the same thickness (40 nm; Figure 3.8 A). The geometry of the holes alone causes a homogeneous increase in transmission across all measured wavelengths, which can be seen for example as a boost in transmission at ~600 nm (Figure 3.8 A, green asterisks). However, holey gold exhibits SPPs when excited at a certain wavelength range (for details, see Hondrich et al. (2019a)). Therefore, its transmission is further increased non-uniformly by a transmission peak of

~45% at 726 nm (Figure 3.8 A, green arrowhead). This plasmonically induced peak is unique for holey gold and is not detectable in solid gold (Escobedo, 2013; Qi et al., 2018) (compare black and red curves in Figure 3.8 A at the position of the green arrowhead). As position and strength of the SPP transmission peak depends strongly on the refractive index of the materials on top of holey gold, its transparency was further increased in cell culture medium (Figure 3.8 B, solid lines). Finite-difference time domain simulations could reproduce these results very well (Figure 3.8 B, dashed lines). Moreover, by varying (in the simulations) the nanohole diameter, and especially the lattice constant of the nanoholes, transparency could theoretically be increased up to 70% (Hondrich et al., 2019a). This transparency is comparable with, or higher than, many other materials used as electrode materials (Cao et al., 2014).

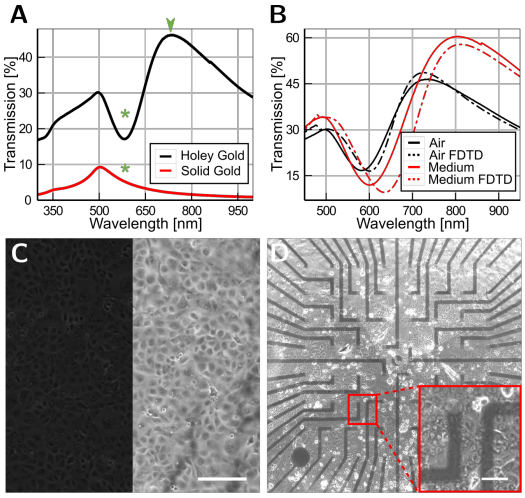

Figure 3.8 – Transparency of holey gold. (A) Transmission spectra of solid gold (red) and holey gold (black) in air. Green asterisks indicate a wavelength at which transmission is linearly increased. The green arrowhead indicates the SPP-induced peak. **(B)** Transmission spectra of holey gold in air (black solid line) and medium (red solid line). Dashed lines represent the respective finite-difference time domain simulations in air and medium. **(C)** Phase contrast micrographs of HL-1 cells imaged through the quartz substrate with 40 nm of solid (left) and holey (right) gold. Scale bar: 200 µm. **(D)** Phase contrast micrograph of HL-1 cells imaged through a holey MEA. The inset shows a magnified region containing one transparent electrode and two transparent feedlines. Transparency is the same as in **C** (right) but image brightness was decreased to see cells on non-metalized areas. Scale bar: 200 µm; inset: 37 µm. Figure modified from Hondrich et al. (2019a).

To demonstrate that holey gold's high transparency could be used for imaging cells directly through the material, I cultured HL-1 cells on top of holey gold. Micrographs obtained with an inverted microscope show that the cells are more clearly visible on holey gold than on solid gold (Figure 3.8 C). To quantify this relation, I defined the relative

transmission as the ratio of the mean intensity of a rectangular window in the image with cells and the mean intensity of such a window at the plastic dish background. The relative transmission of holey gold is 3-fold higher (32%) than that of solid gold (10%). Due to the tunability of holey gold, its transmission can be tuned by varying the lattice constant of the nanoholes to modify the peak transmission wavelength (see figure S5 in Hondrich et al. (2019a)). By this, the material could serve as an optical filter, for example for an improved compatibility with optogenetic techniques.

Finally, HL-1 cells were also cultured on holey MEAs. Cells are visible through all metalized areas such as feedlines and electrode openings (Figure 3.8 D). Thus, correlation of electrophysiological with anatomical data is possible by imaging through transparent holey MEAs. Thereby, special objectives with very high working distances (and suboptimal imaging due to the differences in refractive indices of air and water) or the need for (potentially contaminating) immersion do not have to be used.

3.3.2 Electrophysiological Recordings with Holey MEAs

Before culturing electrogenic cells, the electrochemical impedance of the electrode-electrolyte interface and resistance of the electrodes of holey MEAs were characterized. Due to the nanoholes, the area of holey MEAs is slightly smaller (403.7 vs 452.4 μm^2, respectively, for an electrode of 24 µm diameter). This results in a higher impedance for holey MEAs (2.65 ± 0.67 MΩ at 1 kHz) than for standard MEAs ((1.50 ± 0.64 MΩ at 1 kHz; see figure S4 A in Hondrich et al. (2019a)). The volume of conducting material is reduced even more than its area. Therefore, the resistance between contact pad and electrode opening is higher in holey MEAs (614.7 ± 44.1 Ω) than in standard MEAs (126.4 ± 61.5 Ω; see figure S4 B in Hondrich et al. (2019a)).

To test if holey MEAs could be used for electrophysiological recordings, the HL-1 cell line provides an optimal test system. Within days, these cells form an adhesive confluent (and therefore tightly sealing) layer of cells, which develops rhythmic APs that are easily recognizable as cellular activity (see example recording in Figure 3.9 A). As described in section 1.1.1.2, APs depend on the ionic equilibrium between the extracellular and intracellular space. Increasing the extracellular KCl concentration therefore shifts equilibrium

potential to higher values so that the repolarization of the cells after an AP is blocked. To ensure the cellular origin of the MEA recordings, only voltage traces that could be blocked by application of 400 mM KCl were analyzed (Figure 3.9 B). Recordings of these cells with holey MEAs showed APs with an average spike frequency of 0.42 ± 0.11 Hz. Because this spike frequency is slightly lower than the frequencies reported in previous studies (Kireev et al., 2017b; Lai et al., 2018; Sartiani et al., 2002), cells of the same cell line and passage were measured on one standard MEA with solid gold. The frequency (0.34 ± 0.01 Hz) was comparable to the one on holey MEAs, attributing the lower frequency to a property of the particular lot of cells. For these calculations, individual MEAs were compared because the cells should roughly beat with the same frequency of the population's pacemaker cell(s) (Yang and Murray, 2011).

To compare the shape of individual APs, I calculated the ratio of the APs' full width at half-maximum (FWHM) and amplitude on holey and standard MEAs (Figure 3.9 C). This ratio has a statistically significantly different ($p = 0.039$) distribution in holey (1.4, Q1: 0.8, Q3: 1.8) and standard (1.4, Q1: 1.0, Q3: 2.3) MEAs. However, this difference results from the very high APs measured with one single electrode (Figure 3.9 D, red circle). This electrode is probably sealed very tightly to one or multiple cells by chance, leading to a sharp increase in amplitude and signal-to-noise ratio (see section 1.2.2 and Denyer et al. (1998)). As this behavior is only expressed at this one electrode, it was excluded from the comparison of AP shapes. APs of comparable amplitude (magnified region in black box in Figure 3.9 D) have roughly the same shape in holey (1.4, Q1: 0.8, Q3: 1.8) and standard (1.4, Q1: 1.0, Q3: 2.0) MEAs (p = 0.154, Figure 3.9 E). To conclude, these results demonstrate that transparent, holey MEAs with additional plasmonically tunable properties can be used to record APs, a stepping stone towards the improved combination of electrical and optical recording techniques and simplified cell culture monitoring during electrical measurements.

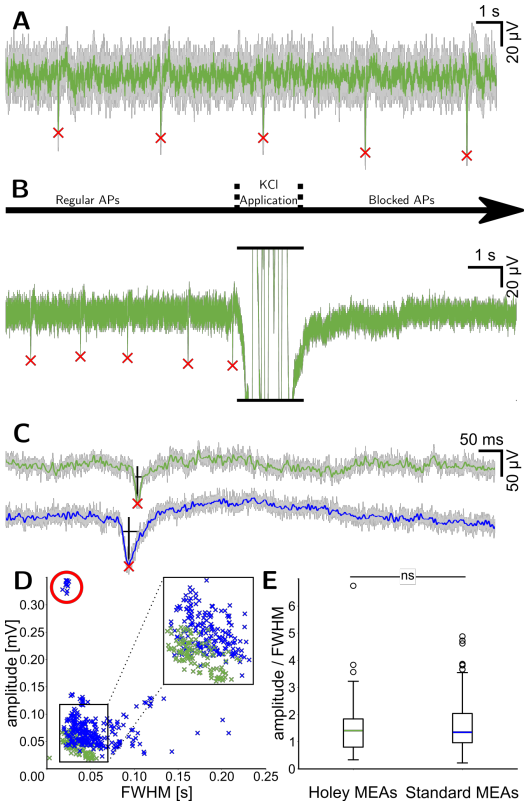

Figure 3.9 – **Cell recordings with holey MEAs. (A)** Exemplary HL-1 potentials recorded with a holey MEA as a raw (gray) or a 100 Hz low-pass filtered (green) trace. **(B)** Example raw trace during AP blockade with KCl as indicated at the arrow. KCl application during recording caused an artifact (clipped at black horizontal lines) due to the introduction of noise by the pipette. **(C)** Magnified APs recorded with holey MEAs (green) or standard MEAs (blue). Full width at half-maximum (FWHM) and amplitude are indicated as black bars. **(D)** Correlation of FWHM and amplitude of APs on holey MEAs (green; n = 193) and standard MEAs (blue; n = 250). A small population of outliers is indicated by a red circle (n = 11). The main population (black box) of APs is not significantly different. In the black box, green dots are brought to the foreground to clarify the similarity of distributions. **(E)** Comparison of the ratio of amplitude and FWHM as a measure for AP shape. Outliers from **D** were removed (standard MEA APs: n = 239). Mann-Whitney-U test was used as a significance test. Figure modified from Hondrich et al. (2019a).

3.4 Conclusions and Outlook

An ideally controllable system for investigation of neuronal networks *in vitro* would be an electrophysiological device with extremely high spatial resolution, and stimulation and recording capabilities, upon which neuronal networks grow in perfectly designed patterns with defined connectivity.

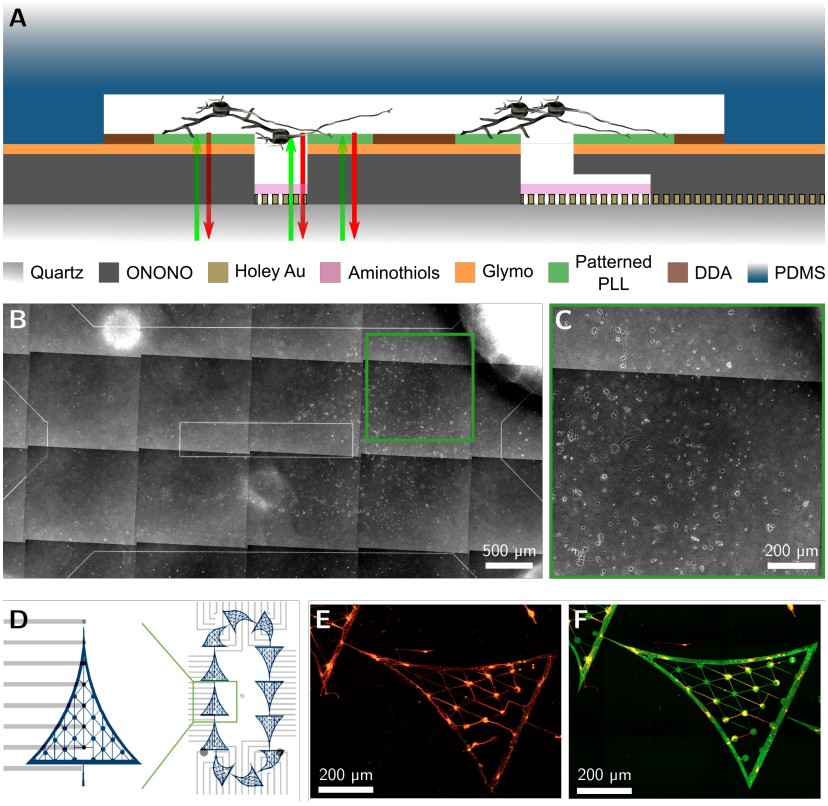

Figure 3.10 – A possible future of fully controllable patterned neuronal networks. **(A)** Theoretical future combination of methods improved, developed and tested in this thesis to achieve highly controllable investigations of neuronal networks. **(B-C)** Exemplary fluorescence micrographs of microchambers containing healthy neurons. The green area in **B** is magnified in **C**. **(D)** Design of a new pattern combining the neuroCapTiH population pattern with single cell patterns for soma positioning. **(E-F)** Fluorescence micrographs of an immunocytochemical staining of neurons growing in the patterns shown in **D** with the neuronal marker MAP2 (red) and the axonal and neuronal marker NFH (orange), excluding (**E**) or including (**F**) the PLL-FITC stained pattern (green). **D-F** were adapted from Grannemann (2019).

Such a system is far beyond our reach although recent breakthroughs with high density MEAs (Bakkum et al., 2013) promise some aspects of this ideal system to be reachable in the future. However, even with low density MEAs and a combination of available technologies, high resolution recordings and stimulations of patterned neuronal networks should be possible (Figure 3.10 A). Holey MEAs (see section 3.3) could serve as a transparent, tunable electrophysiological device to correlate optogenetic recordings and stimulations to electrical AP recordings. Patterning on holey MEAs with transparent and less autofluorescent ONONO passivation (see section 3.1.2) could be achieved with improved μCP using Glymo and DDA (see section 3.1.1.1). To improve MEA recording quality of population patterns, aminothiols (see section 3.2.2 and section 3.2.1) may play a minor role in improving cell adhesion on (holey) gold electrodes. However, microchambers adapted from microfluidic chambers could serve as a means of greatly improving signal-to-noise ratio of MEA recordings (FitzGerald et al., 2008; Forró et al., 2018). First tests of these microchambers (first designed by Grannemann (2019) and modified during this thesis) on glass showed that neurons were indeed growing in an area corresponding to the later positions of MEA electrodes without adverse effects to their health (Figure 3.10 B-C). Additionally, population patterns could be split into "pseudo-population" patterns by combining single cell patterns with population shapes, thereby more effectively positioning neuronal somata exactly on MEA electrodes (Figure 3.10 D; first designs by Grannemann (2019) under close supervision). First immunocytochemical stainings showed neurons growing in these patterns in a well-defined manner (Figure 3.10 E-F). Thus, the techniques developed and improved in this Chapter help to come closer to the ideal system depicted in Figure 3.10 A although further work needs to be invested into this system.

Chapter 4

Small populations: from linear to circular activity

Neuronal cell cultures offer a highly controllable system (see previous Chapter) of greatly reduced complexity to investigate neuronal network function. In this simple system, neuronal cell cultures can be combined with basic concepts from electrical engineering to study the interplay between organic, random neural networks and defined electrical elements such as logic gates, delay lines and oscillators (Feinerman et al., 2008). This interplay can help uncover basic principles of neuronal networks regarding signal integration and propagation within, and communication between these microcircuits. Additionally, such investigations may help to improve novel computational principles like neuromorphic chips and artificial neural networks by combining them with classical engineering approaches. These combined neuronal network architectures not only rely on precisely defined patterns (see Chapter 3) but also on the directionality of AP propagation in what may be called "neuronal diodes". Such diodes were first developed by Feinerman et al. (2008) and later reproduced and improved by Albers and Offenhäusser (2016) with the μCP technique.

4.1 Pattern Designs

After experimenting with different diode designs (Albers and Offenhäusser, 2016; Albers et al., 2015), Albers (2016) determined that a curved triangular design (CT1; Figure 4.1 A) led to increased axonal growth towards the tip of the triangle. Moreover, signal propagation was directed towards the next triangle in a daisy chain of these structures. To investigate the effect of network size on spontaneous network activity and directionality, the CT1 pattern was downscaled by Irina Tihaa during her PhD thesis (dsCT; unpublished work). This scaling ranged from 100% (CT1) over 75% (also called CT2 by Albers et al. (2015)), 60%, 50%, 40%, 30%, 20%, 10% , 5%, and 2% down to 1%. In the latter three only one neuron can fit per triangle. Thus a range from populations to individual neurons is spanned (Figure 4.1 B). I used these scaled triangles to investigate directionality in different sizes of neuronal populations with the patch clamp technique (see section 1.2.1) and stimulation via optogenetic actuators (see section 1.3.2).

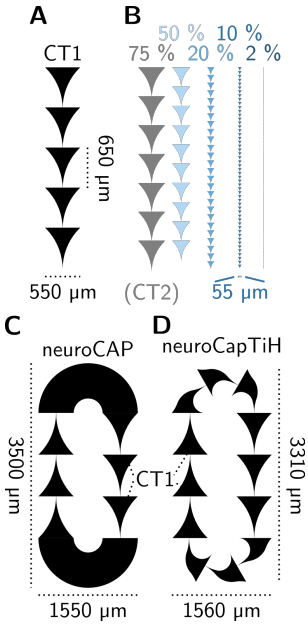

Figure 4.1 – Patterns for directed population growth. **(A)** The original curved triangle (CT1) structure. **(B)** Downscaled CT1 structures. Percentages indicate the percentage of the size of the CT1 structure. The 75% structure is also termed CT2. **(C)** The original neuroCAP design with big arc structures. **(D)** The modified neuroCapTiH design with triangles in the arc.

To create a neuronal oscillation device similar to the one published by Feinerman et al. (2008), and investigate principles of recurrent signaling pathways, Albers (2016) further developed a µCP pattern for potentially circulating APs (neuroCAP). In this design, two daisy chains made of three CT1 structures placed in parallel and pointing in opposite directions are connected by two large semi-circular blocks ending in a triangular structure (arcs; Figure 4.1 C). In these arcs, SNEs are propagated from the preceding triangle to the succeeding one less than 25% of the time as the network size within the arc is probably large enough to generate its own SNEs (Al-

bers, 2016). Therefore, I modified the neuroCAP design by replacing the arc structures with equally bent CT1 structures (Figure 4.1 D). In this new neuroCAP design (neuroCapTiH), the base of a bent triangle is still at a 90° angle to the tip of the preceding triangle to minimize neurites crossing from tip to base outside of the pattern (Albers and Offenhäusser, 2016). I used the calcium indicators GCaMP6f and jRCaMP1b to investigate spontaneous (section 4.3) and evoked (section 4.5) APs and SNEs within complete neuroCapTiH structures (as opposed to parts of the neuroCAP structure conducted by Albers (2016)). Thus, the effect of network size (dsCT) and modularity (neuroCapTiH) on directionality and synchronicity could be investigated.

4.2 Large Triangles Propagate Electrical Activity

Continuing from Irina Tihaa's work, I first investigated whether the directional signal propagation witnessed in CT1 structures (Albers and Offenhäusser, 2016) is preserved in neuronal dsCT patterns (see section 4.1). For this, I recorded the electrophysiological activity from one cell in an arbitrarily chosen triangle within a daisy chain of dsCT structures via current clamp (see section 2.4.4 and section 2.4.1.2). Simultaneously, I optically stimulated neurons growing in the same triangle, and triangles further up- or downstream (Figure 4.2 A). The last stimulus was always presented to the patched cell. In total, nine neurons growing in dsCT pattern with the scalings of 10%, 20%, 30%, 40%, 60%, 75%, and 100% were investigated. Due to the limited field-of-view needed for laser stimulation, 75% and 60% dsCTs could only be stimulated in one upstream triangle and the same triangle as the patched cell. 100% dsCTs could only be stimulated in the same triangle. The resulting voltage traces (Figure 4.2 B) were analyzed for their response to the presented stimuli (section 2.4.4.1). Since my main focus lay on determining directionality of signal propagation PSPs and APs were pooled for further analysis. Specifically, I investigated whether the mean number of response peaks per stimulus (activity ratio), the mean amplitude of the response, and the delay between stimulus onset and response were changed depending

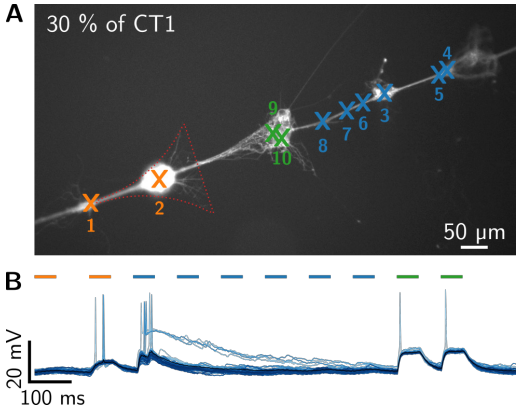

Figure 4.2 – Stimulation and recording of downscaled triangles. (A) Fluorescence micrograph of the ChR2-mKate expression in an exemplary 30% downscaled CT1 neuronal network grown on a glass coverslip without GLYMO application. The red dashed lines highlight that cells are growing in the intended CT1 design. Laser stimulation sites are marked in orange (downstream), blue (upstream), and green (same triangle as patched cell). **(B)** Exemplary voltage traces from the cell at laser stimulation site 10 in **A**. The lightest blue trace was recorded first, and later traces have darker blue tones. Laser stimulation times are marked by horizontal bars in colors corresponding to **A**.

on the stimulus position and the size of the triangles. For this analysis, the dsCT patterns were divided into two categories ($> 50\%$; $\leq 50\%$) to provide a rough overview over the influence of the size. Alternatively, three categories ($> 66.7\%$; $33.3\% <$ dsCTs $\leq 66.7\%$; $\leq 33.3\%$) for a more detailed view into the differences in size were used.

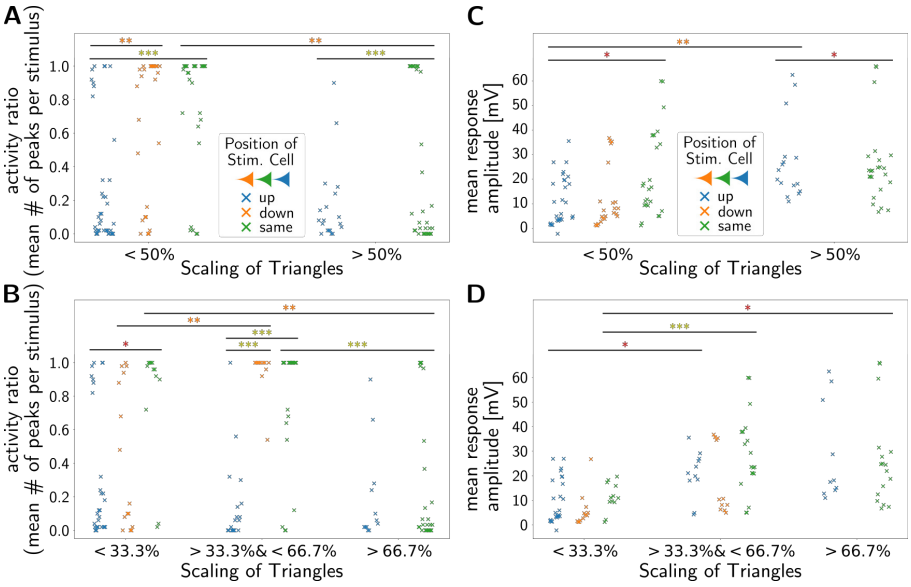

Figure 4.3 – Activity ratio and mean amplitude of the patched neuron in response to stimulation. (A-B) Comparison of the activity ratios defined as the mean number of peaks per stimulus evoked by stimulation of neurons in triangles upstream (blue), downstream (orange), or in the same triangle as the patched cell (green). **(C-D)** Comparison of the amplitudes evoked by stimulation of neurons in triangles as in **A**-**B**. **(A,C)** Comparison of triangles downscaled to below 50% of CT1 and triangles downscaled to above 50% of CT1. **(B,D)** Comparison of triangles downscaled to below 33.3% of CT1, above 33.3% but below 66.7% of CT1, and above 66.7% of CT1. **(A-D)** Stimulation and recording of 60% or larger dsCTs was limited due to the field-of-view (see corresponding section). The bootstrap significance test was used. Asterisks indicate p values as described in section 2.6.

If directionality is preserved in dsCT structures, the activity ratio should be higher when stimulating an upstream triangle than when stimulating a downstream triangle. However, the activity ratio is significantly lower when stimulating an upstream triangle than when stimulating a downstream or the same triangle (Figure 4.3 A). The only exceptions are the very large triangles (Figure 4.3 B, $> 66.7\%$) of 75% and 100% scal-

ing, where the activity ratios due to stimulation of an upstream and the same triangle do not differ significantly. The activity ratios of these large triangles are similar because the activity ratio in response to same triangle stimulation is significantly lower in large triangles than in smaller triangles (compare green data points in Figure 4.3). This is probably due to the fact that more neurons are growing on a larger area in a large triangle. On the one hand, this sparsity reduces network efficiency and efficiency to evoke an AP in the patched neuron. On the other hand, the higher density in smaller triangles increases the chance of stimulating neurites of another cell in the same triangle, including the patched cell, thereby also increasing activity ratio. This is possible even with laser stimulation of somatic resolution (~ 20 µm laser spot diameter) if neurites are growing on top of somata or if cells are growing very densely. Moreover, due to a more linear growth within smaller triangles (and therefore strong axon bundles leading through multiple triangles), the chance for backpropagation of APs to an upstream triangle is higher. Taken together, the activity ratio does not show directionality in dsCT patterns, especially in smaller versions. Comparing the response amplitude shows that stimulating cells in the same triangle as the patched cell generally results in a higher amplitude (green data points in Figure 4.3 C). This is not surprising, as the patched neuron is also contained in this category. Since APs and PSPs are pooled, more APs (which is usually the case in the patched neuron) increase the mean amplitude. However, in small dsCTs this effect is not existent (Figure 4.3 D; $\leq$ 33.3%), hinting that AP generation may be not as effective in small dsCTs. Since in

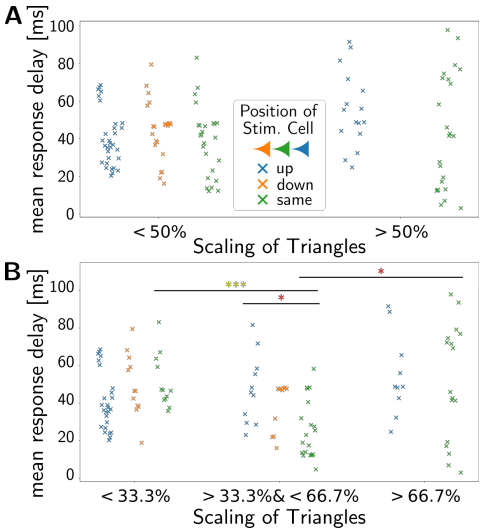

Figure 4.4 – Delay of the response to onset of stimulation. Comparison of the delays between the onset of stimulation and the response of neurons in triangles upstream (blue), downstream (orange), or in the same triangle as the patched cell (green). **(A,B)** See description in Figure 4.3.

small structures the cell networks are smaller, maturation could be slower or the cells could be less healthy. Moreover, the amplitude of the response to upstream stimulation is also increased in larger triangles (blue data points in Figure 4.3 C, and partly as a trend in B). This indicates that large amplitude responses (e.g. APs) are more reliably elicited in large triangles when stimulating an upstream triangle. This is in line with the results from the activity ratio, suggesting that dsCTs are not showing as clear directionality as the original CTs.

Finally, the delay of stimulate onset to the response peak is not different between any of the rough categories (Figure 4.4 A). Interestingly, in the fine categories (Figure 4.4 B) middle-sized triangles seem to have shorter delays when stimulating the same triangle (and as a trend also downstream triangles). However, all in all the delay does neither confirm nor disprove the theory that smaller dsCTs are less well suited for directional signal propagation.

Taken together, stimulating dsCTs of different sizes while patching a neuron indicates the possibility that smaller dsCTs exhibit less directionality than larger triangles. This could be explained by the confined space in small patterns. Here, the neurons have fewer options of growth such that axon bundles form earlier and follow a rather linear path. Firstly, this could lead to backpropagation of APs evoked by stimulating neurites growing very close to laser-targeted somata. Secondly, axons could start growing backwards along those axon bundles, further preventing a directional signal propagation. Although laser stimulation and patching is a valid approach for determining directionality in younger neuronal cultures growing in single cell patterns (Jin, 2016), it might offer insufficient precision for investigation of older cultures with multiple overlapping neurites. Dual patch clamp experiments (Yamamoto et al., 2016; Zhu et al., 2016) of neurons in two triangles could help to further investigate the contribution of each of the two explanations in the future.

4.3 neuroCapTiH - Spontaneous activity dynamics

4.3.1 Establishing Calcium Imaging and Subsequent Analysis

To investigate spontaneously occurring SNEs exhibited by neuronal networks growing in neuroCapTiH patterns (see section 4.1), I used calcium imaging with the genetically encoded calcium indicator (GECI) GCaMP6f (Chen et al., 2013). GCaMP6f is very bright and highly expressed via AAV-mediated transduction (see section 2.2.4). Therefore, it was possible to monitor calcium activity using low magnification within an entire neuroCapTiH pattern (Figure 4.5 A). The AAV titer used for GCaMP6f was determined by Irina Tihaa (unpublished work), and resulted in expression levels suitable for calcium imaging. To be precise, a median of approx. 87% (Q1: 68%, Q3: 90%; not significantly lower than 100%, determined by one sample t-test) of all neurons (determined by a MAP2 immunocytochemical staining) were expressing GCaMP6f.

As calcium imaging is a well-established technique, many methods exist for post-processing calcium imaging data (see section 1.3.1). However, these tools mostly do not offer complete analysis pipelines, or if they do, they apply only for specific data sets (mostly acquired from *in vivo* experiments (Mölter et al., 2018; Stringer and Pachitariu, 2019)). Moreover, some tools offer accurate ROI detection but they lack methods to manually check the results of ROI- and peak detection. Additionally, tools are written in different languages (most often MATLAB® or `Python`, the latter of which is used in this thesis). Tools provided in `Python` may depend on a specific version of `Python` or even its packages, ruling out simple co-implementation with other tools. The scripts used by Albers (2016) were optimized for usage with the fluorescent calcium indicator Fluo-4, and the CT1 and original neuroCAP patterns.

For those reasons, I established my own post-processing pipeline for calcium imaging that combines elements of different published tools and techniques (Burchert and Schneider, 2016; Reichinnek et al., 2012; Rueckl et al., 2017) (compare Figure 2.9, excluding elements of stimulation). The pipeline starts at recording calcium imaging data with a fluorescence microscopy setup extended by a stimulating laser originally intended for fluorescence recovery after photobleaching experiments (section 2.4.1, section 2.4.2).

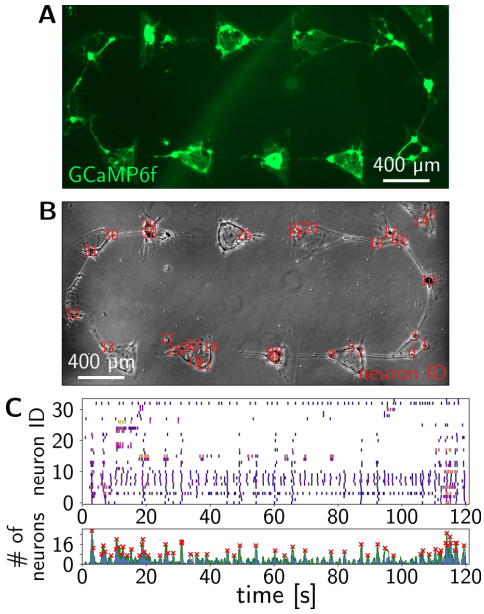

Figure 4.5 – Calcium imaging recordings in neuroCapTiH structures. **(A)** Fluorescence micrograph of the GCaMP6f-expressing neurons grown in a neuroCapTiH pattern on a polystyrene (PS) substrate (see section 2.1.3). GCaMP6f expressing cells were either grown on PS or glass without GLYMO. **(B)** Phase contrast micrograph of the same neurons. Regions of interest (ROIs) are marked with red numbers that correspond to the neuron ID in **C**. **(C)** Top: Raster plot showing the time points of individual calcium events as small vertical bars. The amplitude is color coded from blue (low) over orange to yellow (high). Neuron ID corresponds to the ROIs in **B**. Bottom: Histogram (blue) and combined peak rate of the calcium peak count within 500 ms time windows (see section 2.5.2) . The combined peak rate was used for SNE detection. Detected SNEs indicated by red crosses.

Next, ROIs are detected (Reichinnek et al., 2012) and manually checked in a GUI (Rueckl et al., 2017) (section 2.4.2.1; see Figure 4.5 B for example locations). After this, peaks are detected and also manually confirmed (section 2.5.1; see Figure 4.5 C). After peaks are detected, SNEs are detected and further analysis conducted, depending on the experiment (see section 2.5.2 and and following sections and Chapters).

Figure 4.5 C shows exemplary results of this pipeline. Two different thresholds were chosen to detect SNEs. At a threshold of 20% of recorded neurons, a median of 0.51 SNE/s (Q1: 0.21 SNE/s; Q3: 0.86 SNE/s; see section 2.6) are detected. These SNEs correspond to minor network events from very small microcircuits. At a threshold of 50% of recorded neurons, a median of 0.08 SNE/s (Q1: 0.03 SNE/s; Q3: 0.22 SNE/s) are detected. These SNEs correspond to major, substrate-spanning events. Major events are the most commonly detected events in literature and the detected rates correspond well to previously published results (Wagenaar et al., 2006b).

4.3.2 Spontaneous SNEs are not Trapped in Arcs

The original neuroCAP design (Albers, 2016) featured two large arcs in which such dense neuronal subnetworks formed that in many cases APs did not propagate through the arc to a subsequent triangle or were exclusive to the arc. The main purpose of modifying this design was to remove the arcs at both sides of the daisy-chained CT1 triangles. To check if this modification had the desired effect, I determined the fraction of SNEs that were initiated in the arc or in straight triangles. The fraction of minor SNEs starting in arc triangles (0.43; Q1: 0.37; Q3: 0.55) and starting in straight triangles (0.57; Q1: 0.45; Q3: 0.63) is not significantly different (Figure 4.6 A). The fraction of major events is also not significantly different (arc: 0.50; Q1: 0.40; Q3: 0.70; straight: 0.50; Q1: 0.30; Q3: 0.60). The fraction of minor and major SNEs ending in arc triangles (minor: 0.50; Q1: 0.40; Q3: 0.60; major: 0.50; Q1: 0.39; Q3: 0.67) and in straight triangles (minor: 0.50; Q1: 0.40; Q3: 0.60; major: 0.50; Q1: 0.33; Q3: 0.61) are equally similar. Additionally, all ratios lie approximately at 0.5, which is the expected value for an equal distribution as the number of straight triangles is equal to the number of arc triangles (both 6). Moreover, the fraction of arc triangles (minor: 0.99; Q1: 0.90; Q3: 1.00; major: 1.00; Q1: 1.00; Q3: 1.00) and straight triangles (minor: 1.00; Q1: 0.93; Q3: 1.00; major: 1.00; Q1: 1.00; Q3: 1.00) participating in a SNE is not significantly different (Figure 4.6). It is close to or at 1.00 for all conditions, meaning that an arc triangle and a straight triangle participate in almost every SNE. Thus, the modified version neuroCapTiH did remove the trap for APs in the curves/arcs of the neuroCAP pattern.

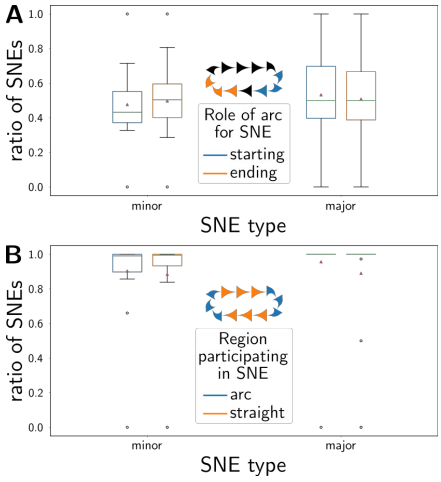

Figure 4.6 – Arc contribution to SNEs. Arc and straight triangles are equally participating in SNEs. **(A)** Comparison of the fraction or ratio of minor and major SNEs starting (blue) or ending (orange) in arc triangles. **(B)** Comparison of the fraction or ratio of SNEs in which at least one arc triangle (blue) or straight triangle (orange) participated. Box plots are explained in section 2.6.

4.3.3 APs Propagate Mostly Forward for up to 11 Triangles

In a first investigation of neuroCAP activity, Albers (2016) was restricted to parts of the whole pattern due to the neurotoxicity and low intensity of the calcium indicator Fluo-4. However, using GCaMP6f I could monitor the whole neuroCapTiH pattern as opposed to focusing on the AP propagation at the tip of a CT1 pattern (Albers and Offenhäusser, 2016). I started by examining the propagation direction and distance of SNEs in a neuroCapTiH neuronal network.

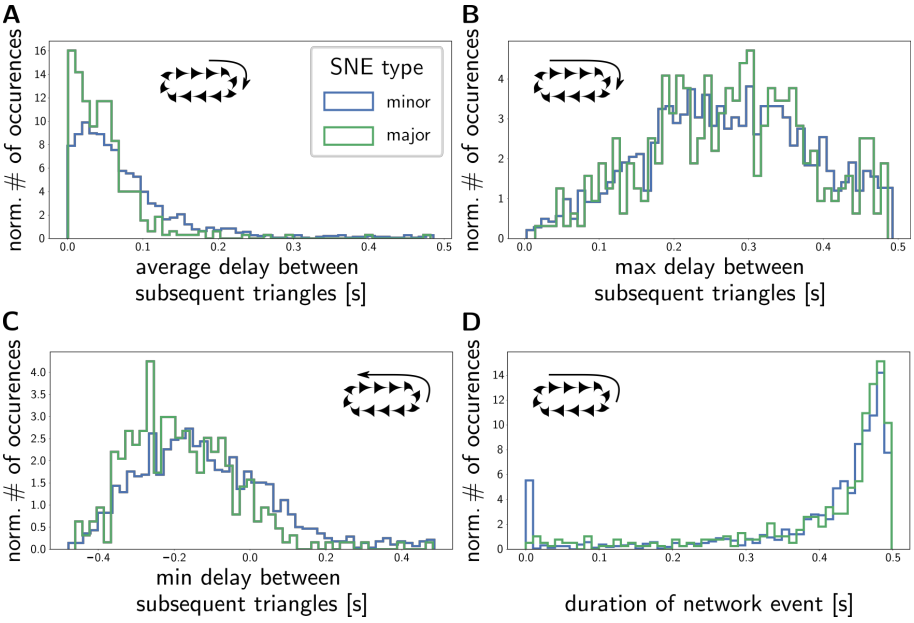

Figure 4.7 – Delay between triangles as a measure for the direction of network events. **(A-C)** Histograms of the average (**A**), maximum (**B**), and minimum (**C**) delays between the individual triangles in each minor (blue) or major (green) SNE. The average delay can serve as a measure for the overall direction of the SNEs in the neuroCapTiH pattern. Maximum and minimum delays indicate the strongest forward and backward step in each SNE. **(D)** Histogram of the duration of an SNE defined as the time difference between the first and the last calcium peak in the event. The duration can serve as an indicator for the effectiveness of SNE generation.

The prevailing propagation direction in a neuroCapTiH pattern was measured by the time delay between triangles within a SNE. For each triangle, the median time point of

all calcium events in this triangle was determined relative to the onset of a SNE. Starting from the first triangle in the SNE (with the lowest median time point), the difference in median time points between two subsequent triangles participating in the SNE was calculated. The average, minimum and maximum time delays within each SNE could then be derived from the differences or delays between the individual triangles (Figure 4.7 A-C). The average time delays are always positive (Figure 4.7 A) although in the majority of SNEs, at least one delay is negative (Figure 4.7 C). The delays range around a minimum of -0.201 s (major SNEs, Q1: -0.283 s, Q3: -0.091 s; minor: -0.142 s, Q1: -0.248 s, Q3: -0.012 s) to a maximum of 0.277 s (major SNEs, Q1: 0.199 s, Q3: 0.350 s; minor: 0.273 s, Q1: 0.193 s, Q3: 0.353 s; Figure 4.7 B). The delays last for an average of 0.040 s (major SNEs, Q1: 0.016 s, Q3: 0.061 s; minor: 0.057 s, Q1: 0.028 s, Q3: 0.098 s). The mean of the average delays is close to 0. This indicates that in the large majority of SNEs, the direction of the SNE cannot be determined clearly as APs propagate between triangles in both directions. Alternatively, it suggests that SNEs combine many fast and some slow inter-triangular AP propagations into the direction of the triangle tips. In any case, the overall positive nature of the average delays means that the preferred AP propagation direction towards the tip of a CT1 pattern is preserved even on a large scale.

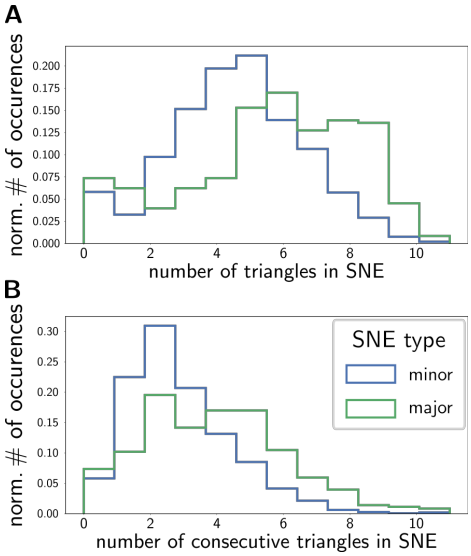

Figure 4.8 – Number of triangles participating in SNEs. (A-B) Histograms of the number of triangles (**A**) and the number of consecutive triangles (**B**) participating in minor (blue) or major (green) SNEs.

The duration of SNEs in neuroCapTiH structures shows a distribution that is almost the reverse of the average time delays (Figure 4.7 D). Its median is at 0.45 s (Q1: 0.38 s, Q3: 0.48 s) for both minor and major SNEs. As the maximum duration of a SNE is limited to 0.5 s due to the detection

method using a window of this size, the majority of SNEs are almost as long as this maximum duration. Interestingly, the duration of minor SNEs is similarly distributed as that of major SNEs, indicating larger delays between the (fewer) individual neurons participating in such SNEs. This is only slightly represented by a small shift in the average and minimum delays distribution (compare blue and green lines in Figure 4.7 A,C). In conclusion, neurons in neuroCapTiH structures exhibit mostly forward propagating SNEs that move slower when containing fewer neurons.

How far do these SNEs move through the whole neuroCapTiH pattern? Minor SNEs span in total a median of 5 triangles (Q1: 3, Q3: 6; Figure 4.8 A) while major SNEs span a median of 6 triangles (Q1: 4, Q3: 8) and up to 11 triangles. The number of consecutive triangles is lower (minor: 2, Q1: 1, Q3: 4; major: 4, Q1: 2, Q3: 5, also up to 11; Figure 4.8 B) than the total number. A reason for this could be that not 100% of cells express GCaMP6f, therefore providing the basis for some hidden activity. Alternatively, some axons might span multiple triangles, or some random calcium events in an uncorrelated triangle could be occurring simultaneously with the SNE. The number of active triangles seems to be correlated to the number of cells growing on the substrate. Significantly more cells grow on substrates that exhibit activity of more than 6 triangles (73.0, Q1: 69.0, Q3: 83.5; Figure 4.9 A) than on substrates with 6 or less triangles (54.0, Q1: 37.0, Q3: 65.0). However, when excluding neuroCapTiH patterns with less than 10 cells growing outside of the pattern, the number of cells leading to more active triangles is not significantly higher anymore ($>$ 6: 63.5, Q1: 58.0, Q3: 88.5; $\leq$ 6: 54.0, Q1: 37.0, Q3: 60.0). This shows that neurons growing in the defined triangular modules within a neuroCapTiH pattern generate SNEs of different sizes depending on the intrinsic connectivity of the network. This intrinsic connectivity can be governed by the connections between the triangular modules (Okujeni and Egert, 2019) or the presence of certain neuron types such as hub cells (Cossart, 2014). On the contrary, the size of SNEs in networks that grow in a less modular fashion depends more on the size and/or density of the network than on other connectivity properties (Biffi et al., 2013).

To sum up, neurons grown in neuroCapTiH patterns do not exhibit full circulating APs as claimed for example by Feinerman et al. (2008). However, the modular structure

and ability to track individual neurons to specific triangles provides a good system for investigating SNE initiation and propagation through multiple microcircuits. Therefore, I next investigated this pattern using an all optical system for stimulation and recording.

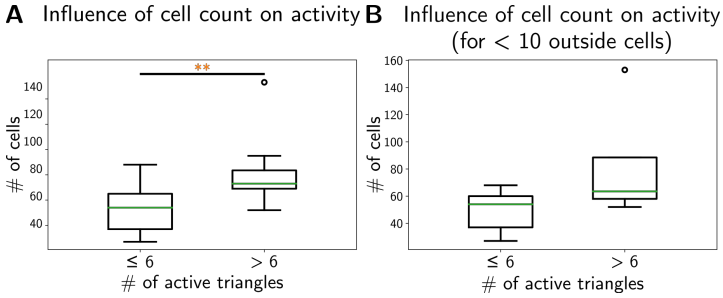

Figure 4.9 – Influence of cell count on SNEs. (A)-B Comparison of the cell number in neuronal networks growing in neuroCapTiH patterns showing a maximum number of active triangles larger, or smaller or equal than 6 for all patterned networks (**A**) or only those with fewer than 10 cells growing outside the pattern (**B**). The cell count is only significantly different between smaller and larger SNEs in patterns with many cells growing outside of the pattern. The Mann-Whitney-U test was used to determine significance. Asterisks and boxplots explained in section 2.6.

4.4 Interlude - Establishing an All Optical Recording and Stimulation System

Can individual triangles elicit SNEs, and how far are these SNEs able to travel through the neuroCapTiH structure as compared to spontaneous ones? To answer these questions, I established a double optogenetic system using the GECI jRCaMP1b and the actuator ChR2(H134R) labeled with GFP (ChR2-GFP; section 2.2.4; Figure 2.9). Such a system was rarely used in *in vitro* studies before (see Introduction), and therefore posed some challenges.

To ensure proper functioning of both optogenetic tools, I tested the proteins separately in unpatterned, random neuronal networks grown on PLL-coated glass coverslips. Calcium imaging of neurons transduced only with jRCaMP1b (section 2.4.3, excluding stimulation) showed individual and concerted calcium events in neurons throughout the whole substrate (an exemplary region is shown in Figure 4.10 A). Whole-cell patch-clamp (current clamp) of neurons transduced with only ChR2-GFP revealed that normally-shaped APs could reliably be evoked by 473 nm laser pulses of 50-150 ms duration (an exemplary trace is shown in Figure 4.10 B; see also section 2.4.4). In voltage-clamp mode, photocurrents of around -125 pA could be elicited, which is a physiologically relevant value for excitatory currents (Deisseroth and Hegemann, 2017).

As both proteins were introduced into the cells via AAV-mediated transduction, the combination may pose some stress to the neurons. Therefore, an optimal multiplicity of infection (MOI) for both AAVs had to be found that did not prevent the experiments due to low expression levels while at the same time minimizing harm to the cells. A low MOI of ChR2-GFP (0.33×10^5 GC/cell) combined with a high MOI of jRCaMP1b (5.86×10^5 GC/cell) at a transduction on the same DIV yielded most active cells (cells displaying calcium events), comparable to expression of only jRCaMP1b (Figure 4.10 C). This MOI is calculated using the seeding density of cells, and on patterned substrates many cells die and/or disattach after seeding. Therefore, the determined MOIs were down-scaled to 0.25×10^5 GC/cell for ChR2-GFP and 4.395×10^5 GC/cell for jRCaMP1b on patterned substrates.

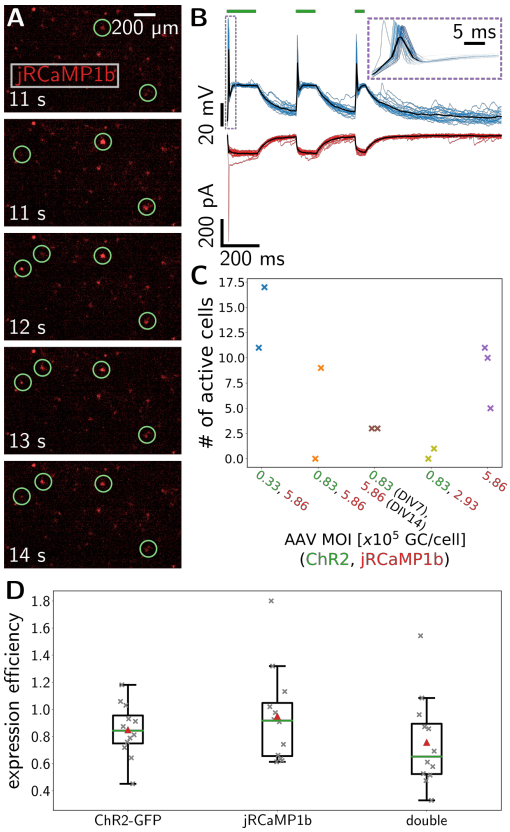

Figure 4.10 – Optical stimulation and recording via optogenetic constructs. (A) Selected frames of a calcium imaging movie recorded from neurons only expressing jRCaMP1b. Green circles highlight active neurons. **(B)** Voltage (blue) and current (red) traces recorded during current-clamp (blue) or voltage-clamp (red) experiments. Green vertical bars at the top represent laser stimulations. The violet box magnifies the stimulus response. **(C)** Comparison of the number of active neurons at different MOIs of AAVs containing jRCaMP1b (red) and ChR2-GFP (green). DIV7 and DIV14 in the middle experiment indicates the transduction days for this experiment. All others were transduced at DIV11 (see also section 2.2.4). All cultures were recorded at DIV20. **(D)** Expression efficiency of the different constructs. Box plots are explained in section 2.6.

Next, the expression efficiencies of jRCaMP1b, ChR2-GFP, and both in the same neuron were checked. For this, the ratio of the number of neurons expressing the respective protein(s) and the number of neurons labeled by an antibody against the neuronal marker neurofilament H (see section 2.2.6) was calculated. The cells were counted automatically using the background subtraction, thresholding, and `Analyze particles` plugin in `Fiji`(Schindelin et al., 2012). The expression levels were determined on patterned substrates with fComInput patterns (see Chapter 5 and Figure 5.1 B). Expectedly, expression levels of the individual proteins are higher (ChR2-GFP: 0.84, Q1: 0.75, Q2: 0.96; jRCaMP1b: 0.92, Q1: 0.66, Q3: 1.05) than of both proteins together (0.65, Q1: 0.52, Q3: 0.89; Figure 4.10 D). This difference is not statistically significant. No expression level differs significantly from 1.00 although of course all are in fact lower than 1.00. The theoretical probability of a double transduction based on the single protein efficiencies is $0.84 \times 0.92 = 0.77$. Therefore, the median of 0.65 is even closer to this probability

of 0.77 than to 1.00. Due to inhomogeneities in and the inefficiency of immunocytochemistry, these expression levels are just rough approximations. However, they demonstrate clearly that the expression levels are very high, and the majority of neurons expresses both proteins.

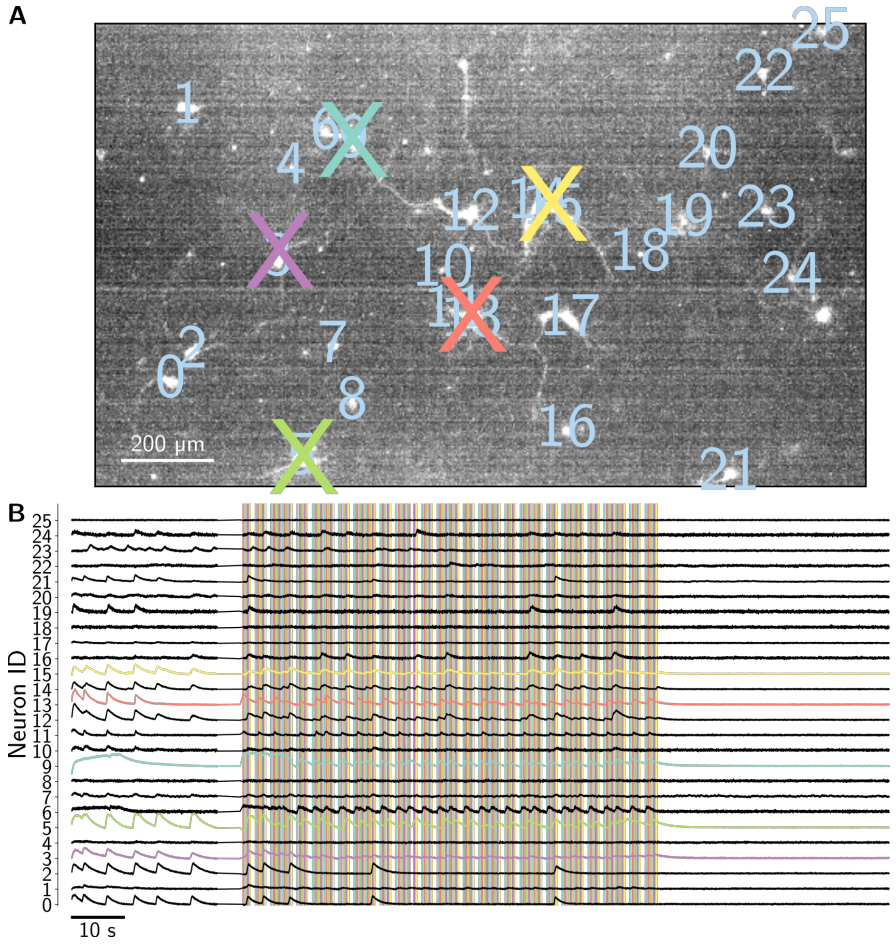

Figure 4.11 – Stimulation and calcium events of 5 neurons in double-transfected cultures. (A) Neurons on unpatterned substrates expressing jRCaMP1b (white) depicted as a maximum intensity projection of a calcium imaging movie. Active neurons are labeled with unique IDs, which correspond to **B**. Stimulated neurons are marked with crosses (color corresponds to **B**). **(B)** Normalized (see section 2.4.2.1) mean intensity traces of all neurons in **A**.

Next, I tested if stimulating such double-transduced neurons on unpatterned substrates resulted in a calcium response. To make sure that a potential response was due to stimulation of ChR2-GFP and not an artificial effect of the laser on the intensity of jRCaMP1b, I stimulated cultures only expressing jRCaMP1b. Expectedly, these cultures did not show any response to the laser stimuli (data not shown). On the other hand, stimulation of 5 neurons in double-transduced cultures (Figure 4.11 A) resulted in a reliable calcium response (see for example green and cyan traces in Figure 4.11 B). As the laser stimulation leads to stimulation artifacts in the calcium imaging movie, the post-processing procedure described in section 2.4.2.1 had to be extended. This extension introduces an additional step for removal of those artifacts (see section 2.4.3.1; indicated as vertical colored bars in Figure 4.11 B).

For quantification of this response, the response rate of a neuron was defined as the mean number of peaks occurring in a 400 ms window after the end of all stimuli at a certain position. Additionally, a peak was only counted as a valid (non-random) response if a peak was present in less than 10% of 50 randomly shuffled variants of the

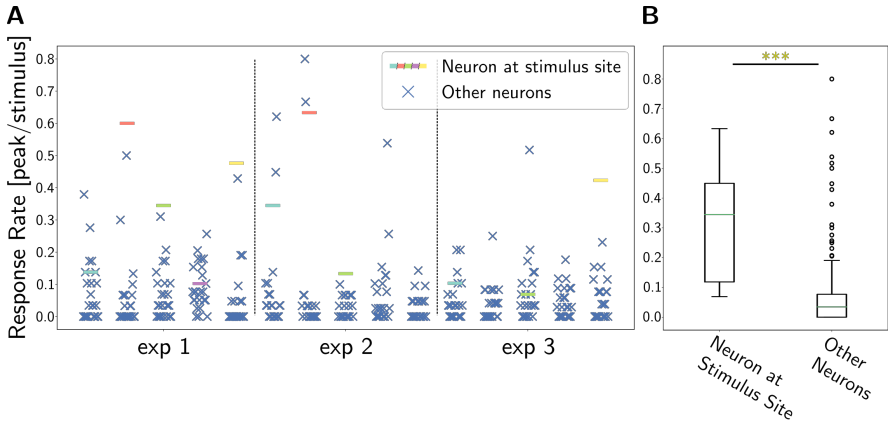

Figure 4.12 – Stimulated neurons respond more often to stimuli than others. (A) Response rate (mean number of peaks occurring in a 400 ms window after the end of all stimuli at a certain position) of each active neuron in 3 experiments (exp 1 to 3). A peak was only counted as a valid (non-random) response if a peak was present in less than 10% of 50 randomly shuffled variants of the peak train under investigation. Colored horizontal bars represent the stimulated neurons. If no bar is present, the stimulated neuron did not express jRCaMP1b. **(B)** Comparison of the the categories of all neurons depicted in **A**. Mann-Whitney-U yielded $p < 0.001$.

peak train under investigation. Thus, the mean response rate of neurons with a very high firing rate, and therefore a high probability of falsely identifying a random peak as a response, was downscaled. In all three experiments, at least some stimulated neurons exhibited high response rates (>0.5) as compared to the rest of the neurons (Figure 4.12 A). However, some stimulated neurons did not seem to respond strongly to the stimuli (compare experiments 2 and 3 in Figure 4.12 A). This may be due to a low expression level of ChR2-GFP (unlikely, as neurons with strong GFP fluorescence were chosen), a reduced activity due to a very strong expression of both optogenetic proteins, or a low expression level of jRCaMP1b. Some stimulated neurons are not measurable as they only express ChR2-GFP but insufficient amounts of jRCaMP1b (e.g. violet and yellow in experiment 2, or orange and violet in experiment 3). All in all, when comparing the rates of all stimulated neurons (0.345 peaks/stimulus, Q1: 0.118; Q3: 0.450) with the rates of all others (0.034 peaks/stimulus, Q1: 0.000; Q3: 0.077), they are on average significantly higher in the first group ($p < 0.001$; Figure 4.12 B). In conclusion, these first tests on unpatterned substrates show that the all optical system is suitable to elicit neuronal responses recordable with calcium imaging.

4.5 neuroCapTiH - Evoked activity dynamics

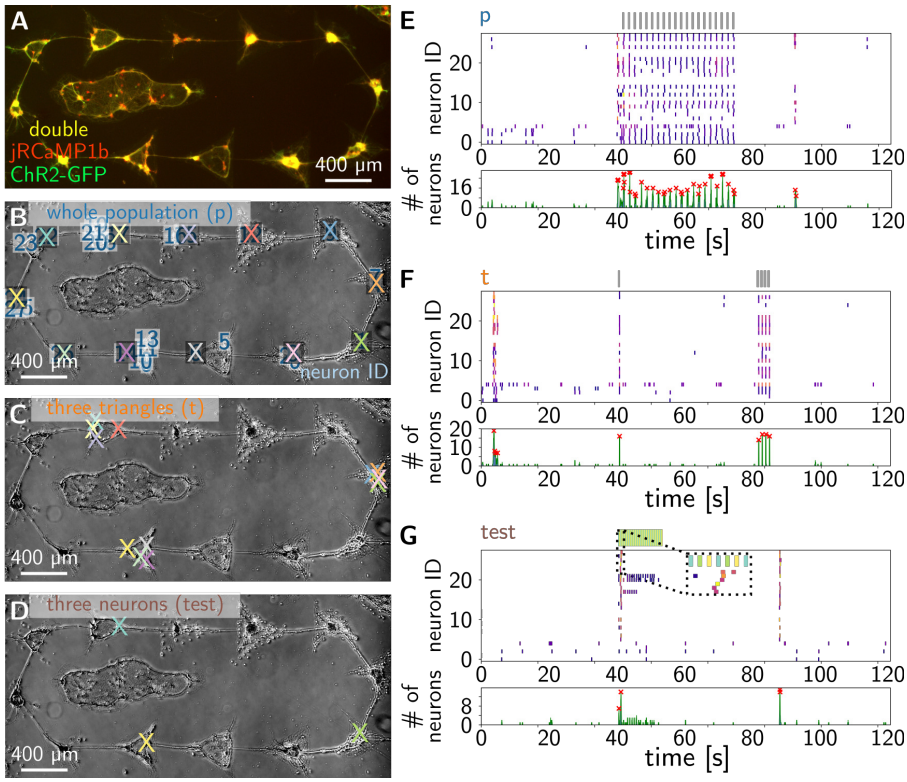

Figure 4.13 – Optical stimulation and recording of neurons in neuroCapTiH patterns. (A) Fluorescence micrograph of neurons expressing jRCaMP1b (red calcium indicator) and ChR2-GFP (GFP-tagged light sensitive cation channel) grown in a neuroCapTiH pattern on a GLYMO-treated glass substrate (see section 3.1.1.1). **(B-D)** Three times the same phase contrast micrograph of the same neurons as in **A** with marked stimulation locations of the *p* (**B**), *t* (**C**), and *test* (**D**) stimulation routines (see also section 2.4.3). Regions of interest (ROIs) in **B** for mean intensity trace extraction (see corresponding sections in section 2.4) are marked with light blue numbers that correspond to the neuron ID in **E-G**. **(E-G)** Top: Raster plots showing the time points of individual calcium events as small vertical bars. The amplitude is color coded from blue (low) over orange to yellow (high). Neuron ID corresponds to the ROIs in **B**. Vertical bars above each plot correspond to the blind regions during laser stimulation. In **G**, the individual stimulation locations can be separated and are color coded as in **D**. A magnified region is shown in the inset (see also Figure 4.11). Bottom: Combined peak rate (see section 2.5.2) of the calcium peak count within 500 ms time windows. The combined peak rate was used for SNE detection. Detected SNEs indicated by red crosses.

After establishing a system for an all optical recording and stimulation, I applied this approach to investigate the behavior of neurons grown in neuroCapTiH patterns upon stimulation (Figure 4.13 A). Three different stimulation routines were chosen (for details, see section 2.4.3 and Figure 2.6 C-D): stimulation of individual neurons within the whole population with 50 ms pulses and a short delay of 95 ms (p; Figure 4.13 B); near-simultaneous stimulation of three locally confined locations (1-2 triangles) with 5 ms pulse duration and no delay (t; Figure 4.13 C); and individual stimulation of three neurons with 50 ms pulse length and a long delay of 500 ms ($test$; Figure 4.13 D). All of these stimulation types were able to elicit some neuronal response (Figure 4.13 E-G; Figure 4.14 A-C).

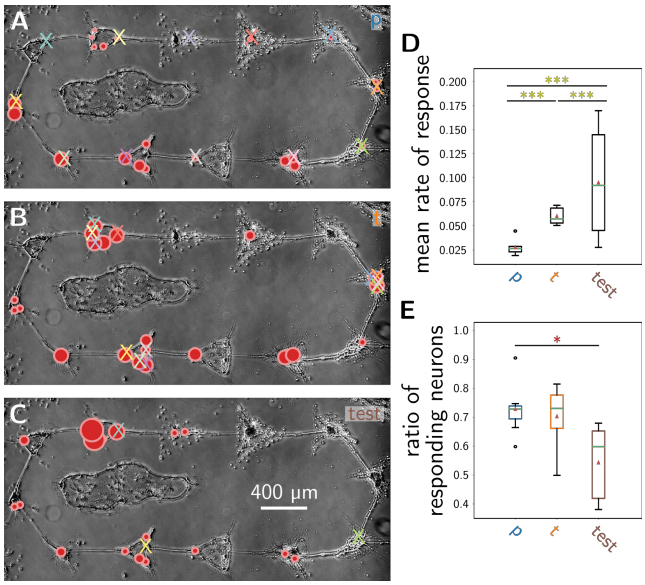

Figure 4.14 – Stimulation response of individual neurons. Stimulated selected triangles elicit higher response rates than global stimulation. **(A-C)** Response rates of each recorded neuron (ROIs in Figure 4.13 B) for the p (**A**), t (**B**), and $test$ (**C**) stimulation routines. The size of the red circles correlates with the response rate. **(D-E)** Comparison of the mean response rate (**D**; mean of the rates displayed in **A-C**) or the ratio of responding neurons (**E**; number of responding neurons divided by the total number of ROIs) for the different stimulation routines. The bootstrap significance test was used. Asterisks and box plots as explained in section 2.6.

To quantify the neuronal response in a way comparable between stimulation routines, the number of calcium events elicited by one iteration over all stimulus locations was determined. The response rate was defined as the mean number of such events over

all iterations of the stimulus locations, and was normalized to the number of stimulus locations. Individually stimulated neurons (*test*) exhibited significantly higher and more variable response rates (0.09, Q1: 0.05, Q3: 0.14) than neurons stimulated with the t (0.06, Q1: 0.05, Q3: 0.07) or p (0.03, Q1: 0.02, Q3: 0.03) stimulation routines (Figure 4.14 D). The p stimulation routine showed the lowest response rates. This difference between *test*

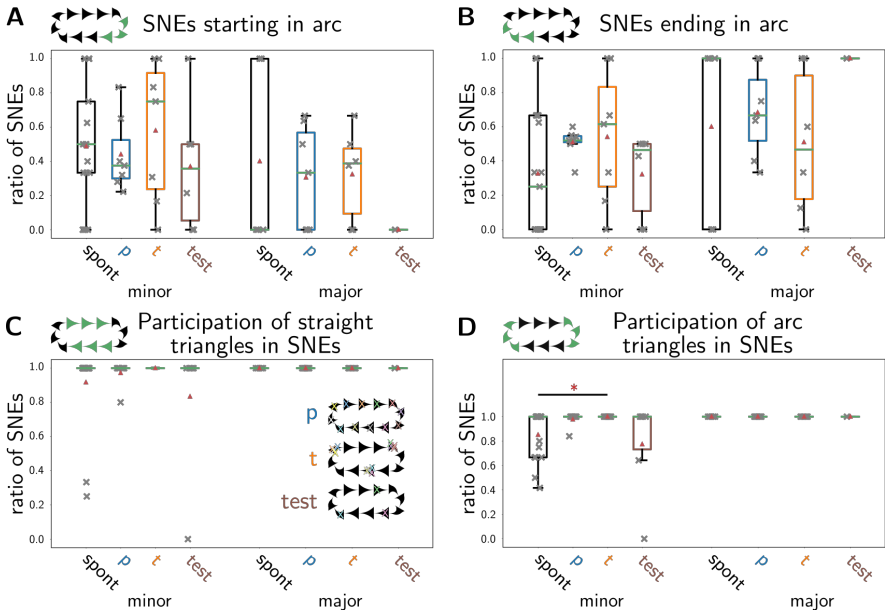

Figure 4.15 – Arc participation in spontaneous and evoked SNEs. Arc and straight triangles are participating similarly in SNEs. **(A-B)** Comparison of the fraction or ratio of minor and major SNEs starting (**A**) or ending (**B**) in arc triangles for the different stimulation conditions. **(C-D)** Comparison of the fraction or ratio of SNEs in which at least one straight triangle (**C**) or arc triangle (**D**) participated. The bootstrap significance test was used. Box plots are explained in section 2.6.

and p/t is probably caused by the higher probability to fail evoking a response in some neurons when more neurons are stimulated. The difference between t and p indicates that individual triangles form subnetworks. These subnetworks may act as modules with an increased response rate upon stimulation of other neurons in the same triangle (see also Figure 4.16 C and D). Alternatively, the higher synchronicity of the t stimulation routine evokes the response of a larger subnetwork inducing a SNE-like behavior (see following section). At the same time, a smaller fraction of recorded neurons responded to *test*

stimulation types (0.60, Q1: 0.42, Q3: 0.65) as compared to p (0.73, Q1: 0.70, Q3: 0.74) or t (0.73, Q1: 0.66, Q3: 0.78; not significant; Figure 4.14 E). This is to be expected as a smaller fraction of neurons is stimulated.

4.5.1 The Spatial Structure of SNEs Varies Between Conditions

Are the responding neurons distributed equally through the neuroCapTiH structure? To answer this question, I determined whether arc and straight triangles participated equally in SNEs. For spontaneous SNEs monitored in GCaMP6f expressing neurons, no preference between these categories exists (see also section 4.3.2). The same is true for evoked SNEs.

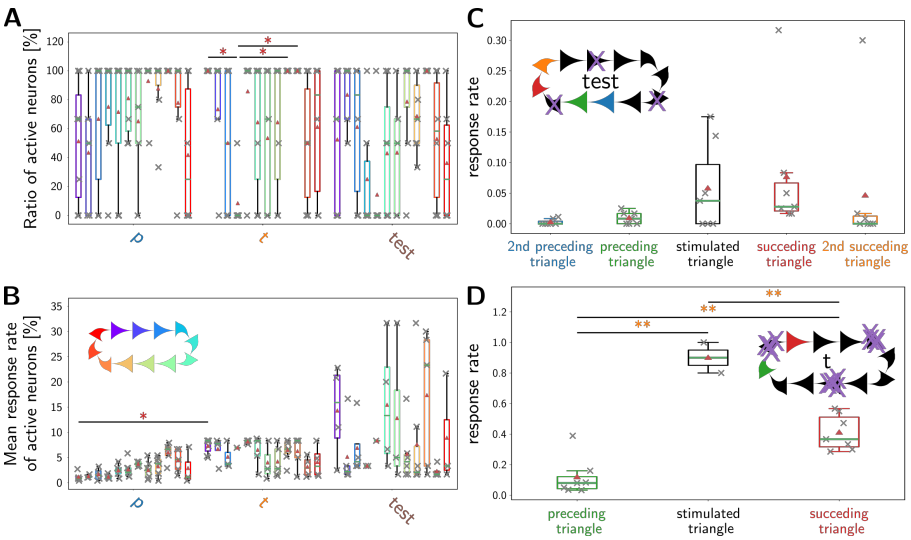

Figure 4.16 – Distribution of evoked responses over the neuroCapTiH pattern. The neuronal response is differently distributed through the individual triangles in the neuroCapTiH networks. **(A-B)** Comparison of the ratio of responding neurons (**A**; normalized to the number of ROIs within the respective triangle) or the mean response rate (**B**) within each triangle of the neuroCapTiH networks for the different stimulation routines. Color code corresponds to the neuroCapTiH sketch in **B**. The bootstrap significance test was used. Asterisks and box plots as explained in section 2.6. **(C-D)** Mean response rate of triangles before and after the stimulated triangles in *test* (**C**) and **t** (**D**) stimulations. The respective triangles are color coded as indicated for one exemplary region out of the three stimulated regions in a sketch in **C** or **D**. All three stimulated regions are indicated with violet crosses. For all comparisons, the bootstrap significance test was used. Asterisks and box plots as explained in section 2.6.

SNEs start and end in arcs almost equally with the exception of p-induced SNEs (described below; Figure 4.15 A, B; Table A.1). All conditions are not significantly different from 0.5 (determined by one sample t-test). An arc and a straight triangle participate in almost every SNE evoked by the p and t stimulation routines (Figure 4.15 C, D; Table A.1). This high ratio is achieved because these routines directly stimulate cells in both categories. Spontaneously occurring and *test*-induced SNEs do not always include a straight and an arc triangle (see especially significant difference in Figure 4.15 D) as no or only three neurons are stimulated randomly. in *test* stimulations, one of the stimulations could therefore fail to evoke a response, thus biasing participation. However, these ratios are still not significantly different from 1.0. Only for (especially major) SNEs induced by p stimulation the equality between arc triangles starting and ending SNEs is slightly skewed. Here, the ratio of arc triangles starting a SNE seems to be lower than the ratio of arc triangles ending a SNE. This is probably caused by the nature of the stimulation, as this always started in a straight triangle (top left). Although this imbalance is not reflected by the ratio of neurons responding in the individual triangles (violet to blue straight triangles in Figure 4.16 A), it is reflected by a slightly, not significantly lower mean response rate of responding neurons in the first stimulated triangles (violet to blue straight triangles in Figure 4.16 B). This lower mean response rate indicates that some of the responses from the first stimulated triangles are hidden within the blind period during stimulation. Thus, it is more likely that straight triangles begin a SNE while arc triangles (orange to red in Figure 4.16) end it although starting and ending fractions do not differ significantly from a 0.5 (chance level) ratio (see above). All other conditions show no such imbalance.

However, t stimulation induces uneven distributions of the ratio of responding neurons in each triangle (Figure 4.16 A). As the triangles stimulated in this routine are selected randomly but depend on the growth and expression of the network, some triangles are under-represented. The same is true for the uneven, albeit not significantly different, distribution of the mean response rates when stimulating with the t or *test* routine. Therefore, I calculated the mean response rate distribution centered on the stimulated region in these stimulation routines, excluding the response of actually stimulated neurons. The mean response rate of the stimulated triangles in the *test* routine expectedly is highest (0.050,

Q1: 0.000, Q3: 0.103; Figure 4.16 C). Response rates in the downstream triangles (triangle 1: 0.028, Q1: 0.021, Q3: 0.067; triangle 2: 0.000, Q1: 0.000, Q3: 0.013) are only slightly lower than in the stimulated triangles. On the other hand, response rates in the preceding triangles are more strongly reduced (triangle 1: 0.008, Q1: 0.000, Q3: 0.017; triangle 2: 0.000, Q1: 0.000, Q3: 0.004) as compared to stimulated triangles. A similar, but even clearer, distribution is seen for the t stimulation routine. The mean response rate in the stimulated triangles is highest (0.900, Q1: 0.850, Q3: 0.950). Downstream triangles respond significantly more reliably (0.367, Q1: 0.317, Q3: 0.511) than preceding triangles (0.080, Q1: 0.043, Q3: 0.122). This not only demonstrates that APs propagate towards the tip of the triangle (see section 4.5.3) but also that the response distribution is not as homogeneous as indicated by the average response in each triangle (Figure 4.16 B). Thus different stimulations clearly activate different subnetworks, which are most strongly functionally connected in individual triangles.

4.5.2 Different network stimulation elicits different types of SNEs

In the previous section, I determined that stimulation was able to elicit a neuronal response that was distributed equally through the neuroCapTiH network. Next, I checked the effect of different stimulation routines on the measures calculated for spontaneous activtiy recorded via GCaMP6f-based calcium imaging (see section 4.3). Interestingly, the rate of spontaneous SNEs is much lower than in the previous experiments with GCaMP6f (major SNEs: median, Q1, Q3: 0.00 SNE/s; minor: 0.01 SNE/s, Q1: 0.00 SNE/s, Q3: 0.01 SNE/s; Figure 4.17 A) albeit still in the range of reported values (Wagenaar et al., 2006b). The dual AAV transduction and resulting expression under the Synapsin promoter probably consumes cellular resources usually reserved for the production of growth- and synapse-related proteins. Moreover, neurons in neuroCapTiH patterns were grown on GLYMO-treated substrates (see section 3.1.1.1) with less cells growing outside of the actual pattern. As described in section 4.3 (Figure 4.9), the number of cells growing outside increases the number of large SNEs with the disadvantage of losing the clearly defined modularity of neuroCapTiH networks. Therefore, these networks are very sparse, exchanging only a few maturation-driving signals of biological and electrophysiological nature. Thirdly, at least

imaging with chemical green fluorescent calcium indicators like fluo-4 increase network activity as an artifact (Ghirga et al., 2020). This could also be the case for imaging the green fluorescent GCaMP6f. In combination, the sparse network, few outlying cells, and the dual expression system can lead to a slowed maturation process. Nevertheless, the relative effect of the different stimulation routines on neuroCapTiH neuronal networks can be investigated.

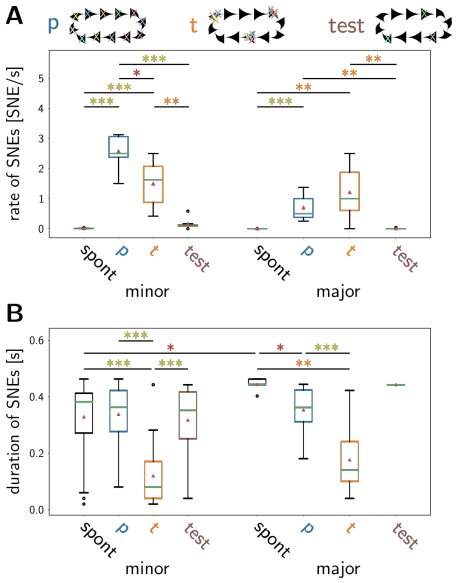

Figure 4.17 – Rate and duration of spontaneous and evoked SNEs. (A-B) Comparison of the rate (**A**) and duration (**B**) of minor and major SNEs. The duration was defined as in Figure 4.7 D. The rate and duration can serve as an indicator for the efficiency of SNE generation and coherence individual events within an SNE, respectively. The bootstrap significance test was used. Asterisks and box plots as explained in section 2.6.

Even though the spontaneous condition does not show many SNEs, minor and major SNEs are evoked very reliably during stimulation. On the background of the strongly reduced spontaneous SNEs, this evoked activity gains additional significance. As opposed to the mean response rate, SNEs are elicited most strongly in networks stimulated by p and t stimulations. On the other hand, *test* stimulation yielded similarly low rates (major: median, Q1, Q3: 0.00 SNE/s, mean: 0.01 SNE/s; minor: 0.08 SNE/s, Q1: 0.08 SNE/s, Q3: 0.13 SNE/s) as witnessed in spontaneous activity (Figure 4.17 A). For minor events, even the relation between p (2.50 SNE/s, Q1: 2.38 SNE/s, Q3: 3.06 SNE/s) and t (1.63 SNE/s, Q1: 0.88 SNE/s, Q3: 2.07 SNE/s) stimulations is reversed as compared to the response rate with p eliciting most SNEs. However, major events are elicited equally well by p (0.50 SNE/s, Q1: 0.38 SNE/s, Q3: 1.00 SNE/s) and t (1.00 SNE/s, Q1: 0.61 SNE/s, Q3: 1.88 SNE/s) stimulations, with a trend towards higher rates for t stimulations.

The duration of minor SNEs is similar throughout almost all conditions (spont: 0.382 s,

Q1: 0.272 s, Q3: 0.413 s; p: 0.363 s, Q1: 0.277 s, Q3: 0.422 s; *test*: 0.352 s, Q1: 0.251 s, Q3: 0.417 s). Only t stimulation (0.081 s, Q1: 0.040 s, Q3: 0.171 s) leads to shorter SNEs (Figure 4.17 B). In minor SNEs, the direct response of the near-simultaneously activated neurons (t) could artificially shorten these SNEs. Major SNEs are also shortest in t-stimulated networks (0.141 s, Q1: 0.101 s, Q3: 0.242 s), followed by p stimulated (0.362 s, Q1: 0.312 s, Q3: 0.424 s) and finally spontaneously active (0.444 s, Q1: 0.443 s, Q3: 0.463 s) networks. Major SNEs elicited by *test* stimulation show a similar duration (0.442 s, Q1: 0.442 s, Q3: 0.442 s) to spontaneous but statistical significance cannot be determined ($n < 3$). An artificial reduction of the SNE duration for t stimulation by the direct response of stimulated neurons could also play a role in major SNEs. Yet, the difference to the other conditions is so strongly pronounced that this explanation is unlikely to be the solitary reason.

In conclusion, the following theory can be derived from the results regarding major SNEs. Small, synchronized subnetworks are able to recruit the majority of a network to elicit a short, global network response. This may provide evidence for the model proposed by Lonardoni et al. (2017) in which functional communities elicit SNEs. The definition of functional communities is based on spontaneous activity whereas functional subnetworks in neuroCapTiH patterns are determined by evoked activity. However, the missing dependence of spontaneous activity on cell number (section 4.3.3) also provides some evidence for modularity. Many, asynchronously active, individual neurons can also elicit such a response but the recruitment process of the majority of neurons is slower. Spontaneous SNEs are slower and rarer than p and t stimulation-induced ones. Probably, evoked SNEs are skipping the recruitment process induced by some sporadically active pacemaker cells usually precedes a naturally occurring SNE (Fardet et al., 2018; Gritsun et al., 2010). Therefore, stimulation immediately recruits many neurons of the network that in turn recruit more neurons, resulting in more efficient generation of short SNEs.

4.5.3 Evoked SNEs Travel Mostly Forward for up to 11 Triangles

After learning that stimulation can evoke SNEs of different duration than spontaneous ones, I compared the traveling distance of SNEs withing the different stimulation routines.

The number of triangles (minor: 3; major: 7; Figure 4.18 A) participating in a spontaneous SNE is comparable to the results from GCaMP6f-expressing networks (Figure 4.8). The number of consecutive triangles (minor: 2; major: 5; Figure 4.18 B) is also comparable. Thus, although the rate of SNEs is much smaller in the double transduction system, the distance covered by SNEs is similar.

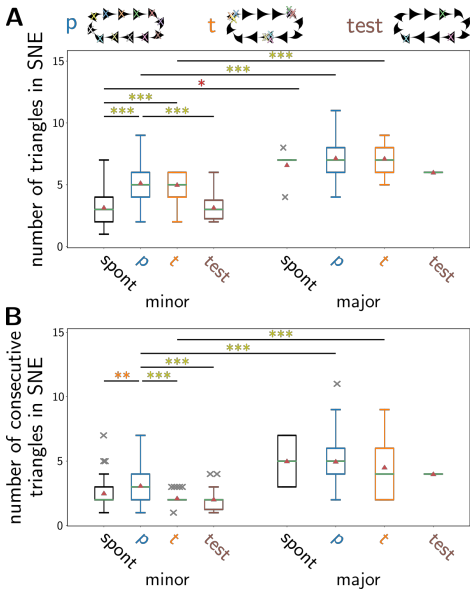

Figure 4.18 – Number of triangles covered spontaneous and evoked SNEs. Only minor SNEs show strong differences in their propagation length. **(A-B)** Comparisons of the number of triangles (**A**) and the number of consecutive triangles (**B**) participating in minor or major SNEs for the different stimulation routines. The bootstrap significance test was used. Asterisks and box plots as explained in section 2.6.

All numbers of triangles (p: 7; t: 7; *test*: 6) and consecutive triangles (p: 5; t: 4; *test*: 4) traversed by major SNEs are similar to each other. These numbers are higher (up to 11 triangles triggered by p stimulation) than the numbers for minor SNEs. All such differences are highly significant except for *test* stimulations and the number of consecutive triangles traversed by spontaneous SNEs. In *test* stimulations, significance tests fail as only one major SNE, which traveled for 6 triangles and 4 consecutive triangles, was evoked by this routine. However, in spontaneous SNEs case a clear trend is present (compare black boxplots in Figure 4.18 B). Despite the differences in rate and duration of major SNEs, they follow one of the planned working principles of the neuroCapTiH pattern - the propagation through multiple consecutive triangles in the pattern.

For minor SNEs, significantly more total triangles are participating in SNEs stimulated by the p routine (5, Q1: 4, Q3: 6) than in SNEs stimulated by the *test* routine (3, Q1: 2, Q3: 6) or occurring spontaneously. The t routine (5, Q1: 4, Q3: 6) also recruits more triangles than spontaneously occurring minor SNEs. On the other hand, the amount of

consecutive triangles is higher in minor SNEs evoked by the p routine (3, Q1: 2, Q3: 4) compared to all other SNEs (t: 2, Q1: 2, Q3: 2; *test*: 2, Q1: 1, Q3: 2). Again, this provides evidence that minor SNEs evoked by stimulation routines are highly influenced by the calcium activity of the directly stimulated neurons. The p routine activates neurons around the whole pattern, evoking also a higher proportion of neurons in consecutive triangles. The t routine activates equally many neurons at three triangles but they are not connected in minor SNEs. The *test* routine activates three random neurons, not eliciting spatially long minor SNEs in general. And in minor SNEs spatially close neurons with many synaptic connections are more likely to exhibit synchronous events outside of major SNEs than spatially distant ones.

When analyzing the numbers of participating triangles in evoked and spontaneous major SNEs, the principle of propagating APs through multiple CT1 structures is functional. As neurons are stimulated in the direction of the triangle tips during all stimulation routines, the SNE directionality should be forward in evoked SNEs. Thus, the average delays between triangles within SNEs should be equally positive as in spontaneous events (section 4.3.3; Figure 4.7). However, the average delay is lower in major SNEs evoked by t stimulation than in the other conditions (statistically significant only for the difference to p; Figure 4.19 A and Table A.2). This behavior is consistent also in the average of maximum delays between triangles (Figure 4.19 B) but the average of minimum delays is highest for major SNEs evoked by t stimulation (Figure 4.19 C and Table A.2). Thus, t stimulation elicits major SNEs with the smallest delays and no clearly definable directionality as most neurons participating in the SNE are active almost simultaneously. Yet, all average delays are positive albeit small, indicating a general tendency toward forward SNEs. This is consistent with the short duration of SNEs evoked by t stimulation.

The delays of minor SNEs behave similar to those of major SNEs. However, in minor SNEs the average delay between triangles is reduced in SNEs evoked by p stimulation. This reduction seems to be caused by both longer positive and negative delays as the average of maximum delays is higher for minor SNEs evoked by p stimulation, and the average of minimum delays is lower than for the other conditions (see Table A.2). Intuitively, this suggests a longer duration of such SNEs but the duration of minor SNEs evoked by p is

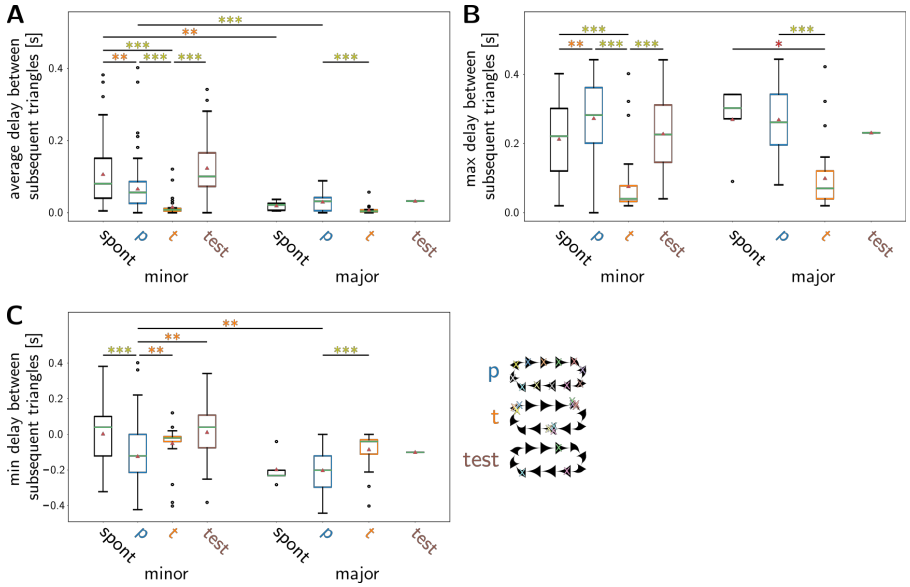

Figure 4.19 – Directionality of spontaneous and evoked SNEs. (A-C) Comparisons of the average (**A**), maximum (**B**), and minimum (**C**) delays between the individual triangles in each minor or major SNE. The average delay can serve as a measure for the overall direction of the SNEs in the neuroCapTiH pattern. Maximum and minimum delays indicate the strongest forward and backward step in each SNE. The bootstrap significance test was used. Asterisks and box plots as explained in section 2.6.

equal to that of spontaneous minor SNEs and even shorter than spontaneous SNEs for major SNEs (compare section 4.5.2 and Figure 4.17 B). On the other hand, the average delays are closer to 0 than for spontaneous minor SNEs, fitting well with the shorter or equal duration of p-induced SNEs. This indicates that p stimulation evokes different multi-triangular subnetworks that are all tightly interconnected and therefore elicit very coherent activity (low average delays). However, when propagation within a SNE skips to the next of such subnetworks, a larger delay occurs than within subnetworks (large max. and min. delays). However, all these subnetworks are still functionally linked to each other, thus not increasing duration of the SNEs.

For the *test* and t stimulation routines, it is possible to determine the direction of signal propagation more directly by calculating the mean response rates (i.e. the relative number of responses of each neuron to a stimulus) in the stimulated and its successive and

preceding triangles (see Figure 4.16 C, D). In *p*, this is not possible as all triangles are stimulated, and therefore it is not possible to determine if a calcium response was elicited in a preceding or succeeding triangle. In both stimulation routines (*t* and *test*), the successive triangles clearly exhibit a higher response than the preceding triangles. Therefore, calcium events (and most likely APs) are preferably propagated towards the triangle tip. This further proves the results by Albers and Offenhäusser (2016), and extends them to multiple triangles instead of just one.

Thus, the delays between triangles provide further evidence that small subnetworks induce SNEs. Individual neurons evoke SNEs that can also be more coherent than spontaneous ones. Those SNEs are also very variable as they depend on the ability of all 12 stimulated neurons to a) respond to a stimulus and b) recruit other neurons into the SNE. Moreover, special types of neurons such as hub neurons (Cossart, 2014) (see section 2.5.6.1) or leader neurons (Pasquale et al., 2017) may influence SNE generation differently than others. Additionally, small responses might sometimes be hidden in the blind period during laser stimulation, thus adding variability to the SNE (compare also section 4.5.1).

4.6 Conclusions and Outlook

The CT1 pattern was developed by Albers and Offenhäusser (2016) to direct axonal growth and consequently AP propagation in the direction of the triangle tip. By investigating AP propagation between neurons growing in downscaled CT1 patterns, I found that the directionality is most likely not preserved in much smaller versions of the CT1 pattern. This could be due to an increasing linearity of the patterns, failing to prevent backward growth of axons. On the other hand, neuroCapTiH patterns (in which the CT1 pattern is implemented) show calcium event propagation with the preferred directionality towards the triangle tips for up to 11 triangles within SNEs. While being consistent with the results published by Forró et al. (2018), the neuroCapTiH system seems to show less strong clustering and therefore allows for an individual neuronal analysis. Moreover, replacing the arcs in the original neuroCAP design with bent CT1 structures could prevent calcium signals from getting trapped, and allowed them to propagate longer through the whole pattern. This demonstrates the reliability of CT1 patterns as the calcium signal is transferred through multiple triangles, even if a full circulation through the neuroCapTiH pattern was not achieved. A full circle is probably prevented by the constant decrease in transfer probability due to the bottleneck character of the connecting elements, the triangle tips. To achieve a neuronal "oscillator" with fully circulating APs, the number of triangles in the neuroCapTiH pattern could be reduced. To further characterize the properties of AP propagation in CT1-based patterns, electrophysiological techniques such as MEA (see also Chapter 3) or patch clamp would be beneficial for a higher temporal resolution. While MEA recordings were already combined in a system published by Forró et al. (2018), patch clamp recordings would not be possible in this system relying on closed microchambers. In combination with the high spatial resolution of calcium imaging, the properties of APs propagating through multiple subnetworks could be investigated. Such an investigation was recently conducted by Barral et al. (2019) but only by examining individual neurons (by patch clamp) in each layer of a multi-layered network.

Furthermore, I could demonstrate that an all optical system could be used to monitor evoked calcium activity during optical stimulation. By applying this dual optogenetic sys-

tem to neuroCapTiH patterns, I found that this pattern can be used to investigate certain properties of neuronal networks and SNE generation. Neurons growing in one triangle seem to be functionally connected more strongly to each other than to other triangles in the pattern. This could be a hint that the triangles serve as (functional) neuronal communities although these communities are usually defined based on spontaneous activity correlations (Lonardoni et al., 2017; Okujeni and Egert, 2019; Tsai et al., 2008). Additionally, I found that activity of multiple neurons in the network induces SNEs that propagate as far as spontaneous SNEs but are more coherent. The most coherent SNEs are generated by near-synchronous activity in spatially confined subnetworks (the triangles). This could fit with the theory that functional communities induce SNEs (Lonardoni et al., 2017).

Chapter 5

Large populations: investigating network synchronicity

Neuronal cell cultures can be grown not only in patterns inspired by electrical engineering (see Chapter 4) principles, but also by those based on biological concepts. The CT1 "diodes" (see section 4.1; Albers and Offenhäusser (2016)) can also be described as small modules or microcircuits of neuronal networks with a directed output. The anatomical modularity of neuronal networks has an effect on information processing (Yamamoto et al., 2016). On the other hand, functional modules were proposed to initiate and steer synchronous network events (Lonardoni et al., 2017). Neurons growing in triangle patterns are anatomically segregated through the triangle tip, therefore displaying anatomical modules with separately examinable cells. Such triangle patterns seem to represent functional modules as well (see Chapter 4). Similarly weak connections as the axons growing through the triangle tip were shown by Yamamoto et al. (2018) to lead to functionally segregated networks. By combining patterning and optogenetics, the investigation of the effect of neuronal activity in small modules on a larger population of neurons can be extended.
This chapter was in part reproduced from the manuscript by Hondrich et al. (In preparation.).

5.1 Pattern Design

A downscaled version of the CT1 pattern (75% of original) designed by Albers and Offenhäusser (2016) was used as a starting point (Figure 5.1 A; see also Figure 4.1 B). This structure (from now on called triangle) was placed upstream of a large population of neurons (from now on called population; Figure 5.1 B). The population pattern was based on a rectangle with edge lengths of 1660 µm × 1000 µm. A corner of this rectangle was removed in a way to ensure that a) the triangle tip is perpendicular to the population (to minimize backwards growth (Albers, 2016)) and b) to maximize the distance between the base of the triangle and the population. Similarly to the neuroCapTiH design, the triangle was intended to serve as an anatomical and functional community. The highly confined space within the triangle was assumed to lead to more abundant and stronger anatomical and functional interconnections within this structure than with the population (compare also the design used by Yamamoto et al. (2018)). Therefore, the pattern is termed "functional community input" and will be abbreviated as fComInput. The whole pattern was designed to fit exactly into the field-of-view of the microscope used for calcium imaging during optical stimulation (see section 2.4.1.1). On the other hand, AAVs exhibit a high transduction efficiency (see section 4.3.1 and section 4.4). Thus, a very large fraction of all cells within the entire investigated system can be monitored with an extremely high spatial resolution. Additionally, an equally large fraction of cells can be stimulated optically, also with a high spatial resolution limited by the precision of the motors of the targeting system and the laser spot size.

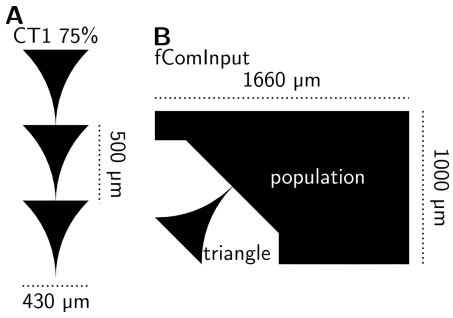

Figure 5.1 – Pattern for functional community investigation. (A) Triangle pattern with 75% of the size of the CT1 pattern (see also Figure 4.1 B). **(B)** Functional community input (fComInput) pattern, in which a triangle pattern (**A**) is placed upstream of a large population of neurons.

5.2 Stimulus Location and Synchronicity Impact Neuronal Response

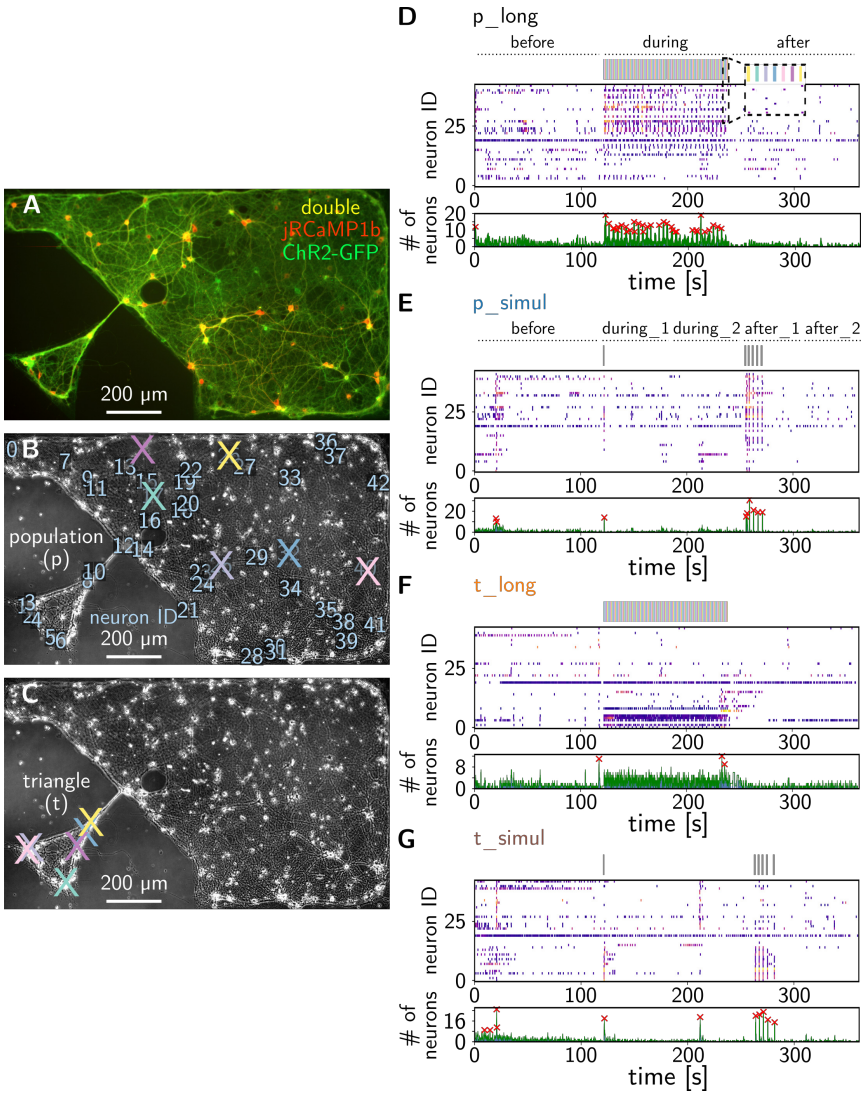

← **Figure 5.2 – Optical stimulation and recording of neurons in fComInput patterns.** **(A)** Fluorescence micrograph of neurons expressing jRCaMP1b (red calcium indicator) and ChR2-GFP (GFP-tagged light sensitive cation channel) grown in a fComInput pattern on a GLYMO-treated glass substrate (see section 3.1.1.1). **(B-C)** Two times the same phase contrast micrograph of the same neurons as in **A** with marked stimulation locations of the *p_long* and *p_simul* (**B**), and *t_long* and *t_simul* (**C**) stimulation routines (see also section 2.4.3). Regions of interest (ROIs) in **B** for mean intensity trace extraction (see corresponding sections in section 2.4) are marked with light blue numbers that correspond to the neuron ID in **D-G**. **(D-G)** Top: Raster plots showing the time points of individual calcium events as small vertical bars. The amplitude is color coded from blue (low) over orange to yellow (high). Neuron ID corresponds to the ROIs in **B**. Vertical bars above the raster plots correspond to the blind regions during laser stimulation. In **D** and **F**, the individual stimulation locations can be separated and are color coded as in **B** and **C**. For an exemplary, magnified region of the color code, see the inset in **D**. Bottom: Histogram (blue) and combined peak rate (see section 2.5.2) of the calcium peak count within 500 ms time windows. The combined peak rate was used for SNE detection. Detected SNEs indicated by red crosses.

The dual optogenetic approach for all optical stimulation and recording (see section 4.4) proved to be reliable for neuronal networks growing in neuroCapTiH patterns and was therefore also used for the fComInput patterns. About 127 ± 26 neurons (determined by an immunostaining of NFH, see section 4.4) were growing in well-defined patterns due to the improved μCP method (section 3.1.1.1). These cells were strongly expressing both the calcium indicator jRCaMP1b and the GFP-tagged light-responsive ion channel ChR2 (Figure 5.2 A; see section 4.4). To examine the influence of concerted and individual activity within the triangle and population (see section 5.1) on the network, four different stimulation routines were used (see section 2.4.3): *p_long* & *p_simul* - individual *long* or near-simultaneous (*simul*) stimulation of neurons in the population (Figure 5.2 B); *t_long* & *t_simul* - individual *long* or near-simultaneous (*simul*) stimulation of neurons in the triangle (Figure 5.2 C).

5.2.1 Synchronous Stimulation Increases Response Reliability

The response rate of each neuron in the fComInput network in form of calcium peaks within 400 ms after the end of each stimulus was determined as described in section 4.4 and section 4.5 (Figure 5.3). The mean response rates of neurons showing any response differ significantly between all conditions, with *t_long* eliciting the lowest response rates (0.05). Response rates evoked by *p_long* (0.08) and *t_simul* (0.09) stimulations follow. Finally, *p_simul* (0.10) induces the highest response rate (Figure 5.3 E). The fraction (or ratio) of responding neurons to all neurons does not show as strong differences. However, the

triangular stimulation routines show the lowest ratios (*t_long*: 0.51 peaks/s; *t_simul*: 0.46 peaks/s).

Ratios for population stimulation routines are higher than for triangle stimulations (*p_long*: 0.70 peaks/s; *p_simul*: 0.66 peaks/s; Figure 5.3 F).

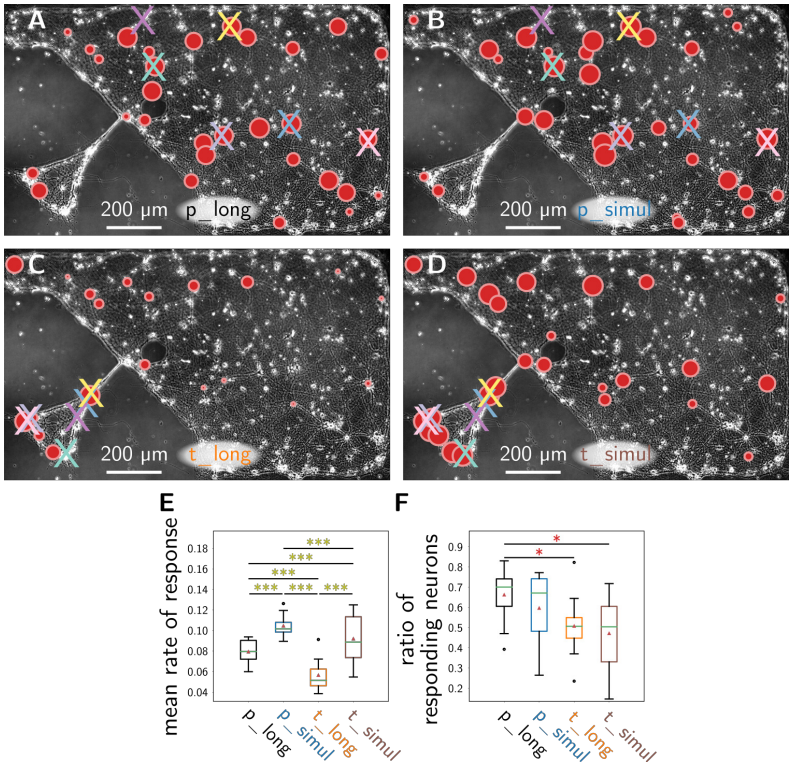

Figure 5.3 – Stimulation response of individual neurons. Near-simultaneous stimulations evoke higher response rates, and triangle stimulation activates fewer neurons. **(A-D)** Response rates of each recorded neuron (ROIs in Figure 5.2 B) for the *p_long* (**A**), *p_simul* (**B**), *t_long* (**C**), and *t_simul* (**D**) stimulation routines. The size of the red circles correlates with the response rate. **(E-F)** Comparison of the mean response rate (**E**; mean of the rates displayed in **A**-**D**) or the ratio of responding neurons (**F**; number of responding neurons divided by the total number of ROIs) for the different stimulation routines. The bootstrap significance test was used. Asterisks and box plots as explained in section 2.6.

Thus, synchronized activity of neurons elicits a more reliable response than individual activity in similar numbers of neurons. Moreover, activity in the triangle subpopulation

does not elicit this response as reliably and not in as many neurons as the population subpopulation. These lower response metrics in the triangle population are a first indication that the original purpose of the triangle to serve as a SNE-initiating functional community may not be fulfilled as intended. However, it is an indication that different subnetworks are addressed by the two stimulation locations.

5.2.2 Functional Separation and Triangle Directionality

Is the triangle exhibiting directionality (as published before by Albers and Offenhäusser (2016)) and functional separation from the population? To answer this question, I analyzed the response of neurons specifically growing in the triangle and population when stimulating with the different routines (Figure 5.4). Population stimulations activate most neurons in the populations (Figure 5.4 A, gray plots; *p_long*: 0.70; *p_simul*: 0.69). Triangle stimulations activate less neurons in the population than population stimulations (Figure 5.4 A, gray plots; *t_long*: 0.50; *t_simul*: 0.44). Therefore, the difference in the overall ratio of responding neurons (Figure 5.3 F) can be attributed to this more efficient activation of population neurons by population stimulations. This indicates a functional separation of the two subpopulations (triangle and population). On the other hand, roughly the same ratio of neurons in the triangle responds to triangular (*t_long*: 0.60; *t_simul*: 0.83) and population (*p_long*: 0.50; *p_simul*: 0.33) stimulation routines (Figure 5.4 A, vi-

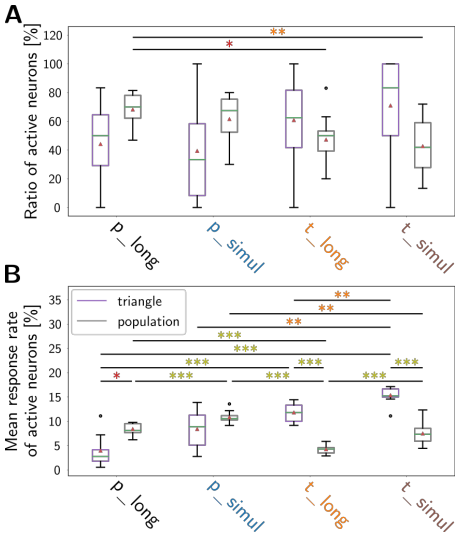

Figure 5.4 – Specific responses in triangle and population in the fComInput pattern. Neuronal response correlates with stimulus location, and the triangle shows directionality. Comparison of the fraction (or ratio) of responding neurons (**A**; normalized to the number of ROIs within the respective triangle) or the mean response rate (**B**) within the triangle (violet) and population (gray) of the fComInput networks for the different stimulation routines. The bootstrap significance test was used. Asterisks and box plots as explained in section 2.6.

olet plots). This indicates that directionality of the triangular structure towards the tip of the triangle and beyond is not preserved in fComInput patterns. One explanation for this may be that a 75% downscaled CT1 instead of an original CT1 pattern was implemented into the fComInput pattern. Downscaled CT patterns exhibit a slight loss of uni-directionality in signal propagation (see section 4.2).

However, this loss of directionality is not represented by the mean response rate of neurons (Figure 5.4 B). The triangle reacts more reliably to triangle stimulations (violet plots; *t_long*: 0.13; *t_simul*: 0.15) than to population stimulations (violet plots; *p_long*: 0.03; *p_simul*: 0.09). This indicates that connecting axons from the triangle to the population form more effective and/or numerous connections than the axons in the opposite direction. The higher response rate due to near-simultaneous stimulations occurs both in triangles and populations, recapitulating the overall rates (Figure 5.3 E). Moreover, the evidence for a functional separation of the triangle and population indicated by the fractions of responding neurons is reinforced by the mean response rate (Figure 5.4 B). This rate is increased more in the population (gray plots; *p_long*: 0.08; *p_simul*: 0.10) than in the triangle (violet plots; *p_long*: 0.03; *p_simul*: 0.09) when the population is stimulated. Also, it is higher in the triangle (violet plots; *t_long*: 0.13; *t_simul*: 0.15) than in the population (gray plots; *t_long*: 0.04; *t_simul*: 0.07) when the triangle is stimulated. This offers first, strong evidence that the two stimulation types activate different functional networks of neurons.

5.3 SNEs Are Influenced by Stimulus Location and Type

After finding that individual calcium activity was indeed changed in neurons growing in fComInput patterns upon stimulation with different routines, I investigated the effect of these stimulations on SNEs (see also section 2.5.2 and section 4.5.2). Pasquale et al. (2017) showed that evoked SNEs are similar to spontaneous ones in their intra-SNE firing pattern. Moreover, Lonardoni et al. (2017) could show in simulations that SNEs could be elicited by stimulation of functional communities in a network.

5.3.1 Synchronized Population Activity Increases SNE Rate and Decreases SNE Duration

First, I quantified the commonly determined rate, duration, mean inter-peak interval (IPI), and number of calcium peaks of minor and major SNEs (Fardet et al., 2018; Pasquale et al., 2008; Teppola et al., 2019). Minor SNEs are defined by a peak participation of 20% to 50% of neurons, major SNEs show a peak participation of more than 50% of neurons. The time between SNEs was not used as a measure because periodic stimulation leads to an artificially regular time. SNE correlograms were also not calculated due to the sparse nature of calcium events. The rate of SNEs can serve as a measure of how efficiently a certain stimulation can elicit SNEs. On the other hand, the duration, IPI and number of peaks in a SNE are measures for the coherence of the events within a SNE and of its internal structure.

The rate of major SNEs evoked by the *p_simul* stimulation routine (0.50 SNE/s) is highest. Spontaneously occurring SNEs exhibit lower rates (0.00 SNE/s, Q3: 0.00 SNE/s). Similarly low are the rates of SNEs evoked by *t_long* (0.00 SNE/s, Q3: 0.01 SNE/s) or *p_long* (0.00 SNE/s, Q3: 0.02 SNE/s) stimulation (Figure 5.5 A, right). Major SNEs induced by *t_simul* stimulation are more frequent (0.00 SNE/s, Q3: 0.44 SNE/s) than SNEs induced by *long* stimulations or spontaneously occurring ones, albeit not significantly. The rate of minor SNEs shows exactly the same behavior but even more pronounced (Figure 5.5 B, left). Thus, synchronized activity in any part of the whole network can reliably elicit SNEs. However, a more separate subpopulation (the triangle) will less efficiently induce

SNEs that span the entirety of the neuronal network.

The duration of major SNEs is only significantly reduced in SNEs evoked by *p_simul* (0.24 s) stimulation compared to spontaneous SNEs (0.46 s; Figure 5.5 B, right). A tendency toward shorter SNEs evoked by *t_simul* (0.46 s) or *t_long* (0.48 s) is also noticeable.

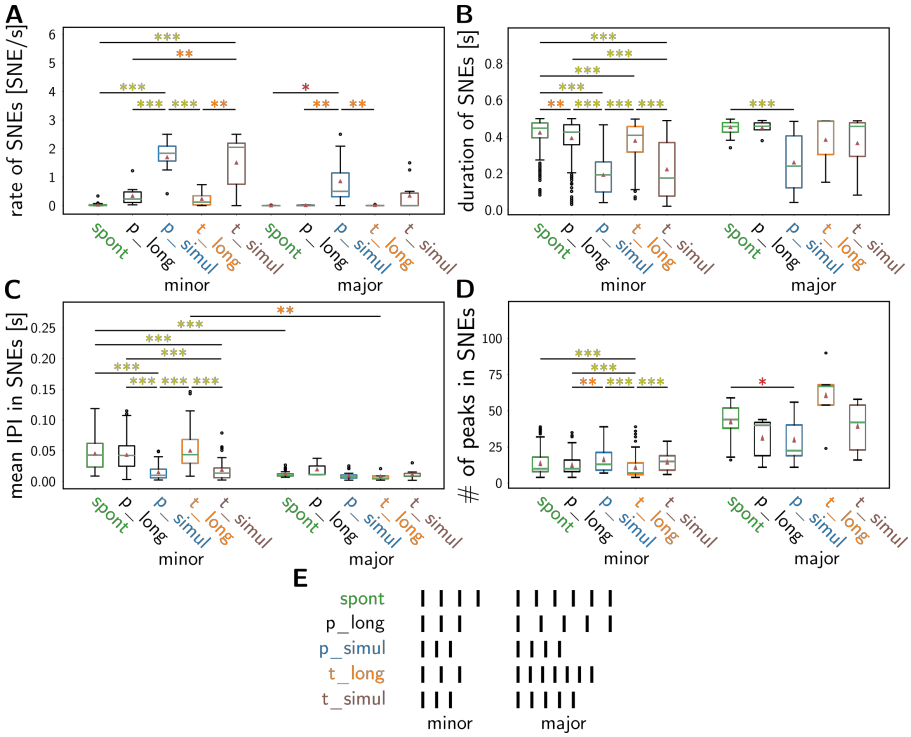

Figure 5.5 – Rate, duration, IPIs, and peak number of spontaneous and evoked SNEs. **(A-D)** Comparison of the rate (**A**), duration (**B**), inter-peak interval (IPI; **C**), and number of peaks within a SNE (**D**) of minor and major SNEs. The duration was defined as in Figure 4.7 D. The bootstrap significance test was used to compare minor/major SNEs between all conditions and the same condition between minor and major SNEs. Asterisks and box plots as explained in section 2.6. **(E)** Schematic representation of SNEs in different conditions as a summary of **B**-**C**, taking into account duration, IPIs and numbers of peaks. Each vertical bar represents a calcium peak within a SNE.

A reason for the shorter *t* stimulations might be, as for the rates (see above), the anatomical separation by the triangle tip. This might induce quicker, spatially confined SNEs in the triangle. To test whether the anatomical connection between triangle and population had an influence on the duration of *t*-induced SNEs, I measured its correlation to

the width of the triangle tip in jRCaMP1b and ChR2-GFP fluorescence images of the networks. However, the width is not correlated to the duration of SNEs in any type of stimulation (very variable, high Pearson's correlation coefficients R and insignificant differences from a regression slope of 0). Only *p_long* induces major SNEs that are similar in length (0.46 s) to spontaneous ones. As for the SNE rates, the majority of tendencies in major SNE durations are reflected in minor SNEs in a more pronounced fashion (Figure 5.5 B, left). As opposed to major SNEs, minor SNEs evoked by *p_long* stimulation are shorter (0.43 s) than spontaneous ones (0.45 s) but less so than all others. These durations are similar to the results in neuroCapTiH structures (Figure 4.17 B) in that synchronous activity induces shorter SNEs.

To gain more insights into the internal structure of a SNE, I determined the mean IPI and number of peaks in a SNE and compared them with SNE durations. In major SNEs, the IPI does not differ significantly between any conditions (Figure 5.5 C, right). However, major SNEs induced by *p_long* stimulation seem to have longer intervals between their peaks (0.012 s) than all others. Longer IPIs in combination with a similar duration suggest a reduction in the number of peaks within a SNE. Indeed, the number of peaks is (albeit non-significantly) reduced in *p_long*-induced major SNEs (40; Figure 5.5 D, right), making these SNEs more sparse than spontaneous ones (Figure 5.5 E). The mean IPI of spontaneous major SNEs (0.011 s) is followed by SNEs induced by *t_simul* (0.009 s), *p_simul* (0.008 s), and *t_long* (0.005 s). The number of peaks in major SNEs induced by *t_simul* (42) is also slightly reduced as compared to spontaneous SNEs (44). Major SNEs evoked by *p_simul* stimulation contain fewest peaks (23), explaining their short duration. Thus, the duration of these SNEs (Figure 5.5 B, right) is so strongly shortened that a lower number of peaks still leads to slightly shorter intervals between the peaks. These SNEs elicited by near-simultaneous stimulation, especially of the population, are therefore the most compressed and coherent (Figure 5.5 E). Finally, major SNEs induced by *t_long* stimulation contain slightly more peaks (67) than spontaneous major SNEs. Their duration is not as strongly reduced as the duration of SNEs evoked by *simul* stimulations. However, the increase in peaks makes these SNEs also more coherent than spontaneous major SNEs or those induced by *p_long* stimulation (Figure 5.5 E).

As for the SNE rate and duration, minor SNEs follow the behavior of major SNEs in a more pronounced fashion with some differences. Minor SNEs elicited by *simul* stimulation routines are the most compressed or coherent ones. However, minor SNEs induced by *long* stimulation routines do not show the same differences as major SNEs. Both types are just shorter than spontaneous SNEs (Figure 5.5 B, left) due to a reduced number of peaks (Figure 5.5 D and E, left). Therefore, the mean IPI is the same as in spontaneous minor SNEs.

Taken together, all stimulation routines influence SNEs to a certain degree but near-simultaneous stimulations do so more strongly. The longer duration and greater sparsity of spontaneous SNEs probably results from the slow pre-phase of the SNE (Gritsun et al., 2010). In this pre-phase, sporadic neuronal activity slowly creates a neuronal avalanche (Pasquale et al., 2008), finally leading to a full SNE. Synchronous activity of neurons more effectively induces this recruitment of a functional network, therefore limiting the SNE to its main phase. Individual activity probably only "nudges" the network into a certain direction, skipping some of the stochastic parts in the pre-phase of a SNE. The more coherent nature of (major) SNEs resulting from triangular individual activity than from population activity could be evidence for more efficient communication within the spatially confined triangle. Thus, triangularly addressed connections may be sparser but more strongly connected. These stronger connections could also lead to an increased number of peaks recruited to a SNE during synchronous activity. This would be an indication that the triangle indeed serves as a sort of functional community.

5.3.2 Intra-SNE Event Patterns Differ Between All Conditions

To investigate whether the spatiotemporal pattern of calcium events within a SNE is influenced by the location and type of stimulation, I chose to investigate the edit or Levenshtein distance between all SNEs (Figure 5.6; see also section 2.5.3). The edit distance is calculated by determining the number of operations needed to change one string of characters into another. By assigning a character to each neuron participating in a SNE (and normalizing to account for strings of variable length), the spatiotemporal pattern of these neurons can be quantified. Pasquale et al. (2017) implemented and used the ratio of SNEs with

a similar normalized edit distance (below 0.05, see section 2.5.3) to compare spontaneous with evoked SNEs. They found that evoked SNEs resulting from stimulation at different MEA electrodes are less similar to each other than SNEs evoked at the same electrode. However, SNEs elicited by different stimulations are still more similar to each other than different clusters of spontaneous SNEs. Moreover, the ratio of similar SNEs between spontaneous and evoked, clustered SNEs was higher than expected by chance.

The experiments in this thesis yielded fewer spontaneous SNEs (see previous section and section 4.5.2) than recorded in the study cited above. Moreover, only SNEs in the same network (or experiment) could be compared to each other due to the differing assignment of characters in differently grown networks. Therefore, I was not able to effectively use clustering algorithms as in the study cited above. Additionally, the activity patterns within SNEs are inherently different for calcium imaging and electrophysiology due to the sparse nature of calcium events (see also section 1.3.1). However, I did use the edit distance to compare the similarity of calcium peak patterns of all pairs of SNEs between different conditions (Figure 5.6). For this, the ratio of similar normalized edit distances (<0.05) was calculated between each condition. Then, the ratio of similar SNEs between the two conditions was compared with the combined ratios within each of the two conditions (Figure 5.7). Additionally, the mean ratio

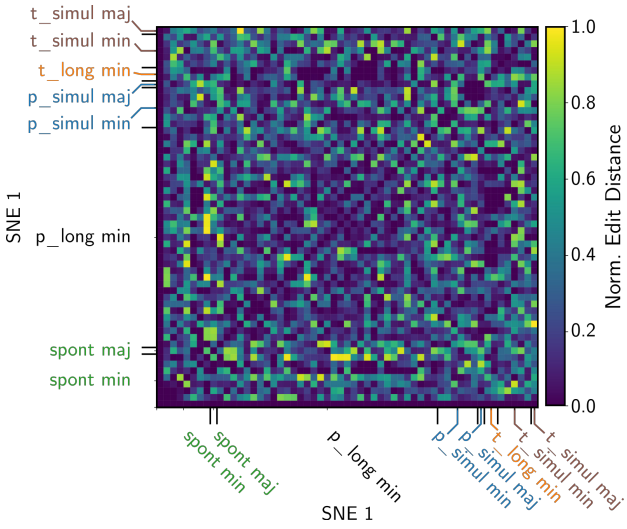

Figure 5.6 – Edit distances between each SNE in one exemplary network. The edit distance was calculated between each pair of SNEs in all conditions (indicated at the figure axes). A lower edit distance corresponds to a more similar SNE pair. The labels min and maj at each condition refer to minor and major SNEs. Color code corresponds to the normalized edit distance.

of similar SNEs was determined for SNE character sequences that were randomly shuffled 50 times.

All ratios of similar pairs do not differ from the similarity ratios of randomly shuffled sequences (compare red and violet triangles for mean values of original and shuffled data, respectively, in Figure 5.7). Because the sequence of neurons within each SNE is shuffled,

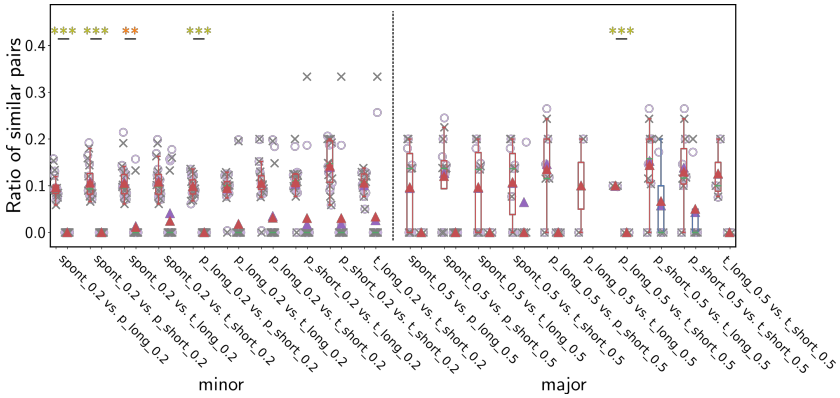

Figure 5.7 – Comparison of the ratio of SNEs with similar activity patterns. Minor, spontaneous SNEs are different from stimulations while major SNEs are mostly similar. The ratio of similar SNE pairs between two conditions (blue boxes, on the right side of each comparison) were compared with the ratio of similar SNE pairs within the two compared conditions (red boxes). Each comparison between the conditions (blue boxes) was compared to all other such comparisons within the categories of minor and major SNEs (however, here no significant differences wer found). The comparison of minor and major SNEs are separated by a dashed vertical line. Mean similarity ratios of randomly shuffled SNE sequences are plotted as light violet circles, and their mean is indicated by a violet triangle. The numbers 0.2 and 0.5 refer to the detection threshold of minor (0.2) and major (0.5) SNEs (see section 2.5.2), and the descriptor "short" is equivalent to "simul". The bootstrap significance test was used. Asterisks and box plots as explained in section 2.6.

the similarity of original and shuffled data means that the order of peaks is randomly distributed in each condition. However, the identity of the neurons within each SNE may still differ between conditions, which would indicate the activation of variable sub-populations of neurons. In major SNEs, the differences in similarity ratios between conditions and within conditions are all insignificant except from the comparison of *p_long* and *t_simul*. However, this comparison is based on very few data points, as especially *long* stimulations elicited extremely few major SNEs per investigated network. Nevertheless, the significantly lower similarity of these particular two stimulation routines may be expected as

they share neither their location nor type. This rather high similarity in major SNEs between (almost) all conditions (even between spontaneous and evoked SNEs) reinforces the results published by Pasquale et al. (2017) that stimulation evokes inherent SNEs.
On the other hand, minor spontaneous SNEs differ from most evoked SNEs except for SNEs induced by *t_simul* stimulation. This indicates that when stimulation (or sporadic spontaneous activity) fails to initiate a major SNE, the initial neurons that can trigger such an event do differ between spontaneous and evoked SNEs. Only the major event that sometimes follows the initial neuronal activation is similar. The difference between *p_simul*- and *p_long*-induced minor SNEs probably reflect highly conserved subnetworks of neurons that are activated by either simultaneous or individual activation of neurons in the population. In the triangle, there is probably more overlap due to the confined nature of this sub-population. The increase in similarity between spontaneous and *t_simul*-induced SNEs could be evidence that SNEs elicited (synchronously) in the triangle might be similar to spontaneous ones. This in turn is a hint that the triangle drives SNEs with a similar mechanism as spontaneous SNEs. A possible such mechanism would be that the original intention of a functional community within the triangle was fulfilled. Alternatively, minor SNEs induced by the *t_simul* routine could just be more similar to major SNEs than *p_simul*, as spontaneous and major SNEs are similar (see above and Pasquale et al. (2017)). This last explanation could also be valid for the increased similarity between most evoked SNEs.

5.4 Functional Network Connectivity Is Different Between Stimulations

After finding changes in SNE generation and behavior, I studied the functional connectivity of the fComInput networks (see also section 1.1.3.2). This functional connectivity can offer insights into the underlying (emergent) network properties that lead to altered SNE attributes and individual response characteristics (Shanahan, 2008; Yamamoto et al., 2018). To conduct this analysis, I used graph theoretical models whose connection strength was based on a modified generalized transfer entropy (GTE; section 2.5.5) or cross correlation (Xcor; section 2.5.4) between each pair of (normalized) mean intensity traces. With these graph models, it is possible to determine global connectivity changes during different stimulation routines (Figure 5.8). Moreover, the influence of stimulations on special neurons (such as hub, sink, or source cells) can be determined.

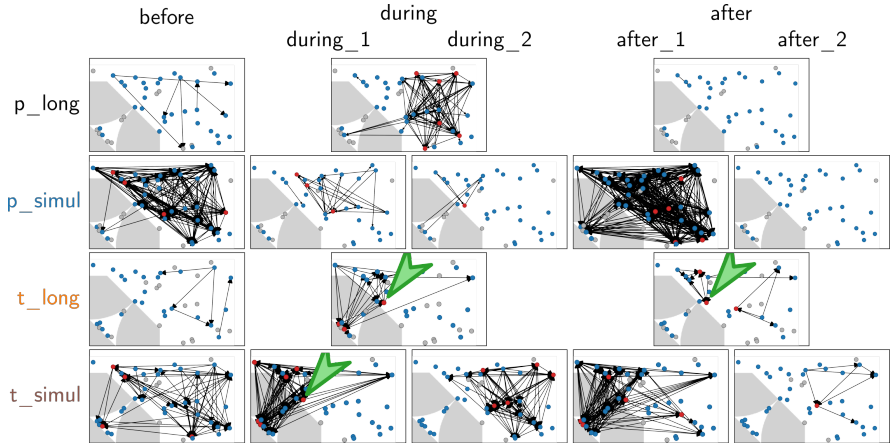

Figure 5.8 – Exemplary functional graph models derived from neuronal activity during each experimental condition and period in the same anatomical network. The models are based on modified GTE (section 2.5.5). Directionality of functional connections (or edges; black lines) is indicated by arrowheads at each line, whereas weight is not indicated for simplicity. Circles indicate the neurons (or nodes) of the network. Nodes can be either inactive (gray; representing a neuron with no calcium event in this condition) or active (blue/red). Special types of nodes can be determined in the network (section 5.4.3). Out of these, hub nodes are depicted in red as an example. Green arrowheads highlight an exemplary node that has consistent hub node characteristics in some functional networks of the displayed exemplary anatomical network.

5.4.1 Average Clustering is Altered in Functional Networks

Global connectivity measures are changed when the information processing within a network is restructured. For example, Yamamoto et al. (2018) showed that the strength of inter-modular connections within a modular network influences the global efficiency of the network (see also section 1.1.3.2). Figure 5.8 indicates that the network is in different functional states in the different experimental conditions. The most obvious difference seems to be the number of edges (black lines in Figure 5.8) and active nodes (blue and orange circles in Figure 5.8) in the networks. The relation between edges and nodes can be expressed as a measure called the density of the graph (see section 2.5.6). The graph density was calculated for each stimulation type and each time period within the stimulation experiments for both variants of graph construction (Xcor, Figure 5.9 A, and GTE, Figure 5.9 B). Although not statistically significant, functional network densities during stimulation periods tend to be higher than during control periods before or after stimulation. This is reflected in graphs derived from Xcor (Figure 5.9 A) and GTE (Figure 5.9 B). Only the stimulation period of the *t_long* routine (orange boxes in Figure 5.9 A and B) elicits a slightly different behavior.

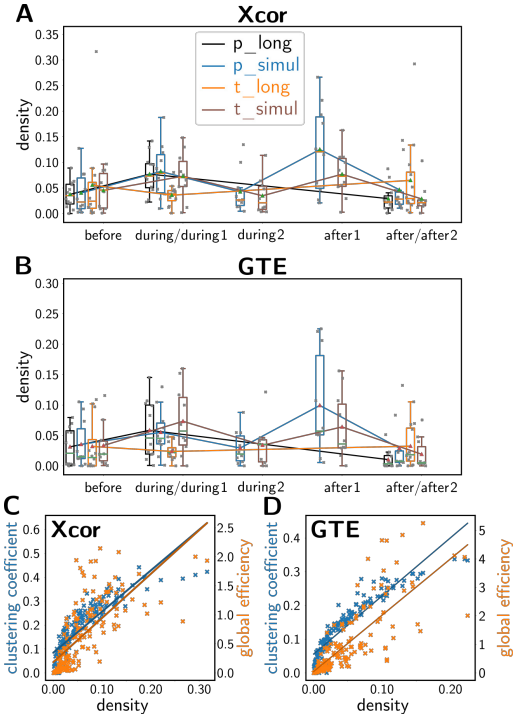

Figure 5.9 – Density of the fComInput networks and their correlations. (A-B) Density of the graphs based on Xcor (**A**) or GTE (**B**). All conditions in **A** and **B** were compared using the bootstrap method but were not significantly different. **(C-D)** The correlation of the global efficiency or clustering coefficient and the density based on Xcor (**C**; GEf: $R = 0.725$; $p = 3.58 \times 10^{-29}$; ACC: $R = 0.859$; $p = 6.36 \times 10^{-51}$) or GTE (**D**; GEf: $R = 0.789$; $p = 3.61 \times 10^{-34}$; ACC: $R = 0.923$; $p = 1.79 \times 10^{-65}$). Box plots and correlation as explained in section 2.6.

This is in line with the lower response rates of neurons in the population (Figure 5.4 B) and the whole network (Figure 5.3 E) to this routine. Thus, stimulation acutely increases communication between neurons which is reflected by an increase of functional links between neurons and leads to shorter and more coherent SNEs (see section 5.3). This communication seems to be perturbed by the anatomical separation (the triangle tip) of an input from its target population.

The general tendency in graph density could be related to the anatomical connections in the network. However, the anatomical connections in fComInput patterns are very dense so an accurate estimation of the anatomical connections is hard to achieve. Therefore, I quantified the intensity of a synaptic immunocytochemical marker (synaptotagmin) normalized to the expression of jRCaMP1b to estimate synaptic density withing the network. This normalized intensity can be compared to the graph density of the different functional networks and analyzed for correlation. However, this correlation is very low for all different stimulation types and experimental periods. When pooling all functional networks and comparing them to the respective anatomical synaptic strength, Pearson's correlation coefficient is $R = -0.13$ with $p = 0.08$ for GTE-based graphs. For Xcor-based graphs correlation is at $R = 0.06$ with $p = 0.42$.

The underlying equations of ACC (Equation 2.12) and GEf (Equation 2.11) suggest that the density of a network will influence these connectivity measures. GEf relies heavily on the shortest path length, which varies with density. ACC relies on the number of node triangles, which should also be reduced in less dense networks. Indeed, the correlation between density and ACC or GEf is very strong (Figure 5.9 C-D) for graphs based on Xcor (Figure 5.9 C) or GTE (Figure 5.9 D). Therefore, I investigated the ratio of ACC and GEf with the density instead of the raw values of ACC and GEf (Figure 5.10). Neither clustering nor efficiency of the network changes significantly during the different periods (control before, during stimulation(s), control(s) after, see Figure 2.6 B) of the experiment. However, the networks were also compared to randomly shuffled graphs with the same number, weights and directions of edges (but between different neurons). Surprisingly, some network states in fact do display significantly higher ACCs than expected from a random network. This behavior is most clearly pronounced in the networks during stimulation

(or first stimulation in case of *simul* experiments). ACCs are increased in all conditions in graphs derived from either Xcor or GTE. Interestingly, the only graph whose ACC is increased significantly in both graph types (Xcor and GTE) is the one derived from *t_long* stimulation. Amongst all other conditions, clustering is increased only in either one of the two construction methods (Xcor or GTE) but not in both of them (as for *t_long*).

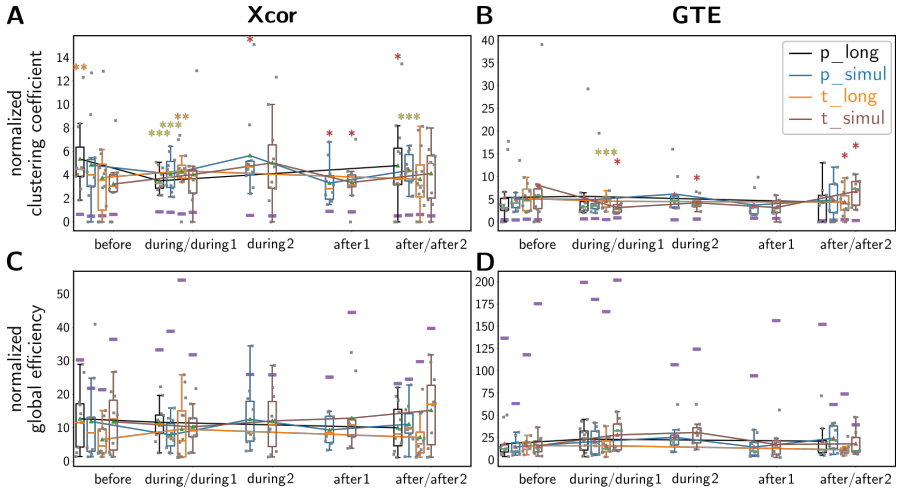

Figure 5.10 – Comparison of connectivity measures in different experimental conditions. The graph network models (for a GTE example, see Figure 5.8) were compared for their ACC (**A**-**B**) and GEf (**C**-**D**). Measures were derived from graph models based on Xcor (**A**, **C**) or GTE (**B**, **D**). The bootstrap significance test was used to compare each condition with each other condition and with a randomized network with the same number, weights, and directions of edges. Small, violet vertical bars (one for each condition) indicate the mean of the value expected for randomized networks. Asterisks and box plots as explained in section 2.6.

Apart from the period during stimulation (during/during 1), ACC seems to be increased by equal amounts in controls and stimulation conditions, with the after/after 2 control period showing even lower p-values than the second stimulation phase (after 1) of the *simul* experiments. Taken together, this suggests that neurons in general tend to form functional clusters, i.e. subpopulations or modules of neurons that interact more strongly with each other, which is consistent with previous findings (Meunier et al., 2010). During stimulation, the sub-populations activated by the stimulation seem to further increase clustering (during/during 1). This applies especially if the sub-population is segregated (t) and individual neurons activate their respective communication partners (*t_long*).

As opposed to the ACC, GEf is not significantly different from random networks in any condition although a weak trend towards a decrease can be seen. This is slightly counter-intuitive as biological networks tend to have small-world properties (Meunier et al., 2010) with high clustering and high efficiency/short paths. However, in fComInput functional networks, neurons seem to form functional clusters that do not communicate via specific projection pathways but with multiple unspecific (and inefficient) connections. Stimulation seems to increase this behavior.

5.4.2 Intra-Triangle Connectivity is Increased During Stimulation

Functional communities are defined by Lonardoni et al. (2017) as subnetworks of higher functional connectivity based on spontaneous network activity. To finally determine if the triangle in the fComInput pattern is a functional community by the aforementioned definition, I calculated the ratio of the mean functional connectivities of edges only in the triangle or the population and in the complete neuronal network (Figure A.5). In graphs based both on GTE (Figure A.5 B) and Xcor (Figure A.5 A), the ratio of the population connectivity is around 1.0. The ratio of the triangle connectivity is around 0.2 for GTE (Figure A.5 D) Xcor (Figure A.5 C). This proves that the triangle is probably not serving as a functional community by the definition of Lonardoni et al. (2017).

5.4.3 Conserved Special Neuron States Indicate Distinct Evoked Communities

Upon qualitative inspection of the functional graphs (Figure 5.8), different stimulation types seemed to activate different functional subnetworks or communities of neurons. Thus, I decided to quantify this impression of communities and further investigate the slight increase in functional clustering in stimulated networks. For this, the behavior of special nodes within the graph models (see previous section) was determined. The dual optogenetic system in combination with patterning is optimally suited for such an analysis. In this system, most neurons in the network are accessible and therefore an investigation of the role of individual neurons is possible. Such an investigation poses a serious challenge in a complex environment such as a brain slice or a living brain, and even in a more

densely growing and unpatterned neuronal cell culture (Forró et al., 2018; Okujeni and Egert, 2019; Tsai et al., 2008).

Specifically, I compared functional hub, sink, and source nodes in the different stimulations and control periods (see section 2.5.6, Figure 5.11 A-C, and Rubinov and Sporns (2010)). Hub nodes are neurons through which many computational paths lead. Therefore, they are key players in the communication of a network. Sinks integrate information of many other neurons and output the integrated signal to few other nodes (possibly of coordinating function). Sources receive only few inputs and distribute this signal to many other neurons, thereby exhibiting the ability to make decisions influencing global network activity.

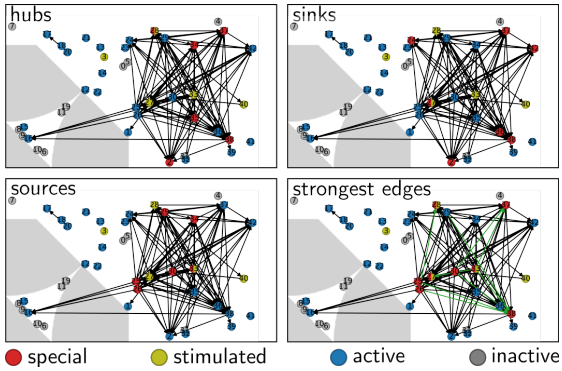

Figure 5.11 – Exemplary graph model with special nodes. Hubs, sinks, sources, and nodes connected by the strongest 0.2% of edges (marked in green in the bottom right graph) in a network model resulting from *p_long* stimulation during stimulation (see Figure 5.8). Color code is indicated at the bottom.

Hubs, sinks and sources have been pooled as "operational hubs" (Cossart, 2014) before because in most experimental systems it is impractical to further distinguish between those sub-classes. Moreover, I compared the strongest 0.5% of edge weights of the graph models and the nodes participating in these strongest connections (Figure 5.11 D). These strongest nodes probably contribute most to information processing of the network although also weak connections can serve essential computational functions (Meunier et al., 2010). All of these nodes can vary in their identity depending on the network state and the active subnetwork or community of neurons. As such variable elements, they are not to be confused with anatomical neurons. Therefore, I will refer to these special graph nodes as special neuronal or neuron states and not as neurons. For example, a neuron may occupy a "hub" state when the network is stimulated in one specific way but not occupy any special state when the network is not stimulated.

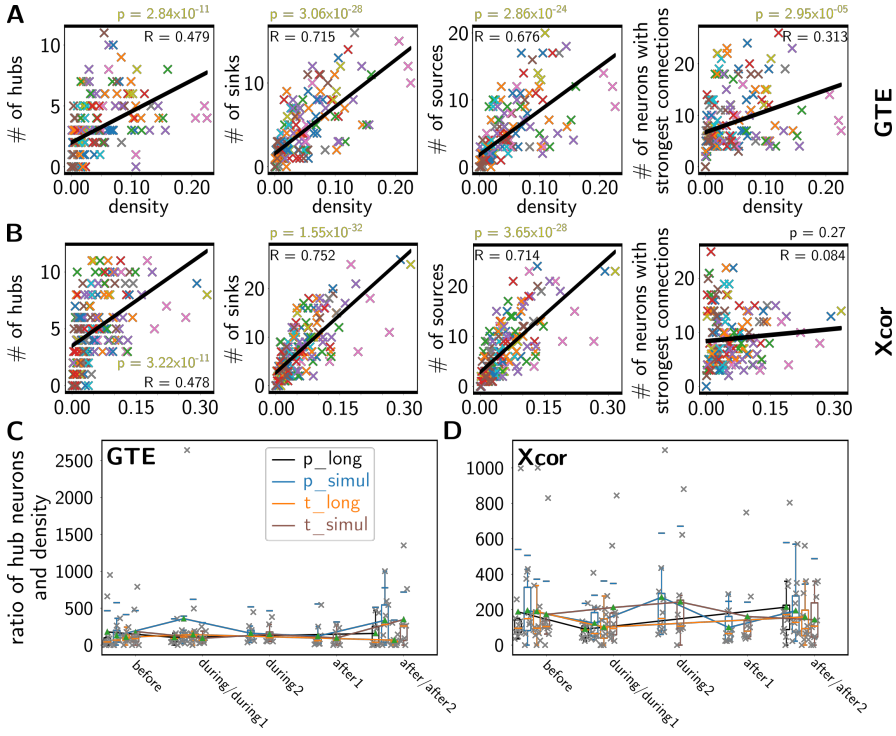

Figure 5.12 – Numbers of special neuronal states and their relation to graph density. **(A-B)** Correlation of the absolute number of special neuronal states and the graph density for GTE (**A**) or Xcor (**B**) weight estimation. The type of special neuronal state is indicated on the y-axes. Calculations of R- and p-values (see plots) are explained in section 2.6. **(C-D)** Normalized numbers of neuronal hub states in the different experimental conditions and periods. The normalized number of hub states is the ratio of absolute number and density, and is based on weights estimated with GTE (**C**) or Xcor (**D**). The label of the y-axis in **C** applies also for **D**. Different colors of data points indicate different experimental conditions. The bootstrap test did not show significant differences. Asterisks and box plots as explained in section 2.6.

5.4.3.1 The Number of Special Neuron States does not Vary

Do stimulations induce variations in the number of special neuronal states? To answer this question, I first compared the absolute numbers of neurons to the density of the graphs. Comparably to ACC and GEf, the derivation of special neuronal states suggests that it is highly dependent on the number and types of connections in the graph (e.g. for hub nodes, see Equation 2.9). Indeed, the correlation between sink and source states and the

density is very high. Neuronal hub states do not depend as strongly on the density of the underlying graph (Figure 5.12 A-B). The number of neuronal states participating in the strongest connections of a graph shows the weakest correlation to the density. This behavior is independent of the method of weight estimation, i.e. GTE (Figure 5.12 A) or Xcor (Figure 5.12 B). The absolute number of special neuronal states varies (data not explicitly shown, compare Figure 5.12 A-B). However, the ratio of these numbers and the density does not vary between conditions and is not different from the numbers of special neuronal states in randomly shuffled graphs. An exemplary comparison for neuronal hub states is shown in Figure 5.12 C and D but other special states follow similar trends (data not shown). These unaltered numbers of special states indicate that the general mechanism of information processing is similar throughout each condition. However, the identity of these key network elements might be different.

5.4.3.2 Special Neuron State Identities are Similar in Same-Location Stimulations

The neuronal networks in fComInput patterns differ between experiments. Neuronal cultures are derived from different progenitor cells and form different networks within the boundaries of the pattern. To compare the special neuron states between such completely different network architectures with each other, I determined the ratio of equal special neuronal states between experimental conditions (e.g. *p_long*-during vs. *t_long*-during). More specifically, I only compared all periods within one stimulation routine (e.g. all periods within *p_long*) and all stimulation routines during one period with each other (e.g. all "before" control periods in *p_long*, *t_long*, etc...). This ratio was calculated between the number of equal special neuronal states (interception of the sets of states) and the number of all unique special neuronal states of the compared conditions (union of sets of states). For each original graph (e.g. *p_long-during*), the same ratios were calculated for the special neuronal states of 50 randomly shuffled graphs based on the original graph (see section 2.5.6). Afterwards, the average over all 50 randomly shuffled graphs for each original graph was calculated. The large majority of these ratios is not significantly different from the random ratios (a comparison of only neuronal `hub` states derived from

GTE-based graphs as an example for all states - sinks, sources, strongest connections - is shown in Figure 5.13 A). However, the higher ratios in each distribution (the upper parts

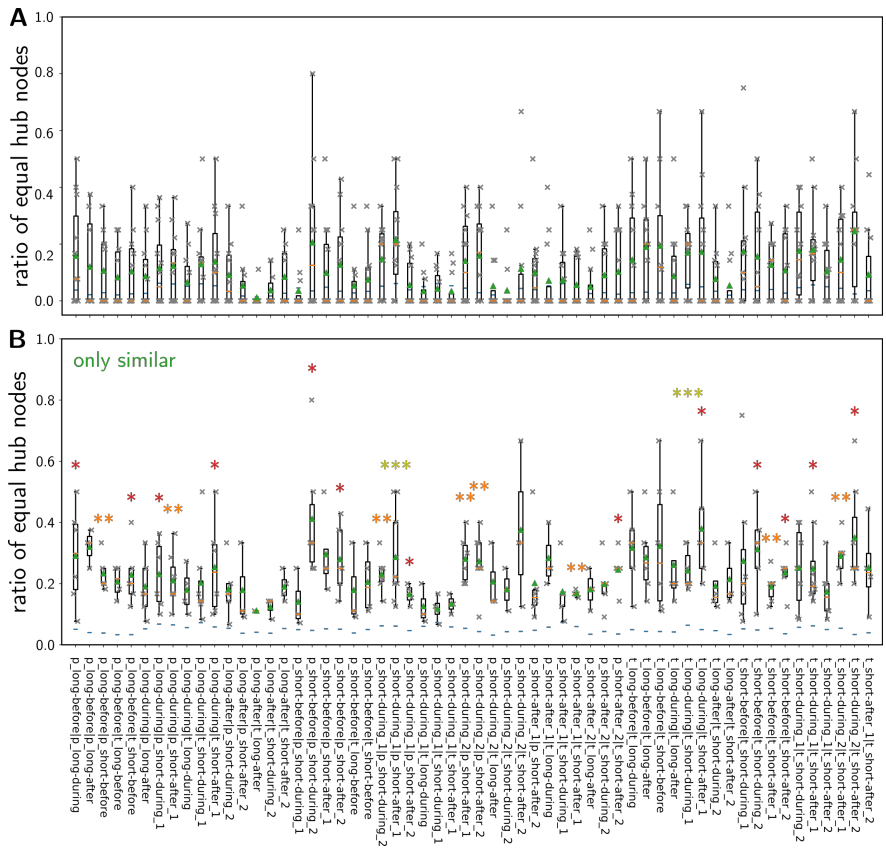

Figure 5.13 – **Ratios of equal hub nodes for GTE-based graphs.** All ratios (**A**) and only ratios > 0 (**B**). **B** therefore shows only ratios of graphs sharing at least one hub node/state. Blue horizontal lines are the mean ratios derived from 50 randomly shuffled graphs with the same number of nodes and edges and the same, but shuffled, edge weights. The x-axis labels in **B** also correspond to **A**. The bootstrap test was used to compare the ratios with the mean ratios derived from 50 randomly shuffled graphs. Asterisks and box plots as explained in section 2.6.

of the box plots) seem to differ rather strongly. Therefore, I re-analyzed the ratios only for those graphs that shared at least one respective special neuronal state (ratios > 0; Figure 5.13 B for `hub` states derived from GTE-based graphs). The ratios derived from randomly shuffled graphs were treated equally. As suspected, the ratios of similar graphs

differ more strongly (and sometimes statistically significantly) from the random ratios (Figure 5.13 B) than the ratios including completely dissimilar graphs (Figure 5.13 A).

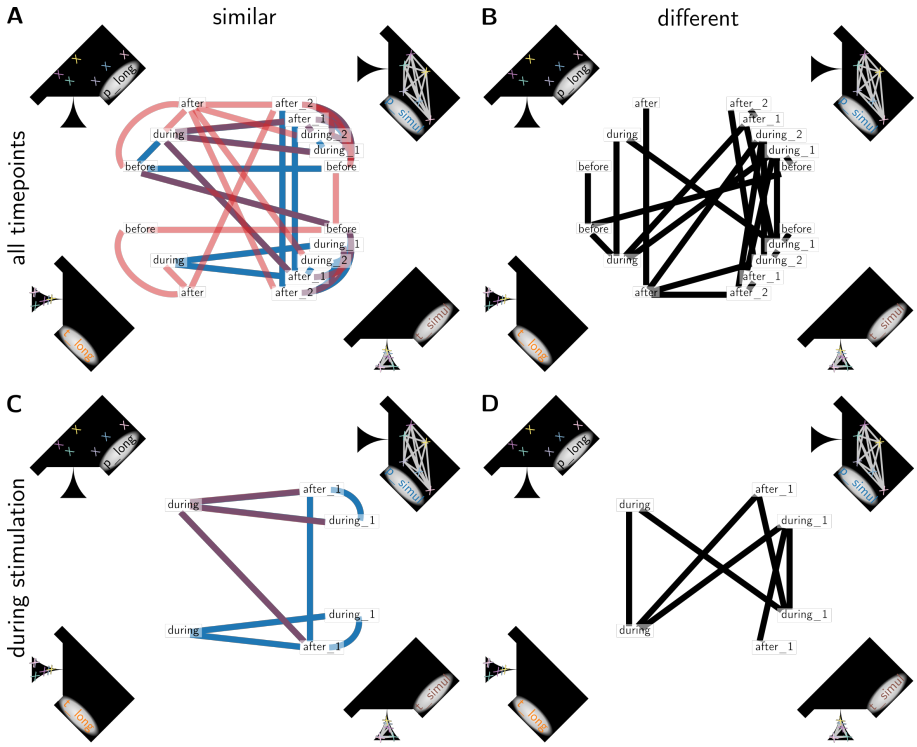

Figure 5.14 – Similarity and differences in hub nodes between different stimulation routines and periods. (A-B) Comparison of equal hub nodes all periods within one stimulation routine (lines within each of the four corners) and all stimulation routines during one period (lines between different corners). Conditions with similar hub nodes are indicated in **A** and conditions with dissimilar hubs nodes in **B**. Hub nodes were determined in graphs based on GTE (blue lines in **A**) or Xcor (red lines in **A**). Violet lines indicate similarity in both graph types. **(C-D)** The same comparison as in **A-B** but only between the actual stimulation periods ("during"). Color code in **C** as in **A**.

Thus, between all conditions that do not rely on completely different neurons to be in a special state some are more similar to each other than others - they share more equal special neuron states than others. To make the results more comprehensible, I extracted all comparisons for all special neuronal states (hubs, sinks, etc...) that showed significantly higher ratios than in random graphs. These extracted most similar conditions with respect

to neuronal hub states are connected by a line in Figure 5.14 A (blue lines: graphs based on GTE, red: Xcor, violet: both). The inverse of this extraction, i.e. graphs that are dissimilar with respect to hub states in graphs based either on GTE or on Xcor, is displayed

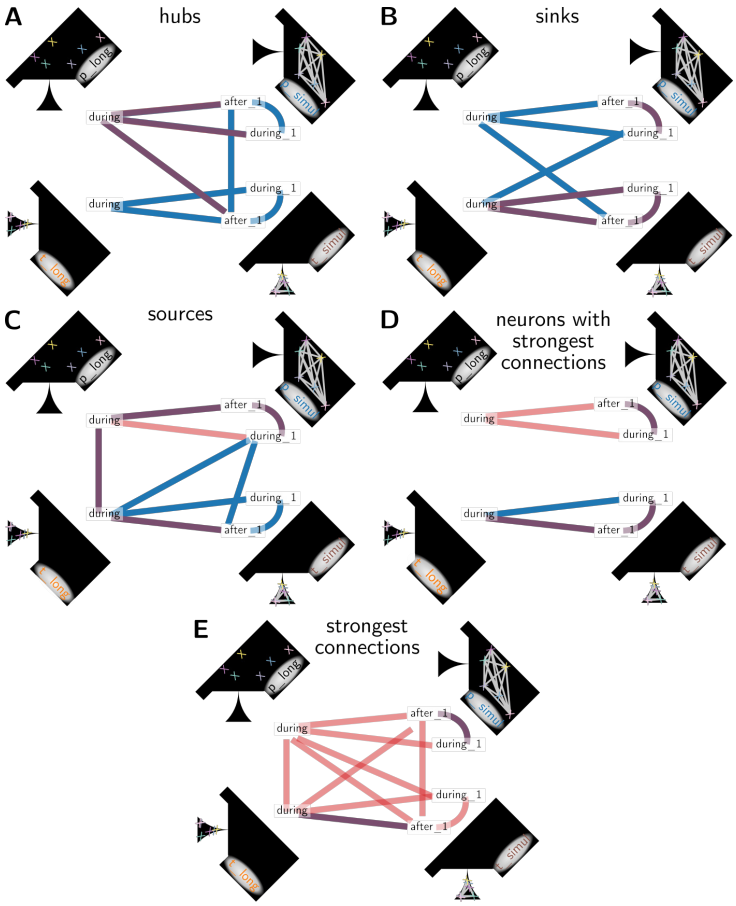

Figure 5.15 – Similarity of special nodes between different stimulation routines during actual stimulation. The same comparison shown in Figure 5.14 C for hub nodes (**A**), sink nodes (**B**), source nodes (**C**), nodes participating in the 0.5% strongest edges (**D**), and the strongest edges themselves (**E**). **A** is a duplicate of Figure 5.14 C.

in Figure 5.14 B. Most of the control periods (e.g. "before" or "after", 74%) share many hub states (Figure 5.14 A), whereas the minority of control periods shares sink states (33%), source states (37%), nodes participating in strongest edges (41%), or strongest

edges (19%; Figure A.3 B-E). A possible explanation for this discrepancy between hub and all other states is of a rather technical nature. By definition, hubs are more robust to changes in the overall network architecture as they are determined by the number of shortest paths running through these particular nodes. On the other hand, the other special nodes depend only on their direct neighbors. If individual functional connections are changed, this might therefore change the identity of sinks, sources and nodes with strongest edges more easily than that of hubs. This explanation implies that the spontaneous activity does indeed rely on conserved computational pathways (represented by the hubs) in many cases. SNEs contribute strongly to weight estimation via GTE and Xcor (see section 2.5.5 and section 2.5.4). Therefore, the variability of the networks with some stable pathways at its core could also explain why the identity of neurons is similar in about 10% of spontaneous SNEs (see Figure 5.7).

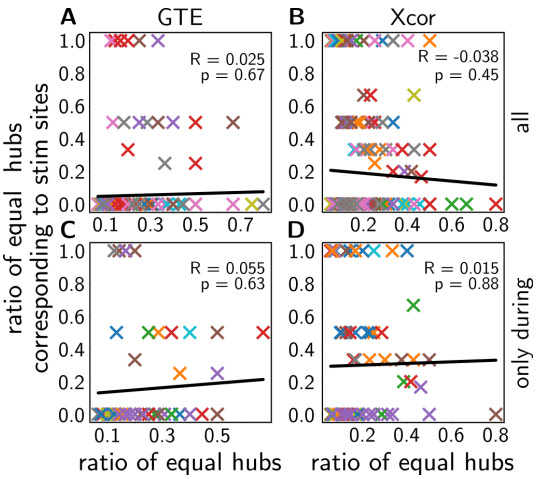

Figure 5.16 – Exemplary correlations for the ratios of equal hub nodes and the ratio of these equal hub nodes that are also stimulation sites. Ratios are plotted for all comparisons between conditions (**A**-**B**) and only periods during stimulation (**C**-**D**). Graphs were derived either based on GTE (**A**, **C**) or Xcor (**B**, **D**). Different colors of data points indicate different experimental conditions and periods. Correlation calculations are described in section 2.6.

While the control conditions seem to correspond with the edit distance, they do not offer very meaningful insights into the generation of spontaneous SNEs. Therefore, I continued by investigating the acute influence of stimulations on similarity of special neuron states. For this, I reduced the number of connections displayed in Figure 5.14 A-B to only the periods during the actual stimulation, thereby excluding the above discussed control periods (Figure 5.14 C - similar, D - dissimilar). In these simplified visualizations, a pattern is apparent: triangle stimulations induce `hub` states that are similar to the states induced by other tri-

angle stimulations (left-right connections in Figure 5.14 C). On the other hand, population stimulations induce `hub` states that are similar to the states induced by other population stimulations. However, only a few triangle stimulations induce `hub` states that are similar to population stimulations and vice versa (top-bottom connections in Figure 5.14 C). This pattern is consistent throughout all special neuron states (Figure 5.15 A-D). The consistency of this pattern contrasts the inconsistency of similar conditions in the control periods (see above), raising the pattern's significance. Special neuron states are always similar during stimulations at one location (population or triangle) at least in graphs of one estimation method. Between stimulations in different locations (top-bottom connections in Figure 5.15 A-D) similarity is different for each special neuron state type. Only the strongest edges in a network (Figure 5.15 E) seem to be similar between almost all conditions. However, even these strongest edges differ between *p_simul* and *t_simul*, and therefore different stimulation locations. Peculiarly, the ubiquitous similarity in strongest edges is only valid for graphs based on Xcor, whereas GTE-based graphs lead to almost completely opposite results (compare red and blue lines in Figure 5.15 E). An explanation for this disparity could be that Xcor might be more strongly influenced by SNEs because the large and synchronous intensity fluctuations during a SNE contribute more directly to this measure than to GTE (see section 2.5.5 and section 2.5.4). As the edit distance shows that SNEs are rather similar between different stimulation conditions, this might explain the larger similarity of special neuron states derived from Xcor-based graphs. Nevertheless, the similarity of special neuron states between stimulations at the same location seems to indicate that the stimulated neurons activate a specific sub-network.

An alternative explanation for these similar networks is that the stimulation of neurons itself induces special states within these particular neurons. Therefore, I analyzed the correlation between the ratio of equal special neuron states and the ratio of equal special neuron states that were also stimulation sites in one or the other compared condition. More specifically, the second ratio was derived between the number of equal special neuron states that were also stimulation sites and the number of equal special neuron states in total. The correlation between the two ratios is very low for all special neuron states and the slope of linear regression did in all but two cases not differ significantly from 0

Special States	Periods	Weight Estimation	R	p
Hubs	all	GTE	0.05	0.37
Hubs	all	Xcor	-0.01	0.88
Hubs	during	GTE	0.08	0.47
Hubs	during	Xcor	-0.05	0.59
Sinks	all	GTE	0.11	0.03
Sinks	all	Xcor	0.03	0.50
Sinks	during	GTE	0.11	0.22
Sinks	during	Xcor	-0.03	0.13
Sources	all	GTE	-0.06	0.24
Sources	all	Xcor	0.06	0.22
Sources	during	GTE	-0.13	0.13
Sources	during	Xcor	0.13	0.13
Strong Nodes	all	GTE	-0.11	0.02
Strong Nodes	all	Xcor	0.03	0.47
Strong Nodes	during	GTE	-0.11	0.20
Strong Nodes	during	Xcor	-0.03	0.76

Table 5.1 – All values of correlations between ratios of equal special nodes and the ratio of these equal special nodes that are also stimulation sites in Figure 5.16.

(exemplary plots for `hubs` in Figure 5.16; all values in Table 5.1). This is true for graphs derived from both weight estimation methods (compare Figure 5.16 A and C with B and D). Additionally, it is also true if comparing all conditions (Figure 5.16 A, B) and only periods during actual stimulation (Figure 5.16 C, D).

Thus, stimulation of neurons at the same location does actually seem to induce specific subnetworks. However, these subnetworks must be activated in different fashions, as the properties of SNEs (section 5.3) and individual neuronal responses (section 5.2) behave not completely according to these subnetworks. On the other hand, the triangle does not seem to behave as a functional community during periods of spontaneous activity.

5.5 Conclusions and Outlook

The fComInput pattern was designed to investigate how activity in a small segregated population (triangle) of neurons influences a larger population (population) to which the small population is connected via a directed axonal tract. More specifically, I set out to investigate the underlying network principles of SNE generation in such a segregated network. First of all, directionality seems to be preserved to a certain degree. However, it is not as apparent as for example in neuroCapTiH patterns (see section 4.5).
The individual and concerted (SNE) response of neurons suggest that population stimulation and triangle stimulation activate different subnetworks of neurons. Evidence for such separate functional (because only apparent when activated) subnetworks also comes from a high amount of shared neurons that exhibit special functions when stimulating the network at the same location. Amongst these special neuronal states, hubs are probably most preserved because they reflect stable information processing pathways in the different functional networks. Similar hub states are not only shared by functional networks created through stimulation routines at the same locations but also by a majority of unstimulated control networks. Hubs are often the connecting elements between clusters of neurons (Meunier et al., 2010). Therefore, the existence of such shared hubs might also explain increased clustering, i.e. segregated information processing, of many functional networks, including - to a lesser extent - unstimulated controls. Functional clustering seems to be highest in asynchronous stimulations of the triangle (*t_long*), which indicates that the intended functional separation of the triangle indeed seems to be achieved. The high segregation in asynchronous, triangular stimulations might also explain why communication between the neurons of the network, measured by the density, seems to be not as strongly increased for this stimulation as for other stimulation routines. However, the density in any functional state is not correlated to the synaptic density of the anatomical networks.
The functional separation of subnetworks induced by triangle and population stimulation can in turn explain other observed effects. Firstly, the rates of evoked individual and concerted (SNE) calcium events are lower for triangle stimulations. Secondly, the response of individual neurons in the population is stronger when stimulating the population than

when stimulating the triangle. Thirdly, triangle stimulations do (sometimes) not seem to activate similar neurons during SNEs. Fourthly, SNEs induced by asynchronous triangular stimulation are slightly more coherent than those induced by asynchronous population stimulation. A correlation between this coherence and the thickness of the axon bundle at the triangle tip could not be observed (as could be assumed from the relation of anatomical connection strength and dynamic neuronal richness by Yamamoto et al. (2018)). An increased coherence in combination with lower response rates indicates that fewer connections are activated more rarely. Such a diversity in neuronal activity was for example reported by Yamamoto et al. (2018). But if they are activated they very efficiently activate a (small) subnetwork that leads to a dense SNE.

Apart from the location of stimulation, synchronicity of the stimulation affects neuronal response (but not the network connectivity) even more strongly. Near-synchronous stimulation elicits more individual and concerted calcium events. SNEs elicited by such stimulations are most coherent. Therefore, directly activating multiple components of a subnetwork at almost the same time seems to increase efficiency of recruiting more neurons by introducing a certain redundancy into the activation. Probably, the pre-phase of the SNE (Gritsun et al., 2010) is skipped entirely by such a stimulation, immediately activating the main phase with the complete subnetwork participating in a SNE.

Functional communities in spontaneously active networks have been suggested as initiation regions for SNEs (Lonardoni et al., 2017). Although the system in the present thesis, is not suitable to directly confirm this theory, it adds indirect evidence and extends the theory towards stimulated events. The system is not suitable because the triangle does not act as a functional community defined by spontaneous network activity (section 5.4.2). It provides indirect evidence by a) the different characteristics of SNEs evoked by triangle stimulation (section 5.3.1), b) the segregation of neuronal responses to different stimulations (section 5.2 and section 4.5.3), and c) the slightly different functional clustering of individual triangle stimulation (section 5.4.1). Additionally, my results suggest that functional communities can be triggered by randomly selecting neurons in a network. Thus, the identity of these communities is highly dependent on the inputs certain subnetworks receive from inside a population and from other populations projecting axons into the

investigated population. Such a variable nature of modules communicating with other modules was also reported by Tsai et al. (2008). In fact, in a highly interconnected neuronal network, the anatomical connections seem to play a minor role in defining these communities although pronounced landmarks, such as the triangle tip bottleneck, have a certain influence. Although the neuronal identities in large SNEs are mainly similar (comparable to Pasquale et al. (2017)), the internal dynamics of the SNE depend on the functional community triggering the SNE, and even more strongly, the synchronicity of the activity in the triggering functional community.

In the future, the fComInput pattern can be used for further research of neuronal networks. By streamlining and simplifying the analysis pipeline, closed-loop experiments can potentially be conducted (Mosbacher et al., 2020). In this way, the simulations carried out by Lonardoni et al. (2017) (activating a spontaneously occurring functional community) can be replicated experimentally. Moreover, hub nodes or other special states can be determined in a specific stimulation or in spontaneous activity and afterwards directly stimulated to investigate their network effect. By determining special nodes like this, they can also be further examined using the patch clamp technique to determine their exact firing and subthreshold behavior (similar to Barral et al. (2019)). To gain a deeper insight into the firing pattern within SNEs induced by different stimulation routines, MEAs with improved recording or transparency can also be used (see Chapter 3). Moreover, more stimulation routines can be investigated. For example, high frequency stimulation could potentially induce neuroplastic effects that would open the field of learning and memory for this system. Additionally, different promoters for the genetically encoded calcium indicators or actuators can be used to investigate the effect of neuronal subtypes, such as GABAergic neurons on the observed network events. Furthermore, the pattern itself can be modified. Firstly, different triangle tip widths can be designed to further investigate the effect of this bottleneck. Secondly, a second or even third triangle can be introduced to investigate the effect of the combined input of multiple subnetworks into a large population. Thus, further continuing the work in the described system or its modifications can help to further understand how neuronal networks generate emergent properties used for higher information processing from individual neuronal activity.

Conclusions

The research of neuronal networks can help to uncover the basic mechanisms underlying brain function, discover therapeutic approaches, and improve deep learning algorithms. Amongst such basic mechanisms of neuronal networks are synchronous network events and directional signal propagation, which I examined in patterned neuronal cell cultures using optogenetics. For an improved investigation of such principles, I also refined and/or optimized different *in vitro* techniques - patterned neuronal networks, MEAs, and optogenetics - used for controlling the behavior of neuronal cell cultures.

Although microcontact printing is a well-established technique for patterning neuronal cultures, its pattern-to-background contrast had to be optimized by introducing GLYMO to chemically uncouple the substrate from the patterned coating. Ideally, such reliably well-defined patterns would be investigated with a combined approach using microelectrode arrays as an electrophysiological technique and optogenetic calcium imaging and/or stimulation. However, the population patterns used in this thesis were not suitable for simple microelectrode array recordings. Even improving the adhesive properties of gold electrodes via aminothiols did not result in more reliable recordings. On the other hand, I could use holey gold as a transparent electrode material with plasmonic properties in cellular recordings. Holey gold's plasmonically enhanced transparency is even tunable by varying the nanohole parameters and could be used as an optical filtering mechanism for microscopic and optogenetic techniques. Moreover, I could successfully record from population patterns on ONONO-passivated standard nanocavity microelectrode arrays with reduced autofluorescence. Finally, I could establish a dual optogenetic system for monitoring and stimulating a very large fraction of the neurons in a patterned network on the GLYMO-treated glass.

Using some standard techniques such as patch clamp and some of the above described improved methodologies, I could set out to investigate network function. For examining

action potential propagation in a modular network, I used the downscaled CT1 pattern as chains of triangles and the neuroCapTiH pattern as a loop of such triangles. Smaller versions of the CT1 pattern do not seem to share the original CT1's preference for a directional action potential propagation towards the tip of the triangle, probably because of their more linear design. However, in neuroCapTiH patterns action potentials propagate almost through the entire loop with a strong preference towards the triangle tip and independent of triangle curvature. By reducing the number of triangles in the loop, the transformation of an evoked action potential passing through multiple neurons could be investigated in the future by monitoring and stimulating individual neurons in the loop. Additionally, neuroCapTiH patterns provided evidence that the CT1 triangles serve as functional communities with a strong intra-triangular response to stimulation.

To further investigate such functional communities, I designed the fComInput pattern, in which a downscaled CT1 triangle is placed upstream of a larger population of neurons. Both in neuroCapTiH and fComInput experiments I found evidence that more synchronized neuronal activity leads to more coherent and numerous synchronous network events than individual, asynchronous activity. On the other hand, these synchronous events cannot only be generated by the triangle but also, and even more efficiently, by the population. This could indicate that triangles do not serve as spontaneous functional communities, or that other functional communities exist in the population that more efficiently generate network events. On the other hand, the ability to generate network events and the conservation of special network nodes when stimulating either of the two randomly chosen sets of neurons suggests that functional communities can actually be generated when a (sub)network receives stimuli. These stimuli could be either generated within the network, e.g. by neuromodulatory events, or without the network, e.g. via projections from another region.

"How do we think?" Of course I cannot answer this question in this thesis. However, I could develop or improve a set of methods for investigation of *in vitro* networks. Moreover, I could use these methods to uncover some of the principles governing synchronous network events and directional action potential propagation, basic processes involved in higher brain function.

References

Aebersold, M. J., Dermutz, H., Forró, C., Weydert, S., Thompson-Steckel, G., Vörös, J., and Demkó, L. (2016). **"Brains on a chip": Towards engineered neural networks**. TrAC - Trends Anal. Chem., *78:*, 60–69, doi: 10.1016/j.trac.2016.01.025.

Ahn, Y., Lee, H., Lee, D., and Lee, Y. (2014). **Highly conductive and flexible silver nanowire-based microelectrodes on biocompatible hydrogel**. ACS Appl. Mater. Interfaces, *6:* 18401–18407, doi: 10.1021/am504462f.

Akerboom, J., Carreras Calderón, N., Tian, L., Wabnig, S., Prigge, M., Tolö, J., Gordus, A., Orger, M. B., Severi, K. E., Macklin, J. J., Patel, R., Pulver, S. R., Wardill, T. J., Fischer, E., Schüler, C., Chen, T.-W., Sarkisyan, K. S., Marvin, J. S., Bargmann, C. I., Kim, D. S., Kügler, S., Lagnado, L., Hegemann, P., Gottschalk, A., Schreiter, E. R., and Looger, L. L. (2013). **Genetically encoded calcium indicators for multi-color neural activity imaging and combination with optogenetics.** Front. Mol. Neurosci., *6:*, doi: 10.3389/fnmol.2013.00002.

Albers, J. *Entwicklung axonaler Dioden zur Untersuchung des gerichteten Informationsflusses in neuronalen Strukturen.* Phd, RWTH Aachen, (2016).

Albers, J. and Offenhäusser, A. (2016). **Signal Propagation between Neuronal Populations Controlled by Micropatterning**. Front. Bioeng. Biotechnol., *4:*, doi: 10.3389/fbioe.2016.00046.

Albers, J., Toma, K., and Offenhäusser, A. (2015). **Engineering connectivity by multiscale micropatterning of individual populations of neurons**. Biotechnol. J., *10:* 332–338, doi: 10.1002/biot.201400609.

Ali, F. and Kwan, A. C. (2019). **Interpreting in vivo calcium signals from neuronal cell bodies, axons, and dendrites: a review**. *7:*, doi: 10.1117/1.nph.7.1.011402.

Augustine, G. J., Santamaria, F., and Tanaka, K. (2003). **Local Calcium Signaling in Neurons**. Neuron, *40:* 331–346, doi: 10.1016/S0896-6273(03)00639-1.

Bacakova, L., Filova, E., Parizek, M., Ruml, T., and Svorcik, V. (2011). **Modulation of cell adhesion, proliferation and differentiation on materials designed for body implants**. Biotechnol. Adv., *29:*, 739–767, doi: 10.1016/j.biotechadv.2011.06.004.

Bakkum, D. J., Frey, U., Radivojevic, M., Russell, T. L., Müller, J., Fiscella, M., Takahashi, H., and Hierlemann, A. (2013). **Tracking axonal action potential propagation on a high-density microelectrode array across hundreds of sites**. *4:*, doi: 10.1038/ncomms3181.

Barral, J., Wang, X.-J., and Reyes, A. D. (2019). **Propagation of temporal and rate signals in cultured multilayer networks**. *10:*, doi: 10.1038/s41467-019-11851-0.

Bauermeister, C., Keren, H., and Braun, J. (2020). **Unstructured network topology begets order-based representation by privileged neurons**. Biol. Cybern., *114:*, 113–135, doi: 10.1007/s00422-020-00819-9.

Bazargani, N. and Attwell, D. (2016). **Astrocyte calcium signaling: the third wave**. Nat. Neurosci., *19:*, 182–189, doi: 10.1038/nn.4201.

Bear, M. F., Connors, B. W., and Paradiso, M. A. (2007)a. **Synaptic Transmission**. In: Neurosci. - Explor. Brain. Editors Lupash, E., Connolly, E., Dilernia, B., and Williams, P. C., third edition, Lippincott Williams & Wilkins, Philadelphia (PA), Chapter 5, p. 102 ff. ISBN 0-7817-6003-8.

Bear, M. F., Connors, B. W., and Paradiso, M. A. (2007)b. **Phototransduction**. In: Neurosci. - Explor. Brain. Editors Lupash, E., Connolly, E., Dilernia, B., and Williams, P., third edition, Lippincott Williams & Wilkins, Philadelphia (PA), Chapter 9, p. 292 ff. ISBN 0-7817-6003-8.

Bear, M. F., Connors, B. W., and Paradiso, M. A. (2007)c. **The Neuronal Membrane at Rest**. In: Neurosci. - Explor. Brain. Editors Lupash, E., Connolly, E., Dilernia, B., and Williams, P., third edition, Lippincott Williams & Wilkins, Philadelphia (PA), Chapter 3, p. 51 ff. ISBN 0-7817-6003-8.

Bear, M. F., Connors, B. W., and Paradiso, M. A. (2007)d. **The Action Potential**. In: Neurosci. - Explor. Brain. Editors Lupash, E., Connolly, E., Dilernia, B., and Williams, P., third edition, Lippincott Williams & Wilkins, Philadelphia (PA), Chapter 4, p. 75 ff. ISBN 0-7817-6003-8.

Bear, M. F., Connors, B. W., and Paradiso, M. A. (2007)e. **Neuroscience: Past, Present, and Future**. In: Neurosci. - Explor. Brain. Editors Lupash, E., Connolly, E., Dilernia, B., and Williams, P., third edition, Lippincott Williams & Wilkins, Philadelphia (PA), Chapter 1, p. 3 ff. ISBN 0-7817-6003-8.

Benjamin Kacerovsky, J. and Murai, K. K. (2016). **Stargazing: Monitoring subcellular dynamics of brain astrocytes.** Neuroscience, *323:*, 84–95, doi: 10.1016/j.neuroscience.2015.07.007.

Biffi, E., Regalia, G., Menegon, A., Ferrigno, G., and Pedrocchi, A. (2013). **The influence of neuronal density and maturation on network activity of hippocampal cell cultures: A methodological study**. *8:*, doi: 10.1371/journal.pone.0083899.

Blau, A., Ziegler, C., Heyer, M., Endres, F., Schwitzgebel, G., Matthies, T., Stieglitz, T., Meyer, J. U., and Göpel, W. (1997). **Characterization and optimization of microelectrode arrays for in vivo nerve signal recording and stimulation**. Biosens. Bioelectron., *12:* 883–892, doi: 10.1016/S0956-5663(97)00017-1.

Bonifazi, P. and Massobrio, P. (2019). **Reconstruction of Functional Connectivity from Multielectrode Recordings and Calcium Imaging.**. In: Vitr. Neuronal Networks. (Advances Neurobiol. vol. 22). Editors Chiappalone, M., Pasquale, V., and Frega, M., 1 edition, Springer, Cham.

Boyden, E. S., Zhang, F., Bamberg, E., Nagel, G., and Deisseroth, K. (2005). **Millisecond-timescale, genetically targeted optical control of neural activity**. Nat. Neurosci., *8:* 1263–1268, doi: 10.1038/nn1525.

Branch, D. W., Corey, J. M., Weyhenmeyer, J. A., Brewer, G. J., and Wheeler, B. C. (1998). **Microstamp patterns of biomolecules for high-resolution neuronal networks**. Med. Biol. Eng. Comput., *36:*, 135–141.

Brewer, G. J., Torricelli, J. R., Eve, E. K., and Price, P. J. (1993). **Optimized Survival of Hippocampal Neurons in B27-Supplemented Neurobasal, a New Serum-free Medium Combination**. J. Neurosci. Res., *35:*, 567–576.

Burchert, C. and Schneider, M. (2016).

Buzsáki, G. (2015). **Hippocampal sharp wave-ripple: A cognitive biomarker for episodic memory and planning**. Hippocampus, *25:*, 1073–1188, doi: 10.1002/hipo.22488.

Cantu, D. A., Wang, B., Gongwer, M. W., He, C. X., Goel, A., Suresh, A., Kourdougli, N., Arroyo, E. D., Zeiger, W., and Portera-Cailliau, C. (2020). **EZcalcium: Open-Source Toolbox for Analysis of Calcium Imaging Data**. Front. Neural Circuits, *14:*, doi: 10.3389/fncir.2020.00025.

Cao, W., Li, J., Chen, H., and Xue, J. (2014). **Transparent electrodes for organic optoelectronic devices: a review**. *4:*, doi: 10.1117/1.jpe.4.040990.

Capogna, M. and Pearce, R. A. (2011). **GABAA,slow: Causes and consequences**. Trends Neurosci., *34:* 101–112, doi: 10.1016/j.tins.2010.10.005.

Chang, J. C., Brewer, G. J., and Wheeler, B. C. (2001). **Modulation of neural network activity by patterning**. Biosens. Bioelectron., *16:*, 527–533, doi: 10.1016/S0956-5663(01)00166-X.

Charrier, A., Martinez, D., Monette, R., Comas, T., Movileanu, R., Py, C., Denhoff, M., Krantis, A., and Mealing, G. (2010). **Cell placement and guidance on substrates for neurochip interfaces**. Biotechnol. Bioeng., *105:* 368–373, doi: 10.1002/bit.22539.

Chen, H.-C. I., Wolf, J., and Smith, D. (2017). **Multichannel activity propagation across an engineered axon network**. *14:*, doi: 10.1088/1741-2552/aa5ccd.

Chen, T.-W., Wardill, T. J., Sun, Y., Pulver, S. R., Renninger, S. L., Baohan, A., Schreiter, E. R., Kerr, R. a., Orger, M. B., Jayaraman, V., Looger, L. L., Svoboda, K., and Kim, D. S. (2013). **Ultrasensitive fluorescent proteins for imaging neuronal activity.** Nature, *499:*, 295–300, doi: 10.1038/nature12354.

Chiu, C. and Weliky, M. (2001). **Spontaneous activity in developing ferret visual cortex in vivo**. J. Neurosci., *21:* 8906–8914, doi: 10.1523/jneurosci.21-22-08906.2001.

Claycomb, W. C., Lanson, N. A., Stallworth, B. S., Egeland, D. B., Delcarpio, J. B., Bahinski, A., and Izzo, N. J. (1998). **HL-1 cells: A cardiac muscle cell line that contracts and retains phenotypic characteristics of the adult cardiomyocyte**. Proc. Natl. Acad. Sci., *95:*, 2979–2984, doi: 10.1073/pnas.95.6.2979.

Cossart, R. (2014). **Operational hub cells: A morpho-physiologically diverse class of GABAergic neurons united by a common function**. Curr. Opin. Neurobiol., *26:*, 51–56, doi: 10.1016/j.conb.2013.12.002.

Dana, H., Mohar, B., Sun, Y., Narayan, S., Gordus, A., Hasseman, J. P., Tsegaye, G., Holt, G. T., Hu, A., Walpita, D., Patel, R., Macklin, J. J., Bargmann, C. I., Ahrens, M. B., Schreiter, E. R., Jayaraman, V., Looger, L. L., Svoboda, K., and Kim, D. S. (2016). **Sensitive red protein calcium indicators for imaging neural activity**. *5:*, doi: 10.7554/eLife.12727.

Dana, H., Sun, Y., Mohar, B., Hulse, B. K., Kerlin, A. M., Hasseman, J. P., Tsegaye, G., Tsang, A., Wong, A., Patel, R., Macklin, J. J., Chen, Y., Konnerth, A., Jayaraman, V., Looger, L. L., Schreiter, E. R., Svoboda, K., and Kim, D. S. (2019). **High-performance calcium sensors for imaging activity in neuronal populations and microcompartments**. Nat. Methods, *16:*, 649–657, doi: 10.1038/s41592-019-0435-6.

Dayan, P. and Abbott, L. (2001)a. **Spike Trains and Firing Rates**. . In: Theor. Neurosci., 1st edition, The MIT Press, Cambridge (MA), Chapter 1.2, p. 13 ff. ISBN 0-262-04199-5.

Dayan, P. and Abbott, L. (2001)b. **The Hodgkin-Huxley Model**. . In: Theor. Neurosci., 1st edition, The MIT Press, Cambridge (MA), Chapter 5.6, p. 173 ff. ISBN 0-262-04199-5.

de Winter, J. C. (2013). **Using the student's t-test with extremely small sample sizes**. Pract. Assessment, Res. Eval., *18:*.

Deisseroth, K. (2015). **Optogenetics: 10 years of microbial opsins in neuroscience**. Nat. Neurosci., *18:* 1213–1225, doi: 10.1038/nn.4091.

Deisseroth, K. and Hegemann, P. (2017). **The form and function of channelrhodopsin**. *357:*, doi: 10.1126/science.aan5544.

DeMarse, T. B., Pan, L., Alagapan, S., Brewer, G. J., and Wheeler, B. C. (2016). **Feed-forward propagation of temporal and rate information between cortical populations during coherent activation in engineered in vitro networks**. Front. Neural Circuits, *10:*, doi: 10.3389/fncir.2016.00032.

Dent, E. W., Gupton, S. L., and Gertler, F. B. (2011). **The Growth Cone Cytoskeleton in Axon Outgrowth and Guidance**. *3:*, doi: 10.1101/cshperspect.a001800.

Denyer, M. C. T., Riehle, M., Britland, S. T., and Offenhauser, A. (1998). **Preliminary study on the suitability of a pharmacological bio-assay based on cardiac myocytes cultured over microfabricated microelectrode arrays**. Med. Biol. Eng. Comput., *36:*, 638–644, doi: 10.1007/BF02524437.

Deußen, O. Surface Engeneering of Glass Surfaces for Optimization of Neuron Growth Directing by Micro Contact Printing. Technical report, RWTH Aachen, Faculty 1, Jülich, (2019).

Diego, F., Reichinnek, S., Both, M., and Hamprecht, F. A. Automated identification of neuronal activity from calcium imaging by sparse dictionary learning. . In: 2013 IEEE 10th Int. Symp. Biomed. Imaging 1058–1061. IEEE, (2013). ISBN 978-1-4673-6455-3, doi: 10.1109/ISBI.2013.6556660http://ieeexplore.ieee.org/document/6556660/.

Dranias, M. R., Ju, H., Rajaram, E., and VanDongen, A. M. J. (2013). **Short-Term Memory in Networks of Dissociated Cortical Neurons**. J. Neurosci., *33:* 1940–1953, doi: 10.1523/JNEUROSCI.2718-12.2013.

Dwivedi, A. K., Mallawaarachchi, I., and Alvarado, L. A. (2017). **Analysis of small sample size studies using nonparametric bootstrap test with pooled resampling method**. Stat. Med., *36:* 2187–2205, doi: 10.1002/sim.7263.

Ecken, H., Ingebrandt, S., Krause, M., Richter, D., Hara, M., and Offenhäusser, A. (2003). **64-Channel Extended Gate Electrode Arrays for Extracellular Signal Recording**. Electrochim. Acta, *48:*, 3355–3362, doi: 10.1016/S0013-4686(03)00405-5.

Egorov, A. V. and Draguhn, A. (2013). **Development of coherent neuronal activity patterns in mammalian cortical networks: Common principles and local hetereogeneity**. Mech. Dev., *130:*, 412–423, doi: 10.1016/j.mod.2012.09.006.

Eichler, M., Dahlhaus, R., and Sandkühler, J. (2003). **Partial correlation analysis for the identification of synaptic connections**. Biol. Cybern., *89:*, 289–302, doi: 10.1007/s00422-003-0400-3.

Eick, S., Wallys, J., Hofmann, B., van Ooyen, A., Schnakenberg, U., Ingebrandt, S., and Offenhäusser, A. (2009). **Iridium oxide microelectrode arrays for in vitro stimulation of individual rat neurons from dissociated cultures.** Front. Neuroeng., *2:*, doi: 10.3389/neuro.16.016.2009.

Emiliani, V., Cohen, A. E., Deisseroth, K., and Häusser, M. (2015). **All-Optical Interrogation of Neural Circuits**. J. Neurosci., *35:* 13917–13926, doi: 10.1523/JNEUROSCI.2916-15.2015.

Escobedo, C. (2013). **On-chip nanohole array based sensing: A review**. Lab Chip, *13:*, 2445–2463, doi: 10.1039/c3lc50107h.

Fagiolo, G. (2007). **Clustering in complex directed networks**. *76:*, doi: 10.1103/PhysRevE.76.026107.

Faid, K., Voicu, R., Bani-Yaghoub, M., Tremblay, R., Mealing, G., Py, C., and Barjovanu, R. (2005). **Rapid fabrication and chemical patterning of polymer microstructures and their applications as a platform for cell cultures**. Biomed. Microdevices, *7:* 179–184, doi: 10.1007/s10544-005-3023-8.

Fardet, T., Ballandras, M., Bottani, S., Métens, S., and Monceau, P. (2018). **Understanding the generation of network bursts by adaptive oscillatory neurons**. Front. Neurosci., *12:*, doi: 10.3389/fnins.2018.00041.

Feinerman, O., Segal, M., and Moses, E. (2005). **Signal Propagation Along Unidimensional Neuronal Networks**. J. Neurophysiol., *94:*, 3406–3416, doi: 10.1152/jn.00264.2005.

Feinerman, O., Rotem, A., and Moses, E. (2008). **Reliable neuronal logic devices from patterned hippocampal cultures**. Nat. Phys., *4:*, 967–973, doi: 10.1038/nphys1099.

Feldt, S., Bonifazi, P., and Cossart, R. (2011). **Dissecting functional connectivity of neuronal microcircuits: Experimental and theoretical insights**. Trends Neurosci., *34:* 225–236, doi: 10.1016/j.tins.2011.02.007.

FitzGerald, J. J., Lacour, S. P., McMahon, S. B., and Fawcett, J. W. (2008). **Microchannels as axonal amplifiers**. IEEE Trans. Biomed. Eng., *55:* 1136–1146, doi: 10.1109/TBME.2007.909533.

Forró, C., Thompson-Steckel, G., Weaver, S., Weydert, S., Ihle, S., Dermutz, H., Aebersold, M. J., Pilz, R., Demkó, L., and Vörös, J. (2018). **Modular microstruture design to build neuronal networks of defined functional connectivity**. Biosens. Bioelectron., *122:*, 75–87, doi: 10.1016/j.bios.2018.08.075.

Fricke, R., Zentis, P. D., Rajappa, L. T., Hofmann, B., Banzet, M., Offenhäusser, A., and Meffert, S. H. (2011). **Axon guidance of rat cortical neurons by microcontact printed gradients**. Biomaterials, *32:*, 2070–2076, doi: 10.1016/j.biomaterials.2010.11.036.

Friedrich, J., Yhou, P., and Paninski, L. (2017). **Fast online deconvolution of calcium imaging data**. PLoS Comput. Biol., *13:* e1005423, doi: 10.1371/journal.pcbi.1005423.

Fries, P. (2015). **Rhythms for Cognition: Communication through Coherence**. Neuron, *88:*, 220–235, doi: 10.1016/j.neuron.2015.09.034.

Fukata, Y., Kimura, T., and Kaibuchi, K. (2002). **Axon specification in hippocampal neurons**. Neurosci. Res., *43:*, 305–315, doi: 10.1016/S0168-0102(02)00062-7.

Gal, E., London, M., Globerson, A., Ramaswamy, S., Reimann, M. W., Muller, E., Markram, H., and Segev, I. (2017). **Rich cell-type-specific network topology in neocortical microcircuitry**. Nat. Neurosci., *20:* 1004–1013, doi: 10.1038/nn.4576.

Gallo, G. and Letourneau, P. C. (2004). **Regulation of growth cone actin filaments by guidance cues**. J. Neurobiol., *58:* 92–102, doi: 10.1002/neu.10282.

Ghirga, S., Pagani, F., Rosito, M., Di Angelantonio, S., Ruocco, G., and Leonetti, M. (2020). **Optonongenetic enhancement of activity in primary cortical neurons**. J. Opt. Soc. Am. A, *37:* 643–652, doi: 10.1364/JOSAA.385832.

GhoshMoulick, R., Vu, X. T., Gilles, S., Mayer, D., Offenhäusser, A., and Ingebrandt, S. (2009). **Impedimetric detection of covalently attached biomolecules on field-effect transistors**. Phys. Status Solidi Appl. Mater. Sci., *206:* 417–425, doi: 10.1002/pssa.200880482.

Gilles, S., Winter, S., Michael, K. E., Meffert, S. H., Li, P., Greben, K., Simon, U., Offenhäusser, A., and Mayer, D. (2012). **Control of Cell Adhesion and Neurite Outgrowth by Patterned Gold Nanoparticles with Tunable Attractive or Repulsive Surface Properties**. Small, *8:* 3357–3367, doi: 10.1002/smll.201200465.

Giovannucci, A., Friedrich, J., Gunn, P., Kalfon, J., Brown, B. L., Koay, S. A., Taxidis, J., Najafi, F., Gauthier, J. L., Zhou, P., Khakh, B. S., Tank, D. W., Chklovskii, D. B., and Pnevmatikakis, E. A. (2019). **CaImAn an open source tool for scalable calcium imaging data analysis**. *8:*, doi: 10.7554/eLife.38173.

Neuroscience in Ancient Egypt. https://blogs.ucl.ac.uk/researchers-in-museums/2018/02/21/neuroscience-in-ancient-egypt/comment-page-1/. (accessed 2020-06-26).

Grannemann, C. *Micropatterning techniques for electrical and optogenetic investigation of induced activity in designed neuronal populations.* Msc, RWTH Aachen, (2019).

Grienberger, C. and Konnerth, A. (2012). **Imaging Calcium in Neurons**. Neuron, *73:*, 862–885, doi: 10.1016/j.neuron.2012.02.011.

Gritsun, T. A., Le Feber, J., Stegenga, J., and Rutten, W. L. C. (2010). **Network bursts in cortical cultures are best simulated using pacemaker neurons and adaptive synapses**. Biol. Cybern., *102:*, 293–310, doi: 10.1007/s00422-010-0366-x.

Gross, G. W., Wen, W. Y., and Lin, J. W. (1985). **Transparent indium-tin oxide electrode patterns for extracellular, multisite recording in neuronal cultures**. J. Neurosci. Methods, *15:*, 243–252, doi: 10.1016/0165-0270(85)90105-0.

Guru, A., Post, R. J., Ho, Y. Y., and Warden, M. R. (2015). **Making sense of optogenetics**. *18:*, doi: 10.1093/ijnp/pyv079.

Haq, F., Anandan, V., Keith, C., and Zhang, G. (2007). **Neurite development in PC12 cells cultured on nanopillars and nanopores with sizes comparable with filopodia**. Int. J. Nanomedicine, *2:* 107–115, doi: 10.2147/nano.2007.2.1.107.

Heka Elektronik Dr. Schulze GmbH. a. **EPC 9 Manual**.

Tida User's Manual. .

Hodgkin, A. L. and Huxley, A. F. (1952). **A quantitative description of membrane current and its application to conduction and excitation in nerve**. J Physiol, *117:*, 500–544, doi: 10.1113/jphysiol.1952.sp004764.

Hofmann, B. *Communicating with electrogenic cells.* Phd, RWTH Aachen, (2009)http://darwin.bth.rwth-aachen.de/opus3/volltexte/2010/3140/.

Hofmann, B., Kätelhön, E., Schottdorf, M., Offenhäusser, A., and Wolfrum, B. (2011). **Nanocavity electrode array for recording from electrogenic cells**. Lab Chip, *11:*, 1054–1058, doi: 10.1039/c0lc00582g.

Hondrich, T. J., Lenyk, B., Shokoohimehr, P., Kireev, D., Maybeck, V., Mayer, D., and Offenhäusser, A. (2019)a. **MEA Recordings and Cell-Substrate Investigations with Plasmonic and Transparent, Tunable Holey Gold**. ACS Appl. Mater. Interfaces, *11:*, 46451–46461, doi: 10.1021/acsami.9b14948.

Hondrich, T. J., Müllender, L., Maybeck, V., and Offenhäusser, A. The effects of input synchronicity and localization on connectivity and synchronous network events in an all-optical investigation of anatomically modular and patterned neuronal cell cultures. (In preparation.).

Hondrich, T. J. J., Deußen, O., Grannemann, C., Brinkmann, D., and Offenhäusser, A. (2019)b. **Improvements of Microcontact Printing for Micropatterned Cell Growth by Contrast Enhancement**. *10:*, doi: 10.3390/mi10100659.

Hu, C., Sam, R., Shan, M., Nastasa, V., Wang, M., Kim, T., Gillette, M., Sengupta, P., and Popescu, G. (2019). **Optical excitation and detection of neuronal activity**. *12:*, doi: 10.1002/jbio.201800269.

Huang, Y. T., Chang, Y. L., Chen, C. C., Lai, P. Y., and Chan, C. K. (2017). **Positive feedback and synchronized bursts in neuronal cultures**. PLoS One, *12:* e0187276, doi: 10.1371/journal.pone.0187276.

Im, C. and Seo, J. M. (2016). **A review of electrodes for the electrical brain signal recording**. Biomed. Eng. Lett., *6:*, 104–112, doi: 10.1007/s13534-016-0235-1.

James, C. D., Spence, A. J. H., Dowell-Mesfin, N. M., Hussain, R. J., Smith, K. L., Craighead, H. G., Isaacson, M. S., Shain, W., and Turner, J. N. (2004). **Extracellular recordings from patterned neuronal networks using planar microelectrode arrays**. IEEE Trans. Biomed. Eng., *51:* 1640–1648, doi: 10.1109/TBME.2004.827252.

Jeong, Y. C., Lee, H. E., Shin, A., Kim, D. G., Lee, K. J., and Kim, D. (2020). **Progress in Brain-Compatible Interfaces with Soft Nanomaterials**. , doi: 10.1002/adma.201907522.

Jewell, S. W., Hocking, T. D., Fearnhead, P., and Witten, D. M. (2019). **Fast nonconvex deconvolution of calcium imaging data**. Biostatistics, *00:* 1–18, doi: 10.1093/biostatistics/kxy083.

Jin, L. *Optical control of primary rat cortical neural activity in vitro.* Phd, RWTH Aachen, (2016).

Jin, L., Lange, W., Kempmann, A., Maybeck, V., Günther, A., Gruteser, N., Baumann, A., and Offenhäusser, A. (2016). **High-efficiency transduction and specific expression of ChR2opt for optogenetic manipulation of primary cortical neurons mediated by recombinant adeno-associated viruses**. J. Biotechnol., *233:*, 171–180, doi: 10.1016/j.jbiotec.2016.07.001.

Joo, S., Song, S. Y., Nam, Y. S., and Nam, Y. (2018). **Stimuli-Responsive Neuronal Networking via Removable Alginate**

Masks. *2:*, doi: 10.1002/adbi.201800030.

Jun, N. Y. and Cardin, J. A. (2020). **Activation of distinct channelrhodopsin variants engages different patterns of network activity**. *7:*, doi: 10.1523/ENEURO.0222-18.2019.

Jungblut, M., Knoll, W., Thielemann, C., and Pottek, M. (2009). **Triangular neuronal networks on microelectrode arrays: An approach to improve the properties of low-density networks for extracellular recording**. Biomed. Microdevices, *11:*, 1269–1278, doi: 10.1007/s10544-009-9346-0.

Kaifosh, P., Zaremba, J. D., Danielson, N. B., and Losonczy, A. (2014). **SIMA: Python software for analysis of dynamic fluorescence imaging data**. Front. Neuroinform., *8:*, doi: 10.3389/fninf.2014.00080.

Kaiser, A. and Schreiber, T. (2002). **Information transfer in continuous processes**. Phys. D Nonlinear Phenom., *166:*, 43–62, doi: 10.1016/S0167-2789(02)00432-3.

Kapucu, F. E., Valkki, I., Christophe, F., Tanskanen, J. M., Johansson, J., Mikkonen, T., and Hyttinen, J. A. (2017). **On electrophysiological signal complexity during biological neuronal network development and maturation**. Proc. Annu. Int. Conf. IEEE Eng. Med. Biol. Soc. EMBS 3333–3338, doi: 10.1109/EMBC.2017.8037570.

Kiessling, V., Kreutzberger, A. J., Liang, B., Nyenhuis, S. B., Seelheim, P., Castle, J. D., Cafiso, D. S., and Tamm, L. K. (2018). **A molecular mechanism for calcium-mediated synaptotagmin-triggered exocytosis**. Nat. Struct. Mol. Biol., *25:*, 911–917, doi: 10.1038/s41594-018-0130-9.

Kim, C. K., Adhikari, A., and Deisseroth, K. (2017). **Integration of optogenetics with complementary methodologies in systems neuroscience**. Nat. Rev. Neurosci., *18:*, 222–235, doi: 10.1038/nrn.2017.15.

Kireev, D., Seyock, S., Lewen, J., Maybeck, V., Wolfrum, B., and Offenhäusser, A. (2017)a. **Graphene Multielectrode Arrays as a Versatile Tool for Extracellular Measurements**. , doi: 10.1002/adhm.201601433.

Kireev, D., Zadorozhnyi, I., Qiu, T., Sarik, D., Brings, F., Wu, T., Seyock, S., Maybeck, V., Lottner, M., Blaschke, B. M., Garrido, J., Xie, X., Vitusevich, S., Wolfrum, B., and Offenhäusser, A. (2017)b. **Graphene Field-Effect Transistors for In Vitro and Ex Vivo Recordings**. IEEE Trans. Nanotechnol., *16:* 140–147, doi: 10.1109/TNANO.2016.2639028.

Klapoetke, N. C., Murata, Y., Kim, S. S., Pulver, S. R., Birdsey-Benson, a., Cho, Y. K., Morimoto, T. K., Chuong, a. S., Carpenter, E. J., Tian, Z., Wang, J., Xie, Y., Yan, Z., Zhang, Y., Chow, B. Y., Surek, B., Melkonian, M., Jayaraman, V., Constantine-Paton, M., Wong, G. K., and Boyden, E. S. (2014). **Independent optical excitation of distinct neural populations**. Nat Methods, *11:* 338–346, doi: 10.1038/nmeth.2836.

Lai, M. C., Hung, T. Y., Lin, K. M., Sung, P. S., Wu, S. J., Yang, C. S., Wu, Y. J., Tsai, J. J., Wu, S. N., and Huang, C. W. (2018). **Sodium Metabisulfite: Effects on Ionic Currents and Excitotoxicity**. Neurotox. Res., *34:*, 1–15, doi: 10.1007/s12640-017-9844-4.

Langhans, S. A. (2018). **Three-dimensional in vitro cell culture models in drug discovery and drug repositioning**. Front. Pharmacol., *9:*, doi: 10.3389/fphar.2018.00006.

Lin, J. Y., Knutsen, P. M., Muller, A., Kleinfeld, D., and Tsien, R. Y. (2013). **ReaChR: A red-shifted variant of channelrhodopsin enables deep transcranial optogenetic excitation**. Nat. Neurosci., *16:* 1499–1508, doi: 10.1038/nn.3502.

Lin, M. Z. and Schnitzer, M. J. (2016). **Genetically encoded indicators of neuronal activity**. Nat. Neurosci., *19:* 1142–1153, doi: 10.1038/nn.4359.

Litvin, F. F., Sineshchekov, O. A., and Sineshchekov, V. A. (1978). **Photoreceptor electric potential in the phototaxis of the alga Haematococcus pluvialis**. Nature, *271:*, 476–478, doi: 10.1038/271476a0.

Lonardoni, D., Amin, H., Di, S., Maccione, A., Berdondini, L., and Nieus, T. (2017). **Recurrently connected and localized neuronal communities initiate coordinated spontaneous activity in neuronal networks**. PLoS Comput. Biol., *13:* e1005672, doi: 10.1371/journal.pcbi.1005672.

London, M. and Häusser, M. (2005). **Dendritic Computation**. Annu. Rev. Neurosci., *28:*, 503–532, doi: 10.1146/annurev.neuro.28.061604.135703.

Lowery, L. A. and Vactor, D. V. (2009). **The trip of the tip: understanding the growth cone machinery**. Nat. Rev. Mol. Cell Biol., *10:*, 332–343, doi: 10.1038/nrm2679.

Luhmann, H. J., Sinning, A., Yang, J. W., Reyes-Puerta, V., Stüttgen, M. C., Kirischuk, S., and Kilb, W. (2016). **Spontaneous neuronal activity in developing neocortical networks: From single cells to large-scale interactions**. Front. Neural Circuits, *10:*, doi: 10.3389/fncir.2016.00040.

Luo, X., Xing, Y., Galvan, D. D., Zheng, E., Wu, P., Cai, C., and Yu, Q. (2019). **Plasmonic Gold Nanohole Array for Surface-Enhanced Raman Scattering Detection of DNA Methylation**. ACS Sensors, *4:* 1534–1542, doi: 10.1021/acssensors.9b00008.

Lüthi, A. and McCormick, D. A. (1998). **H-Current: Properties of a Neuronal and Network Pacemaker**. Neuron, *21:*, 9–12, doi: 10.1016/s0896-6273(00)80509-7.

Markov, A., Wolf, N., Yuan, X., Mayer, D., Maybeck, V., Offenhäusser, A., and Wördenweber, R. (2017). **Controlled Engineering of Oxide Surfaces for Bioelectronics Applications Using Organic Mixed Monolayers**. ACS Appl. Mater. Interfaces, *9:* 29265–29272, doi: 10.1021/acsami.7b08481.

Markov, A., Maybeck, V., Wolf, N., Mayer, D., Offenhäusser, A., and Wördenweber, R. (2018). **Engineering of Neuron Growth and Enhancing Cell-Chip Communication via Mixed SAMs**. ACS Appl. Mater. Interfaces, *10:*, 18507–18514, doi: 10.1021/acsami.8b02948.

Markram, H., Helm, P. J., and Sakmann, B. (1995). **Dendritic calcium transients evoked by single back-propagating action potentials in rat neocortical pyramidal neurons**. J. Physiol., *485:* 583–600, doi: 10.1113/jphysiol.1995.sp020902.

Martinez-Rivas, A., González-Quijano, G. K., Proa-Coronado, S., Séverac, C., and Dague, E. (2017). **Methods of micropatterning and manipulation of cells for biomedical applications**. *8:*, doi: 10.3390/mi8120347.

Masquelier, T. and Deco, G. (2013). **Network Bursting Dynamics in Excitatory Cortical Neuron Cultures Results from the Combination of Different Adaptive Mechanism**. PLoS One, *8:* e75824, doi: 10.1371/journal.pone.0075824.

Maybeck, V. *Tools for non-invasive communication with electrogenic cells: optogenetic stimulation and diamond recording devices.* Phd, RWTH Aachen, (2011)http://darwin.bth.rwth-aachen.de/opus/volltexte/2012/3963/.

Maybeck, V., Schnitker, J., Li, W., Heuschkel, M., and Offenhäusser, A. (2016). **An evaluation of extracellular MEA versus optogenetic stimulation of cortical neurons**. *2:*, doi: 10.1088/2057-1976/2/5/055017.

Meunier, D., Lambiotte, R., and Bullmore, E. T. (2010). **Modular and hierarchically modular organization of brain networks**. Front. Neurosci., *4:*, doi: 10.3389/fnins.2010.00200.

Millet, L. J. and Gillette, M. U. (2012). **New perspectives on neuronal development via microfluidic environments**. Trends Neurosci., *35:* 752–761, doi: 10.1016/j.tins.2012.09.001.

Milos, F., Belu, A., Mayer, D., Maybeck, V., and Offenhäusser, A. **Polymer Nanopillars Accelerate Axon Initiation and Promote Guidance of Primary Cortical Neurons**. Prep.

Mölter, J., Avitan, L., and Goodhill, G. J. (2018). **Detecting neural assemblies in calcium imaging data**. *16:*, doi: 10.1186/s12915-018-0606-4.

Moriya, S., Yamamoto, H., Akima, H., Hirano-Iwata, A., Niwano, M., Kubota, S., and Sato, S. Modularity-dependent modulation of synchronized bursting activity in cultured neuronal network models. . In: 2017 Int. Jt. Conf. Neural Networks 1163–1168. IEEE, (2017). ISBN 978-1-5090-6182-2, doi: 10.1109/IJCNN.2017.7965983http://ieeexplore.ieee.org/document/7965983/.

Mosbacher, Y., Khoyratee, F., Goldin, M., Kanner, S., Malakai, Y., Silva, M., Grassia, F., Simon, Y. B., Cortes, J., Barzilai, A., Levi, T., and Bonifazi, P. (2020). **Toward neuroprosthetic real-time communication from in silico to biological neuronal network via patterned optogenetic stimulation**. *10:*, doi: 10.1038/s41598-020-63934-4.

Mourzina, Y., Kaliaguine, D., Schulte, P., and Offenhäusser, A. (2006). **Patterning chemical stimulation of reconstructed neuronal networks**. Anal. Chim. Acta, *575:*, 281–289, doi: 10.1016/j.aca.2006.06.010.

Mrksich, M., Dike, L. E., Tien, J., Ingber, D. E., and Whitesides, G. M. (1997). **Using microcontact printing to pattern the attachment of mammalian cells to Self-Assembled Monolayers of Alkanethiolates on Transparent Films of Gold and Silver**. Exp. Cell. Res., *235:*, 305–313.

Mukamel, E., Nimmerjahn, A., and Schnitzer, M. (2009). **Automated analysis of cellular signals from large-scale calcium imaging data.** Neuron, *63:* 747–760, doi: 10.1016/j.neuron.2009.08.009.Automated.

Müllender, L. *Graph Theoretical Analysis of Calcium Events in Designed Neuronal Networks.* Bachelor thesis, RWTH Aachen / FZ Jülich, (2020).

Multichannel systems. https://www.multichannelsystems.com/products/microelectrode-arrays. (accessed 2019-10-10).

Nagel, G., Szellas, T., Huhn, W., Kateriya, S., Adeishvili, N., Berthold, P., Ollig, D., Hegemann, P., and Bamberg, E. (2003). **Cation-Selective Membrane Channel**. Pnas, *100:* 13940–13945, doi: 10.1073/pnas.1936192100.

Nakai, J., Ohkura, M., and Imoto, K. (2001). **A high signal-to-noise Ca(2+) probe composed of a single green fluorescent protein.** Nat. Biotechnol., *19:*, 137–41, doi: 10.1038/84397.

Nam, Y., Branch, D. W., and Wheeler, B. C. (2006). **Epoxy-silane linking of biomolecules is simple and effective for patterning neuronal cultures**. Biosens. Bioelectron., *22:*, 589–597, doi: 10.1016/j.bios.2006.01.027.

Nikitin, E. S., Bal, N. V., Malyshev, A., Ierusalimsky, V. N., Spivak, Y., Balaban, P. M., and Volgushev, M. (2017). **Encoding of High Frequencies Improves with Maturation of Action Potential Generation in Cultured Neocortical Neurons**. Front. Cell. Neurosci., *11:*, doi: 10.3389/fncel.2017.00028.

Novak, J. L. and Wheeler, B. C. (1988). **Multisite hippocampal slice recording and stimulation using a 32 element microelectrode array**. J. Neurosci. Methods, *23:*, 149–159, doi: 10.1016/0165-0270(88)90187-2.

Obien, M. E. J., Deligkaris, K., Bullmann, T., Bakkum, D. J., and Frey, U. (2015). **Revealing neuronal function through microelectrode array recordings**. Front. Neurosci., *8:*, doi: 10.3389/fnins.2014.00423.

Offenhäusser, A., Bocker-Meffert, S., Decker, T., Helpenstein, R., Gasteier, P., Groll, J., Moller, M., Reska, A., Schafer, S., Schulte, P., and Vogt-Eisele, A. (2007). **Microcontact printing of proteins for neuronal cell guidance**. Soft Matter, *3:*, 290–298, doi: 10.1039/b607615g.

Ohsugi, I., Yamada, T., Inoue, Y., Mizuno, K., Okumoto, T., and Yoshimura, Y. Effect of Oxygen Plasma Treatment for Cell Adhesion Properties on Silicone Surface. . In: Wound Repair Regen., volume 13 A8, (2005), doi: 10.1111/j.1067-1927.2005.

130116q.xhttp://doi.wiley.com/10.1111/j.1067-1927.2005.130116q.x.

Okujeni, S. and Egert, U. (2019). **Self-organization of modular network architecture by activity-dependent neuronal migration and outgrowth**. Elife, *8:*, doi: 10.7554/eLife.47996.

Okujeni, S., Kandler, S., and Egert, U. (2017). **Mesoscale Architecture Shapes Initiation and Richness of Spontaneous Network Activity**. J. Neurosci., *37:* 3972–3987, doi: 10.1523/JNEUROSCI.2552-16.2017.

Orlandi, J. G., Soriano, J., Alvarez-Lacalle, E., Teller, S., and Casademunt, J. (2013). **Noise focusing and the emergence of coherent activity in neuronal cultures**. Nat. Phys., *9:*, 582–590, doi: 10.1038/nphys2686.

Pan, R. K. and Sinha, S. (2009). **Modularity produces small-world networks with dynamical time-scale separation**. *85:*, doi: 10.1209/0295-5075/85/68006.

Park, S., Loke, G., Fink, Y., and Anikeeva, P. (2019). **Flexible fiber-based optoelectronics for neural interfaces**. Chem. Soc. Rev., *48:*, 1826–1852, doi: 10.1039/c8cs00710a.

Pasquale, V., Massobrio, P., Bologna, L. L., Chiappalone, M., and Martinoia, S. (2008). **Self-organization and neuronal avalanches in networks of dissociated cortical neurons**. Neuroscience, *153:*, 1354–1369, doi: 10.1016/j.neuroscience.2008.03.050.

Pasquale, V., Martinoia, S., and Chiappalone, M. (2017). **Stimulation triggers endogenous activity patterns in cultured cortical networks**. *7:*, doi: 10.1038/s41598-017-08369-0.

Penn, Y., Segal, M., and Moses, E. (2016). **Network synchronization in hippocampal neurons**. Proc. Natl. Acad. Sci., *113:* 3341–3346, doi: 10.1073/pnas.1515105113.

Peyrin, J.-M., Deleglise, B., Saias, L., Vignes, M., Gougis, P., Magnifico, S., Betuing, S., Pietri, M., Caboche, J., Vanhoutte, P., Viovy, J.-L., and Brugg, B. (2011). **Axon diodes for the reconstruction of oriented neuronal networks in microfluidic chambers**. *11:*, doi: 10.1039/c1lc20014c.

Pickard, R. S. (1979). **A review of printed circuit microelectrodes and their production**. J. Neurosci. Methods, *1:*, 301–318, doi: 10.1016/0165-0270(79)90019-0.

Pnevmatikakis, E. A. (2019). **Analysis pipelines for calcium imaging data**. Curr. Opin. Neurobiol., *55:*, 15–21, doi: 10.1016/j.conb.2018.11.004.

Pnevmatikakis, E. A., Soudry, D., Gao, Y., Machado, T. A., Merel, J., Pfau, D., Reardon, T., Mu, Y., Lacefield, C., Yang, W., Ahrens, M., Bruno, R., Jessell, T. M., Peterka, D. S., Yuste, R., and Paninski, L. (2016). **Simultaneous Denoising, Deconvolution, and Demixing of Calcium Imaging Data**. Neuron, *89:*, 285–299, doi: 10.1016/j.neuron.2015.11.037.

Qi, H., Niu, L., Zhang, J., Chen, J., Wang, S., Yang, J., Guo, S., Lawson, T., Shi, B., and Song, C. (2018). **Large-area gold nanohole arrays fabricated by one-step method for surface plasmon resonance biochemical sensing**. Sci. China Life Sci., *61:* 476–482, doi: 10.1007/s11427-017-9270-x.

Rajnicek, A., Britland, S., and McCaig, C. (1997). **Contact guidance of CNS neurites on grooved quartz: influence of groove dimensions, neuronal age and cell type.** J. Cell Sci., *110:*, 2905–2913.

Reichinnek, S., von Kameke, A., Hagenston, A. M., Freitag, E., Roth, F. C., Bading, H., Hasan, M. T., Draguhn, A., and Both, M. (2012). **Reliable optical detection of coherent neuronal activity in fast oscillating networks in vitro**. Neuroimage, *60:*, 139–152, doi: 10.1016/j.neuroimage.2011.12.018.

Reina, G., González-Domínguez, J. M., Criado, A., Vázquez, E., Bianco, A., and Prato, M. (2017). **Promises, facts and challenges for graphene in biomedical applications**. Chem. Soc. Rev., *46:*, 4400–4416, doi: 10.1039/c7cs00363c.

Renault, R., Sukenik, N., Descroix, S., Malaquin, L., Viovy, J. L., Peyrin, J. M., Bottani, S., Monceau, P., Moses, E., and Vignes, M. (2015). **Combining microfluidics, optogenetics and calcium imaging to study neuronal communication in vitro**. PLoS One, *10:* e0120680, doi: 10.1371/journal.pone.0120680.

Renault, R., Durand, J.-B., Viovy, J.-L., and Villard, C. (2016). **Asymmetric axonal edge guidance: a new paradigm for building oriented neuronal networks**. Lab Chip, *16:*, 2188–2191, doi: 10.1039/C6LC00479B.

Rizo, J. and Xu, J. (2015). **The Synaptic Vesicle Release Machinery**. Annu. Rev. Biophys., *44:*, 339–367, doi: 10.1146/annurev-biophys-060414-034057.

Ronzitti, E., Emiliani, V., and Papagiakoumou, E. (2018). **Methods for Three-Dimensional All-Optical Manipulation of Neural Circuits**. *12:*, doi: 10.3389/fncel.2018.00469.

Roth, S., Bugnicourt, G., Bisbal, M., Gory-Fauré, S., Brocard, J., and Villard, C. (2012). **Neuronal architectures with axo-dendritic polarity above silicon nanowires**. Small, *8:* 671–675, doi: 10.1002/smll.201102325.

Rubinov, M. and Sporns, O. (2010). **Complex network measures of brain connectivity: Uses and interpretations**. Neuroimage, *52:*, 1059–1069, doi: 10.1016/j.neuroimage.2009.10.003.

Rueckl, M., Lenzi, S. C., Moreno-Velasquez, L., Parthier, D., Schmitz, D., Ruediger, S., and Johenning, F. W. (2017). **SamuROI, a Python-Based Software Tool for Visualization and Analysis of Dynamic Time Series Imaging at Multiple Spatial Scales**. Front. Neuroinform., *11:*, doi: 10.3389/fninf.2017.00044.

Rybak, I. A., Molkov, Y. I., Jasinski, P. E., Shevtsova, N. A., and Smith, J. C. (2014). **Rhythmic bursting in the pre-bötzinger**

complex: Mechanisms and models. Prog. Brain Res., *209:*, 1–23, doi: 10.1016/B978-0-444-63274-6.00001-1.

Ryynänen, T., Pekkanen-Mattila, M., Shah, D., Kreutzer, J., Kallio, P., Lekkala, J., and Aalto-Setälä, K. (2018). **Microelectrode array for noninvasive analysis of cardiomyocytes at the single-cell level**. *57:*, doi: 10.7567/JJAP.57.117001.

Saberi-Moghadam, S., Simi, A., Setareh, H., Mikhail, C., and Tafti, M. (2018). **In vitro Cortical Network Firing is Homeostatically Regulated: A Model for Sleep Regulation**. *8:*, doi: 10.1038/s41598-018-24339-6.

Sakmann, B. and Neher, E. (1984). **Patch Clamp Techniques for Studying Ionic Channels in Excitable Membranes**. Annu. Rev. Physiol., *46:*, 455–472, doi: 10.1146/annurev.ph.46.030184.002323.

Samhaber, R., Schottdorf, M., El Hady, A., Bröking, K., Daus, A., Thielemann, C., Stühmer, W., and Wolf, F. (2016). **Growing neuronal islands on multi-electrode arrays using an accurate positioning-μCP device**. J. Neurosci. Methods, *257:*, 194–203, doi: 10.1016/j.jneumeth.2015.09.022.

Sanes, D., Reh, T., and Harris, W. A. (2011)a. **Axon Growth and Guidance**. . In: Dev. Nerv. Syst., 3 edition, Academic Press, Oxford (UK), Chapter 5, p. 105 ff. ISBN 978-0-12-374539-2.

Sanes, D., Reh, T., and Harris, W. A. (2011)b. **Target Selection**. . In: Dev. Nerv. Syst., 3 edition, Academic Press, Oxford (UK), Chapter 6, p. 143 ff. ISBN 978-0-12-374539-2.

Sardi, S., Vardi, R., Sheinin, A., Goldental, A., and Kanter, I. (2017). **New Types of Experiments Reveal that a Neuron Functions as Multiple Independent Threshold Units**. *7:*, doi: 10.1038/s41598-017-18363-1.

Sartiani, L., Bochet, P., Cerbai, E., Mugelli, A., and Fischmeister, R. (2002). **Functional expression of the hyperpolarization-activated non-selective cation current/fin immortalized HL-1 cardiomyocytes**. J. Physiol., *545:* 81–92, doi: 10.1113/jphysiol.2002.021535.

Schindelin, J., Arganda-Carreras, I., Frise, E., Kaynig, V., Longair, M., Pietzsch, T., Preibisch, S., Rueden, C., Saalfeld, S., Schmid, B., Tinevez, J.-Y., White, D. J., Hartenstein, V., Eliceiri, K., Tomancak, P., and Cardona, A. (2012). **Fiji: an open-source platform for biological-image analysis.** Nat. Methods, *9:* 676–82, doi: 10.1038/nmeth.2019.

Schoenfisch, M. H. and Pemberton, J. E. (1998). **Air stability of alkanethiol self-assembled monolayers on silver and gold surfaces**. J. Am. Chem. Soc., *120:*, 4502–5413, doi: 10.1021/ja974301t.

Schöps, V., Lenyk, B., Huhn, T., Boneberg, J., Scheer, E., Offenhäusser, A., and Mayer, D. (2018). **Facile, non-destructive characterization of 2d photonic crystals using UV-vis-spectroscopy**. Phys. Chem. Chem. Phys., *20:* 4340–4346, doi: 10.1039/c7cp07498k.

Schreiber, T. (2000). **Measuring information transfer**. Phys. Rev. Lett., *85:* 461–464, doi: 10.1103/PhysRevLett.85.461.

Schwaab, D., Zentis, P., Winter, S., Meffert, S., Offenhäusser, A., and Mayer, D. (2013). **Generation of Protein Nanogradients by Microcontact Printing**. *52:*, doi: 10.7567/JJAP.52.05DA19.

Seo, K. J., Qiang, Y., Bilgin, I., Kar, S., Vinegoni, C., Weissleder, R., and Fang, H. (2017). **Transparent Electrophysiology Microelectrodes and Interconnects from Metal Nanomesh**. ACS Nano, *11:* 4365–4372, doi: 10.1021/acsnano.7b01995.

Shanahan, M. (2008). **Dynamical complexity in small-world networks of spiking neurons**. *78:*, doi: 10.1103/PhysRevE.78.041924.

Shaner, N. C., Lin, M. Z., McKeown, M. R., Steinbach, P. A., Hazelwood, K. L., Davidson, M. W., and Tsien, R. Y. (2008). **Improving the photostability of bright monomeric orange and red fluorescent proteins**. Nat. Methods, *5:* 545–551, doi: 10.1038/nmeth.1209.

Sharpe, J. C., Mitchell, J. S., Lin, L., Sedoglavich, N., and Blaikie, R. J. (2008). **Gold nanohole array substrates as immunobiosensors**. Anal. Chem., *80:* 2244–2249, doi: 10.1021/ac702555r.

Shein-Idelson, M., Cohen, G., Ben-Jacob, E., and Hanein, Y. (2016). **Modularity Induced Gating and Delays in Neuronal Networks**. PLoS Comput. Biol., *12:* e1004883, doi: 10.1371/journal.pcbi.1004883.

Shibue, R. and Komaki, F. (2020). **Deconvolution of calcium imaging data using marked point processes**. PLoS Comput. Biol., *16:* e1007650, doi: 10.1371/journal.pcbi.1007650.

Simitzi, C., Ranella, A., and Stratakis, E. (2017). **Controlling the morphology and outgrowth of nerve and neuroglial cells: The effect of surface topography**. Acta Biomater., *51:*, 21–52, doi: 10.1016/j.actbio.2017.01.023.

Smetters, D., Majewska, A., and Yuste, R. (1999). **Detecting action potentials in neuronal populations with calcium imaging**. Methods A Companion to Methods Enzymol., *18:*, 215–221, doi: 10.1006/meth.1999.0774.

Soltanian-Zadeh, S., Sahingur, K., Blau, S., Gong, Y., and Farsiu, S. (2019). **Fast and robust active neuron segmentation in two-photon calcium imaging using spatiotemporal deep learning**. Proc. Natl. Acad. Sci. U. S. A., *116:* 8554–8563, doi: 10.1073/pnas.1812995116.

Spira, M. E. and Hai, A. (2013). **Multi-electrode array technologies for neuroscience and cardiology**. Nat. Nanotechnol., *8:*, 83–94, doi: 10.1038/nnano.2012.265.

Sporns, O., Tononi, G., and Edelman, G. (2000). **Theoretical Neuroanatomy: Relating Anatomical and Functional Connectivity in Graphs and Cortical Connection Matrices**. Cereb. Cortex, *10:*, 127–141, doi: 10.1093/cercor/10.2.127.

Stett, A., Egert, U., Guenther, E., Hofmann, F., Meyer, T., Nisch, W., and Haemmerle, H. (2003). **Biological application**

of microelectrode arrays in drug discovery and basic research. Anal. Bioanal. Chem., *377:*, 486–495, doi: 10.1007/s00216-003-2149-x.

Stetter, O., Battaglia, D., Soriano, J., and Geisel, T. (2012). **Model-Free Reconstruction of Excitatory Neuronal Connectivity from Calcium Imaging Signals**. PLoS Comput. Biol., *8:* e1002653, doi: 10.1371/journal.pcbi.1002653.

Stringer, C. and Pachitariu, M. (2019). **Computational processing of neural recordings from calcium imaging data**. Curr. Opin. Neurobiol., *55:*, 22–31, doi: 10.1016/j.conb.2018.11.005.

Takahashi, N., Sasaki, T., Matsumoto, W., Matsuki, N., and Ikegaya, Y. (2010). **Circuit topology for synchronizing neurons in spontaneously active networks**. Proc. Natl. Acad. Sci., *107:* 10244–10249, doi: 10.1073/pnas.0914594107.

Taylor, A. M., Blurton-Jones, M., Rhee, S. W., Cribbs, D. H., Cotman, C. W., and Jeon, N. L. (2005). **A microfluidic culture platform for CNS axonal injury, regeneration and transport**. Nat. Methods, *2:* 599–605, doi: 10.1038/nmeth777.

Teller, S., Granell, C., De Domenico, M., Soriano, J., Gómez, S., and Arenas, A. (2014). **Emergence of Assortative Mixing between Clusters of Cultured Neurons**. PLoS Comput. Biol., *10:* e1003796, doi: 10.1371/journal.pcbi.1003796.

Teppola, H., Aćimović, J., and Linne, M.-L. (2019). **Unique Features of Network Bursts Emerge From the Complex Interplay of Excitatory and Inhibitory Receptors in Rat Neocortical Networks**. Front. Cell. Neurosci., *13:*, doi: 10.3389/fncel.2019.00377.

Theis, L., Berens, P., Froudarakis, E., Reimer, J., Román Rosón, M., Baden, T., Euler, T., Tolias, A. S., and Bethge, M. (2016). **Benchmarking Spike Rate Inference in Population Calcium Imaging**. Neuron, *90:*, 471–482, doi: 10.1016/j.neuron.2016.04.014.

Thompson, A. C., Stoddart, P. R., and Jansen, E. D. (2014). **Optical Stimulation of Neurons**. Curr. Mol. Imaging, *3:* 162–177, doi: 10.2174/2211555203666141117220611.

Thunemann, M., Lu, Y., Liu, X., Kılıç, K., Desjardins, M., Vandenberghe, M., Sadegh, S., Saisan, P. A., Cheng, Q., Weldy, K. L., Lyu, H., Djurovic, S., Andreassen, O. A., Dale, A. M., Devor, A., and Kuzum, D. (2018). **Deep 2-photon imaging and artifact-free optogenetics through transparent graphene microelectrode arrays**. *9:*, doi: 10.1038/s41467-018-04457-5.

Tian, L., Hires, S. A., Mao, T., Huber, D., Chiappe, M. E., Chalasani, S. H., Petreanu, L., Akerboom, J., McKinney, S. A., Schreiter, E. R., Bargmann, C. I., Jayaraman, V., Svoboda, K., and Looger, L. L. (2009). **Imaging neural activity in worms, flies and mice with improved GCaMP calcium indicators**. Nat. Methods, *6:* 875–881, doi: 10.1038/nmeth.1398.

Tran, D.-P., Lu, H.-I., and Lin, C.-K. (2018). **Conductive Characteristics of Indium Tin Oxide Thin Film on Polymeric Substrate under Long-Term Static Deformation**. *8:*, doi: 10.3390/coatings8060212.

Tsai, C. Y., Chang, M. C., and I, L. (2008). **Robustness and variability of pathways in the spontaneous synchronous bursting of clusterized cortical neuronal networks in vitro**. J. Phys. Soc. Japan, *77:* 084803, doi: 10.1143/JPSJ.77.084803.

Tyukin, I. Y., Iudin, D., Iudin, F., Tyukina, T., Kazantsev, V., Mukhina, I., and Gorban, A. N. (2019). **Simple model of complex dynamics of activity patterns in developing networks of neuronal cultures**. PLoS One, *14:* e0218304., doi: 10.1371/journal.pone.0218304.

Vitriol, E. A. A. and Zheng, J. Q. Q. (2012). **Growth Cone Travel in Space and Time: the Cellular Ensemble of Cytoskeleton, Adhesion, and Membrane**. Neuron, *73:*, 1068–1081, doi: 10.1016/j.neuron.2012.03.005.

Vosgueritchian, M., Lipomi, D. J., and Bao, Z. (2012). **Highly conductive and transparent PEDOT:PSS films with a fluorosurfactant for stretchable and flexible transparent electrodes**. Adv. Funct. Mater., *22:*, 421–428, doi: 10.1002/adfm.201101775.

Wagenaar, D. A., Nadasdy, Z., and Potter, S. M. (2006)a. **Persistent dynamic attractors in activity patterns of cultured neuronal networks**. *73:*, doi: 10.1103/PhysRevE.73.051907.

Wagenaar, D. A., Pine, J., and Potter, S. M. (2006)b. **An extremely rich repertoire of bursting patterns during the development of cortical cultures**. *7:*, doi: 10.1186/1471-2202-7-11.

Wang, K., Frewin, C. L., Esrafilzadeh, D., Yu, C., Wang, C., Pancrazio, J. J., Romero-Ortega, M., Jalili, R., and Wallace, G. (2019)a. **High-Performance Graphene-Fiber-Based Neural Recording Microelectrodes**. *31:*, doi: 10.1002/adma.201805867.

Wang, W., Kim, C. K., and Ting, A. Y. (2019)b. **Molecular tools for imaging and recording neuronal activity**. Nat. Chem. Biol., *15:*, 101–110, doi: 10.1038/s41589-018-0207-0.

Wei, W., Song, Y., Wang, L., Zhang, S., Luo, J., Xu, S., and Cai, X. (2015). **An implantable microelectrode array for simultaneous L-glutamate and electrophysiological recordings in vivo**. *1:*, doi: 10.1038/micronano.2015.2.

Weidlich, S. D. *Nanoscale 3D structures towards improved cell-chip coupling on microelectrode arrays.* Phd, RWTH Aachen, (2017)http://publications.rwth-aachen.de/record/710199.

Wheeler, B. C. and Brewer, G. J. (2010). **Designing neural networks in culture**. Proc. IEEE, *98:* 398–406, doi: 10.1109/JPROC.2009.2039029.

Wilson, H. R. and Cowan, J. D. (1972). **Excitatory and Inhibitory Interactions in Localized Populations of Model Neurons**. Biophys. J., *12:*, doi: 10.1016/S0006-3495(72)86068-5.

Wrosch, J. K., Einem, V. V., Breininger, K., Dahlmanns, M., Maier, A., Kornhuber, J., and Groemer, T. W. (2017). **Rewiring of**

neuronal networks during synaptic silencing. *7:*, doi: 10.1038/s41598-017-11729-5.

Wu, C., Zhu, X., Man, T., Chung, P. S., Teitell, M. A., and Chiou, P. Y. (2018). **Lift-off cell lithography for cell patterning with clean background**. Lab Chip, *18:*, 3074–3078, doi: 10.1039/c8lc00726h.

Xu, B., Zhu, M., Zhang, W., Zhen, X., Pei, Z., Xue, Q., Zhi, C., and Shi, P. (2016). **Ultrathin MXene-Micropattern-Based Field-Effect Transistor for Probing Neural Activity**. Adv. Mater., *28:*, 3333–3339, doi: 10.1002/adma.201504657.

Yamamoto, H., Matsumura, R., Takaoki, H., Katsurabayashi, S., Hirano-Iwata, A., and Niwano, M. (2016). **Unidirectional signal propagation in primary neurons micropatterned at a single-cell resolution**. *109:*, doi: 10.1063/1.4959836.

Yamamoto, H., Moriya, S., Ide, K., Hayakawa, T., Akima, H., Sato, S., Kubota, S., Tanii, T., Niwano, M., Teller, S., Soriano, J., and Hirano-Iwata, A. (2018). **Impact of modular organization on dynamical richness in cortical networks**. *4:*, doi: 10.1126/sciadv.aau4914.

Yang, Z. and Murray, K. T. (2011). **Ionic mechanisms of pacemaker activity in spontaneously contracting atrial HL-1 cells**. J. Cardiovasc. Pharmacol., *57:* 28–36, doi: 10.1097/FJC.0b013e3181fda7c4.

Yizhar, O., Fenno, L. E., Prigge, M., Schneider, F., Davidson, T. J., Ogshea, D. J., Sohal, V. S., Goshen, I., Finkelstein, J., Paz, J. T., Stehfest, K., Fudim, R., Ramakrishnan, C., Huguenard, J. R., Hegemann, P., and Deisseroth, K. (2011). **Neocortical excitation/inhibition balance in information processing and social dysfunction**. Nature, *477:*, 171–178, doi: 10.1038/nature10360.

Yoo, J., Kwak, H., Kwon, J., Ha, G. E., Lee, E. H., Song, S., Na, J., Lee, H. J., Lee, J., Hwangbo, A., Cha, E., Chae, Y., Cheong, E., and Choi, H. J. (2020). **Long-term Intracellular Recording of Optogenetically-induced Electrical Activities using Vertical Nanowire Multi Electrode Array**. *10:*, doi: 10.1038/s41598-020-61325-3.

Youssef, W., Randall Wickett, R., and Hoath, S. B. (2001). **Surface free energy characterization of vernix caseosa. Potential role in waterproofing the newborn infant**. Ski. Res. Technol., *7:*, 10–17, doi: 10.1034/j.1600-0846.2001.007001010.x.

Ypey, D. L. and DeFelice, L. J. (1997). **The Patch-Clamp Technique Explained and Exercised With the Use of Simple Electrical Equivalent Circuits.** . In: Electr. Prop. Cells, 1 edition, Springer US, New York, New York. ISBN 9780306453458, doi: 10.1007/978-1-4899-0248-1.

Yuan, X., Wolf, N., Hondrich, T. J., Shokoohimehr, P., Milos, F., Glass, M., Mayer, D., Maybeck, V., Prömpers, M., Offenhäusser, A., and Wördenweber, R. (2020). **Engineering Biocompatible Interfaces via Combinations of Oxide Films and Organic Self-Assembled Monolayers**. ACS Appl. Mater. Interfaces, *12:*, 17121–17129, doi: 10.1021/acsami.0c02141.

Yuste, R. (2015). **From the neuron doctrine to neural networks**. Nat. Rev. Neurosci., *16:*, 487–497, doi: 10.1038/nrn3962.

Zhao, Y., Araki, S., Wu, J., Teramoto, T., Chang, Y.-F., Nakano, M., Abdelfattah, A. S., Fujiwara, M., Ishihara, T., Nagai, T., and Campbell, R. E. (2011). **An Expanded Palette of Genetically Encoded Ca2+ Indicators**. Science (80-.)., *333:*, 1888–1891, doi: 10.1126/science.1208592.

Zhu, G., Du, L., Jin, L., and Offenhäusser, A. (2016). **Effects of morphology constraint on electrophysiological properties of cortical neurons**. *6:*, doi: 10.1038/srep23086.

Own Publications

Journal Articles

Hondrich, T. J. J., Deußen, O., Grannemann, C., Brinkmann, D., Offenhäusser A. (2019). **Improvements of Microcontact Printing for Micropatterned Cell Growth by Contrast Enhancement.** Micromachines. 10(659). doi:10.3390/mi10100659

Hondrich, T. J. J., Lenyk, B., Shokoohimehr, P., Kireev, D., Maybeck, V., Mayer, D., Offenhäusser, A. (2019). **MEA Recordings and Cell-Substrate Investigations with Plasmonic and Transparent, Tunable Holey Gold.** ACS Applied Materials and Interfaces, 11, 46451–46461. doi:10.1021/acsami.9b14948

Hondrich, T. J. J., Müllender, L., Maybeck, V., Offenhäusser, A. (*In preparation*). **The effects of input synchronicity and localization on connectivity and synchronous network events in an all-optical investigation of anatomically modular and patterned neuronal cell cultures.**

Conference Posters and Talks

Poster - Hondrich, T. J. J., Tihaa, I., Lewen, J., Offenhäusser A. (2018). **Directing Neuronal Growth And Signal Propagation On MEA.** MEA Meeting 2018, Reutlingen, Germany. doi:10.3389/conf.fncel.2018.38.00056

Poster - Hondrich, T. J. J., Brinkmann, D., Tihaa, I., Lanzrath, H., Offenhäusser A. (2018). **Loops and Triangles: Investigating network activity in engineered neuronal networks.** INM-ICS Retreat 2018, Jülich, Germany.

Talk - Hondrich, T. J. J., Grannemann, C., Brinkmann, D., Offenhäusser A. (2019). **Lighting Up Neurons - All Optical Interrogation of Designed Neuronal Networks.** INM-ICS Retreat 2019, Jülich, Germany.

Poster - Hondrich, T. J. J., Müllender, L., Grannemann, C., Brinkmann, D., Maybeck, V., Offenhäusser A. (2020). **The effect of sub-populations and input synchronicity on neuronal network properties and network event initiation.** FENS Virtual Forum 2020, Online.

Other Talks

Talk - Hondrich, T. J. J. (2018). **Functional Near-Infrared Spectroscopy - Background, Design, Application.** Int. Workshop Bioelectronics - New Challenges Outlook, Hirschegg, Austria.

Talk - Hondrich, T. J. J. (2019). **Classical signal processing vs artificial intelligence in neuronal signal processing.** Int Workshop Neuroelectronics, Hirschegg, Austria.

Acknowledgments

This PhD thesis would not have been possible without the direct and indirect help of so many people. First of all, thank you to Prof. Andreas Offenhäusser (a.k.a. Chef) for providing support, supervision, tips of whom to ask for help, rooms, equipment, and open door policy - and most of all - a high amount of freedom to pursue my ideas. Also, I am grateful to Dr. Vanessa Maybeck for her huge biological knowledge, her constant efforts in making the lab run smoothly, her close supervision and tips and tricks (both practical and theoretical), and for her chili-con-or-sin-carnes during the day of the lab. Thank you also to Dr. Dirk Mayer for offering advice in the field of chemistry and scientific and non-scientific discussions during seminars and lunch breaks. My thanks also goes to Tina Breuer for keeping the cells coming and the lab running (Danke, Tina!). Moreover, I would like to thank Marko Banzet, Michael Prömpers, Regina Stockmann, and Elke Brauweiler-Reuters for answering my uninformed questions about cleanroom technology and providing me with chips, stamps, FIB cuts, and molds (Danke, allerseits).

Of course I would also like to thank my fellow PhD and other students who also walked the way through ICS8-PGI8/ICS8/IBI3. These include Irina, Vivi, Niko, Frano, Bohdan, Pegah, Xiaobo, Dmitry, Caro, Olli, Kagithiri, Corinna, Dominik, Lukas, Jana, Adel, Erfan, Jamal, Jelena, Dieter, Christian, Matthias, Mattis, Johannes, Ann, Chris, Gabi, Ekaterina, Lena, Jiali, Ruoyan, Lei, Joscha, and many more.

Last, but definitely not least, I would like to thank my family. Emil, weil du eine wunderbare Ablenkung bist, ohne die vieles irgendwie langweiliger wäre; Solveig, for having my back, for your constant love and support, and getting my head out of work when I was stuck in non-productive thought circles, and for just being great. My mother I thank for her constant support and love. Her and my parents-in-law I thank for relaxing family meetings, and many other things - and without your help in taking care of Emil (especially during the Corona crisis) I could not have written this thesis.

Appendix A

Additional Figures and Tables

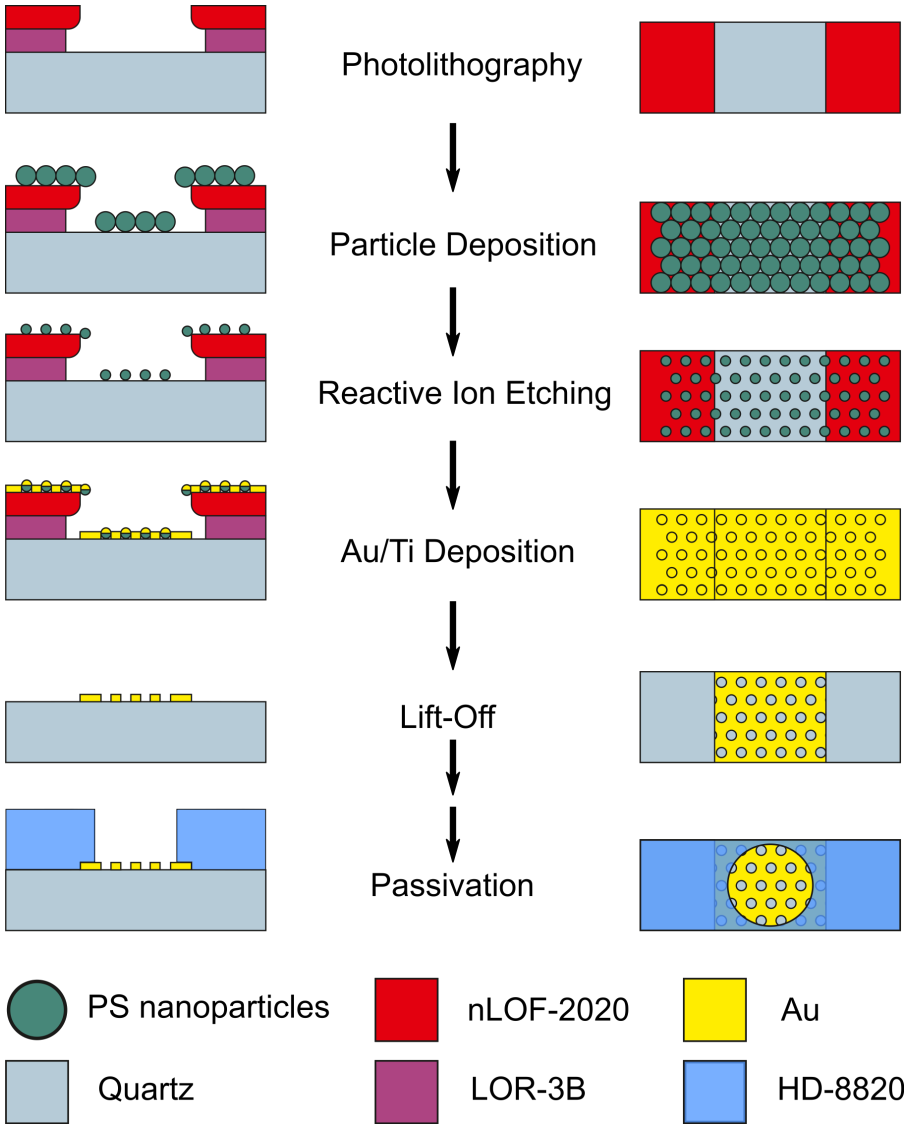

Figure A.1 – Fabrication process of Holey MEAs. Taken from Hondrich et al. (2019a).

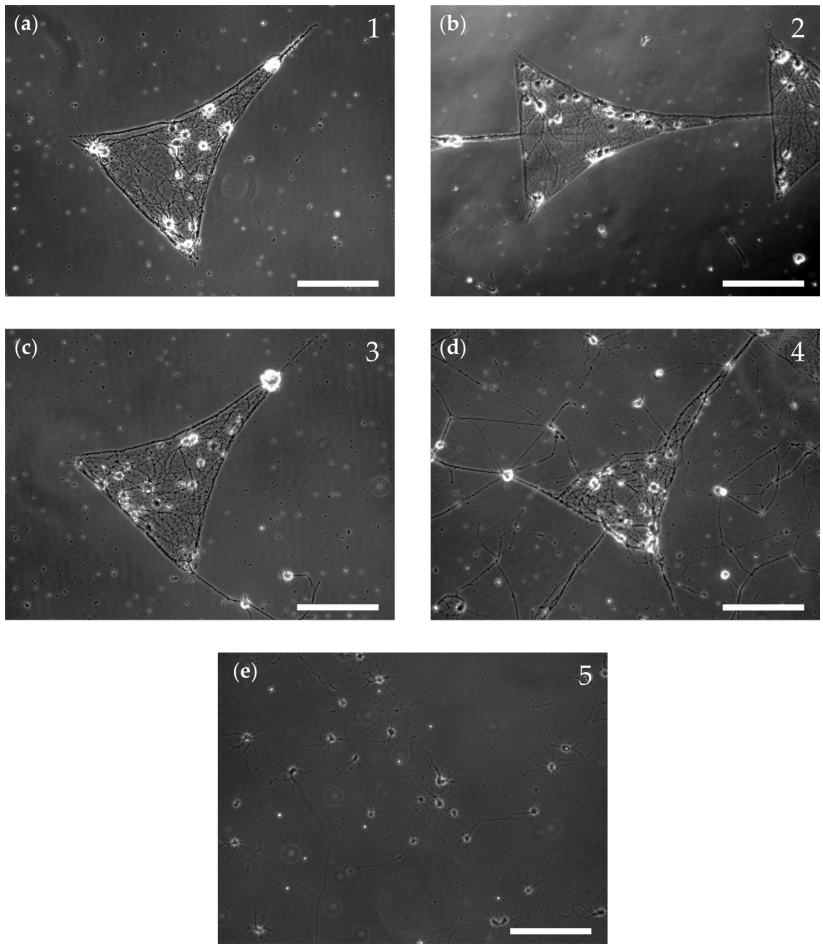

Figure A.2 – Quality categories 1-5 of patterns. Example micrographs for clarification of categories quantified section 3.1.1.1.

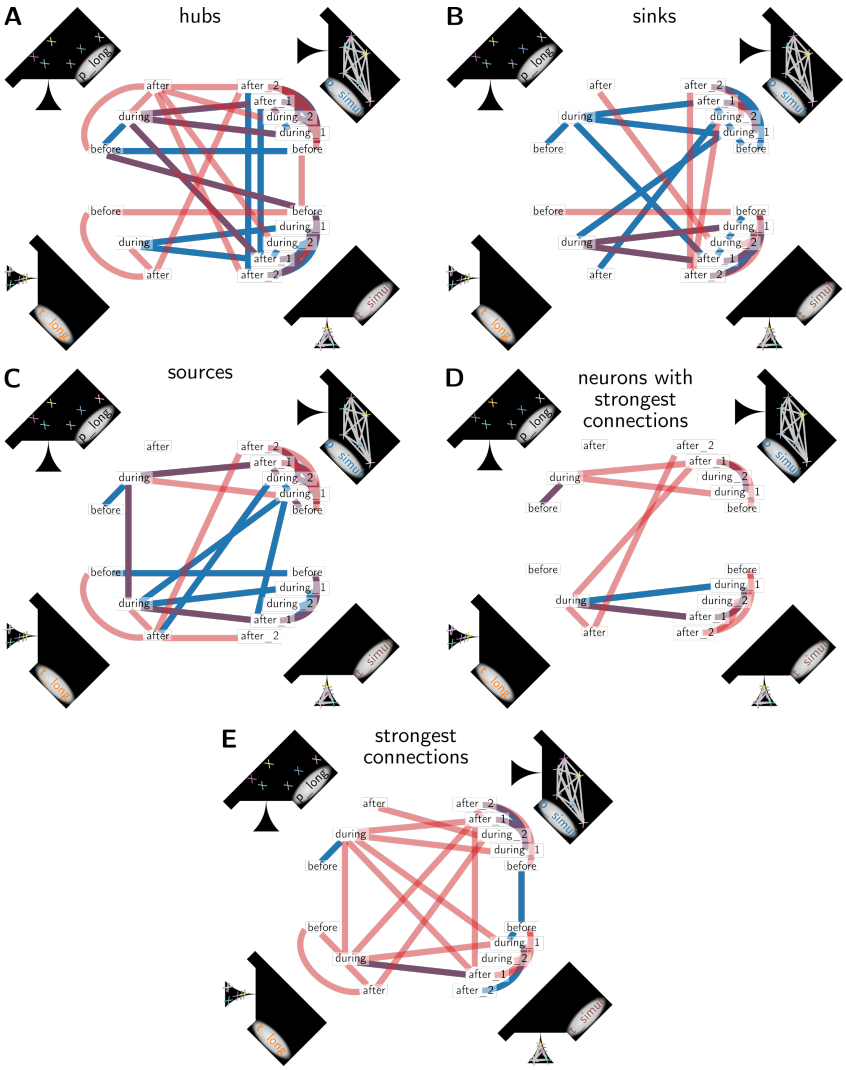

Figure A.3 – Similarity special nodes between different stimulation routines. The same comparison shown in Figure 5.14 A for hub nodes (**A**), sink nodes (**B**), source nodes (**C**), nodes participating in the 0.5% strongest edges (**D**), and the strongest edges themselves (**E**). **A** is a duplicate of Figure 5.14 A.

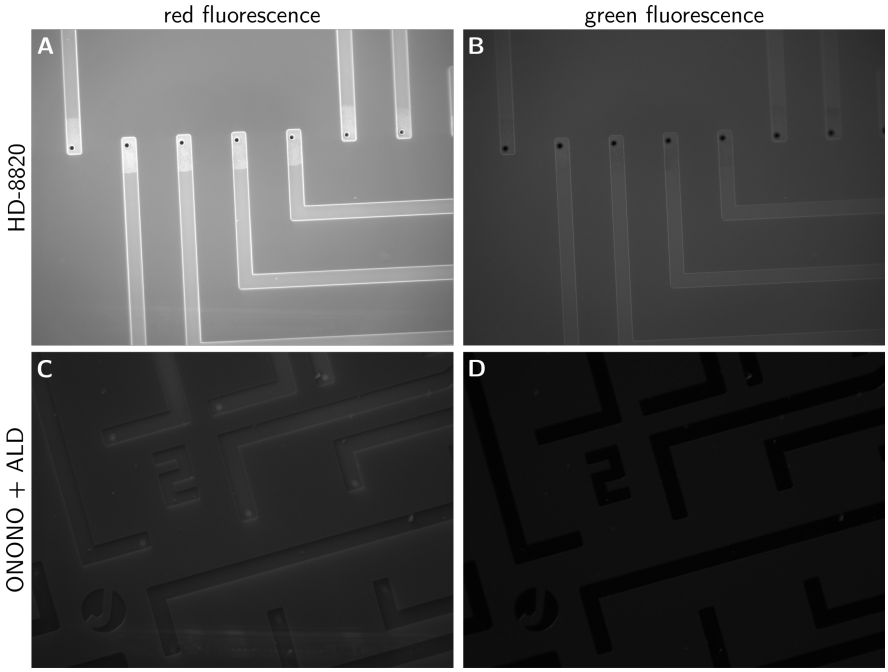

Figure A.4 – Autofluorescence of ONONO and HD-8820. Example fluorescence micrographs of MEAs with HD-8820 passivation (**A**-**B**) and with ONONO passivation (**C**-**D**). ONONO passivation is covered with an additional metal-oxide layer applied by atomic layer deposition (ALD). Figure corresponds to section 3.1.2.

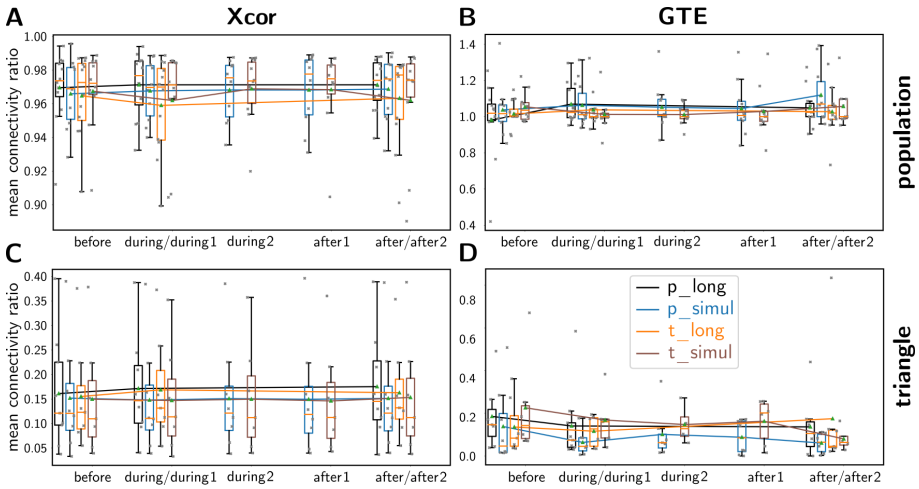

Figure A.5 – Mean connectivity ratio in triangle and population. (A-D) Ratio of the mean edge weights in the population (**A**, **B**) or the triangle (**C**, **D**) and the mean edge weights of the complete network. **(A-D)** Graphs were based on Xcor (**A**, **C**) or GTE (**B**, **D**). Figure corresponds to section 5.4.2. Asterisks and box plots as explained in section 2.6.

Measure	Condition	Mi Med	Mi Q1	Mi Q3	Maj Median	Maj Q1	Maj Q3
Arc Start	spont	0.500	0.333	0.750	0.000	0.000	1.000
Arc Start	*p*	0.375	0.300	0.525	0.333	0.000	0.568
Arc Start	*t*	0.750	0.237	0.917	0.388	0.094	0.475
Arc Start	*test*	0.357	0.054	0.500	0.000	0.000	0.000
Arc End	spont	0.250	0.000	0.667	1.000	0.000	1.000
Arc End	*p*	0.520	0.510	0.546	0.667	0.518	0.875
Arc End	*t*	0.615	0.250	0.833	0.467	0.177	0.900
Arc End	*test*	0.464	0.107	0.500	1.000	1.000	1.000
Str. Part.	spont	1.000	1.000	1.000	1.000	1.000	1.000
Str. Part.	*p*	1.000	1.000	1.000	1.000	1.000	1.000
Str. Part.	*t*	1.000	1.000	1.000	1.000	1.000	1.000
Str. Part.	*test*	1.000	1.000	1.000	1.000	1.000	1.000
Arc Part.	spont	1.000	0.667	1.000	1.000	1.000	1.000
Arc Part.	*p*	1.000	1.000	1.000	1.000	1.000	1.000
Arc Part.	*t*	1.000	1.000	1.000	1.000	1.000	1.000
Arc Part.	*test*	1.000	0.732	1.000	1.000	1.000	1.000

Table A.1 – Exact values of arc participation in Figure 4.15. Q1 is the upper, Q3 the lower quartile, and Med the median. Mi and Maj indicate minor and major SNEs, respectively. Str. Part. and Arc Part. correspond to Figure 4.15 C and D, respectively

Measure	Condition	Mi Med	Mi Q1	Mi Q3	Maj Median	Maj Q1	Maj Q3
Ave. Del.	spont	0.080	0.040	0.151	0.022	0.007	0.026
Ave. Del.	*p*	0.056	0.026	0.086	0.032	0.006	0.042
Ave. Del.	*t*	0.008	0.005	0.012	0.004	0.003	0.008
Ave. Del.	*test*	0.101	0.073	0.166	0.032	0.032	0.032
Min. Del.	spont	0.040	-0.121	0.101	-0.232	-0.232	-0.201
Min. Del.	*p*	-0.121	-0.214	0.000	-0.201	-0.297	-0.121
Min. Del.	*t*	-0.020	-0.040	-0.013	-0.040	-0.111	-0.030
Min. Del.	*test*	0.040	-0.075	0.108	-0.101	-0.101	-0.101
Max. Del.	spont	0.221	0.121	0.302	0.303	0.271	0.342
Max. Del.	*p*	0.282	0.201	0.362	0.262	0.196	0.343
Max. Del.	*t*	0.040	0.033	0.078	0.070	0.040	0.121
Max. Del.	*test*	0.226	0.146	0.312	0.231	0.231	0.231

Table A.2 – Exact values of delays in Figure 4.19. Q1 is the upper, Q3 the lower quartile, and Med the median. Mi and Maj indicate minor and major SNEs, respectively.

Band / Volume 54
Optimization of powder and ceramic processing, electrical characterization and defect chemistry in the system $Yb_xCa_{1-x}MnO_3$
M. Rahmani (2018), XIV, 164 pp
ISBN: 978-3-95806-323-5

Band / Volume 55
Organic-Metal Hybrid Interfaces at the Mesoscopic Scale
G. Zamborlini (2018), xi, 133 pp
ISBN: 978-3-95806-328-0

Band / Volume 56
Configurable frequency synthesizer for large scale physics experiments
N. Parkalian (2019), xxi, 114 pp
ISBN: 978-3-95806-393-8

Band / Volume 57
Resistive switching phenomena in stacks of binary transition metal oxides grown by atomic layer deposition
H. Zhang (2019), ix, 196 pp
ISBN: 978-3-95806-399-0

Band / Volume 58
Element-Selective Investigation of Femtosecond Spin Dynamics in Ni_xPd_{1-x} Magnetic Alloys using Extreme Ultraviolet Radiation
S. Gang (2019), 93, xx pp
ISBN: 978-3-95806-411-9

Band / Volume 59
Defect engineering in oxide thin films
F. V. E. Hensling (2019), 10, 164 pp
ISBN: 978-3-95806-424-9

Band / Volume 60
Chemical control of the electrical surface properties of *n*-doped transition metal oxides
M. Andrä (2019), X, 150, XXXVIII pp
ISBN: 978-3-95806-448-5

Band / Volume 61
Digital Signal Processing and Mixed Signal Control of Receiver Circuitry for Large-Scale Particle Detectors
P. Muralidharan (2020), xv, 109 pp
ISBN: 978-3-95806-489-8

Band / Volume 62
Development of Electromagnetic Induction Measurement and Inversion Methods for Soil Electrical Conductivity Investigations
X. Tan (2020), ix, 124 pp
ISBN: 978-3-95806-490-4

Band / Volume 63
Novel System Approach for a mm-range Precision Indoor Positioning System
R. Xiong (2020), xi, 144 pp
ISBN: 978-3-95806-517-8

Band / Volume 64
Quantitative investigation of group III-nitride interfaces by a combination of scanning tunneling microscopy and off-axis electron holography
Y. Wang (2021), 102 pp
ISBN: 978-3-95806-534-5

Band / Volume 65
Scalable Control Electronics for a Spin Based Quantum Computer
L. Geck (2021), xiv, 114, xv-xxxiii
ISBN: 978-3-95806-540-6

Band / Volume 66
DNA-capped silver nanoparticles for stochastic nanoparticle impact electrochemistry
L. Nörbel (2021), VI, 142 pp
ISBN: 978-3-95806-541-3

Band / Volume 67
Development, characterization, and application of intraretinal implants
V. Rincón Montes (2021), XII, 173 pp
ISBN: 978-3-95806-553-6

Band / Volume 68
Optogenetic and electrical investigation of network dynamics in patterned neuronal cultures
T. J. J. Hondrich (2021), x, 177 pp
ISBN: 978-3-95806-555-0

Information
Band / Volume 68
ISBN 978-3-95806-555-0

Mitglied der Helmholtz-Gemeinschaft

JÜLICH
Forschungszentrum